



Dynamics of VEGF-A binding at VEGFR2 and NRP1

Chloe J. Peach, BSc (Hons)

Thesis submitted to the University of Nottingham
for the degree of Doctor of Philosophy

APRIL 2020

This thesis is entirely the candidate's own work. The experiments described in this thesis were performed by the author between October 2016 and February 2020 in the Cell Signalling Research Group at the Centre of Membrane Proteins and Receptors, University of Nottingham, UK. No part of this material has been submitted previously for a degree or any other qualification at any University.

i. ABSTRACT

Vascular Endothelial Growth Factor A (VEGF-A) is a key mediator of angiogenesis, a process dysregulated in tumour development. Alternative splicing of the *Vegfa* gene leads to distinct endogenous VEGF-A isoforms with differential signalling and expression. These include pro-angiogenic $VEGF_{165}a$, 'anti-angiogenic' $VEGF_{165}b$ and freely diffusible $VEGF_{121}a$. VEGF-A primarily signals via its cognate receptor tyrosine kinase (RTK), VEGF Receptor 2 (VEGFR2). Signalling can be potentiated by its co-receptor Neuropilin-1 (NRP1), a transmembrane protein also found at high levels in malignant tumours. Despite numerous approved anti-cancer therapeutics targeting VEGF-A/VEGFR2 signalling, there is limited quantitative pharmacological understanding of VEGF-A isoforms at full-length VEGFR2 or NRP1 in living cells. This thesis explored the spatial and temporal dynamics of ligand binding to VEGFR2 and its co-receptor NRP1.

First, $VEGF_{165}a$, $VEGF_{165}b$ and $VEGF_{121}a$ were stoichiometrically labelled with tetramethylrhodamine (TMR) in collaboration with Promega Corporation. $VEGF_{xxx}x$-TMR ligand binding was quantified in real-time at 37°C using bioluminescence resonance energy transfer (BRET) with VEGFR2 or NRP1 tagged with NanoLuciferase (NanoLuc). This technique was used to discriminate between VEGF-A binding to two distinct classes of membrane protein expressed in isolation in HEK293T cells. While all VEGF-A isoforms had similar nanomolar affinities at NanoLuc-VEGFR2, not all isoforms were able to interact with NanoLuc-NRP1. This also revealed marked differences in the kinetic binding profiles of $VEGF_{165}a$-TMR for NRP1 and VEGFR2, despite similar binding affinities. Using live cell imaging, we identified differences between the localisation of HaloTag-VEGFR2 and HaloTag-NRP1. Whereas NRP1 remained at the plasma membrane, VEGFR2 was subject to constitutive and ligand-driven endocytosis in HEK293T cells.

Second, we investigated the relationship between receptor localisation and ligand binding given the complex trafficking of VEGFR2 observed in Chapter 3. Each fluorescent VEGF-A isoform was internalised with VEGFR2 within 30 minutes. At NanoLuc-VEGFR2, there was a decline in BRET signal for each fluorescent VEGF-A isoform following a peak at 20 minutes in living cells. This was absent for ligand binding at NanoLuc-NRP1.
We further exploited these techniques to gain insight into how inhibition of VEGFR2 phosphorylation influenced ligand binding and endocytosis using a tyrosine phosphorylation deficient receptor mutant. In the absence of phosphorylation, there was an elevation in the BRET signal upon stimulation with fluorescent VEGF-A. VEGFR2 phosphorylation at Y951, Y1054, Y1059, Y1175 or Y1214 was not required for endocytosis. Membrane preparations were then used to probe VEGF-A/VEGFR2 binding in the absence of this endocytic component. Here, ligand binding profiles were

maintained for 90 minutes and reached equilibrium. This assay was exploited to directly probe how ligand/receptor interactions were influenced by the acidic pH in the endosomal microenvironment. Interestingly, VEGF-TMR had a shorter residence time at NanoLuc-VEGFR2 at a pH similar to that in endosomes.

Third, we investigated the effect of co-expressing VEGFR2 and NRP1 in the same living cell. Colocalisation was monitored between HaloTag-VEGFR2 and SnapTag-NRP1 in live cells upon stimulation with $VEGF_{165}$b or $VEGF_{165}$a. Using receptor-receptor BRET, we confirmed that VEGFR2 and NRP1 were in close proximity in the absence of ligand. We isolated the real-time pharmacology of $VEGF_{xxx}$x-TMR at a defined VEGFR2/NRP1 complex using split NanoLuc Binary Technology (NanoBiT). As NanoBiTs require complementation to emit luminescence, BRET can only occur from a heteromeric complex of LgBiT-VEGFR2 and HiBiT-NRP1. Despite having faster kinetics at NRP1 in isolation, $VEGF_{165}$a-TMR bound to the VEGFR2/NRP1 complex with dynamics comparable to those of NanoLuc-VEGFR2. $VEGF_{165}$b-TMR had a ligand binding profile that largely remained elevated in cells over 90 minutes, despite being selective for VEGFR2. This thesis applied quantitative technologies to monitor real-time ligand binding at receptors that contribute to physiological and patho-physiological angiogenesis. These findings have implications for how NRP1 modulates VEGFR2 as a potential target in drug discovery.

ii. PUBLICATIONS ARISING

PAPERS

Peach CJ, Kilpatrick LE, Woolard J, Hill SJ. (2019) Comparison of the ligand binding properties of fluorescent VEGF-A isoforms to VEGFR2 in living cells and membrane preparations using NanoBRET. *British Journal of Pharmacology*. 176: 3220–35.

Kilpatrick LE*, Alcobia DC*, White CW, Peach CJ, Glenn JR, Zimmerman K, Kondrashov A, Pfleger KDG, Friedman-Ohana R, Robers MB, Wood KV, Sloan EK, Woolard J, Hill SJ. (2019) Complex formation between VEGFR2 and the β_2-adrenoceptor. *Cell Chemical Biology*. 26: 830–41.

Peach CJ*, Kilpatrick LE*, Friedman-Ohana R, Zimmerman K, Robers MB, Wood KV, Woolard J, Hill SJ. (2018) Real-Time Ligand Binding of Fluorescent VEGF-A Isoforms that Discriminate between VEGFR2 and NRP1 in Living Cells. *Cell Chemical Biology*. 25: 1208–18.

*Authors contributed equally to this work.

REVIEWS

Peach CJ, Mignone VW, Augusta Arruda M, Alcobia DC, Hill SJ, Kilpatrick LE, Woolard J. (2018) Molecular Pharmacology of VEGF-A Isoforms: Binding and Signalling at VEGFR2. *International Journal of Molecular Sciences*. 19: 1-27.

CONFERENCE PROCEEDINGS

Peach CJ, Kilpatrick LE, Woolard J, Hill SJ. (2019) Influence of VEGFR2 phosphorylation on ligand binding and endocytosis.
(Oral communication at Pharmacology 2019, Edinburgh, UK)

Peach CJ, Kilpatrick LE, Woolard J, Hill SJ. (2019) Quantifying binding of VEGF-A isoforms at VEGFR2 in membranes.
(Poster presentation at Experimental Biology 2019, Orlando, USA)

Peach CJ, Kilpatrick LE, Woolard J, Hill SJ. (2018) Kinetics of VEGF-A ligand binding to VEGFR2 in cells and membrane preparations.
(Oral communication at Pharmacology 2018, London, UK)

Martin G, Kilpatrick LE, Peach CJ, Hill SJ, Briddon SJ. (2018) Investigating the effect of a small molecule inhibitor of the ECM on VEGFR2-driven signalling.
(Poster presentation at Pharmacology 2018, London, UK)

Peach CJ, Kilpatrick L, Robers M, Friedman-Ohana R, Woolard J, Hill SJ. (2018) Quantifying VEGF binding at VEGFR2 and Neuropilin-1 using NanoBRET.
(Poster presentation at World Congress of Pharmacology 2018, Kyoto, Japan)

Peach CJ, Kilpatrick LE, Robers M, Friedman-Ohana R, Woolard J, Hill SJ. (2017) Quantifying binding of fluorescent VEGF isoforms at VEGFR2 using NanoBRET.
(Oral communication at Pharmacology 2017, London, UK)

Peach CJ, Kilpatrick LE, Robers M, Friedman-Ohana R, Woolard J, Hill SJ. (2017) Measurement of binding of fluorescent variants of $VEGF_{165}$a, $VEGF_{165}$b and $VEGF_{121}$a to VEGFR2 using NanoBRET in HEK293 cells.
(Poster presentation at Experimental Biology 2017, Chicago, USA)

Peach CJ, Friedman-Ohana R, Robers M, Woolard J, Hill SJ, Kilpatrick L. (2015) Quantifying the internalisation of the VEGFR2 in HEK293 cells using fluorescent $VEGF_{165}$a-TMR.
(Poster presentation at Pharmacology 2015, London, UK)

iii. ACKNOWLEDGEMENTS

"Find people who are better than you are… and then to appreciate them for what they can teach you, and to try to listen to them when they tell you something about yourself, no matter how bad—or good—it might be."

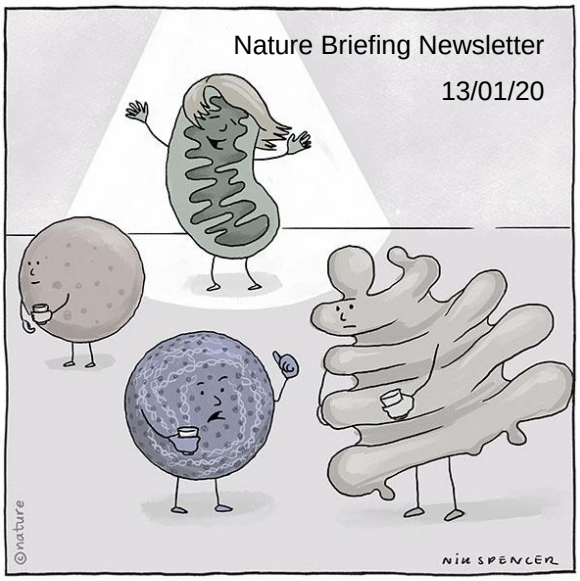
- Hanya Yanagihara, *A Little Life*

First, I would like to thank my supervisory team. Prof. Steve Hill and Prof. Jeanette Woo(d)lard have been incredible supervisors and mentors to me since 2015. You have pushed and inspired me while enabling me to present and network around the world. You empowered me by letting me write my own papers from the outset and shape the path of my research (within reason). Most importantly, you supported me to remain the same overenthusiastic undergraduate exclaiming she 'loves pipetting' until the very end of my PhD. May I embark on the rest of my career haunted by the ghosts of Steve's "What is the question?" and Jeanette's "Why do we care?". Laura Kilpatrick, you have taught me everything from carrying out assays and defending my ideas to the wonders of Beeston Brownies. I hereby promise that we shall perform our interpretive dance of VEGFR2/NRP1 complexes at one of your many future award acceptance ceremonies. I cannot wait to meet your future mentees that have also had their lives changed by your incredible leadership, kindness and wisdom.

Second, I want to thank everyone in the Cell Signalling Research Group and COMPARE. Every single person deserves a paragraph of appreciation. Thank you to June McCulloch and Marleen Groenen for maintaining the lab every day. Thank you to Tim Self, Seema Rajani and the SLIM team, as well as Joelle Goulding, for support with microscopy. I would also like to thank Moly B sensei Mark Soave, 'your receptor isn't real' Carl White, kinetics advice from Leigh Stoddart and David Sykes, BRET advice from Brad Hoare, physiological relevance reminders from Liz Rosethorne, 'stop talking about food' Rick Proudman, a joke a day from Chris McGrath and the eternal dad jokes from Nick Holliday and Steve Briddon. A big thank you to Team VEGF: Diana Alcobia, Vivi Mignone, Maria Arruda, Sam Cooper, Jackie Glenn. Finally, a massive thank you to everyone in the group, especially Desi Nesheva, Nicola Dijon, Jack Lochray, Birgit Caspar, Charlie Lay, Eddy Wragg, Clare Harwood, Lydia Ogrodzinksi, Sean Cullum, Laura Humphrys, Alastair Keen, Arisbel Batista Gondin, Rafa Morales - the list goes on. For the helpful discussions, dancing around the lab and being such an open, genuine and hardworking family - Cell Signalling is a very special place.

Third, I would not have been able to do this project without the British Pharmacological Society. I sincerely thank everyone involved with the Society and the AJ Clark Scholarship. Jono Brüün and the entire team at the Schlid Plot have been instrumental in opportunities throughout my PhD. I would also like to thank the School of Life Sciences and COMPARE for extending this financial support, enabling me to go ahead with the NanoBiT work in Chapter 5 that I was excited for.

Finally, an incredibly big thank you to my loved ones. To my Mum and Dad – thank you for always encouraging and supporting me, even if it involves a motorbike in Thailand, skydiving from 10,000 ft or working overseas. You have always put us first and never pressured us to do anything - if anything suggesting I stop caring so much about straight As. A massive thank you to the other Peaches, Simon and Matt, and not just for thickening my skin by admitting I'm not a good goalkeeper after all. I am lucky to have big brothers like you. I would also like to thank Jason Lawson for his incredibly kind support (and bad jokes) throughout. I must use this opportunity to thank Brenda Rolfe. Despite never having had the same opportunities to do a PhD, she smashed it as a female pharmacologist up until the 1980s (*doi.org/10.1016/0024-3205(85)90619-8*). While I never met my grandma, she is part of the reason I studied Neuroscience, the reason I am here and one of the reasons I feel driven to succeed. Lastly, to my incredible friends - I truly adore you and you make me who I am. In addition to those already mentioned:- Grace (Gracilin) Belshaw (McEagle), Josh Mallins, Ellen Guest, Lizzie Killalea, Rhian Morris, Mark Freeman, Kate McGonigle, Rashi Rajguru, Ellie Keen, Emma Forrester; as well as a very special mention to Ciarán McDonnell. May everyone's lives be filled with such inspirational people who force you to switch off and laugh at least every single day (even during COVID-19 lockdown while I finished this thesis).



"I don't know where she gets all that energy."

-- For me, 'that energy' stems from every person mentioned.

iv. ABBREVIATIONS

AMD	Age-related macular degeneration
ATP	Adenosine 5’-triphosphate
BRET	Bioluminescence resonance energy transfer
BSA	Bovine serum albumin
CAS	CRISPR-associated protein
CRISPR	Clustered regularly interspaced short palindromic repeats
DAG	Diacylglycerol
DMEM	Dulbecco’s modified Eagle’s medium
DMSO	Dimethyl sulfoxide
ECM	Extracellular matrix
EDTA	Ethylenediaminetetraacetic acid
EGFR	Epidermal growth factor receptor
eNOS	Endothelial nitric oxide synthase
ERK	Extracellular-signal regulated kinase
FAK	Focal adhesion kinase
FBS	Fetal bovine serum
FOXO	Forkhead box O
GIPC1	G Alpha Interacting Protein (GAIP) C-terminus-interacting protein
GPCR	G protein-coupled receptor
GTP	Guanosine 5'-triphosphate
HBSS	HEPES buffered saline solution
HEK293T	Human embryonic kidney clone 293, SV40 large T antigen
HUVEC	Human umbilical vein endothelial cells
IG	Immunoglobulin
IL-6	Interleukin-6
IP_3	1,4,5-Inositol trisphosphate
MAM	Mephrin, A5 protein and μ phosphatase
MAPK	Mitogen-activated protein kinases

MEK	MAPK/ERK kinase
NA	Numerical aperture
NFAT	Nuclear factor of activated T-cells
NRP1	Neuropilin-1
PBS	Phosphate buffered saline
PDB	Protein Data Bank
PDGF	Platelet-derived growth factor
PDZ	Post-synaptic density, disk large, zonula occludens-1
PFA	Paraformaldehyde
PI3K	Phosphoinositide 3-kinase
PIP_2	Phosphatidylinositol 4,5-bisphosphate
PIP_3	Phosphatidylinositol (3,4,5)-trisphosphate
PKC	Protein kinase C
PLCγ	Phospholipase C gamma
PTP	Protein tyrosine phosphatase
PTR	Programmed translational readthrough
RAF	Rapidly accelerated fibrosarcoma protein
RFU	Relative fluorescence units
RTKI	Receptor tyrosine kinase inhibitor
SEA	Serine-Glutamate-Alanine
S.E.M.	Standard error of the mean
SHB	SH2 domain-containing adapter protein B
SRPK	Serine/threonine protein kinase
TMR	Tetramethylrhodamine
TPD	Tyrosine phosphorylation deficient
TSAd	T-cell specific adaptor protein
VEGF	Vascular endothelial growth factor
VEGFR2	Vascular endothelial growth factor receptor 2

v. TABLE OF CONTENTS

i. ABSTRACT 3
ii. PUBLICATIONS ARISING 5
PAPERS 5
REVIEWS 5
CONFERENCE PROCEEDINGS 6
iii. ACKNOWLEDGEMENTS 7
iv. ABBREVIATIONS 9
v. TABLE OF CONTENTS 11

Chapter 1. General Introduction 15
1.1 DEVELOPMENT OF VASCULATURE 16
1.1.1 Vasculogenesis and Angiogenesis 16
1.1.2 Pathological Angiogenesis 19
1.2 RECEPTOR TYROSINE KINASES 20
1.2.1 RTK Structure 20
1.2.2 RTK Activation 21
1.2.3 RTK Endocytosis 22
1.3 VASCULAR ENDOTHELIAL GROWTH FACTORS 25
1.3.1 VEGF-A Structure 25
1.3.2 Alternative Splicing 26
1.3.3 VEGF-A Regulation 27
1.4 VEGF RECEPTORS 30
1.4.1 VEGFR2 Structure 32
1.4.2 VEGFR2 Activation 33
1.4.3 VEGFR2 Signalling 35
1.4.4 VEGFR2 Trafficking 38
1.5 NRP1 AS A CO-RECEPTOR 42
1.5.1 Neuropilins 42
1.5.2 NRP1 Structure 43
1.5.3 NRP1 Function in Vascular Development 44
1.6 PHARMACOLOGICAL FOCUS 47
1.6.1 Drugs Targeting VEGF-A, VEGFR2 and NRP1 47
1.6.2 Principles of Quantitative Pharmacology 50
1.7 PROJECT AIMS 52

Chapter 2. Materials & Methods **53**

2.1 MATERIALS 54

2.2 CELL CULTURE 55

2.2.1 Passaging 55

2.2.2 Freezing 56

2.2.3 Seeding 56

2.3 MOLECULAR BIOLOGY 58

2.3.1 Expression Vectors 58

2.3.2 DNA Quantification and Sequencing 62

2.3.3 Polymerase Chain Reaction 62

2.3.4 Restriction Digest 67

2.3.5 Gel Electrophoresis 70

2.3.6 Initial DNA Purification 71

2.3.7 Recombinant Plasmid Ligation 71

2.3.8 Transformation of DNA into Competent E. coli 75

2.3.9 Small-Scale DNA Purification (‘Miniprep’) 76

2.3.10 Large-Scale DNA Purification (‘Maxiprep’) 77

2.4 RECOMBINANT CELL LINES 78

2.4.1 Stable Cell Lines 78

2.4.2 Transient Transfection 78

2.4.3 Membrane Preparations 79

2.5 FLUORESCENT LIGAND PREPARATION 80

2.5.1 $VEGF_{xxx}x$-TMR Purification and Synthesis 80

2.5.2 Liquid Chromatography-Tandem Mass Spectrometry (LC-MS/MS) 81

2.5.3 SDS-PAGE Analysis 81

2.6 FLUORESCENCE MICROSCOPY 83

2.6.1 Live Cell Confocal Microscopy 83

2.6.2 Immunofluorescent Labelling 87

2.6.3 Bioluminescent Imaging 92

2.7 FUNCTIONAL ASSAYS 93

2.7.1 NFAT Reporter Gene Signalling 93

2.7.2 HUVEC Proliferation 97

2.7.3 Fluorescent Ligand Internalisation 97

2.8 BINDING ASSAYS 98

2.8.1 Effect of Membrane Preparations 99

2.8.2 Influence of Inhibiting VEGFR2 Phosphorylation 99

2.8.3 Effect of Buffer pH 99

2.8.4 Binding at LgBiT-VEGFR2 or HiBiT-VEGFR2 100
2.8.5 Binding at a Recomplemented VEGFR2/NRP1 NanoBiT Complex 100
2.9 RECEPTOR-RECEPTOR COMPLEX ASSAYS 102
2.9.1 BRET between Receptors 102
2.9.2 NanoBiT Complementation 102
2.10 DATA ANALYSIS 104
2.10.1 Software 104
2.10.2 Statistics 104
2.10.3 Imaging Quantification 105
2.10.4 Functional Assays 108
2.10.5 Binding Assays 109

Chapter 3. Discriminating between fluorescent VEGF-A isoforms binding VEGFR2 or NRP1 112
3.1 INTRODUCTION 113
3.2 CHAPTER 3 AIMS 117
3.3 RESULTS 118
Characterisation of novel fluorescent VEGF-A isoforms in HUVECs and HEK293T cells 118
High affinity binding of $VEGF_{165}$a-TMR, $VEGF_{165}$b-TMR, and $VEGF_{121}$a-TMR to VEGFR2 136
Real-time binding of $VEGF_{165}$a-TMR to NRP1 using BRET 149
3.4 DISCUSSION 155
3.5 CHAPTER 3 CONCLUSIONS 160

Chapter 4. Influence of VEGFR2 endocytosis and phosphorylation on VEGF-A ligand binding 161
4.1 INTRODUCTION 162
4.2 CHAPTER 4 AIMS 164
4.3 RESULTS 165
Agonist-mediated endocytosis of VEGFR2 in HEK293T cells 165
Influence of VEGFR2 phosphorylation on endocytosis 175
Monitoring ligand binding in the absence of VEGFR2 phosphorylation using BRET 181
Using membrane preparations to probe ligand binding and the effect of pH 184
4.4 DISCUSSION 202
4.5 CHAPTER 4 CONCLUSIONS 207

Chapter 5. Dynamics of ligand binding at VEGFR2/NRP1 complexes in living cells 208

5.1 INTRODUCTION 209

5.2 CHAPTER 5 AIMS 212

5.3 RESULTS 213

Localisation of VEGFR2 and NRP1 co-expressed in HEK293T cells 213

Monitoring heteromeric complex formation between VEGFR2/NRP1 223

Quantifying ligand binding at a defined VEGFR2/NRP1 complex 232

5.4 DISCUSSION 246

5.5 CHAPTER 5 CONCLUSIONS 251

Chapter 6. General Discussion & Conclusions 252

6.1 GENERAL DISCUSSION 253

What are the differences between the pharmacology of VEGF-A isoforms? 254

What is the pharmacology of VEGFR2, NRP1 and the VEGFR2/NRP1 complex? 255

How does local cellular context modulate ligand/receptor pharmacology? 256

6.2 FUTURE DIRECTIONS 258

6.3 KEY CONCLUSIONS 261

Chapter 7. Appendix 262

7.1 Biochemical Characterisation of $VEGF_{xxx}$x-TMR 263

7.2 DNA and Amino Acid Sequences 268

7.3 Buffer Composition 276

7.3.1 HEPES Buffered Saline Solution (HBSS) 276

7.3.2 Tris-acetate-EDTA (TAE) Buffer 276

7.4 Principles of Fluorescence 277

7.5 Principles of Resonance Energy Transfer 278

7.6 Graphical Functions 279

Chapter 8. References 280

Chapter 1.
General Introduction

1.1 DEVELOPMENT OF VASCULATURE

Blood vessels transport gases, nutrients, metabolites and cells to all tissues via a hierarchical network of arteries, veins and capillaries. Arteries and arterioles sustain high pressure blood flow, while venules and capillaries have thinner vessel walls (Potente and Mäkinen, 2017). All vessels are lined by a monolayer of endothelial cells. The endothelium is therefore a key interface between circulating blood and tissues throughout the body that is responsible for leukocyte trafficking, regulating vascular tone and vascular permeability (Alberts et al., 2008). As a highly complex network, the cardiovascular system requires tightly regulated development and maintenance. Blood vessel development is primarily mediated by vasculogenesis and angiogenesis (Poole and Coffin, 1989). These developmental processes are driven by tissue-derived growth factors, notably Vascular Endothelial Growth Factor (VEGF; Adams and Alitalo, 2007).

1.1.1 Vasculogenesis and Angiogenesis

Vasculogenesis involves the formation of blood vessels from the *de novo* generation of endothelial cells from 'angioblasts' or endothelial progenitor cells (*Figure 1.1a*; Sabin, 1917; Risau and Lemmon, 1988). Vasculogenesis is involved in embryonic development (Potente et al., 2011). Angioblasts differentiate into endothelial cells in response to Fibroblast Growth Factor 2 (FGF2). VEGF is then required for their proliferation and survival, developing into a primitive network that can later mature by remodelling into arteries, veins or capillaries (Potente and Mäkinen, 2017).

Angiogenesis is the formation of blood vessels from pre-existing vasculature (Hertig, 1935). It is well established that this process is important in both embryogenesis and adulthood (Carmeliet, 2005). For example, angiogenesis plays a vital role in wound repair (Johnson and Wilgus, 2014), the oestrous cycle and placentation (Lai et al., 2014). First, endothelial cells form angiogenic sprouts (*Figure 1.1b*). This is led by an invasive tip cell, which gains a migratory phenotype in response to pro-angiogenic signals to guide new sprouts. These also have protruding filopodia that probe the environment for guidance cues (Potente et al., 2011). Tip cells are followed by stalk cells (*Figure 1.1b*). These proliferative endothelial cells, specified by Notch signalling, are involved in stabilising and elongating new vessels (Potente and Mäkinen, 2017). Second, stalk cells form a lumen and branching sprouts fuse with neighbouring vessels via anastomosis (Chung and Ferrara, 2011). Vessels are either stabilised by perfusion or regress from lack of blood flow. At this stage, vessels can mature into a hierarchical network with arterial or venous specification (Carmeliet, 2005; Simons and Eichmann, 2015).

Vascular development is highly responsive to the needs of the tissue that it supplies. Growth factors are balanced between those that promote (pro-angiogenic) or inhibit (anti-angiogenic) vessel development (*Figure 1.1c*). There is a low turnover of endothelial cells in quiescent vessels, however endothelial proliferation can be triggered by an 'angiogenic switch' (Hanahan and Folkman, 1996). This can be triggered by oxygen deprivation through the release of hypoxia-inducible factor 1 (HIF1), a transcription factor that upregulates VEGF-A (Shweiki et al., 1992; Goldberg and Schneider, 1994; Liu et al., 1995). This stimulates angiogenesis in tissues with inadequate blood perfusion.

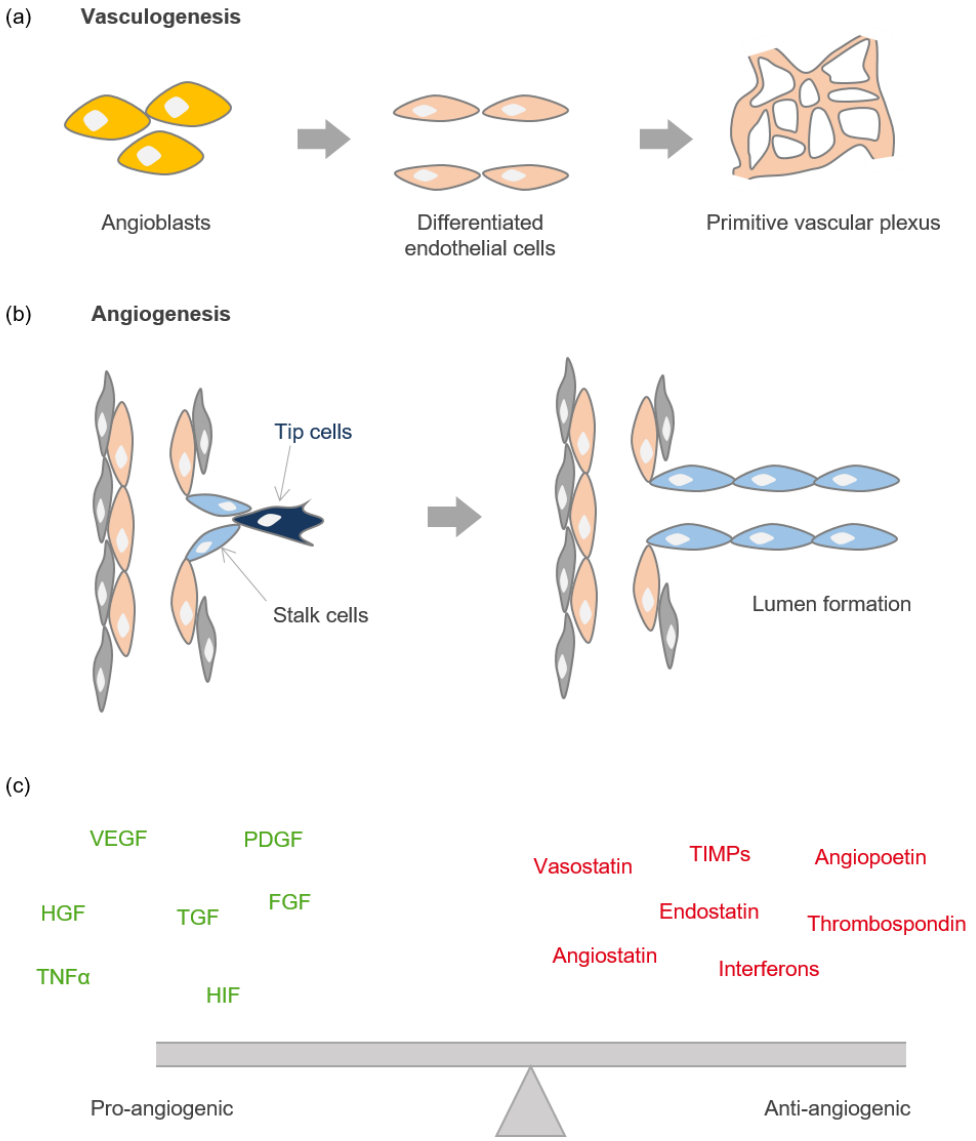


Figure 1.1 ***Development of blood vessels****. (a) Vasculogenesis involves the* de novo *generation of vasculature from angioblasts. Differentiation into endothelial cells allows the formation of primitive vasculature. (b) Sprouting angiogenesis from pre-existing vessels is led by a tip cell. The following stalk cells eventually form a lumen to enable blood perfusion. (c) Vascular quiescence involves a balance between angiogenic factors that promote or inhibit angiogenesis. This balance changes in pathophysiology, such as an angiogenic switch upregulating pro-angiogenic factors. Abbreviations:* ***FGF*** *Fibroblast growth factor;* ***HGF*** *Hepatocyte growth factor;* ***HIF*** *Hypoxia inducible factor;* ***PDGF*** *Platelet-derived growth factor;* ***TGF*** *Transforming growth factor;* ***TIMPs*** *Tissue inhibitor of metalloproteinases;* ***TNFα*** *Tumour necrosis factor α;* ***VEGF*** *Vascular endothelial growth factor.*

1.1.2 Pathological Angiogenesis

As well as its importance in physiology, the dysregulation of angiogenesis is a key process in a wide spectrum of pathologies. Therapeutics targeting angiogenesis were estimated to benefit up to 500 million people (Carmeliet, 2005). Pathologies include cancer (Hanahan and Weinberg, 2011), age-related macular degeneration (AMD; Miller et al., 2013), rheumatoid arthritis (Azizi et al., 2014), psoriasis (Folkman, 1972), diabetes-induced ocular neovascularisation (Ved et al., 2017), inflammatory diseases (Alkim et al., 2015), ischaemia/reperfusion injury (Pallet et al., 2014), infantile haemangioma and atherosclerosis (Shibuya, 2013; Matsumoto and Ema, 2014). Angiogenesis-dependent pathologies are caused or exacerbated by an imbalance between the production or activity of pro- and anti-angiogenic factors (*Figure 1.1c*; Woolard et al., 2009). Most therapeutic interventions targeting the pro-angiogenic effects of VEGF are in the fields of oncology and ophthalmology.

While cancer is a complex group of over 100 diseases with diverse pathologies, angiogenesis is a unifying process amongst all solid tumours (Hanahan and Weinberg, 2000, 2011). Early work proposed that tumour cells secrete factors that stimulate blood vessel growth and confer a growth advantage for tumours (Algire et al., 1945). Folkman hypothesised that this could be a mechanism for anti-cancer drugs to starve a tumour from its own blood supply, as angiogenesis was required for tumour growth beyond 2-3 mm^3 (Folkman, 1971, 1974). The growing tumour mass creates a hypoxic microenvironment, in which tumour cells directly secrete VEGF (Senger et al., 1983; Plate et al., 1992). Tumour-associated vasculature is vital for delivering nutrients, removing metabolic waste and enabling metastasis through the characteristically disorganised and leaky vessels resulting from tumour angiogenesis (Hanahan and Weinberg, 2011; Farnsworth et al., 2014).

Numerous ophthalmological retinopathies involve angiogenesis for neovascularisation, such as AMD (Kvanta et al., 1996) and diabetic retinopathy (Aiello et al., 1994). Michaelson first proposed a hypothesis in 1948 that the developing retina secretes a diffusible factor stimulating neovascularisation (reviewed in Patz, 1984). This was later identified as VEGF-A, a growth factor produced by retinal cells stimulating angiogenesis during ischaemia (Miller et al., 1994; Adamis et al., 1996). During AMD, excess deposition of debris damages the retinal pigment epithelium (Yanagi, 2008). This can impair vision and lead to blindness.

1.2 RECEPTOR TYROSINE KINASES

Receptor Tyrosine Kinases (RTKs) are a superfamily of membrane proteins that respond to extracellular growth factors. They have an intrinsic catalytic domain that functions as a kinase to phosphorylate key intracellular tyrosine residues (Ullrich and Schlessinger, 1990). RTK activation and adaptor protein recruitment triggers signalling that can lead to phenotypic responses such as cell proliferation, migration and survival (Lemmon and Schlessinger, 2010). The human genome contains over 500 kinases (*Figure 1.2a*; Manning et al., 2002). This includes 90 genes that encode tyrosine kinases, of which 58 belong to the RTK receptor family expressed on the membrane (Robinson et al., 2000). Due to their ability to stimulate growth, dysfunctional RTK signalling contributes to many cancers (Gschwind et al., 2004). RTKs are therefore a growing target for drug discovery (Lemmon and Schlessinger, 2010; Rask-Andersen et al., 2014; Wu et al., 2015). RTKs are classified according to their domain structure and kinase domain sequences, each with distinct functional outcomes and endogenous ligands (Alexander et al., 2017). In the context of angiogenesis, VEGF stimulates RTKs belonging to the Class IV family of Vascular Endothelial Growth Factor Receptors (VEGFRs; *Introduction 1.4*; Alexander et al., 2015). VEGFRs are closely related to the Class III Platelet-Derived Growth Factor (PDGF) Receptor family (Verstraete and Savvides, 2012).

1.2.1 RTK Structure

RTKs have a modular architecture with a single transmembrane α-helix (*Figure 1.2b*). Their large extracellular region contain the orthosteric binding site for their cognate growth factor. A number of distinct RTK families contain stable immunoglobulin (Ig)-like domains (Lemmon and Schlessinger, 2010), composed of folded β-sheets of 70-110 residues (Berisio et al., 2012). Their cytoplasmic region contains a catalytic domain with intrinsic tyrosine kinase activity (Ullrich and Schlessinger, 1990; Schlessinger, 2000; Lemmon and Schlessinger, 2010). This catalytic kinase domain is highly conserved amongst kinases (Hanks et al., 1988; Hanks and Hunter, 1995).

RTKs function as a dimer (*Figure 1.2b*). As dimerisation brings intracellular kinase domains close together, phosphorylation can occur across monomers that phosphorylate one another. It is classically thought that ligand binding leads to RTK dimerisation (Ullrich and Schlessinger, 1990), however there is growing evidence for pre-coupled RTK dimers in the absence of ligand (Maruyama, 2014; Freed et al., 2015; Sarabipour and Hristova, 2016). For example, neurotrophin receptors form ligand-independent dimers (Gent et al., 2002; Wimmer-Kleikamp et al., 2004). There is also evidence that RTKs can assemble into higher order oligomers beyond dimers, such as clustering of the Epidermal Growth Factor Receptor (EGFR; Clayton et al., 2005; Saffarian et al., 2007; Wang et al., 2014; Needham et al., 2016).

1.2.2 RTK Activation

According to the consensus model of RTK activation, growth factors usually bind across an RTK dimer (Ullrich and Schlessinger, 1990). Ligand binding causes conformational changes from their extracellular domain, or ectodomain, via the single transmembrane helix to the intracellular portion (Lemmon and Schlessinger, 2010). This allows the catalytic kinase domain to phosphorylate specific tyrosine residues, whereby a phosphoryl group is transferred from the γ-phosphate of ATP (*Figure 1.2c*). RTKs can induce both auto-phosphorylation within the monomer or trans-phosphorylation across the dimer.

The split kinase domain is composed of the amino-terminal (N-) lobe and the carboxyl-terminal (C-) lobe. These undergo flexible and dynamic conformational changes upon activation (Huse and Kuriyan, 2002; Taylor and Kornev, 2011). A kinase must bind ATP and magnesium (Mg^{2+}) for tyrosine phosphorylation (*Figure 1.2c*). ATP docks in a cleft between the N- and C- lobes, interacting with a flexible glycine-rich loop and a Lys/Asp/Asp (K/D/D) motif. Mg^{2+} is chelated by the Asp-Phe-Gly (DFG) motif in the activation loop (Roskoski, 2015a). These regions are highly conserved amongst kinases (Hanks et al., 1988).

Phosphorylated tyrosine residues can interact with proteins containing Src homology 2 (SH2) domains or phosphotyrosine binding (PTB) domains (Waksman et al., 1994; Songyang et al., 1995). These domains are found in adaptor proteins, scaffolding proteins and enzymes (Wagner et al., 2013). This allows the assembly of signalling complexes that initiate downstream pathways from phosphorylated tyrosine residues. Protein phosphatases (PTPs), such as PTP1b, can rapidly disrupt RTK signalling by dephosphorylating tyrosine residues following RTK internalisation (Tonks et al., 1988; Tonks and Neel, 2001; Haj et al., 2002; Stuible and Tremblay, 2010). Protein phosphorylation is a rapid form of reversible intracellular communication downstream of RTK conformational changes in response to growth factor binding.

1.2.3 RTK Endocytosis

Endocytosis is the process by which components at the cell surface, such as RTKs, are transported away from the plasma membrane into the cell (Alberts et al., 2008). Endocytosis of receptors away from the cell surface prevents their exposure to extracellular agonists or antagonists that cannot permeate the plasma membrane. Receptors are internalised into intracellular vesicles, or endosomes, encapsulated by an internal membrane for trafficking around subcellular compartments. Following activation, RTKs can be rapidly internalised from the cell surface into intracellular compartments. There can also be constitutive endocytosis in the absence of ligand (Goh and Sorkin, 2013). While endocytosis was traditionally considered to remove receptors from extracellular stimuli, there is growing evidence that receptors can continue to signal from endosomes (Murphy et al., 2009). RTKs were the first class of receptors for which endosomal signalling was shown, including EGFR (Di Guglielmo et al., 1994) and Insulin Receptors (Kelly and Ruderman, 1993; Kublaoui et al., 1995).

Endocytosis can occur via clathrin-dependent or clathrin-independent mechanisms (Doherty and McMahon, 2009). Clathrin-mediated internalisation is the fastest endocytic pathway (Goh and Sorkin, 2013). Membrane curvature is mediated by clathrin (Pearse, 1976), a triskelion protein that forms a lattice to invaginate the plasma membrane into a clathin-coated pit. Clathrin binds the membrane via adaptor proteins, such as the heterotetrameric adaptor complex AP-2 (Pearse and Robinson, 1984; Traub et al., 1999). This budding structure is pinched off by a large GTPase, dynamin, that mediates membrane scission upon GTP hydrolysis (Praefcke and McMahon, 2004). As with numerous mechanisms in the RTK superfamily, clathin-mediated endocytosis was first observed for EGFRs (Gorden et al., 1978).

Endocytosis can also occur through macropinocytosis, a bulk transport route that occurs from protruding ruffles of the plasma membrane (Doherty and McMahon, 2009). Actin-rich ruffles then fuse to enclose the extracellular fluid and form macropinosomes (Kerr and Teasdale, 2009). This is mediated by both actin polymerisation and Rac1, a member of the Rho family of G proteins (West et al., 2000). This process was observed for EGFR (Haigler et al., 1979; West et al., 1989). There is also evidence for caveolae-mediated endocytosis with RTKs (Sigismund et al., 2005). This clathrin-independent pathway is sensitive to cholesterol depletion (Nabi and Le, 2003). Caveolar invaginations are subject to scission from dynamin (Oh et al., 1998).

Following endocytosis, RTKs are trafficked in these vesicular compartments. Endosomes mature along their route as vesicles can fuse and undergo acidification (Scita and Di Fiore, 2010). Rab GTPases regulate vesicle trafficking to sort cargo into specific endosomal subtypes (Rink et al., 2005). Regardless of the endocytic mechanism, RTKs enter $Rab5^{+}$ early endosomes for sorting. Receptors can recycle back to the surface through short-loop or long-loop pathways (Goh and Sorkin, 2013). The 'fast' recycling pathway is regulated by Rab4 in peripheral early endosomes, while Rab11 mediates the 'slow' recycling pathway (Grant and Donaldson, 2009). Alternatively, RTKs can be targeted for degradation by hydrolytic enzymes in the lysosome following ubiquitination by E3 ligases (Marmor and Yarden, 2004). These processes mediate the spatial distribution of RTKs and other receptor classes in living cells.

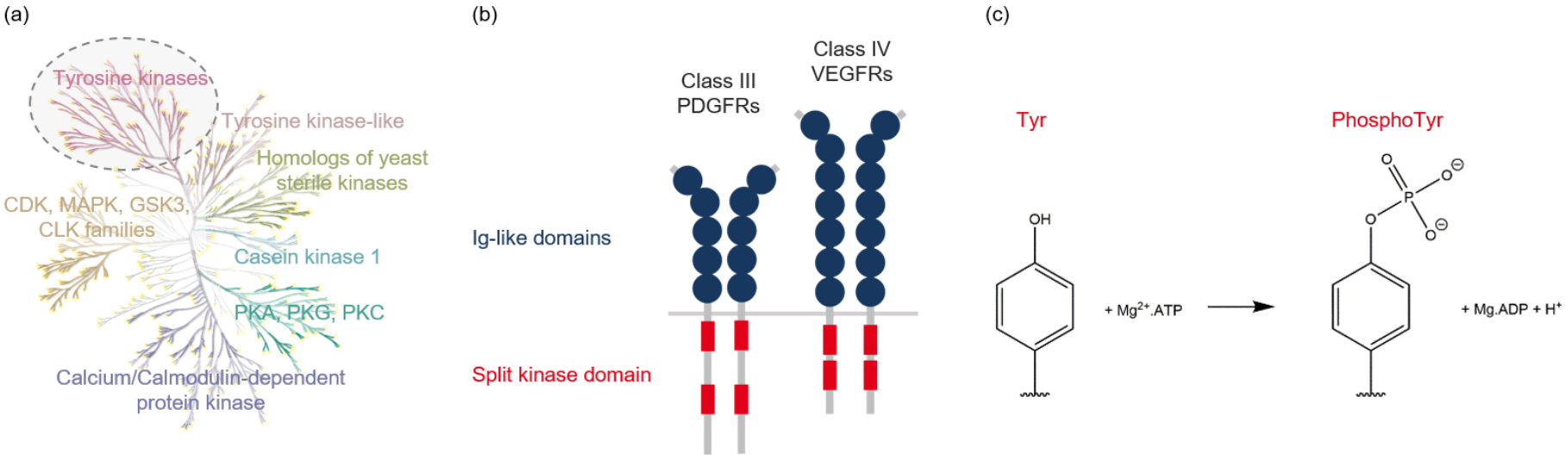


Figure 1.2 ***Family of Receptor Tyrosine Kinases (RTKs)****. (a) Branched representation of the human kinome divided into related families. This was adapted from the Cell Signalling Technologies website and* Manning et al. (2002)*. (b) RTKs function as dimers with a single transmembrane domain. Class III Platelet Derived Growth Factor Receptor (PDGFR) and Class IV Vascular Endothelial Growth Factor Receptor (VEGFR) RTKs are structurally related with 5-7 immunoglobulin (Ig)-like domains in the ectodomain. The cytoplasmic domain contains a kinase domain, split by a kinase insert domain. This region is responsible for the catalytic activity. (c) Kinase enzymes catalyse tyrosine (Tyr) phosphorylation. This enzymatic reaction requires adenosine 5'-triphosphate (ATP) and* Mg^{2+} *for the transfer of a phosphoryl group from ATP to the phenol group on the Tyr side chain.*

1.3 VASCULAR ENDOTHELIAL GROWTH FACTORS

Vascular Endothelial Growth Factors (VEGFs) are a family of secreted proteins that stimulate angiogenesis and lymphangiogenesis (Holmes and Zachary, 2005). This includes mammalian subtypes VEGF-A (Leung et al., 1989), VEGF-B (Olofsson et al., 1996), VEGF-C (Joukov et al., 1996), VEGF-D (Yamada et al., 1997; Achen et al., 1998) and Placental Growth Factor (PlGF; Maglione et al., 1993). This family also includes the virus-encoded VEGF-E and the snake venom-derived VEGF-F (Ogawa et al., 1998; Yamazaki et al., 2009; Iyer and Acharya, 2011). The first discovery of VEGF-A referred to this peptide as Tumour-Angiogenesis Factor (Folkman, 1974). Early work also described it as Vascular Permeability Factor (VPF), due to its ability to increase the permeability of blood vessels (Senger et al., 1983, 1986). Following subsequent observations of its effects on endothelial cells (Ferrara and Henzel, 1989) and cloning (Leung et al., 1989), it was renamed VEGF and subtypes were specified upon the cloning of other family members. Cellular responses to VEGFs are driven by their cognate RTK receptors that belong to the Class IV family of VEGFRs (*Introduction 1.4*). As VEGF-A is widely considered the key driver of angiogenesis (Koch et al., 2011; Moens et al., 2014; Simons et al., 2016), this subtype is the primary focus for this thesis.

1.3.1 VEGF-A Structure

VEGF-A is an anti-parallel homodimeric glycoprotein (26-44 kDa dimer). VEGFs possess a central knot motif of cysteine (Cys) residues that form intramolecular disulphide bonds when assembled into a stable, folded structure (*Figure 1.3a*; Muller et al., 2002). VEGFs belong to the Cys-loop superfamily of growth factors, alongside structurally similar PDGF (Iyer and Acharya, 2011). The dimeric structure is maintained by two additional Cys residues responsible for intermolecular disulphide bonds between VEGF-A monomers (*Figure 1.4*). The latter region of VEGF-A can interact with co-receptors, such as Neuropilin-1 (NRP1; *Introduction 1.5*), or components of the extracellular matrix (ECM; Harper and Bates, 2008). The inability to crystallise both the N-terminus (*Figure 1.3a*) and C-terminus (*Figure 1.3b*) limits our understanding of the full-length structure of VEGF-A, but could suggest flexibility between these spatially distinct regions.

1.3.2 Alternative Splicing

The *Vegfa* gene encompasses eight exons on chromosome *6p21.1* (*Figure 1.3c*; Venables, 2006). VEGF-A isoforms differ in length, whereby xxx in $VEGF_{xxx}$a denotes the number of amino acids present per VEGF-A monomer. $VEGF_{165}$a was the first isoform characterised (Ferrara and Henzel, 1989). VEGF-A mRNA can be alternatively spliced by proteolytic processing to encode distinct isoforms (Tischer et al., 1991). Exons 1-5 are present in all VEGF-A isoforms (*Figure 1.3d*). As a result, all VEGF-A isoforms contain residues interacting with VEGFRs, as well as residues such that all isoforms are dimeric and assembled into the Cys-loop structure (*Figure 1.4*). They all also contain a glycosylated asparagine residue (Peretz et al., 1992; Claffey et al., 1995) and signal sequence to enable growth factor secretion (Guzmán-Hernández et al., 2014).

A major site of alternative splicing occurs at exon 8, where proximal splicing results in $VEGF_{xxx}$a isoforms containing exon 8a (*Figure 1.3d*). Conversely, distal splicing leads to $VEGF_{xxx}$b isoforms containing exon 8b (Bates et al., 2002). Based on *in vitro* and *in vivo* studies, $VEGF_{xxx}$a isoforms stimulate vascular permeability, cell proliferation, survival, migration and angiogenesis (Olsson et al., 2006). In contrast, $VEGF_{xxx}$b isoforms have reported 'anti-angiogenic' properties (Bates et al., 2002; Woolard et al., 2004; Catena et al., 2010b). In quiescent vessels, a high proportion of VEGF-A expression is represented by the $VEGF_{165}$b isoform; this is then downregulated by a switch to pro-angiogenic isoform expression in cancer (Bates et al., 2002; Woolard et al., 2004; Cébe Suarez et al., 2006; Pritchard-Jones et al., 2007). $VEGF_{xxx}$a and $VEGF_{xxx}$b isoforms only differ by six amino acids at their C terminus. $VEGF_{xxx}$a isoforms terminate in residues CDKPRR, whereas $VEGF_{xxx}$b isoforms terminate in SLTRKD (Bates et al., 2002). VEGF-Ax was a recently identified isoform arising from programmed translational readthrough (PTR) at the C-terminus of VEGF-A (Eswarappa et al., 2014; Xin et al., 2016). Translation can extend beyond the canonical stop codon of VEGF-A mRNA due to an alternative stop codon. As a result, VEGF-Ax contains a 22 amino acid extension encompassing both exon 8a-encoded CDKPRR and exon 8b-encoded SLTRKD (*Figure 1.3d, Figure 1.4*). There is evidence that VEGF-Ax exhibits both anti-angiogenic (Eswarappa et al., 2014) and pro-angiogenic (Xin et al., 2016) signalling, therefore possessing functional similarities to $VEGF_{165}$b.

Another major site of alternative splicing occurs around exons 6a and 7 (*Figure 1.3d*). Arginine (Arg) residues in exons 6a and 7 interact with electronegative heparan sulphate in the ECM (*Figure 1.4*; Fairbrother et al., 1998; Krilleke et al., 2007). The ECM is an extensive network composed of transmembrane proteoglycans and glycosaminoglycan chains, including heparan sulphate polysaccharides (Frantz et al., 2010). Some isoforms are unable to bind the ECM, such as $VEGF_{121}$a (Houck et al., 1992; Soker et al., 1996; Ashikari-Hada et al., 2005). These have distinct bioavailability

compared to matrix-bound isoforms that can adhere to this extracellular network. As such, $VEGF_{121}$a is considered a freely diffusible VEGF-A isoform. Interactions between VEGF-A and the ECM can enhance binding with VEGFR2 (Gitay-Goren et al., 1992; Teran and Nugent, 2015) and co-receptor NRP1 (Mamluk et al., 2002).

1.3.3 VEGF-A Regulation

VEGF-A is secreted by endothelial cells (Uchida et al., 1994; Namiki et al., 1995), as well as other cell types including fibroblasts (Nissen et al., 1998), smooth muscle cells (Brogi et al., 1994), platelets (Banks et al., 1998) and neutrophils (Gaudry et al., 1997). VEGF-A is also secreted by ~60% of all tumours (Berse et al., 1992). The expression of VEGF-A can be modulated over different timescales. Long-term changes involve altered transcription of the *Vegfa* gene (Pagès and Pouysségur, 2005). VEGF-A expression can be influenced by the local cellular environment, such as hypoxia (Liu et al., 1995; Forsythe et al., 1996), shear stress (dela Paz et al., 2012), genotoxic agents (Mineur et al., 2007), ischemia and inflammatory stimuli (Franco et al., 2011) and the activity of both oncogenes and tumour suppressor genes (Nowak et al., 2008). There can also be modulation of VEGF-A isoform splicing in tissues during physiology or pathology (Pritchard-Jones et al., 2007; Bates et al., 2013; Vempati et al., 2014; Ye et al., 2016; Barratt et al., 2017). For example, downregulation of 'anti-angiogenic' $VEGF_{165}$b in cancer is mediated by Ser/Arg protein kinase 1 to promote VEGF-A splicing to encode exon 8a instead of 8b (Oltean et al., 2012). Additionally, exposure to genotoxic agents or ultraviolet irradiation can lead to splicing of a shorter isoform, $VEGF_{111}$a (*Figure 1.3d*; Mineur et al., 2007).

Short-term changes in local growth factor concentration gradients can arise from modulating VEGF-A bioavailability by isoforms tethered to the ECM (Vempati et al., 2014). ECM networks are dynamically remodelled, such as their degradation by matrix metalloproteinases (Frantz et al., 2010). This network also differs in pathology with a characteristically stiff ECM in tumours (Gkretsi and Stylianopoulos, 2018). This can create high local concentrations of pro-angiogenic VEGF-A isoforms that amplifies signalling in times of angiogenic need. As well as ECM remodelling, ECM-bound VEGF-A can itself be proteolytically cleaved into shorter fragments resulting in compromised signalling (Keyt and Berleau, 1996).

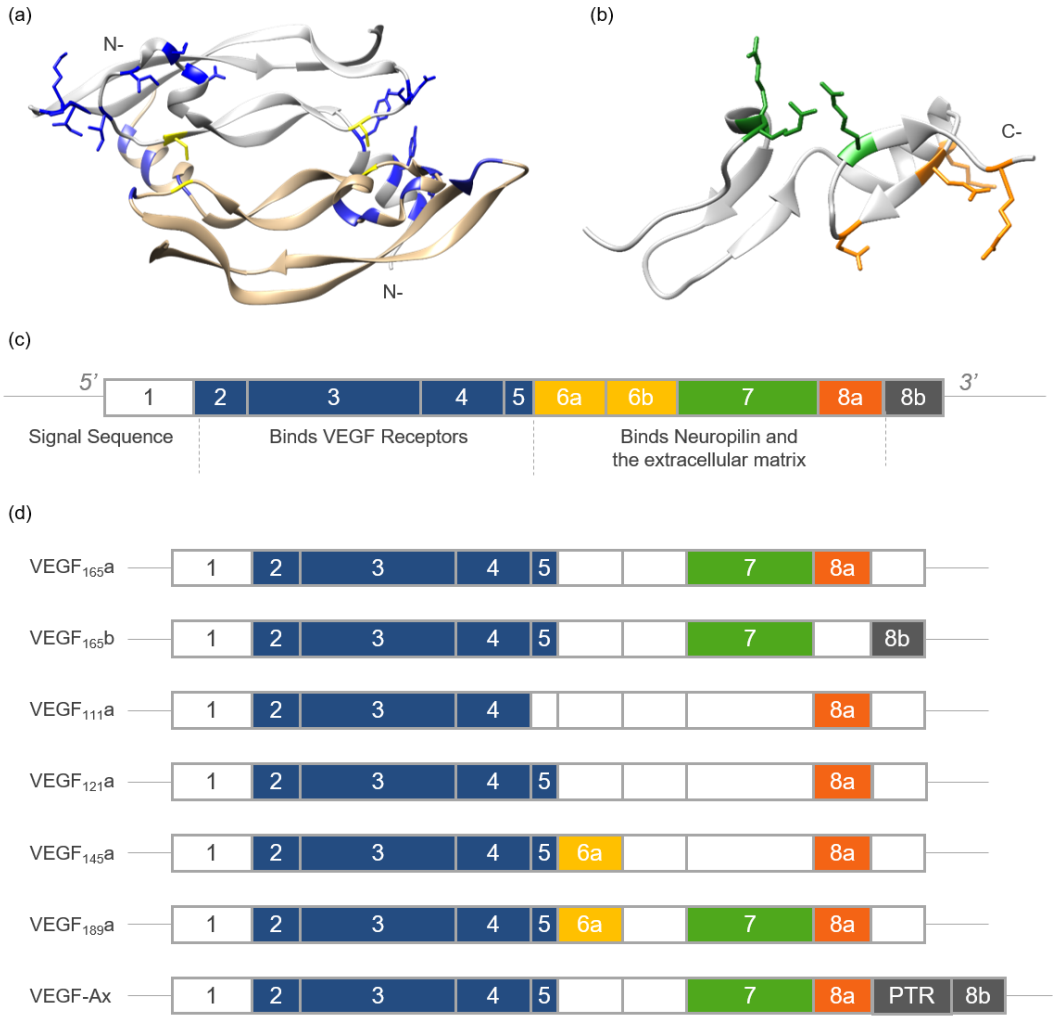


Figure 1.3 ***Structure of Vascular Endothelial Growth Factor A (VEGF-A)****.*

(a) Anti-parallel homodimeric structure of the N-terminus of VEGF-A (PDB ID 1VPF) determined by X-ray crystallography (Muller et al., 1997). Distinct VEGF-A monomers are shown in grey and gold, highlighting residues interacting with VEGF receptors (blue) and intermolecular disulphide bonds (yellow). Amino acid side chains are only shown on the grey monomer. (b) 3D structure of the C-terminus of $VEGF_{165}$*a (PDB 4DEQ, Parker et al., 2012). Residues interacting with the extracellular matrix (green) and Neuropilin-1 (orange) are highlighted. (c) VEGF-A mRNA contains exons that encode amino acids that interact VEGF receptors, Neuropilin-1 and the extracellular matrix. (d) Alternative splicing generates a range of VEGF-A isoforms with specific exons present. Designated* $VEGF_{xxx}$*, xxx represents the number of amino acids present per monomer prior to signal sequence cleavage. VEGF-Ax is subject to Programmed Translational Readthrough (PTR).*

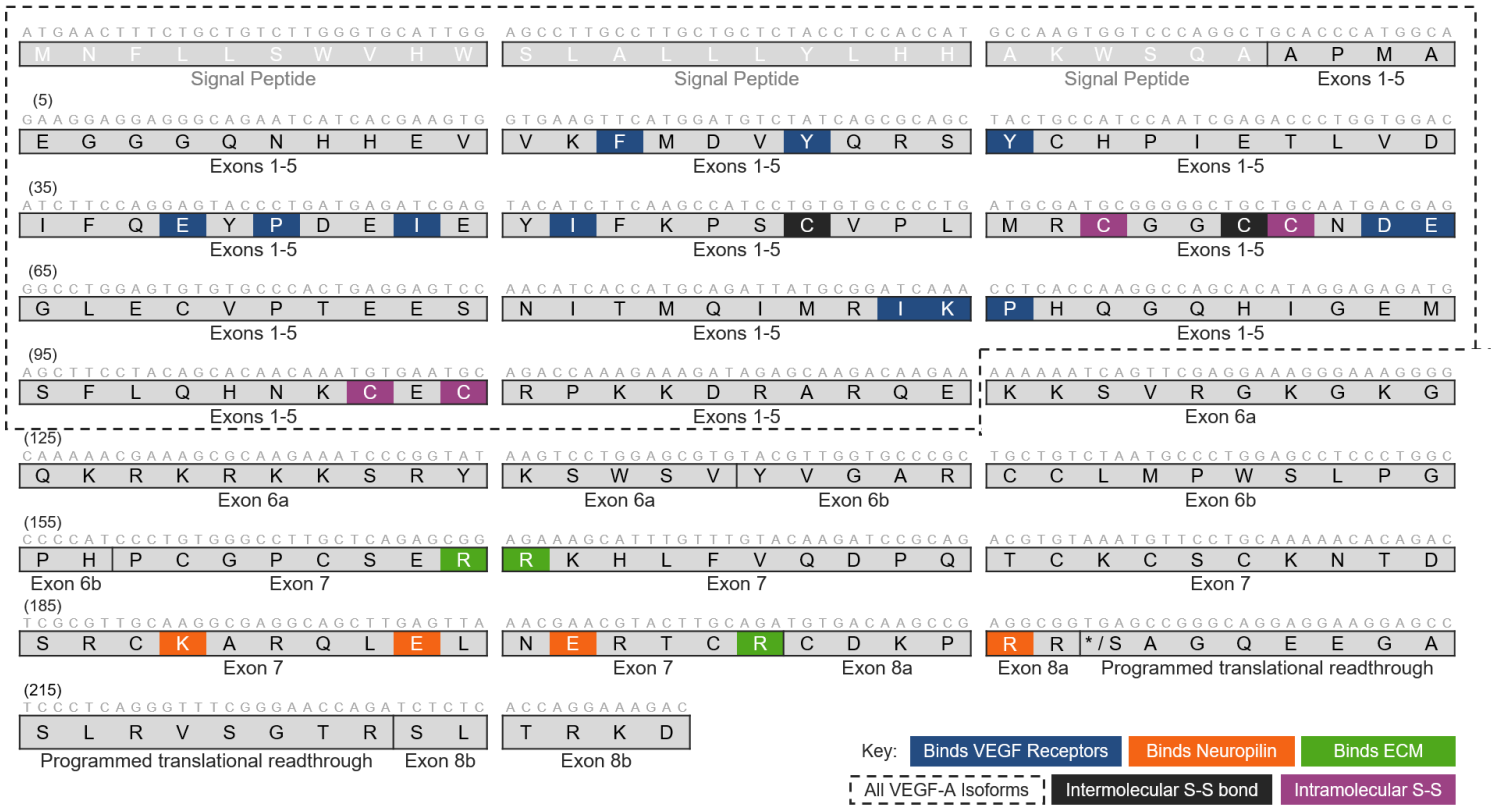


Figure 1.4

***Residues in the VEGF-A sequence that interact with known binding partners**. The open reading frame was derived from transcript NM_001025366.2 with exons according to UniProt P15692. Numbers in parentheses (left) correspond to residues in the VEGF-A peptide following signal sequence cleavage. Based on published X-ray crystal structures, residues are highlighted that form non-covalent interactions with VEGFR2 or VEGFR1 (Brozzo et al., 2011; Markovic-Mueller et al., 2017), Neuropilin-1 (Parker et al., 2012) or the extracellular matrix (ECM) (Krilleke et al., 2007). Cysteine residues are highlighted that form intermolecular or intramolecular disulphide (S-S) bonds, important for dimerisation or folding respectively (Muller et al., 2002).*

1.4 VEGF RECEPTORS

There are three VEGFR subtypes encoded by separate genes. VEGFR1 (*Flt-1* in mice) and VEGFR2 (*Flk-1*; also known as kinase insert domain receptor, KDR) are structurally similar, whereas VEGFR3 (*Flt-4*) has a proteolytically processed extracellular domain (Koch et al., 2011; Smith et al., 2015). Not all VEGF subtypes can interact with each VEGFR (*Figure 1.5*). VEGFRs are expressed by endothelial cells, macrophages, hematopoietic cells and smooth muscle cells (Kabrun et al., 1997; Ishida et al., 2001; Witmer et al., 2002). VEGF-A signals via VEGFR1 and VEGFR2 driving angiogenesis, whereas lymphangiogenesis is mediated by VEGF-C/D isoforms via VEGFR3 (Simons et al., 2016). VEGFR2 can also be activated by non-canonical ligands, such as gremlin (Mitola et al., 2010) and in response to mechanical shear stress (Jin et al., 2003; Domigan et al., 2015). Although VEGFR1 has a higher affinity for VEGF-A than VEGFR2, it shows decreased tyrosine kinase activity (Waltenberger et al., 1994; Meyer et al., 2006). It is therefore largely considered a decoy receptor that can negatively modulate VEGFR2 activity. There is evidence for the transcription of truncated forms of VEGFR1 (Kendall and Thomas, 1993; Hornig et al., 2000), VEGFR2 (Ebos et al., 2004) and VEGFR3 (Singh et al., 2013). These soluble receptors act as decoy receptors that interact with circulating ligand and prevent functional ligand interactions with full-length VEGFRs. As first observed for EGFRs (Blobel, 2005), there is evidence that full-length VEGFRs are subject to ectodomain shedding by membrane-anchored metalloproteinases (Swendeman et al., 2008). Proteolysis releases the ectodomain as a soluble decoy receptor and reduces the number of functional VEGFRs.

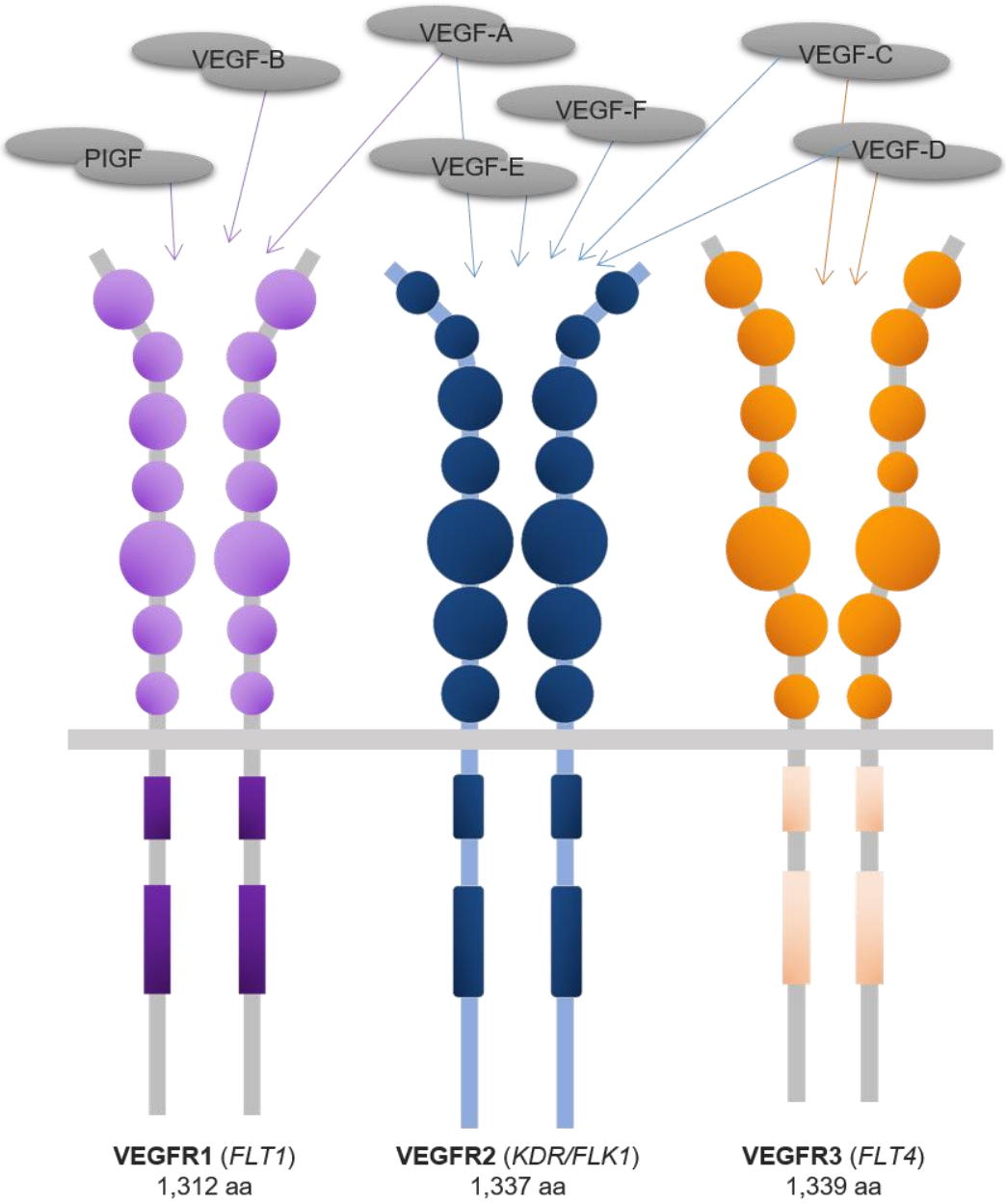


Figure 1.5 ***Subtypes of VEGF Receptors (VEGFRs)****. All VEGFRs possess 7 immunoglobulin (Ig)-like domains, a single transmembrane domain and a split intracellular kinase domain. Schematics are proportional to the number of amino acids (aa) present in each domain. Residues represent the size of VEGFRs following cleavage of the signal sequence.*

1.4.1 VEGFR2 Structure

VEGFR2 is a large 149 kDa membrane protein consisting of 7 extracellular Ig-like domains, a single transmembrane helix and an intracellular split kinase domain (*Figure 1.6a*; Roskoski, 2008). VEGF-A is an endogenous agonist for VEGFR2 that binds across Ig-like domains 2 (D2) and D3 with a stoichiometry of one VEGF-A dimer across a VEGFR dimer (*Figure 1.6b*; Leppanen et al., 2010; Brozzo et al., 2011). X-ray and Nuclear Magnetic Resonance structures have identified binding interfaces via exposed residues at each pole of the VEGF-A homodimer interacting with VEGFR1 (Wiesmann et al., 1997; Starovasnik et al., 1999; Markovic-Mueller et al., 2017) and VEGFR2 (*Figure 1.3a*; Brozzo et al., 2011). While structures have often been limited to isolated receptor domains, the full-length extracellular domain of structurally related VEGFR1 in complex with VEGF-A was recently determined by X-ray crystallography (*Figure 1.6c*; Markovic-Mueller et al., 2017). This emphasised the importance of characterising full-length VEGFRs due to the interplay of individual Ig-like domains in receptor dimerisation and activation.

As well as VEGF-A binding at the orthosteric ligand binding site, homotypic interactions between VEGFR2 monomers at Ig-like D4, D5 and D7 were identified as an additional step necessary for VEGFR2 activation (Ruch et al., 2007; Yang et al., 2010; Brozzo et al., 2011; Kisko et al., 2011; Hyde et al., 2012). Designed ankyrin repeat protein inhibitors, or DARPins, can sterically block these interactions and inhibit VEGFR2 activation (Hyde et al., 2012; Thieltges et al., 2018). These low-affinity energetically unfavourable interactions between VEGFR monomers may be necessary to stabilise the active dimer conformation through reorienting receptor monomers (Brozzo et al., 2011). Similar interactions are seen in related Class III RTKs (Yuzawa et al., 2007; Chen et al., 2008; Yang et al., 2008) and VEGFR1 (*Figure 1.6c*; Markovic-Mueller et al., 2017). While these interactions are largely shown in the presence of VEGF-A, homotypic D4 and D7 interactions also stabilised VEGFR2 dimers in the absence of ligand (Sarabipour et al., 2016).

1.4.2 VEGFR2 Activation

The activation of VEGFR2 is a multi-step process triggered by conformational changes throughout the RTK dimer upon VEGF-A binding (Tao et al., 2001; Ruch et al., 2007; Dosch and Ballmer-Hofer, 2010; Leppanen et al., 2010; Brozzo et al., 2011; Kisko et al., 2011). Ligand binding leads to a conformational twist through the extracellular region of VEGFR2 that reorients distinct Ig-like domains, shown by electron microscopy (Ruch et al., 2007), small angle X-ray scattering (Kisko et al., 2011) and the full-length crystal structure of structurally related VEGFR1 (Markovic-Mueller et al., 2017). VEGF-A binding causes the rotation of transmembrane helices (Dosch and Ballmer-Hofer, 2010; Manni et al., 2014b; Sarabipour et al., 2016). This leads to conformational changes between the N- and C- lobes of the intracellular split kinase domain (*Figure 1.6d*). Intrinsic kinase activity requires ATP (*Figure 1.2c*), which binds to the cleft in the glycine-rich loop and K/D/D motif (*Figure 1.6a*, red; Roskoski, 2008). Upon activation, a catalytic site at K868 is exposed to stabilise ATP binding. As well as containing the Mg^{2+}-binding DFG motif (*Figure 1.6a*, bold), the activation loop contains the site for auto-phosphorylation (Y1054/Y1059; *Figure 1.6a*, underlined). This step precedes subsequent phosphorylation events, as this active conformation enables appropriate orientation with the catalytic loop. This leads to trans-phosphorylation at Y951, Y1175 and Y1214 respectively (Manni et al., 2014a).

Formation of heteromeric complexes between VEGFR2 and other VEGFR subtypes can diversify VEGF-induced signalling outcomes (Rahimi et al., 2000; Dixelius et al., 2003; Nilsson et al., 2010; Cudmore et al., 2012; Coon et al., 2015). There is evidence that VEGFR2 can form heterodimers with VEGFR1 (Huang et al., 2001; Cudmore et al., 2012; Ahmadova et al., 2014) or VEGFR3 (Dixelius et al., 2003; Nilsson et al., 2010; Deng et al., 2015). Although endothelial cells express a higher proportion of VEGFR2 than VEGFR1 (Imoukhuede and Popel, 2011), computational simulations suggest that 10-50% VEGFR2 monomers exist as preassembled VEGFR1/VEGFR2 heterodimers (Mac Gabhann and Popel, 2007; Cudmore et al., 2012). As VEGFR1 has reduced tyrosine phosphorylation in response to VEGF-A (Waltenberger et al., 1994), this endogenous mechanism could prevent aberrant pro-angiogenic signalling.

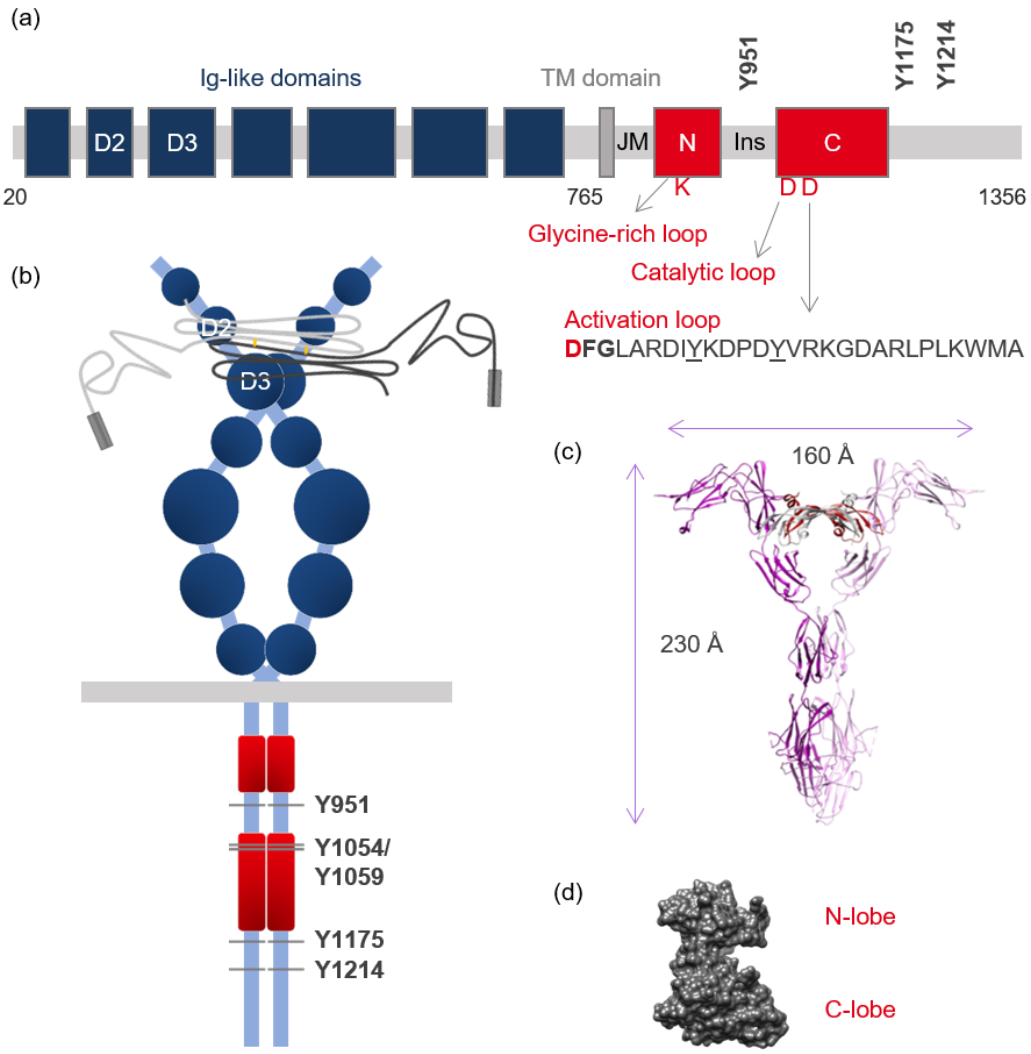


Figure 1.6 ***Structure of VEGF Receptor 2 (VEGFR2)****. (a) Structure of modular domains in VEGFR2, made up of immunoglobulin (Ig)-like domains, a transmembrane (TM) domain, a juxtamembrane (JM) domain and a split kinase domain intercepted by an kinase insert (Ins) domain. Numbers denote the amino acid number prior to signal sequence cleavage. Tyrosine residues, Y1054 and Y1059, are underlined in the activation loop. Y951, Y1175 and Y1214 are also phosphorylated to initiate signalling. K/D/D residues are involved in ATP binding to the tertiary structure. (b) The dimeric VEGF-A protein binds at D2/D3. There are additional D4-D4 and D7-D7 interactions between the VEGFR2 dimer. (C) Structure of VEGF-A bound at the full-length extracellular domain of structurally similar VEGFR1 (PDB 5T89, Markovic-Mueller et al., 2017). (d) Structure of the intracellular split kinase domain, illustrating the amino (N-) and carboxy (C-) lobes (PDB 2OH4, Hasegawa et al., 2007).*

1.4.3 VEGFR2 Signalling

The vital role of VEGFR2 in angiogenesis was evident from *in vivo* studies that inferfere with VEGFR2 expression and result in embryonic lethality. This was accompanied by severe cardiovascular abnormalities in VEGFR2-null mice, including models with global knockout (Shalaby et al., 1995; Sakurai et al., 2005) or endothelial-specific using a Cre-reporter (Oladipupo et al., 2018) or CRISPR-Cas9 (Huang et al., 2017). A similar phenotype was observed for heterozygous VEGF-A knockout mice (Carmeliet et al., 1996; Ferrara et al., 1996). VEGFR2 signalling leads to angiogenesis by stimulating endothelial cell proliferation, survival and motility (*Figure 1.7*). VEGF-A/VEGFR2 signalling also leads to vascular permeability, hence its initial description as VPF (Senger et al., 1983, 1986). Although represented as distinct phenotypic outcomes, signalling cascades downstream of VEGFR2 undergo extensive cross-talk (Simons et al., 2016).

VEGFR2-induced cell proliferation is largely attributed to Extracellular Signal-Regulated Kinase (ERK1/2) activation (*Figure 1.7a*). This is a key Ser/Thr kinase modulating cell cycle progression and transcription (Roskoski, 2012). Phospholipase C γ (PLCγ) directly couples to phosphorylated Y1175 (pY1175) via the SH2 domain at the C-terminus of PLCγ (Cunningham et al., 1997; Takahashi et al., 2001). This leads to IP_3-mediated calcium (Ca^{2+}) release from intracellular stores, enabling signalling via Protein Kinase C (PKC) and Ras-independent ERK1/2 activation (Takahashi et al., 1999). Ca^{2+} release from intracellular stores also activates Calmodulin and Calcineurin. This causes the dephosphorylation of Nuclear Factor of Activated T Cells (NFAT), a family of transcription factors. Both NFAT and ERK1/2 are translocated into the nucleus upon activation to regulate gene transcription (Armesilla et al., 1999; Takahashi et al., 2001). For example, transcription factor c-Fos is modulated in response to NFAT (Macián et al., 2001) or ERK1/2 (Monje et al., 2005). Together with c-Jun, this forms the AP-1 complex that binds DNA to regulate proliferation.

Endothelial cell survival is promoted through Phosphoinositide 3-Kinase (PI3K; *Figure 1.7b*). PI3K enzymes are composed of a catalytic p110 domain and a regulatory p85 subunit. VEGFR2 activation primarily leads to pro-survival signalling through Class I PI3Ks that lead to Phosphatidylinositol (3,4,5)-trisphosphate (PIP_3) production (Graupera and Potente, 2013). This activates AKT, a Ser/Thr kinase also known as Protein Kinase B (Gerber et al., 1998). Following recruitment to PIP_3 lipids in the plasma membrane, AKT can be phosphorylated by PDK1/2 (Bellacosa et al., 1991). Activated AKT can modulate gene expression, such as phosphorylating Forkhead box O (FOXO) to prevent its constitutive role in cell cycle arrest and programmed cell death (Graupera and Potente, 2013).

VEGFR2 is highly expressed at the leading edge of invasive tip cells in angiogenic sprouts (Gerhardt et al., 2003; Jakobsson et al., 2010). This reflects the importance of motility downstream of VEGFR2 activation (*Figure 1.1b*). Focal adhesion kinase (FAK) is a key regulator of VEGFR2-mediated cell migration (Abu-Ghazaleh et al., 2001) and vascular permeability (Chen et al., 2012). FAK is a cytoplasmic tyrosine kinase that initiates multiple pathways that lead to motility (*Figure 1.7c*), such as disassembling focal adhesions (Webb et al., 2004) and reorganising the actin cytoskeleton (Schaller, 2010). Src homology-2 domain containing protein B (SHB) adaptor proteins can initiate FAK signalling in response to VEGFR2 phosphorylation at pY1175 (Holmqvist et al., 2004). FAK signalling can be activated by Src following interactions between pY951 and the SH2 domain of T-cell-specific adaptor protein (TSAd) (Matsumoto et al., 2005; Sun et al., 2012). Src kinases themselves contain an SH2 domain that could recruit to VEGFR2 (Roskoski, 2015b). RhoA GTPases also lead to to motility via FAK and cytoskeletal rearrangements (Le Boeuf et al., 2004; Bryan et al., 2010). There is evidence that migration is stimulated by pY1214-mediated recruitment of adaptor protein Nck. This associates with cytoplasmic tyrosine kinase Fyn, leading to p38 MAPK activation via Cdc42 (Lamalice et al., 2004, 2006). p38 MAPK mediates actin cytoskeleton reorganisation (McMullen et al., 2005). In terms of vascular permeability, Src has a role in disrupting adherens junctions between endothelial cells through inducing the internalisation of vascular endothelial cadherin (VE-cadherin; Gavard and Gutkind, 2006; Sun et al., 2012; Gordon et al., 2016; Li et al., 2016). PI3K/AKT pathways also lead to vascular permeability through activating endothelial nitric oxide synthase (eNOS; Kang et al., 2013; Lee et al., 2014a).

Dephosphorylation of VEGFR2 by phosphatases terminate further adaptor protein recruitment (Corti and Simons, 2017). Interestingly, phosphatase-mediated dephosphorylation of VEGFR2 was particularly observed in stalk cells (Hayashi et al., 2013). There is evidence that VEGFR2 can be dephosphorylated by vascular endothelial T-cell protein tyrosine phosphatase (TCPTP; Mattila et al., 2008), PTP (VE-PTP; Mellberg et al., 2009) and PTP1b (Lanahan et al., 2014).

Functional studies have suggested that distinct VEGF-A isoforms lead to different phenotypic outcomes. $VEGF_{165}a$ is a full agonist for VEGFR2-driven signalling responses, hence its consideration as a prototypical ligand for comparisons against other VEGF-A isoforms. Several groups have demonstrated that VEGF-A isoforms, such as $VEGF_{165}b$ and $VEGF_{121}a$, are partial agonists in stimulating a sub-maximal response relative to $VEGF_{165}a$ in endothelial cells (*Table 1.1*).

Table 1.1 ***Distinctions in signalling of VEGF-A isoforms****. See next page.*

Signalling vs. $VEGF_{165}a$			Experimental system
$VEGF_{165}b$	*In vivo*	<	Rats (Woolard et al., 2004); Mice (Cébe Suarez et al., 2006)
	Sprouting	<	ES cells (Kawamura et al., 2008b)
		<	PC3/CAKI tumour cells (Rennel et al., 2008)
	Proliferation	<	PAECs* (Kawamura et al., 2008b)
		<	HCAECs (Catena et al., 2010a; Hueso et al., 2017)
		<	HUVECs (Delcombel et al., 2013)
	Migration	<	HCAECs (Hueso et al., 2017)
	Permeability	<	HPMECs (Ourradi et al., 2017)
		<	HUVECs (Pang et al., 2017)
	pVEGFR2	<	PAECs* (Kawamura et al., 2008b)
		<	HPMECs (Ourradi et al., 2017)
	pMAPK, pAKT or pERK	</=	HMVECs (Woolard et al., 2004)
		<	HCAECs (Hueso et al., 2017)
		=	HPMECs (Ourradi et al., 2017)
		<	PAECs* (Cébe Suarez et al., 2006; Delcombel et al., 2013)
		<	HUVECs (Delcombel et al., 2013)
		<	HPMECs (Ourradi et al., 2017)
$VEGF_{121}a$	*In vivo*	<	Mice (Cébe Suarez et al., 2006; Kawamura et al., 2008b)
	Sprouting	<	HUVECs (Pan et al., 2007)
		=	Rat aortic rings (Krilleke et al., 2007)
		<	ES cells (Kawamura et al., 2008b)
		<	HUVECs (Fearnley et al., 2014)
	Proliferation	<	BAECs (Keyt and Berleau, 1996)
		=	HUVECs (Poltorak et al., 1997)
		<	HCAECs (Catena et al., 2010a)
		<	HUVECs (Delcombel et al., 2013; Fearnley et al., 2016; Shiying et al., 2017)
	Survival	<	HUVECs (Shiying et al., 2017)
	Migration	<	HUVECs (Fearnley et al., 2016)
	Permeability	<	HPAECs (Becker et al., 2005)
		=	Mice (Xu et al., 2011)
		=	HUVECs (Fearnley et al., 2016)
	pVEGFR2	=	HUVECs (Pan et al., 2007)
		<	HUVECs (Fearnley et al., 2014, 2016; Shiying et al., 2017)
	pERK, pAKT	<	HUVECs (Delcombel et al., 2013; Fearnley et al., 2014, 2016)
$VEGF_{145}a$	Sprouting	<	Embryonic stem cells (Kawamura et al., 2008b)
	Proliferation	<	HUVECs (Poltorak et al., 1997; Fearnley et al., 2016)
	Migration	=	HUVECs (Fearnley et al., 2016)
	Permeability	<	HUVECs (Fearnley et al., 2016)
	pVEGFR2	<	PAECs-R2 (Kawamura et al., 2008b)
		<	HUVECs (Fearnley et al., 2016)
	pERK, pAKT	<	HUVECs (Fearnley et al., 2016)
$VEGF_{189}$	Proliferation	=	HUVECs (Hervé et al., 2005)
		<	Murine ECs (Yamamoto et al., 2016)
	Survival	<	Murine ECs (Yamamoto et al., 2016)
	Migration	=	BAECs (Hervé et al., 2005)

Table 1.1 Legend. Responses were compared to prototypical $VEGF_{165}a$ in the same study. *In vivo* experiments monitored angiogenesis. Western blots were used to investigate phosphorylated proteins: VEGFR2 (pVEGFR2), Mitogen-activated protein kinase (pMAPK), Extracellular Signal Related Kinase (pERK), or pAKT. There was evidence for similar (=) or lower (<) functional responses with respect to $VEGF_{165}a$. *PAECs were transfected with VEGFR2.
Abbreviations: **BAECs** Bovine Aorta Endothelial Cells; **HCAECs** Human Coronary Artery Endothelial Cells; **HMVECs** Human Microvascular Endothelial Cells; **HPAECs** Human Pulmonary Artery Endothelial Cells; **HPMECs** Human Pulmonary Microvascular Endothelial Cells; **HUVECs** Human Umbilical Vein Endothelial Cells; **PAECs** Porcine Aorta Endothelial Cells.

1.4.4 VEGFR2 Trafficking

VEGFR2 can internalise in the absence or presence of ligand stimulation (Ewan et al., 2006; Jopling et al., 2009; Jopling et al., 2011). Constitutive internalisation of VEGFR2 is postulated to, at least in part, protect from protease-mediated ectodomain shedding (Basagiannis and Christoforidis, 2016). VEGFR2 internalises through clathrin-dependent mechanisms (Ewan et al., 2006; Lampugnani et al., 2006). There is also evidence that VEGFR2 is subject to caveolae-mediated endocytosis (Labrecque et al., 2003) and macropinocytosis (Basagiannis and Christoforidis, 2016; Basagiannis et al., 2016). VEGFR2 first accumulates in $Rab5^+$ endosomes (Gampel et al., 2006) (*Figure 1.8*). VEGFR2 can then recycle back to the plasma membrane via short loop recycling routes in $Rab4^+$ endosomes or long loop routes in $Rab11^+$ endosomes (Jopling et al., 2014). Trafficking routes can be determined by post-translational modifications to VEGFR2. Ubiquitination can initiate lysosomal degradation (Smith et al., 2016), while SUMOylation can trigger trafficking to the Golgi apparatus for a subcellular receptor store (Zhou et al., 2018).

There is evidence that VEGFR2 can signal from intracellular endosomes (Lanahan et al., 2010; Nakayama et al., 2013; Fearnley et al., 2016; Xie et al., 2019). It was suggested that ERK1/2 activation required VEGFR2 endocytosis (Gourlaouen et al., 2013; Fearnley et al., 2016), however endocytic inhibitors have off-target effects on ERK activation and requires careful interpretation (Basagiannis et al., 2017). Alongside evidence for endosomal signalling for other receptor classes (Murphy et al., 2009), this highlights the importance of the spatiotemporal dynamics of VEGFR2 signalling. It is suggested that VEGFR2 trafficking is subject to regulation by other membrane proteins, such as NRP1 (Ballmer-Hofer et al., 2011).

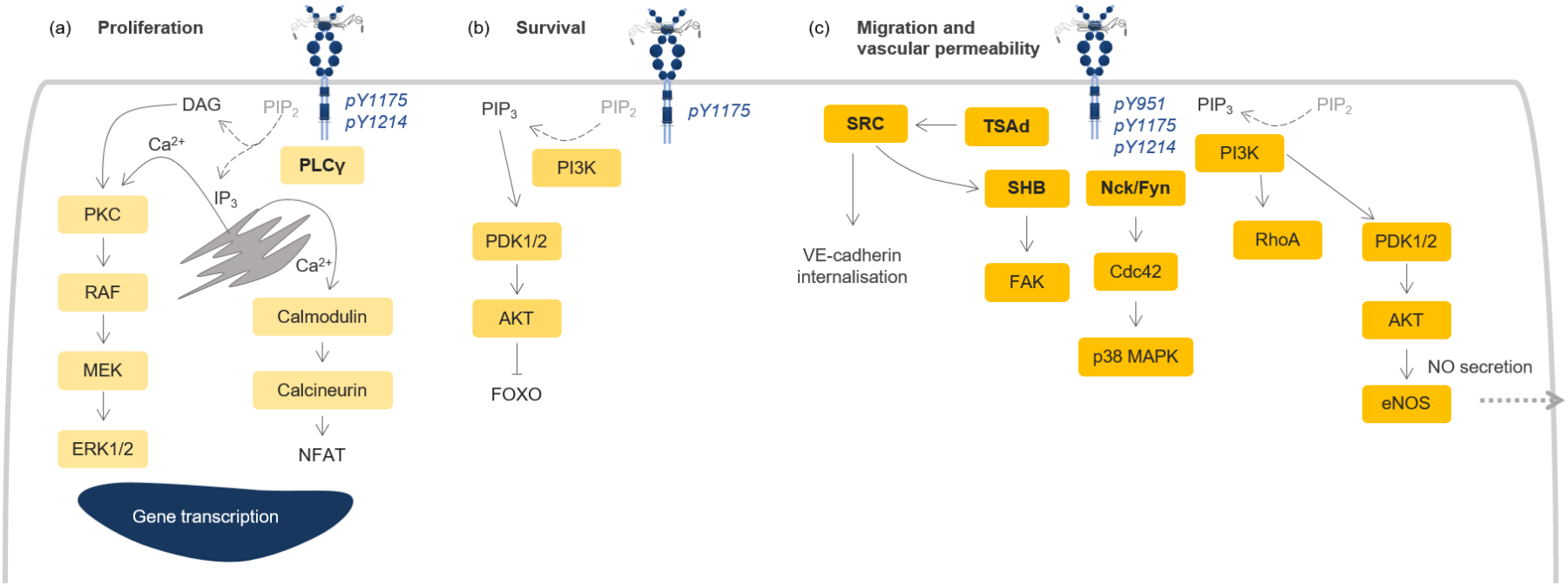


Figure 1.7 ***Intracellular signalling cascades downstream of VEGFR2 activation in endothelial cells.*** *See next page.*

Figure 1.7 Ctd. Signalling pathways are triggered by adaptor proteins docking at major tyrosine phosphorylation sites (pY). This schematic represents direct VEGFR2 interactions (bold) and intracellular signalling amongst effector proteins (yellow boxes). (a) PLCγ leads to IP_3-mediated calcium release from intracellular stores and ERK1/2 activation. Ca^{2+} also leads to NFAT-mediated gene transcription, both of which stimulate cell proliferation. (b) PI3K phosphorylates PIP_2 into PIP_3, enabling AKT activation and cell survival. (c) Migration and vascular permeability are downstream of PI3K/AKT activation, Src-mediated FAK activation and p38 MAPK-mediated cytoskeletal rearrangements. Abbreviations: ***DAG*** *diacylglycerol;* ***ERK*** *Extracellular signal regulated kinase 1/2;* ***FOXO*** *Forkhead box O;* ***IP_3*** *Inositol trisphosphate;* ***MAPK*** *Mitogen-activated protein kinase;* ***MEK*** *MAPK/ERK kinase;* ***NFAT*** *Nuclear factor of activated T-cells;* ***PI3K*** *Phosphoinositide 3-kinase;* ***PIP_2*** *Phosphatidylinositol 4,5-bisphosphate;* ***PIP_3*** *Phosphatidylinositol (3,4,5)-trisphosphate;* ***PLCγ*** *Phospholipase C γ;* ***RAF*** *Rapidly accelerated fibrosarcoma protein;* ***SHB*** *Src homology-2 domain containing protein B;* ***TSAd****, T cell-specific adaptor protein. Adapted from* Simons et al. (2016).

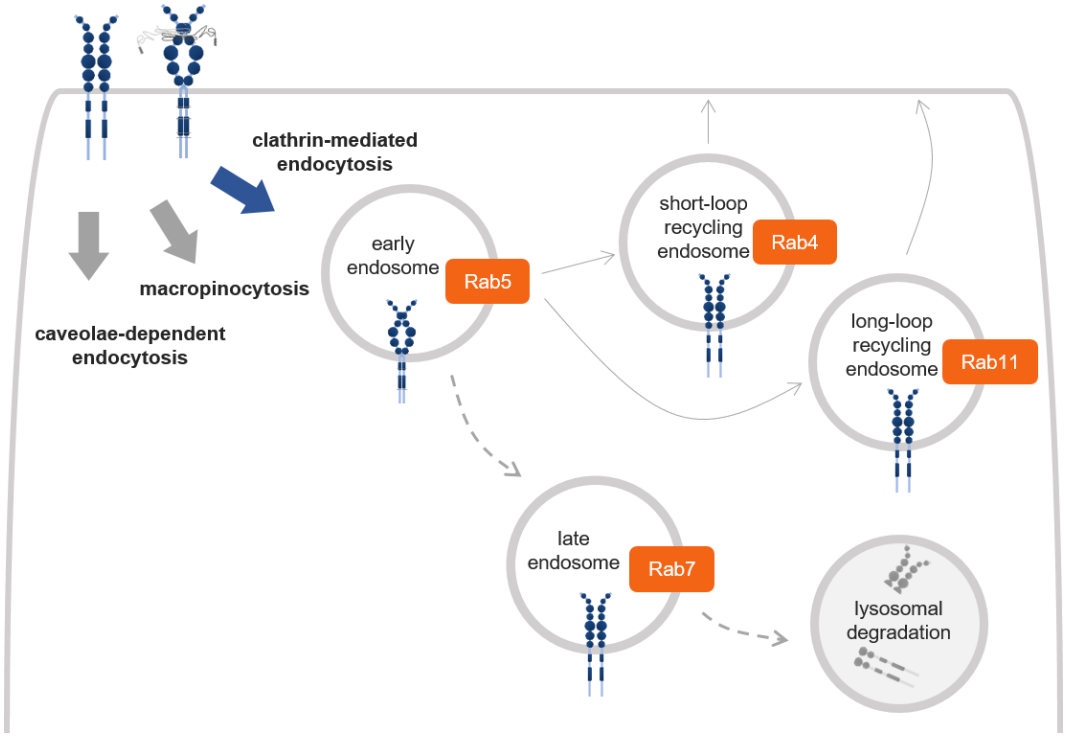


Figure 1.8 ***Endocytosis and trafficking routes of VEGFR2.*** *Endocytosis can be clathrin-dependent (thick blue arrow) or -independent (thick grey arrow). VEGFR2 can internalise in the presence or absence of ligand. Trafficking amongst subcellular endosomal compartments is identified using distinct associated Rab GTPases (orange). VEGFR2 is internalised into Rab5⁺ sorting endosomes. Receptors can be recycled back to the plasma membrane in Rab4⁺ endosomes (fast trafficking) or Rab11⁺ (slow trafficking) endosomes. Alternatively, VEGFR2 is sorted into late Rab7⁺ endosomes for targeting to the lysosome and proteolytic degradation.*

1.5 NRP1 AS A CO-RECEPTOR

Co-receptors are membrane-associated accessory proteins, typically unable to signal independently, that facilitate the signalling of a conventional receptor (Kirkbride et al., 2005). This term often links to antigen binding or pathogen entry into a host cell in the field of immunology (Chen and Flies, 2013). Co-receptors are also involved in diversifying signal transduction in response to ligand stimulation, depending on physiological needs. Co-receptors can be associated with the membrane via a glycosylphosphatidylinositol anchor added during post-translational modifications, such as the co-receptor associated with RET receptors required for Glial cell-Derived Neurotrophic Factor-induced signalling (Mulligan, 2014). Alternatively, co-receptors can be transmembrane proteins possessing a hydrophobic transmembrane domain, such as NRP1.

1.5.1 Neuropilins

Neuropilins are 102 kDa pleiotropic Type I single transmembrane proteins. Neuropilins can interact with structurally and functionally unrelated proteins, VEGF and Class 3 Semaphorins (Sema3; Djordjevic and Driscoll, 2013; Guo and Vander Kooi, 2015). These are involved in promoting angiogenesis and neuronal guidance, acting as co-receptors for VEGFR2 and plexins respectively. There are two subtypes: NRP1 (Chromosome *10p11*), also known as CD304; and NRP2 (Chromosome *2q33*). NRP1 interacts with VEGF-A, VEGF-B, VEGF-E and PIGF, as well as Sema3A, Sema3B, Sema3C, Sema3E and Sema3F (Pellet-Many et al., 2008). In contrast, NRP2 interacts with VEGF-A, VEGF-C, VEGF-D, in addition to Sema 3B, Sema3C, Sema3F and Sema3G (Pellet-Many et al., 2008). NRP1 was first identified for its role in axon guidance in the nervous system (Takagi et al., 1995; He and Tessier-Lavigne, 1997). It was then identified as the receptor for VEGF-A (Soker et al., 1996, 1998), whereby NRP1 is expressed alongside VEGFR2 by endothelial cells (Soker et al., 1998; Lim et al., 2005; Imoukhuede and Popel, 2011). It is also overexpressed in tumours, with NRP1 upregulation correlated to aggressive cancer phenotypes (Jubb et al., 2012; Goel and Mercurio, 2013; Lee et al., 2014b). Due to its role in VEGFR2-mediated angiogenesis, this project will focus on NRP1.

1.5.2 NRP1 Structure

NRP1 is a glycoprotein composed of five extracellular domains and a small cytoplasmic region (*Figure 1.9*). Extracellular domains have structural homology to other motifs (*Figure 1.9a*): domains a1 and a2 contain the structural motif that belong to the complement C1r/C1s, Uegf, Bmp1 (CUB) domains; domains b1 and b2 share homology with coagulation factors V/VII; and domain c is denoted the mephrin, A5 protein and μ phosphatase (MAM) domain (Djordjevic and Driscoll, 2013). The extracellular domain is also subject to O-linked glycosylation (Shintani et al., 2006). VEGF-A interacts at the b1 domain (*Figure 1.9b-d*; Mamluk et al., 2002; Lee et al., 2003; Vander Kooi et al., 2007; Parker et al., 2012). In contrast, semaphorins bind to distinct extracellular domains a1/a2 (Gu et al., 2002; Appleton et al., 2007). The binding interface with VEGF-A at the b1 domain contains a binding pocket with exposed residues, Tyr297 and Asp320 (*Figure 1.9d*; Herzog et al., 2011; Parker et al., 2012; Mota et al., 2018). This interaction occurs with VEGF-A via an arginine residue encoded by exon 8a (CDKPRR, *Figure 1.4*). Other peptides that mimic the C-terminus of $VEGF_{xxx}a$ can interact through the same binding pocket, such as immunomodulatory peptide tuftsin (TKPR; Von Wronski et al., 2006; Vander Kooi et al., 2007) or phage display-derived peptide ATWLPRR (Starzec et al., 2006, 2007). NRP1 has also been shown as a co-receptor for other growth factors. These include Fibroblast Growth Factor (FGF; West et al., 2005), PDGF (Banerjee et al., 2006), EGF (Rizzolio et al., 2012) and hedgehog-induced signalling (Pinskey et al., 2017). Direct binding was identified with FGF (West et al., 2005; Auriau et al., 2018), as well as through the C-terminal arginine of PDGF (Muhl et al., 2017).

Although the short, 44 amino acid cytoplasmic tail lacks catalytic activity, the C-terminus contains a Serine-Glutamate-Alanine (SEA) motif (*Figure 1.9a,b*). This can interact with proteins containing a PDZ domain, named according to proteins first found to contain this domain. These include postsynaptic density 95 (Cho et al., 1992), discs large protein (Woods and Bryant, 1991) and zona occludens-1 (Itoh et al., 1993). Through this SEA motif, NRP1 interacts with the PDZ domain-containing adaptor protein synectin (also known as GAIP-interacting protein, *GIPC1*; Cai and Reed, 1999; Wang et al., 2006; Prahst et al., 2008). There is also evidence for a soluble NRP1 lacking the MAM, transmembrane and cytoplasmic domains (Gagnon et al., 2000; Rossignol et al., 2000). This decoy receptor can bind $VEGF_{165}a$, thus acting as a sink for circulating VEGF-A.

NRP1 assembles into oligomers in endothelial cells (Nakamura et al., 1998). This can be promoted by ECM components (Vander Kooi et al., 2007; Roth et al., 2008; Nasarre et al., 2010). It was first proposed that the MAM domain was involved in oligomerisation, however no interface was identified by the X-ray crystal structure (Yelland and Djordjevic, 2016). It was also suggested that NRP1 oligomerisation is mediated through the GxxxG motif in the NRP1 transmembrane domain (Roth et al., 2008; Nasarre et al., 2010). NRP1 can form heteromeric complexes with VEGFR2 (Whitaker et al., 2001; Prahst et al., 2008; Gelfand et al., 2014; King et al., 2018), with evidence for ligand-independent VEGFR2/NRP1 complex formation (Whitaker et al., 2001; Gelfand et al., 2014; King et al., 2018).

1.5.3 NRP1 Function in Vascular Development

VEGFR2 signalling is enhanced by its co-receptor NRP1 (Djordjevic and Driscoll, 2013; Guo and Vander Kooi, 2015). The functional role of NRP1 in angiogenesis was evident from overexpression of NRP1 in mice. This led to embryonic lethality with a cardiovascular phenotype and excess capillaries (Kitsukawa et al., 1995). There were also severe cardiovascular abnormalities underlying embryonic lethality in *Nrp1* knockout mice (Kawasaki et al., 1999; Takashima et al., 2002), zebrafish (Lee et al., 2002) and endothelial-specific knockout mice (Gu et al., 2003). These had similar phenotypes to heterozygous VEGF-A mice and VEGFR2-null mice (*Introduction 1.4.3*).

NRP1 can potentiate VEGFR2-mediated endothelial cell motility and arterial vessel development *in vivo* (Pan et al., 2007; Fantin et al., 2011; Gelfand et al., 2014). Numerous groups have shown that NRP1 influenced endothelial cell motility downstream of p38 MAPK (Kawamura et al., 2008a; Ballmer-Hofer et al., 2011). Recent work also highlighted VEGF-A/NRP1 in phosphorylating p130Cas (Evans et al., 2011; Seerapu et al., 2013; Evans et al., 2017), a docking protein localised to focal adhesions (Polte and Hanks, 1995; Donato et al., 2010). Inhibiting NRP1 with antibodies (Pan et al., 2007) or siRNA (Fearnley et al., 2014) reduced $VEGF_{165}$a-induced phosphorylation of VEGFR2 or ERK, respectively. A VEGF-A binding-dead mutant of NRP1 (Y297A) had reduced FAK phosphorylation and migration *in vitro*, however there was minimal effect on ERK phosphorylation (Herzog et al., 2011). Interestingly, NRP1 was highly expressed in motile tip cell filopodia at the leading edge of angiogenic sprouts (Fantin et al., 2013, 2015).

NRP1 requires the C-terminal PDZ-binding domain to modulate VEGFR2 signalling, with evidence it was also necessary for heteromeric complex formation with VEGFR2 (Prahst et al., 2008). Truncating the C-terminus of NRP1 similarly affected arterial fate *in vivo* with minimal effect on vasculogenesis or angiogenesis (Fantin et al., 2011; Lanahan et al., 2013). The C-terminal SEA motif binds synectin, an intracellular adaptor protein that also interacts with myosin VI (Naccache et al., 2006; Wang et al., 2006; Katoh, 2013). Zebrafish and mice lacking synectin (Chittenden et al., 2006) or myosin VI (Lanahan et al., 2010) had a disrupted vasculature that specifically implicated arterial-specific phenotypes. Myosin VI is a molecular motor that can bind actin and transport internalised cargo towards the cell body (Wells et al., 1999; Reed et al., 2005; Naccache et al., 2006; Shang et al., 2017). Studies suggested that synectin and myosin VI modulate VEGFR2 endocytosis and trafficking from early endosomes, away from PTP1b-rich domains, to the plasma membrane (Naccache et al., 2006; Salikhova et al., 2008; Lanahan et al., 2010; Ballmer-Hofer et al., 2011). NRP1 expressed by a neighbouring cell can have distinct effects on VEGFR2 trafficking (Koch et al., 2014). While NRP1 is suggested to modulate VEGFR2 trafficking, it is unknown how this affects interactions with VEGF-A.

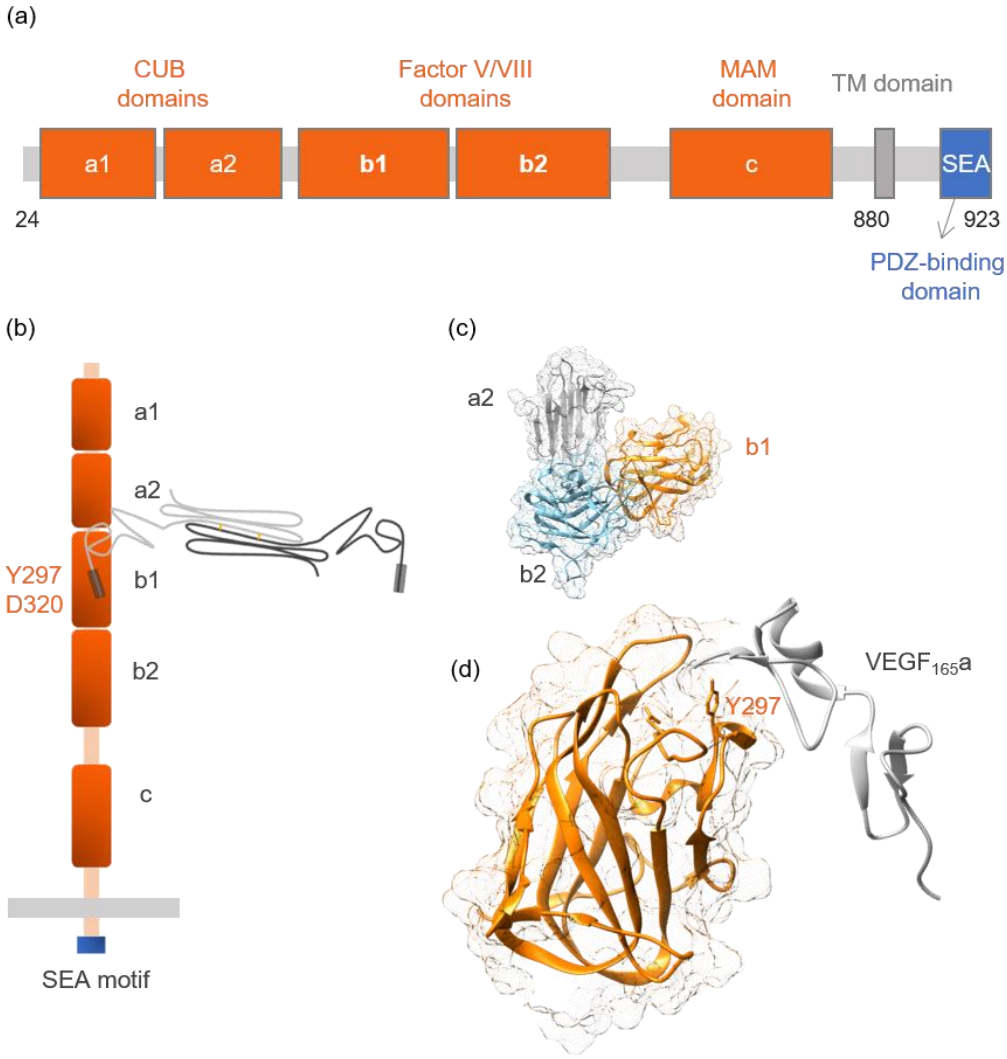


Figure 1.9 ***Structure of NRP1.*** *(a) NRP1 is composed of 5 extracellular domains, a transmembrane (TM) helix and a short cytoplasmic tail. The C-terminus contains a Ser-Glu-Ala (SEA) motif which can interact with proteins containing a PDZ domain (b) Semaphorins interact with a1/a2, whereas growth factors interact with the b1 domain. The C-terminus of VEGF-A interacts with the b1 domain of NRP1. Mutagenesis and X-ray crystallography highlighted interactions with NRP1 residues Y297 and D320. (c) The tertiary structure of NRP1 domains a2, b1 and b2 (PDB 2QQM, Appleton et al., 2007). (d) The binding interface between NRP1 (orange) and the C-terminus of VEGF$_{165}$a (grey) (PDB 4DEQ, Parker et al., 2012). Abbreviations:* ***CUB*** *Complement C1r/C1s, Uegf, Bmp1;* ***MAM*** *mephrin, A5 protein and μ phosphatase;* ***PDZ*** *postsynaptic density 95, discs large protein, zona occludens-1.*

1.6 PHARMACOLOGICAL FOCUS

1.6.1 Drugs Targeting VEGF-A, VEGFR2 and NRP1

Numerous anti-angiogenic therapeutics that target VEGF-A/VEGFR2 signalling have been approved in oncology (*Table 1.2*). These drugs are largely antibodies (suffix -ab) or small molecule inhibitors (suffix -ib), often prescribed in combination with chemotherapy. The first antibody developed was bevacizumab, a monoclonal IgG1 antibody raised against VEGF-A to bind circulating ligand and prevent interactions with VEGFRs (Kim et al., 1992; Presta et al., 1997; Chen et al., 1999). This interacts with residues encoded by exons 1-5, thus also interacting with 'anti-angiogenic' $VEGF_{165}b$ (Varey et al., 2008). Bevacizumab was recently added to the WHO Essential Medicines (World Health Organization, 2019), highlighting its impact on patients. Ramucirumab is a Fab antibody fragment raised against the D3 domain of VEGFR2 to sterically inhibit ligand binding (Lu et al., 2003; Zhu et al., 2003; Miao et al., 2006; Franklin et al., 2011). Aflibercept, also known as 'VEGF-trap', is a recombinant soluble peptide-antibody fusion between the extracellular VEGFR1 D1-D3 and a humanised Fc fragment of IgG1 (Holash et al., 2002). This acts as a decoy receptor binding circulating ligand with high affinity. However, antibody therapeutics incur significant costs (Hernandez et al., 2018).

Most approved anti-angiogenic drugs used in oncology are RTK Inhibitors (RTKIs) that prevent ATP-dependent phosphorylation (*Figure 1.2c*). These block ATP binding in the highly conserved catalytic kinase domain. RTKIs therefore target numerous kinases (Davis et al., 2011). RTKIs are classified according to their mechanism of inhibiting ATP-dependent phosphorylation (Gotink and Verheul, 2010; Dar and Shokat, 2011). Class I RTKIs bind the active kinase conformation and inhibit the ATP-binding domain, such as pazopanib. Class II RTKIs bind the inactive conformation and indirectly prevent ATP binding via the DFG activation loop, such as sorafenib. Class III RTKIs are then non-competitive for ATP binding. Additional classes have been suggested, such as Class IV RTKIs binding at the juxtamembrane domain (McTigue et al., 2012). Many other RTKIs have been developed but failed at various stages of clinical development, such as the Class I/IV RTKI cediranib (AZD-2171; Wedge et al., 2005).

Originally considered a 'silver bullet', the limitations of cancer therapeutics targeting VEGF-A/VEGFR2 quickly become apparent (Hayden, 2009). Drugs lacked long-term efficacy in patient subsets as they eventually became resistant (Kieran et al., 2012; Simon et al., 2017). There were also on-target adverse effects, such as proteinuria and hypertension (Kamba and McDonald, 2007; Carter et al., 2017).

Targeting aberrant VEGF-A/VEGFR2 signalling in ophthalmology had fewer adverse effects, largely limited to those directly attributed to the intravitreal injections (Abramowicz et al., 2015). Pegaptanib (Macugen®, Valeant) was the first approved, as an aptamer oligonucleotide that sequesters circulating VEGF-A (Gragoudas et al., 2005). Ranibizumab (Lucentis®, Novartis) is similar to bevacizumab as a monoclonal humanised antibody against VEGF-A (Narayanan et al., 2006). Aflibercept, the monoclonal VEGFR2 D3-targetted antibody, is also approved for AMD as Eylea® (Bayer plc).

There is growing interest in NRP1 as a drug target due to the correlation between NRP1 upregulation in malignant tumours and aggressive cancer phenotypes (Jubb et al., 2012; Goel and Mercurio, 2013; Lee et al., 2014b). For example, MNRP1685A was a recombinant IgG1 monoclonal antibody developed by Genentech Inc. that binds the b1/b2 domain of NRP1 (Liang et al., 2007). Phase I clinical trials were initially promising when dosed in isolation (Weekes et al., 2014), however development was ceased following nephrotoxity when combined with bevacizumab (Patnaik et al., 2014). Other drug discovery programmes identified small cyclic peptide antagonists based on $VEGF_{165}$a residues encoded by exons 7 and 8. These peptides include EG3287 (RXDKPRR; Jia et al., 2006) and A7R (ATWLPPR; Starzec et al., 2006, 2007). These were compromised by their metabolism and bioavailability properties, leading to the development of peptidomimetics such as EG00229 (Jarvis et al., 2010). Non-peptide antagonists are also being developed based on the arginine-driven interaction, such as NPRa-308 (Borriello et al., 2014).

NRP1 overexpression in different tumour types also led to interest from the perspective of drug delivery. Tumour penetrating peptides targeting NRP1 were discovered from phage libraries with a consensus R/KxxR/K sequence (Teesalu et al., 2009). This C-terminal arginine residue is responsible for binding NRP1 at the b1 domain, similarly to $VEGF_{165}$a (*Figure 1.9d*). This led to the series of 'CendR' penetrating peptides from the Ruoslahti group (Sugahara et al., 2009, 2010; Pang et al., 2014, 2015), as well as Kadonosono et al. (2015), to deliver drugs or imaging probes to tumour cells.

Table 1.2 ***Clinically approved inhibitors for numerous cancer types targeting VEGF-A/VEGFR2 signalling***.

Therapeutic drug	Administration	Approval	Cancer subtype
bevacizumab (Avastin®, Roche)	IV	FDA: Feb 2004 EMC: Jan 2005	Colorectal, breast, NSCLC, renal, ovarian, cervical
sorafenib tosilate (Nexavar®, Bayer plc)	Oral	FDA: Dec 2005 EMC: July 2006	Hepatocellular, renal, thyroid
sunitinib malate (Sutent®, Pfizer)	Oral	FDA: Jan 2006 EMC: July 2006	Renal, pancreatic, gastrointestinal
pazopanib hydrochloride (Votrient®, Novartis)	Oral	FDA: Oct 2009 EMC: June 2010	Renal, sarcoma
vandetanib (Capelsa®, Genzyme)	Oral	FDA: April 2011 EMC: Feb 2012	Thyroid
axitinib (Inlyta®, Pfizer)	Oral	FDA: Jan 2012 EMC: Sept 2012	Renal
ziv-aflibercept (Zaltrap®, Sanofi)	IV	FDA: Aug 2012 EMC: Feb 2013	Colorectal
regorafenib (Stivarga®, Bayer plc)	Oral	FDA: Sept 2012 EMC: Aug 2013	Colorectal, GIST
cabozantinib (Cometriq®, Ipsen Ltd)	Oral	FDA: Nov 2012 EMC: Sept 2016	Thyroid, renal
ramucirumab (Cyramza®, Eli Lilly)	IV	FDA: April 2014 EMC: Dec 2014	Gastric, colorectal, NSCLC
lenvatinib mesilate (Lenvima®, Eisai Ltd)	Oral	FDA: Feb 2015 EMC: May 2015	Thyroid, Renal
midostaurin (Rydapt®, Novartis)	Oral	FDA: April 2017 EMC: Sept 2017	Leukaemia

Obtained from the public database on *www.drugs.com*.

Abbreviations: **IV** Intravenous; **GIST** Gastrointestinal Stromal Cancer; NSCLC Non-Small Cell Lung Cancer.

1.6.2 Principles of Quantitative Pharmacology

Transmembrane receptors include RTKs, G protein-coupled receptors (GPCRs) and ion channels. These typically signal in response to a ligand through conformational changes in the receptor, often stimulating intracellular signalling. An agonist is a ligand that binds to a receptor and causes a biological response (Neubig et al., 2003). The orthosteric site is defined by where the endogenous agonist binds - such as D2/D3 at VEGFR2. An allosteric site is a topographically distinct site on the receptor (De Smet et al., 2014) – such as homotypic VEGFR2 interactions at D4/D7. An antagonist reduces the activity of a ligand. These can either compete for the orthosteric site, bind the receptor at a distinct site to inhibit activity or reduce their functional activity through indirect mechanisms.

Pharmacology is the basis of drug development. This involves a quantitative understanding of drugs and receptors, thus enabling objective comparisons and statistical validation despite biological variability. Fitting experimental data to a model can allow us to infer mechanisms, as in Chemistry and Physics. Drug receptor theory is the cornerstone to understanding the mechanisms of drugs and ligands (Finlay et al., 2020). Early work by Langley and Ehrlich introduced the concept of a selective 'receptive substance' (Langley, 1905; Maehle et al., 2002). The field of pharmacology then progressed into a quantitative understanding, pioneered by Alfred J. Clark (Clark, 1933; Parascandola, 1982). Pharmacological equations are based on a state of equilibrium, whereby interactions between the ligand (L) and receptor (R) are a reversible chemical reaction forming a ligand/receptor complex (LR) shown in Equation 1.1.

Equation 1.1

$$L + R \underset{k_{off}}{\overset{k_{on}}{\rightleftharpoons}} LR$$

Experiments investigating ligand or drug binding are typically quantified according to the Law of Mass Action. Originally described by physicists Guldberg and Waage (1864), this describes the relationship between the rate of association and dissociation at equilibrium (*Methods Equation 2.5*). As such, the rate of a reaction is directly proportional to the concentration of reactants at equilibrium (Kenakin, 2014). This quantitative understanding was later applied to drug/receptor interactions from the Langmuir Adsorption Isotherm, originally describing the adsorption of molecules to metal. Affinity describes the ability for a ligand or drug to interact with its receptor. This is the reciprocal of the equilibrium dissociation constant, K_d, denoting the concentration of ligand

occupying 50% of receptors. Kinetics of ligand/receptor interactions can also be described by the rate of association, k_{on}, and the rate of dissociation, k_{off} (Tummino and Copeland, 2008). It should be noted that applying mathematical models to biological systems inevitably introduces assumptions. For example, the law of mass action assumes simple 1:1 ligand/receptor stoichiometry (Kenakin, 2016).

The degree to which an agonist can then produce a response is defined by efficacy (Stephenson, 1956). Functional experiments quantify responses to agonist stimulation by their potency, the concentration of ligand needed to produce 50% of the maximal effect (EC_{50}/IC_{50}). There is a non-linear relationship between the proportion of occupied receptors and functional responses following signal amplification (Kenakin, 2013). Even at low levels of receptor occupancy, 'high efficacy' agonists can induce a maximal functional response. If 30% of receptors are occupied, there is a large degree of receptor reserve whereby 70% of receptors are not required to produce a maximal response. In contrast, a partial agonist is a 'low efficacy' agonist that can lead to a sub-maximal response compared to a full agonist if systems lack receptor reserve. They cannot produce a maximal response despite 100% receptor occupancy when there are no "spare" receptors. The extent of receptor reserve differs between cell types due to changes in receptor expression, signal amplification and coupling efficiency of receptors to signalling partners. As a result, a ligand can be a partial agonist with low receptor expression but a full agonist with a higher degree of receptor reserve. This system-dependence of partial agonism is important for considering distinctions in signalling between VEGF-A isoforms (*Table 1.1*). VEGF-A signalling has also largely been investigated using fixed concentrations of ligand as opposed to full concentration-response courses to quantify their potency. This limits direct pharmacological comparisons of the relative activity of isoforms across different signalling pathways and cellular backgrounds.

Seminal findings in the VEGF field largely came from gross *in vivo* (Kitsukawa et al., 1995; Shalaby et al., 1995; Carmeliet et al., 1996) and phenotypic *in vitro* studies (Cébe Suarez et al., 2006; Kawamura et al., 2008b; Herzog et al., 2011). At the other end of the spectrum, biophysical and structural techniques have investigated isolated protein domains (Vander Kooi et al., 2007; Brozzo et al., 2011). This is due to the complexity and size of VEGF-A (26-44 kDa), VEGFR2 (149 kDa) and NRP1 (102 kDa). As such, there is limited quantitative understanding of VEGF-A pharmacology at full-length receptors in living cells despite being a 'clinically approved' drug target.

1.7 PROJECT AIMS

This thesis aimed to investigate the molecular pharmacology of VEGF-A isoforms at VEGFR2 and its co-receptor NRP1. This thesis explored the differences between VEGF-A isoforms at the level of ligand binding. Taking advantage of technologies used to study other receptor classes, we aimed to quantify the spatial and temporal dynamics of ligand/receptor binding and endocytosis in living cells at 37°C.

First, studies used novel fluorescent variants of VEGF-A isoforms to monitor ligand binding using bioluminescence resonance energy transfer and isolate interactions at NanoLuc-tagged receptors (Chapter 3). Second, we interrogated the influence of subcellular context and receptor phosphorylation on real-time ligand binding (Chapter 4). Finally, we monitored protein-protein interactions between VEGFR2 and NRP1 to investigate how complex formation influenced ligand binding of distinct VEGF-A isoforms (Chapter 5). The work described in the following Chapters aimed to:

Aim 1. Alongside $VEGF_{165}$a-TMR, characterise novel fluorescent variants of $VEGF_{165}$b and $VEGF_{121}$a isoforms stoichiometrically tagged with tetramethylrhodamine.

Aim 2. Isolate distinctions between VEGF-A isoforms with respect to ligand binding at VEGFR2 and NRP1 using NanoBRET.

Aim 3. Investigate VEGF-A/VEGFR2 endocytosis in terms of ligand-dependency, the role of phosphorylation and its influence on ligand/receptor interactions.

Aim 4. When VEGFR2 and NRP1 are co-expressed in the same living cell, investigate receptor colocalisation and ligand binding comparing VEGF-A isoforms that can or cannot distinguish between receptors.

Chapter 2.

Materials & Methods

2.1 MATERIALS

Human Embryonic Kidney 293 (HEK293) cells were selected as a commonly used model cell line used to express recombinant proteins of interest. This is due to their optimal transfection properties and reliable growth in culture. Wild type HEK293T cells were obtained from a female donor (CRL-3216; ATCC, Virginia). Numerous variants of HEK293 cells have been modified since their original immortalisation (Graham et al., 1977). HEK293T cells were engineered to express the simian virus 40 (SV40) large T antigen (DuBridge et al., 1987). This enhances the transfection of expression vectors that express an SV40 promoter (Pear et al., 1993; Geisse and Fux, 2009). The clonal HEK293T cell line expressing NFAT-RE-luc2P was obtained from Promega (E8510; Madison, US). These cell lines express a Firefly luciferase reporter gene (RE-luc2P) that is inserted downstream of the NFAT promoter (*Methods 2.7.1*). These modified HEK293T-ReLuc2P cells were used in most experiments for a consistent cell background with functional studies performed using the NFAT reporter assay. Human umbilical vein endothelial cells (HUVECs) were also used in this project to investigate endothelial cells. HUVECs were obtained from a single newborn male donor (C0035C; Thermo Fisher Scientific). HUVECs were first isolated by Jaffe et al. (1973). HUVECs typically exhibit a cobblestone morphology that mimic the endothelium (Jiménez et al., 2013).

Recombinant human VEGF isoforms were purchased from R&D Systems (Abingdon, UK). Ligands were made up to 1 µM according to their molecular mass as a dimer (26-42 kDa). Ligands were resuspended in either Phosphate Buffered Saline (PBS) or 4 mM Hydrochloric Acid (HCl) according to manufacturer instructions. Protein ligands were stored in the presence of 0.1% protease-free Bovine Serum Albumin (BSA; #3117332001; Sigma Aldrich, UK). This prevented interactions with the plasticware, as peptide adherence would reduce their free concentration. Their purity was confirmed as >95% by the manufacturer. Fluorescent $VEGF_{165}$a-TMR, $VEGF_{165}$b-TMR and $VEGF_{121}$a-TMR were synthesised at Promega Corporation (*Methods 2.5.1*) and stored at -20°C or -80°C in 2.5 mg/ml protease-free BSA (#126609; Millipore, USA). Cediranib/AZD2171 was purchased from SelleckChem (Houston, US). The HaloTag Mammalian Protein Detection and Purification System (G6795), FuGENE® HD transfection reagent (E2312), furimazine (N1130), purified LgBiT (N401B), purified HiBiT (N301A) and ONE-Glo™ reagent (E6120) were bought from Promega Corporation (Madison, Wisconsin, USA). Unless otherwise stated, cell culture reagents, laboratory equipment and chemical stocks were purchased from Sigma Aldrich (Gillingham, Dorset, UK). Cell culture plasticware was purchased from Fischer Scientific (Loughborough, UK). Reagents for cloning were purchased from Promega (Wisconsin, USA) or New England Biolabs (Massachusetts, USA).

2.2 CELL CULTURE

2.2.1 Passaging

HEK293T cells were grown in Dulbecco's Modified Eagle's Medium containing 2 mM L-glutamine (DMEM; D6429), supplemented with 10% Fetal Bovine Serum (FBS; F2442). This contained inorganic salts, essential amino acids, vitamins and pyruvate for cell growth. DMEM also contains phenol red, a pH indicator that transitions to yellow upon increased acidity due to by-products of cell metabolism or microbial infection. HUVECs were grown in Medium 200 (M-200-500; ThermoFisher Scientific, USA) containing 10% Large Vessel Endothelial Supplement (LVES, 50X; A1460801; Thermo Fisher Scientific, USA). As primary cells, HUVECs were only used between passages 4 and 9. HUVECs were also checked for their characteristic cobblestone morphology. All cells were grown in tissue culture incubators at 37°C with a humidified atmosphere containing 95% air/O_2 and 5% CO_2. Cell morphology and confluence were checked daily using an inverted microscope (Zeiss Primovert) fit with a Pan Apochromat 10X objective. The vast majority of cell lines were used as an adherent monolayer, except for a suspension HEK293T cell line described in *Methods 2.7.1*.

Cells grown in 75 cm^2 flasks were passaged at 70-80% confluency to ensure maximal cell viability and health. Cell culture was performed in a Microbiological Safety Cabinet (TriMAT Class 2; Contained Air Solutions, UK), reducing the risk of contamination. Using reagents warmed to room temperature, medium was removed from the flask and cells were washed with 1-2 ml Dulbecco's Phosphate Buffered Saline (PBS; D8537). Adherent cells were removed from the flask using 1 ml trypsin-EDTA solution (T4174; 0.25% w/v in EDTA solution, diluted from a 10X solution in PBS). Trypsin is a serine protease that cleaves adhesion molecules and detaches cells. As trypsin is inactivated by the Ca^{2+} or Mg^{2+} present in culture media, EDTA was also present to chelate any remaining ions following the PBS wash. Cells were incubated for 3-5 minutes at 37°C for optimal enzymatic activity to ensure the monolayer was disrupted. Detached cells were then washed off into 10 ml culture media (FBS-containing DMEM or LVES-containing Medium 200). Cell suspensions were centrifuged at 1000 rpm for 5 minutes and pellets were resuspended in 5 ml culture media. Cells were then passaged in a new 75 cm^2 flask containing 20 ml culture media.

2.2.2 Freezing

Multiple passages of key cell lines were stored at -80°C (Cryocube F570, Eppendorf) or, for long-term storage, in liquid nitrogen dewars (LS600, Taylor Wharton, Scientific Laboratory Supplies). To reduce cell stress during the freeze-thaw process, cells were frozen in FBS containing 10% dimethylsulfoxide (DMSO; Sigma Aldrich, UK) for optimal cryopreservation. While FBS provides support for the cells, DMSO prevents cell lysis upon freezing. This cryopreservation medium was sterilised prior to use by passing through a 0.2 µm filter to remove potential microbial contaminants. Cells were passaged as in *Methods 2.1.1* until the centrifugation step at 1000 rpm for 5 minutes, after which cell pellets were resuspended in 2 ml cryopreservation media. Cells were aliquoted into cryogenic storage vials (#5000-0020; Nalgene, Thermo Scientific, UK). Optimal cell freezing occurs at -1°C/minute to maintain cell viability. To reduce the rate of freezing, vials were placed in a Mr Frosty™ freezing container (Nalgene, Thermo Fisher Scientific, UK). Both DMSO and slow freezing were used to avoid the formation of ice crystals inside cells that could puncture cell membranes.

2.2.3 Seeding

For cell-based experiments, HEK293T or HUVEC cells were largely used as an adherent monolayer to enable assay protocols that replaced culture media for different assay conditions. To ensure experiments with different plate formats used cells at an optimal confluency (80-90%), the pellet was resuspended in a total volume of 10 ml culture medium to count the number of cells. Alternatively, HUVECs were resuspended in 2 ml to avoid diluting them excessively. Cells were mixed using a P1000 pipette tip to avoid cell damage. Cell densities were determined using the average cell count calculated with a haemocytometer. Cell counts were multiplied by 10,000 for the average number of cells in 1 ml, thus multiplying by 100,000 represented the 10 ml resuspension. Cells were diluted in culture medium to plate at the required density (*Table 2.1*).

Coating plastic- and glass-ware with polymers of D-lysine encouraged cell attachment as a monolayer, thus allowing media to be removed during the assay without losing cells. Poly-D-lysine hydrobromide (P6407; Sigma-Aldrich, UK) is a synthetic chain of positively charged amino acids that interact with negatively charged ions on the plasma membrane, thus encouraging adsorption to the plate surface. This was prepared at 0.01 mg/ml in PBS and filter sterilised using 0.2 µm pores. Volumes described in *Table 2.1* were added to wells and incubated at room temperature for 30 minutes. Having aspirated the poly-D-lysine, plates could be washed with excess PBS for storage for up to 1 month. Prior to seeding cells, plates were washed with excess serum-free DMEM to remove any residual fluid.

Table 2.1 ***Summary of conditions to seeding cells in different assays****.*

Assay Plate	Volume per well		Cell density per well	
	Poly-D-lysine (0.1 mg/ml)	Seeding	1-day plating	2-day plating
Black flat-bottomed 96-well (655090, Greiner Bio-One)	50 µl	100 µl	25,000-30,000	15,000-25,000 HUVECs: 5,000-8,000
White flat-bottomed 96-well (655098, Greiner Bio-One)				
4 compartment 35/10 mm dish with glass bottom (627870, CELLview, Greiner Bio-One)	300 µl	500 µl	50,000-75,000	n/a
8-well coverglass chamber (155411; Nunc Lab-Tek, Thermo Fisher Scientific)	150 µl	200 µl	n/a	20,000-30,000
6-well flat-bottomed plates (3516; Corning Costar, Sigma-Aldrich)	1000 µl	2000 µl	250,000-300,000 HUVECs: 150,000	n/a

Densities are described for HEK293T cells, unless stated otherwise.

Cells were seeded in culture medium of DMEM or Medium 200 containing their respective serum. Cells were plated for 22-24 (1 day) or 44-48 hours (2 days). Due to the presence of growth factors in serum, some cells were serum starved with DMEM lacking FBS following 24 hours. This was necessary for numerous functional experiments as we were investigating a growth factor receptor. The majority of experiments used assay buffers that lacked essential amino acids and phenol red. HEPES buffered saline solution (HBSS) was used in experiments requiring cell maintenance for 1-2 hours (*Appendix 7.3*). This provided cells with physiological inorganic ions and maintained their osmotic balance. HEPES also maintained buffer pH at 7.4 as a zwitterionic buffer insensitive to CO_2, in contrast to the CO_2-bicarbonate buffering system used in conjunction with DMEM. PBS was used in experiments to wash cells as a balanced salt solution maintaining pH and osmolarity, however exposure time to PBS was minimised as it lacks Ca^{2+}, Mg^{2+} and energy sources for aerobic respiration.

2.3 MOLECULAR BIOLOGY

2.3.1 Expression Vectors

Gene expression vectors are used to encode proteins of interest for transfection in mammalian cells (Makrides, 1999). These also allow manipulation of the expressed protein, such as conjugating to a peptide tag or mutating key amino acids. Many expression vectors have been developed to suit different expression systems. These share common features to ensure their transcription, mRNA processing for protein translation, propagation in prokaryotic cells and selection in mammalian cells. Expression vectors contain promoters and enhancers to facilitate the initiation of transcription, such as the human cytomegalovirus (CMV) promoter to enhance protein transcription in mammalian cell lines. Vectors also contain a polyadenylation tail to protect mRNA from degradation, for which a SV40 poly(A) sequence was used (van den Hoff et al., 1993). Each vector contains a Kozak consensus sequence to initiate protein translation (Kozak, 1987).

Receptor sequences encoding VEGFR2 (NM_002253) and NRP1 (NM_003873.5) were obtained from Genscript (New Jersey, USA) or Kazusa DNA Research Institute (Japan), respectively. These sequences lacked the endogenous signal sequence to enable the addition of an N-terminal moiety. Export to the plasma membrane was encouraged using a synthetic signal sequence. This was either derived from the interleukin 6 (IL-6) gene or the murine serotonin 5-hydroxytryptamine 3A (5HT3A) signal sequence inserted before the tag (*Figure 2.1, Figure 2.2*). Sequences encoding the each tag and receptor are detailed in *Appendix 7.2*. Outside of the open reading frame (ORF) encoding the tagged receptor, expression vectors encoded antibiotic resistance genes. These included prokaryotic antibiotic resistance genes against antibiotics that kill Gram negative bacteria used for amplifying DNA (*Methods 2.3.8*), such as kanamycin or ampicillin resistance. Mammalian antibiotic resistance genes were also present in plasmids. These were largely resistant against G418 to allow selection for HEK293T cells that successfully incorporated the plasmid (*Methods 2.4.1*).

VEGFR2 and NRP1 were expressed in mammalian expression vectors originally cloned by colleagues at Promega Corporation as part of a collaborative link grant with the Biotechnology and Biological Sciences Research Council (grant number BB/L019418/1). Plasmids expressing NanoLuc- and HaloTag-tagged receptors were cloned using the CMV Flexi® Vector Cloning System between rare-cutting restriction sites, SgfI and PmeI.

Expression vectors were used to genetically tag receptors with a moiety that could emit luminescence upon addition of a substrate (*Figure 2.1*). Plasmids encoding NanoLuciferase (NanoLuc) were genetically fused to the N-terminus of VEGFR2 and NRP1 using the pFN31K vector (*Figure 2.1b,c*). This encoded a 19.1 kDa luciferase subunit encoded by 510 base pairs (bp), followed by a 7 amino acid residue linker (GSSGAIA) prior to the receptor. These plasmids were kanamycin-resistant and the NanoLuc was preceded by the secretory IL-6 signal peptide. Other vectors were cloned to encode LgBiT, a 17.6 kDa fragment modified from the full-length NanoLuc (Dixon et al., 2016). These were fused to the N-terminus of VEGFR2 (*Figure 2.1d*), as well as NRP1 (vector not shown), via a flexible linker (GSSGGGGSGGGGSSGGAIA). These plasmids were ampicillin-resistant and preceded by the IL-6 signal sequence. The LgBiT tag sequence from N198A pBiT1.1-N, available from the NanoBiT Multiple Cloning Site Starter System (N2014, Promega Corporation), was cut using SacII and SgfI (*Methods 2.3.4*). Vectors were also cloned to encode HiBiT or SmBiT, an 11 amino acid residue tag that recomplements with LgBiT to emit bioluminescence (Dixon et al., 2016). This was inserted between the same restriction sites as LgBiT with a flexible linker (GSSGGSSGAIA; *Figure 2.1e*).

Receptors were also tagged with moieties that could be used as a fluorescent tag upon addition of a fluorophore-conjugated substrate, such as HaloTag-AlexaFluor488 or SnapTag-AlexaFluor488 (*Figure 2.2*). pFN21A vectors were used to encode an N-terminal HaloTag (*Figure 2.2b,c*). This 33 kDa moiety is encoded by 891 base pairs, attached to VEGFR2 or NRP1 via a 16 amino acid linker (EPTTEDLYFQSDNAIA). These plasmids were ampicillin-resistant and, as above, preceded by the signal peptide modified from IL-6. Vectors were also cloned to encode SnapTag, a 20 kDa tag encoded by 546 base pairs (*Figure 2.1d*). This was fused to the N-terminus of NRP1 using a pcDNA3.1 vector encoding SnapTag. This included a murine 5HT3A signal sequence with an linker of 24 amino acid residues (STSPVWWNSADIQHSGGRSSGAIA). The receptor-encoded sequence from NanoLuc-NRP1 vector was used to generate SnapTag-NRP1 using the XhoI and XbaI restriction sites (*Methods 2.3.4*).

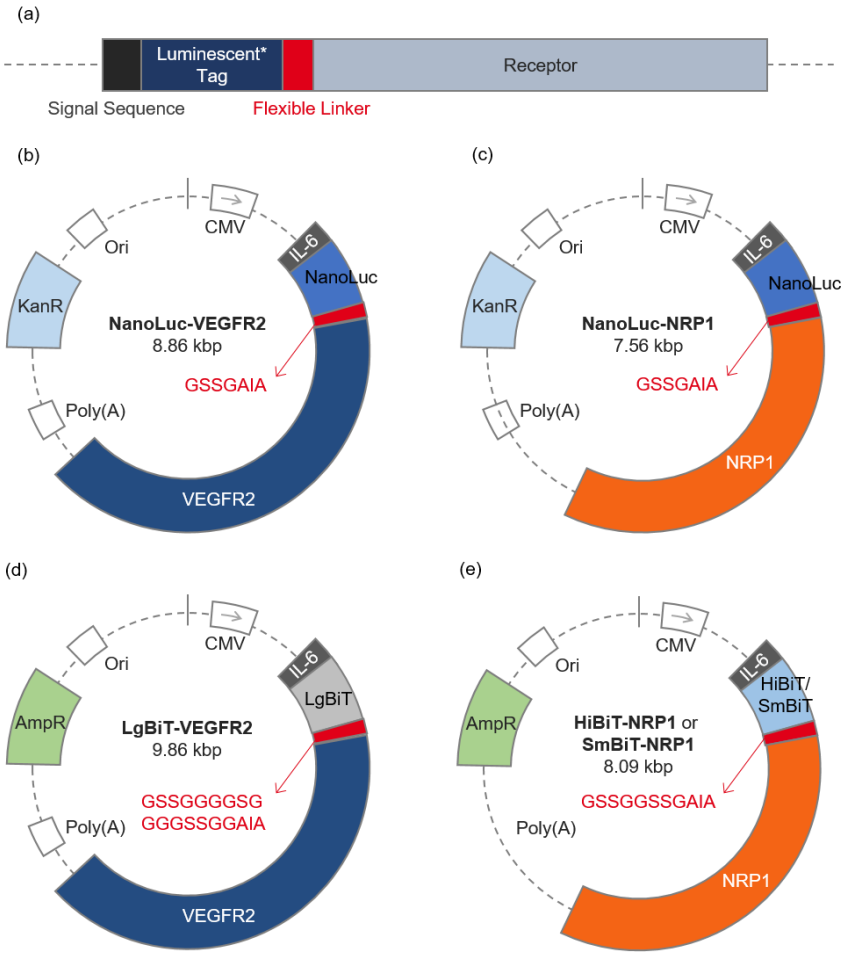


Figure 2.1 ***Vector maps of bioluminescent-based tags genetically fused to receptors.*** *(a) Arrangement of the open reading frame (ORF) for receptors tagged at the N-terminus following a signal sequence for export to the cell surface. *This tag is only luminescent upon addition of the substrate. Furthermore, the NanoBiT fragments (c, d) require recomplementation before emitting bioluminescence. (b,c) NanoLuc-tagged VEGFR2 or NRP1 are encoded by the pFN31K vector with kanamycin resistance (KanR). (d) LgBiT-VEGFR2 was cloned into the pFN21A vector with ampicillin resistance (AmpR). LgBiT-NRP1 was also cloned with an identical vector background and linker (not shown). (e) HiBiT-NRP1 and SmBiT-NRP1 differ by point mutations in the tag, therefore expression vectors are the same size. HiBiT-VEGFR2 and SmBiT-VEGFR2 were also synthesised, with an identical vector background and linker (not shown). Vectors contain the cytomegalovirus (CMV) promoter and a signal sequence derived from interleukin 6 (IL-6).*

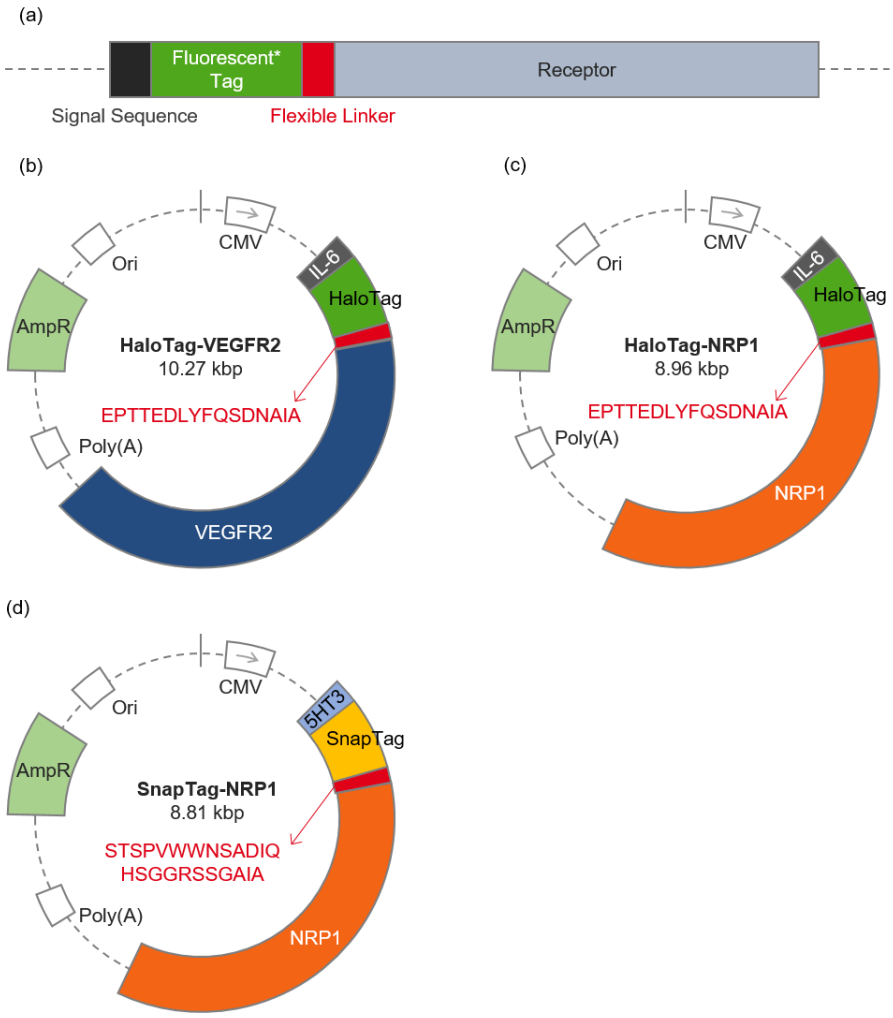


Figure 2.2 ***Vector maps of fluorescence-based tags genetically fused to receptors.*** *(a) Arrangement of the open reading frame (ORF). *This tag is only fluorescent upon addition of the HaloTag or SnapTag substrate conjugated to a fluorophore. (b,c) HaloTag-VEGFR2 and HaloTag-NRP1 are encoded by the pFN21A vector. This has ampicillin resistance (AmpR) and a signal sequence derived from interleukin 6 (IL-6). (d) SnapTag-NRP1 is encoded using a modified pcDNA3.1 vector containing ampicillin resistance (AmpR). This has a signal sequence modified from the murine serotonin 5-hydroxytryptamine 3A (5HT3A) receptor. Vectors also contain the cytomegalovirus (CMV) promoter. As in* Figure 2.1*, full-length VEGFR2 and NRP1 have a large ORF occupying 30-50% total vector size.*

2.3.2 DNA Quantification and Sequencing

DNA concentration was quantified using a NanoDrop 2000 Spectrophotometer (Thermo Fisher Scientific) or the DS-11 FX+ Spectrophotometer (DeNovix, Delaware, US). DNA concentration was calculated by absorbance at 260 nm using a 1 µl sample. Nucleic acid purity was estimated using the ratio between readings at 260 nm and 280 nm, aiming for 1.8 as pure DNA. Lower ratios suggested protein contaminants due to higher absorbance at 280nm, whereas a ratio ~2.0 suggested the presence of RNA.

All DNA sequencing was performed by the DNA Sequencing Facility in the School of Life Sciences at the University of Nottingham, performing Sanger sequencing using the 3130xl ABI PRISM Genetic Analyzer (Life Technologies). Generally, sequencing primers T7T (5'- TATGCT AGTTAT TGCTCA GCGG -3') and T7P (5'- TAATAC GACTCA CTATAG GG -3') were used to sequence regions flanking the plasmid ORF. DNA chromatograms were checked to ensure sufficient clear peaks, particularly in regions of mutated base pairs.

2.3.3 Polymerase Chain Reaction

PCR can be used to amplify DNA strands complementary to a template DNA sequence by several orders of magnitude (Mullis, 1990). DNA synthesis is initiated from primers, or single-stranded oligonucleotides, that are complementary to the template sequence to anneal with complementary bases. Primers are typically designed to be 25-45 base pairs, ideally with guanine/cytosine (GC) content between 40-60%. PCR takes advantage of a DNA polymerase enzyme that catalyses the polymerisation of nucleotides into double stranded DNA (dsDNA) in a 5'-3' direction. In the PCR reactions performed in this thesis, we used the thermostable *Pfu* DNA Polymerase (M774A; Promega Corporation, USA), originally purified from the aquatic species of Archaea *Pyrococcus furiosus*. Unlike *Taq* polymerase, *Pfu* polymerase is a high fidelity enzyme with an additional 3'-5' exonuclease proofreading function.

In order to generate a tyrosine phosphorylation deficient variant of VEGFR2 (VEGFR2 TPD, *Chapter 4*), site-directed mutagenesis was performed using PCR. Primers were designed as two complementary sequences with the mismatch point mutation in the centre (*Table 2.2*; lower case). Mutagenic primers were designed using PrimerX (Bioinformatics), such that the complementary forward and reverse primers annealed to the bottom and top strands respectively. Mutagenic PCR reactions were performed in 0.2 ml thin-walled PCR tubes (PK960; Scientific Lab Supplies, UK). Making up a total volume of 50 µl with double distilled water (ddH_2O), PCR reactions contained: 20 ng template DNA; 0.25 µM forward primer and 0.25 µM reverse primer; 100 µM deoxynucleoside triphosphates (dNTPs); 5 µl *Pfu* 10X Buffer containing Mg^{2+} ions (20 mM $MgSO_4$); and 1 µl *Pfu* polymerase. Reactions were performed using the Mastercycler (Eppendorf, UK) following the sample PCR protocol shown in *Figure 2.3*. This was preceded by an initial step at 95°C for 1 minute 30 seconds to break down the template DNA. Following the 16 cycles, reactants were held at 4°C to prevent breakdown. Where optimisation replicates were required, annealing (55-60°C) and extension (68-72°C) temperatures were altered. Following the PCR reaction, residual parental template was removed using a DpnI digestion reaction at 37°C for 1 hour (R6231; Promega Corporation, USA). DNA from the parental template synthesised by *Escherichia coli* (*E. coli*) is methylated, whereas amplified DNA containing the mutagenic site from the PCR reaction is unmethylated. As a methylation-dependent endonuclease, DpnI digests residual methylated DNA at the adenosine of a GATC sequence. The remaining DNA resistant to DpnI digestion therefore only contains the PCR product, thus containing the point mutations. This DNA can be transformed for amplification (*Methods 2.3.8*).

Although *Pfu* DNA polymerase is a high fidelity polymerase enzyme, there was risk of off-target single nucleotide polymorphisms (SNPs) at 1 in every 7.7×10^5 to 1×10^6 base pairs. Our largest vectors were <11,000 base pairs, therefore was a 1.1-1.4% risk of SNPs occurring anywhere in the plasmid that could compromise plasmid expression. Ideally, this would be addressed by using a restriction digest to transfer the mutated region of the plasmid to a new plasmid that had not been exposed to *Pfu* polymerase. This was not possible after multiple attempts due to difficulties with the large vector encoding VEGFR2, therefore the full VEGFR2 plasmid was sequenced (*Appendix 7.2*).

Table 2.2 ***Primers used for mutagenesis, generating VEGFR2 TPD****.*

SNP	Strand	Sequence (5'-3')	T_m (°C)
Y951F	Forward	GTCAAGGGAAAGACTtCGTTGGAGC AATCCC	61
	Reverse	GGGATTGCTCCAACGaAGTCTTTCC CTTGAC	62
Y1054F	Forward	GCTTGGCCCGGGATATTTtTAAAGA TCCAGATTATGTC	61
	Reverse	GACATAATCTGGATCTTTAaAAATAT CCCGGGCCAAGC	63
Y1059F	Forward	GATATTTTTAAAGATCCAGATTtTGT CAGAAAAGGAGATGCTCGC	59
	Reverse	GCGAGCATCTCCTTTTCTGACAaAA TCTGGATCTTTAAAAATATC	60
Y1175F	Forward	GCAGGATGGCAAAGACTtCATTGTT CTTCCGATATC	62
	Reverse	GATATCGGAAGAACAATGaAGTCTT TGCCATCCTGC	63
Y1214F	Forward	GTGACCCCAAATTCCATTtTGACAA CACAGCAGGAATC	64
	Reverse	GATTCCTGCTGTGTTGTCAaAATGG AATTTGGGGTCAC	65

Altered nucleotides from the original sequences are shown in lower case. Respective melting temperatures (T_m) of the annealed bases were calculated using SnapGene software. Mutagenesis was performed for NanoLuc-VEGFR2 and HaloTag-VEGFR2. Due to their close proximity and resulting overlapping of mutagenesis primers, the Y1054F mutation was performed prior to Y1059F.

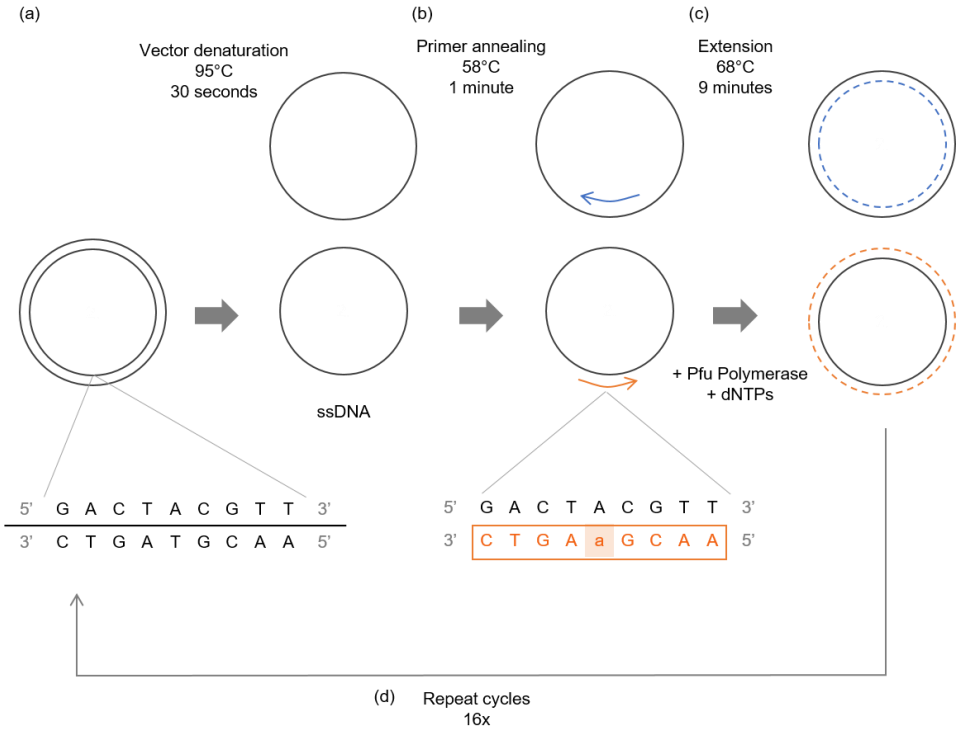


Figure 2.3 ***Using PCR for site-directed mutagenesis****. This represents the PCR protocol to generate VEGFR2 Y951F (Primer* T_m *= 61-62°C). (a) DNA in the template vector was denatured into single stranded DNA (ssDNA) due to the high temperature breaking hydrogen bonds between DNA strands. The template DNA sequence around the target mutation site is shown for both forward (5'-3') and reverse (3'-5') strands. (b) Cooling to temperatures below the primer's melting temperature (*T_m*) allowed primers to anneal to the ssDNA of template DNA. As there were two circular plasmids of ssDNA, both forward and reverse primers annealed to complementary plasmid sequences. The example sequence shows the 5'-3' strand of template DNA annealed to the reverse primer (orange). This mutagenic primer contained 1 base that is not complementary to the template DNA, however this was surrounded by complementary bases to facilitate hybridisation. (c) Sequences were extended using a thermostable* Pfu *DNA polymerase. This was initiated at the region of the annealed primer and added nucleotides in a 5' to 3' direction with complementary bases along the template DNA. (d) This was repeated in multiple cycles using the PCR Thermocycler.*

PCR was also used to amplify the LgBiT fragment for *Chapter 5*. This used a vector, N198A pBiT1.1-N, available from the NanoBiT Multiple Cloning Site Starter System (N2014, Promega Corporation). Primers were designed to introduce restriction sites for SacII and SgfI either side of the LgBiT fragment (*Table 2.3*). Inserted restriction sites are shown in lower case. Primers included 5-10 additional base pairs at the 5' end to aid restriction enzyme digest. There were then 18-30 base pairs that would hybridise with the DNA sequence to be amplified at the 3' end. The melting temperature is determined by the hybridisation sequence of the primer annealing to the pBiT1.1-N vector. The forward and reverse primers encompass the LgBiT fragment and a flexible linker (GSSGGGGSGGGGSSGGAIA). This led to a DNA fragment of 554 base pairs.

Table 2.3 ***Primers used for cloning the LgBiT sequence, flanked by introduced restriction sites****.*

Strand	Restriction Site	Sequence (5'-3')	T_m (°C)
Forward	SacII	CTATTccgcggCTGGTCTTCACACTC GAAGATTTCGTTGGG	62
Reverse	SgfI	CTATTAAAAGgcgatcgcCCCACCGCT CGAGCCTCC	63

Respective melting temperatures of the annealed bases were calculated using SnapGene software. Noted restriction sites are highlighted in the primer sequence (lower case). Melting temperatures (T_m) were calculated using SnapGene for the bases annealed to the template DNA.

For the PCR reaction, reactions were performed in 0.2 ml thin-walled PCR tubes with thermostable *Pfu* DNA Polymerase. Making up a total volume of 50 µl with ddH_2O, PCR reactions contained: 50 ng template DNA; 10 µM forward primer and 10 µM reverse primer; 10 mM dNTPs; 5 µl *Pfu* 10X Buffer containing Mg^{2+} ions (20mM $MgSO_4$); and 0.5 µl *Pfu* polymerase. Reactions were performed using the Mastercycler (Eppendorf, UK). There was an initial 2 minute step at 95°C to break down the template N198A pBiT1.1-N DNA. Each cycle consisted of steps for denaturation (95°C, 30 seconds), annealing via the hybridisation sequence at a temperature 2-3°C lower than the T_m (60°C, 30 seconds) and extension (72°C, 1 minute). The extension time should be ~1 minute per 1000 base pairs of the DNA fragment, however this is the LgBiT/linker fragment is particularly short. This was repeated for 30 cycles before a final extension step (72°C, 10 minutes). The resulting DNA fragment was held at 4°C to prevent breakdown.

2.3.4 Restriction Digest

Restriction digest reactions use endonucleases to cut DNA into smaller fragments at a specific sequence (Loenen et al., 2014). Cloning approaches largely use Type II restriction endonucleases as these cut DNA within the recognition site (Pingoud et al., 2005). This process was used to clone different tags or receptors into new expression vectors. To generate SnapTag-NRP1 (*Chapter 5*), restriction enzyme digests were used to clone the cDNA encoding NRP1 (insert) into a plasmid for the N-terminal SnapTag receptor (vector). Typically, expression plasmids have a multiple cloning site region that contain several restriction enzyme sites to enable this form of manipulation. Two distinct restriction enzymes were used to cut both ends flanking the insert (XhoI and XbaI in *Figure 2.4*). As well as ensuring the correct orientation, restriction enzymes only cut at the appropriate single location in both the insert and vector cDNA. This was made more difficult by the size of both VEGFR2 and NRP1, as they contain many common restriction sites in their native DNA sequence. Enzymes were chosen to produce complementary 'sticky' ends with an overhang of unpaired nucleotides (*Figure 2.4a*), such that they can only be joined together in one orientation. Cutting at the 5'-end of the NRP1 cDNA sequence, XhoI was used as a restriction enzyme derived from *Xanthomonas holcicola* (R6165; Promega Corporation, USA). XbaI, on the other hand, is derived from *Xanthomonas badrii* and cut at the 3'-end (R6185; Promega Corporation, USA). These enzymes were compatible in terms of their distinct sticky ends and both had maximal efficiency in Buffer D at 37°C. The insert from NanoLuc-NRP1 was used to ensure this lined up correctly with the vector sequence (pcDNA3.1 encoding SnapTag and the signal sequence; available in the Hill Lab, University of Nottingham). Digestion reactions were performed in sterile 0.5 ml tubes. Making up in a total volume of 50 µl with ddH_2O, digestion reactions contained: 5 µg plasmid DNA; 2 µl XhoI restriction enzyme; 2 µl XbaI restriction enzyme and 5 µl 10X Buffer D. Digestion reactions were performed at 37°C for 2 hours using the Biometra TRIO Thermoblock (Analytik Jena). The resulting SnapTag-NRP1 expression vector is illustrated in *Figure 2.2d*.

To generate NanoBiT constructs (*Figure 2.1d,e, Chapter 5*), restriction digest reactions were used to clone the cDNA encoding the tag (insert) into the plasmid expressing the IL-6 signal sequence and either VEGFR2 or NRP1 (vector). These used the receptors expressed in the HaloTag FN21A as the appropriate restriction sites followed the IL-6 signal sequence. SacII and SgfI enzymes were used to flank the insert and create 'sticky' ends. SacII is derived from *Streptomyces achromogenes* (R6221, Promega Corporation, USA), cutting at the restriction site CCGC/GG. SgfI is derived from *Streptomyces fulvissimis* (R7103; Promega Corporation, USA), cutting at GCGAT/CGC. These enzymes were compatible in terms of distinct sticky ends and both had maximal efficiency in Buffer C at 37°C. Digestion reactions were performed in sterile 0.5 ml tubes in a total volume of 50 µl. The vectors, HaloTag-VEGFR2 or HaloTag-NRP1, were digested in the presence of Thermosensitive Alkaline Phosphatase (TSAP; M9910, Promega Corporation, USA). This prevented the vector from recircularisation by removing 5' phosphate groups. This was included within the restriction digest reaction of the vector. Made up to a total volume of 50 µl with ddH_2O, digestion reactions of the vector contained: 2 µg plasmid DNA; 2 µl SacII restriction enzyme; 2 µl SgfI restriction enzyme; 5 µl 10X Buffer C and 2 µl TSAP. Digestion reactions were performed at 37°C for 2 hours using the Biometra TRIO Thermoblock. Due to the presence of TSAP in the reaction mixture, this was then inactivated at 74°C for 15 minutes using a heat block. These were used as vectors for generating receptors tagged with LgBiT, HiBiT and SmBiT.

Digestion reactions of the LgBiT insert did not require TSAP. To digest the LgBiT fragment from the PCR reaction, the 50 µl digestion reaction was made up of: 2 µg plasmid DNA; 2 µl SacII restriction enzyme; 2 µl SgfI restriction enzyme; 5 µl 10X Buffer C and ddH_2O. Following the digest, this left the LgBiT fragment (532 base pairs). HiBiT and SmBiT tags were cloned using a different protocol as they are encoded by short amino acid sequences (*Methods 2.3.7*).

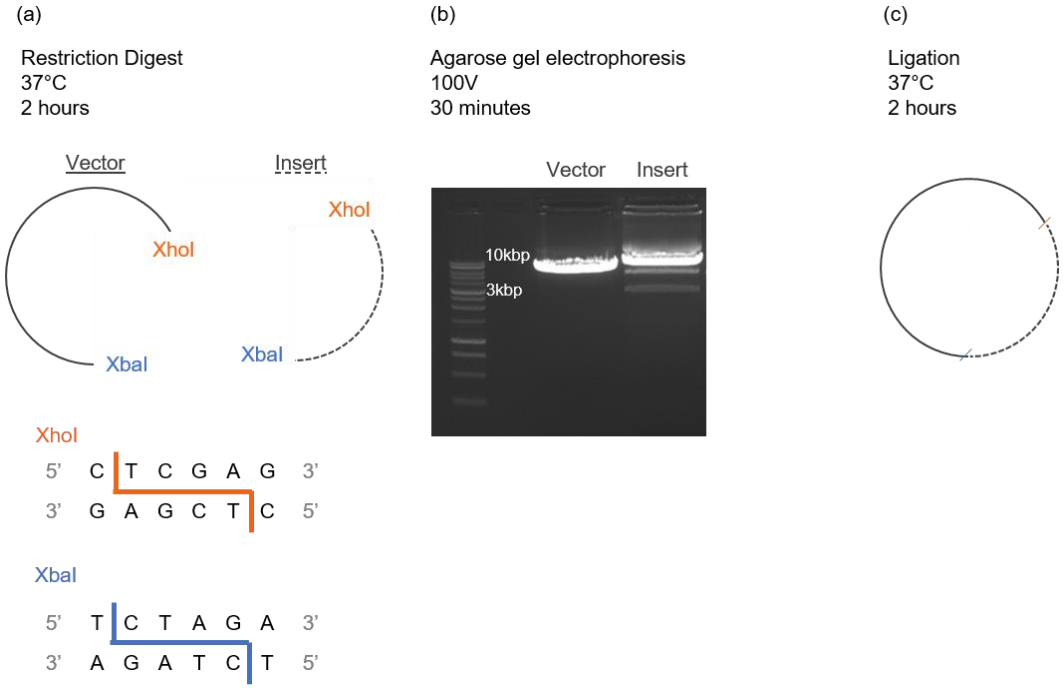


Figure 2.4 ***Restriction digest to generate SnapTag-NRP1****. (a) Restriction enzymes, XhoI and XbaI, were used to digest the vector and insert cDNA (double stranded DNA shown as single lines). The insert sequence (NRP1, dashed line) was flanked by single restriction enzyme sites for XhoI and XbaI. These restriction enzymes cut at a palindromic DNA sequence with 'sticky' overhangs (*Methods 2.3.4*). (b) Products from the restriction digest were separated by size using agarose gel electrophoresis (*Methods 2.3.5*). A 1 kb DNA ladder is displayed on the left. The digested vector (6.05 kbp) shows a single, strong band. The insert (NRP1) was originally obtained from NanoLuc-NRP1. Although there is a strong band showing the undigested vector (7.6 kbp), there is a faint band that represents the receptor fragment (2.8 kbp) cleaved between XhoI and XbaI. The digested vector (6.05 kbp) and receptor fragment (2.8 kbp) were excised for initial DNA purification (*Methods 2.3.6*). (c) Ligation of the sticky ends from the XhoI and XbaI restriction sites allowed the formation of circular plasmid DNA containing the vector and insert (*Methods 2.3.7*).*

2.3.5 Gel Electrophoresis

Agarose gel electrophoresis was used to separate DNA products by size (Aaij and Borst, 1972). This was used following PCR reactions to verify whether DNA synthesis was successful (*Methods 2.3.3*). This was also used to separate fragments following a restriction digest (*Methods 2.3.4*). Electrophoresis uses an electrical field to move negatively charged DNA towards the positive electrode, such that shorter DNA fragments migrate further than longer fragments (*Figure 2.4b*). Agarose is a sulfonated polysaccharide that is soluble in hot water. As the dissolved solution cools, a matrix forms by cross-linking the polysaccharide by hydrogen bonds. Agarose (A9539; Sigma-Aldrich, UK) was used at a 1% solution dissolved in Tris-Acetate-EDTA (TAE) buffer (*Appendix 7.3*). Having allowed the 50 ml or 100 ml solution to cool slightly, ethidium bromide was added to the dissolved solution with a final concentration of 0.2 µg/ml (E1510; Sigma-Aldrich, UK). This is used to localise DNA as a mutagenic agent that intercalates into dsDNA with increased fluorescence yield upon DNA binding. Gels were set in the presence of a standard electrophoresis comb to introduce wells. The blue/orange 6X loading buffer (G1881; Promega Corporation, US) was added to each 50 µl digest reaction and gels were loaded with the entire volume (60 µl/well). Protocols following PCR reactions used smaller volumes to load 12 µl/well, made up as 5µl DNA sample, 5µl ddH_2O and 2µl 6X loading dye. The 1 kbp BenchTop Ladder (G754A; Promega Corporation, USA) was then added to a separate well to indicate the size of DNA bands. Electrophoresis gels were run for 30 minutes at 100V by the Gel PowerPac Basic (Bio-Rad, UK). Bands were visualised using a UV transilluminator GVS-30 (Syngene, UK). For gels performed following a restriction digest (*Figure 2.4b*), bands of the appropriate weight were rapidly excised to minimise DNA damage from exposure to UV light. These isolated gel bands were transferred into a sterile 1.5ml tube and weighed.

2.3.6 Initial DNA Purification

Following initial cloning steps, DNA was purified using a Wizard® DNA Clean-Up Kit (A9282; Promega Corporation, US). This was used to extract DNA from agarose gels (*Methods 2.3.5*) or directly purify DNA from restriction enzymes following a digest reaction (*Methods 2.3.4*). This methods uses column chromatography to extract linear or circular DNA. Membrane binding solution was added at an equal volume to the measured excised agarose gel band and heated to 65°C. Alternatively, an equal volume of membrane binding solution was added to the digest reaction (50 µl). This contained chaotropic salts to disrupt the agarose gel. This also created a hydrophobic environment that encouraged the DNA backbone to bind to the silica of the spin column. This mixture was centrifuged through a column assembled in a 1.5 ml tube for 16,000 x g (1 minute) to remove the gel components. This was followed by two wash steps with ethanol-containing solution through the minicolumn for 30 seconds. This removed contaminants while leaving cDNA on the column as DNA is not soluble in ethanol. Another 60 second centrifugation step aimed to remove residual ethanol. To elute DNA fragments, the minicolumn containing the DNA was transferred to a clean 1.5 ml tube. Nuclease-free ddH_2O (40 µl) was added to each minicolumn. Having incubated at room temperature for 1 minute, this was centrifuged at 16,000 x g for 1 minute for the final DNA elution.

2.3.7 Recombinant Plasmid Ligation

Following the purification of DNA fragments by gel electrophoresis, the concentration of insert and vector DNA was quantified (*Methods 2.3.2*). Fragments with overhanging ends were ligated together using T4 DNA Ligase (M0202; New England Biolabs), an enzyme catalysing the formation of phosphodiester bonds in double stranded DNA. The formation of a phosphodiester bond between a 5' phosphate and 3' hydroxyl catalysed by DNA ligase requires a phosphate group. During the restriction digest, this was exploited to prevent vector recircularisation using TSAP-mediated dephosphorylation. In contrast, insert DNA must possess a phosphate group for ligation with vector DNA. Ligation reactions were performed at a specific molar ratio of insert:vector DNA optimised according to their relative size. The mass of DNA was calculated using the following equation:

Equation 2.1.

$$mass\ of\ insert\ (ng) = desired\ molar\ ratio\ x\ mass\ of\ vector\ (ng)\ x\ \frac{size\ of\ insert}{size\ of\ vector}$$

To synthesise SnapTag-NRP1, the ligation reaction was performed between the digested vector (SnapTag and antibiotic resistance) with the digested insert (NRP1). This was shown in *Figure 2.4c*. This used a 3:1 molar ratio of insert to vector DNA, using the following calculation:

$$\frac{3}{1} x\ 42\ ng\ vector\ DNA\ x\ \frac{2.76\ kb}{6.04\ kb} = 58\ ng\ insert\ DNA$$

Ligation reactions were prepared on ice in sterile 0.5 ml tubes. Making up a total volume of 25 µl with ddH_2O, ligation reactions for SnapTag-NRP1 contained: 42 ng vector DNA (6.05 kb); 58 ng insert DNA (2.76 kb); 2.5 µl of 10X T4 DNA Ligase buffer, and 1.25 µl T4 DNA Ligase. Reactions were either left for 1 hour at room temperature or overnight at 16°C for 16 hours. The T4 DNA ligase enzyme was heat inactivated at 65°C for 10 minutes. Having then cooled this deactivated ligation solution on ice, the ligated DNA was transformed in competent *E. coli* cells. This transformation was performed alongside a negative control (digested vector only) and a positive control (original SnapTag cDNA).

To synthesise LgBiT-VEGFR2 and LgBiT-NRP1, the ligation reaction was performed between the vector (receptor and antibiotic resistance) and the insert (digested LgBiT fragment). In contrast to the previous ligation reaction, the LgBiT-VEGFR2 reaction used a DNA insert that was particularly small. The LgBiT ligation reaction used a 5:1 molar ratio between insert and vector DNA. The total DNA in the reaction was maintained at ~100 ng. Using the example of VEGFR2, the following calculation used:

$$\frac{5}{1} x\ 80\ ng\ vector\ DNA\ x\ \frac{0.535\ kb}{9.33\ kb} = 22.9\ ng\ insert\ DNA$$

Ligation reactions were prepared on ice in sterile 0.5 ml tubes. Making up a total volume of 10 µl with ddH_2O, ligation reactions for LgBiT-VEGFR2 contained: 80 ng vector DNA (9.33 kb); 22.9 ng insert DNA (0.535 kb); 1 µl of 10X T4 DNA Ligase buffer and 0.5 µl T4 DNA Ligase. Reactions were incubated overnight at 16°C for 16 hours in a Biometra TRIO Thermoblock. The T4 DNA ligase enzyme was then heat inactivated at 65°C for 10 minutes. Having cooled this deactivated ligation solution on ice, this DNA was transformed in competent *E. coli* cells (DH5α cells) and selected for on ampicillin-resistant plates. This transformation was performed alongside a negative control (digested vector only) and a positive control (original HaloTag-VEGFR2 cDNA).

An alternative approach was used for generating HiBiT- and SmBiT- receptors due to the small 11 amino acid tag. These were obtained as custom oligonucleotide sequences from Sigma-Aldrich (*Table 2.4*), in a similar approach to custom primer sequences. These sequences had restriction sites for SacII and SgfI exposed as if they were already cut during a restriction digest. Oligonucleotides included complementary forward and reverse sequences that encode the tag with a linker that could reanneal into double stranded DNA. Each oligonucleotide was resuspended in ddH_2O to a final concentration of 100 µM, however a phosphorylation reaction was required to enable its ligation with vector DNA. A reaction mixture was set up to simultaneously perform phosphorylate and anneal oligonucleotides. This reaction used Polynucleotide Kinase (PNK) to catalyse the 5' phosphorylation. Reactions were prepared on ice in sterile 0.5 ml tubes. Making up a total volume of 10 µl with ddH_2O, phosphorylation/annealing reactions for HiBiT and SmBiT fragments contained: 1 µl forward oligonucleotide, 1 µl reverse oligonucleotide, 6 µl ddH_2O, 1 µl of 10X T4 DNA Ligase buffer and 1 µl T4 PNK (M0201S; New England Biolabs). Reactions were performed in a Mastercycler (Eppendorf, UK). They were first incubated at 37°C for 30 minutes. The reaction was heat inactivated and oligonucleotides were denatured at 95°C for 5 minutes. To enable annealing into double stranded DNA, these were cooled by 5°C min^{-1} until they reached 25°C.

Table 2.4 ***Oligonucleotide sequences encoding HiBiT and SmBiT tags***.

Tag	Strand	Sequence (5'-3')
HiBiT	Forward	ggGTGAGCGGCTGGCGGCTGTTCAAGAAGATTAGCG GGAGTTCTGGCGGCTCGAGCGGTgcgat
	Reverse	cgcACCGCTCGAGCCGCCAGAACTCCCGCTAATCTTC TTGAACAGCCGCCAGCCGCTCACccgc
SmBiT	Forward	ggGTGACCGGCTACCGGCTGTTCGAGGAGATTCTCG GGAGTTCTGGCGGCTCGAGCGGTgcgat
	Reverse	cgcACCGCTCGAGCCGCCAGAACTCCCGAGAATCTCC TCGAACAGCCGGTAGCCGGTCACccgc

Indicated tags are highlighted (grey) with the exposed restriction site shown in lower case at either end of the oligonucleotide.

HiBiT and SmBiT fragments were then inserted into vectors between the signal sequence and receptor. These were ligated into vectors previously digested with SacII and SgfI. Vector fragments were obtained from HaloTag-VEGFR2 or HaloTag-NRP1, whereby DNA of the appropriate size corresponding to the vector was excised following agarose gel electrophoresis and DNA purification. Phosphorylated, annealed fragments of HiBiT and SmBiT were first diluted 1 in 200 in ddH_2O. Ligation reactions were then made up in a total volume of 20 µl with ddH_2O, containing: 100 ng vector DNA; 2 µl diluted HiBiT/SmBiT; 2 µl of 10X T4 DNA Ligase buffer and 1 µl T4 DNA Ligase. Reactions were incubated overnight at 16°C for 16 hours in a Biometra TRIO Thermoblock. Similarly, the T4 DNA ligase enzyme was heat inactivated (65°C, 10 minutes) and the ligation solution was cooled on ice. This was transformed into competent *E. coli* cells (DH5α cells) alongside a negative control (HiBiT fragment only) and a positive control (original HaloTag-VEGFR2 cDNA).

2.3.8 Transformation of DNA into Competent E. coli

In order to propagate plasmid DNA in commercially available competent *Escherichia coli* cells, transformations were performed using One Shot® TOP10F´ chemically competent cells (C303003; Invitrogen). Alternatively, DNA generated from ligation reactions were transformed using Subcloning Efficiency DH5α competent cells (18265017; Invitrogen). Competent cells were thawed on ice, then 25 µl was gently transferred to a cool, sterile 0.5 ml tube per transformation reaction. For basic DNA amplification or following site-directed mutagenesis, 0.5-1 µl DNA was added to the tube containing 25 µl TOP10F cells. Alternatively, 1-2 µl ligated DNA was added to 25-50 µl DH5α cells. Tubes were mixed by flicking and then left for 30 minutes on ice to enable plasmid DNA to associate with the outer membrane of the competent cells. To facilitate the uptake of plasmid DNA into the cytoplasm of *E. coli* cells, the reaction mixture was heat shocked at 42°C for 30 seconds using a heat block. This was cooled on ice for 2-3 minutes, then 250 µl Luria Broth (LB) Lennox (L3022; Sigma Aldrich) was aseptically added to each 0.5 ml tube. Bacterial *E. coli* grew in this rich medium containing tryptone (10 g/L), yeast extract (5g/L) and sodium chloride (5g/L). Cells were shaken in LB Broth for 60 minutes at 225 rpm (37°C; SI600 Large Shaking Incubator, Stuart Equipment) to encourage bacterial replication in nutrient-rich broth. All steps encouraging bacterial growth aimed to maintain bacteria in their logarithmic growth phase to exponentially increase in bacteria number, hence plasmid copy number.

Petri dishes containing 20 ml LB Agar (L2897; Sigma Aldrich, UK), as well as either 30 µg/ml kanamycin sulphate (11815-024; Gibco) or 50 µg/ml ampicillin (A0839; PanReac), were solidified at room temperature then warmed to 37°C. Transformed *E. coli* cells were added to the agar plates close to a lit Bunsen burner to maintain sterile conditions. This used either 50 µl bacteria for basic DNA amplification or 250 µl bacteria for mutagenesis or ligation. Cells were spread across the agar plate using a plastic L-shaped spreader then incubated overnight at 37°C, positioning plates upside down to prevent condensation. Bacterial colonies grew from a single bacterium, therefore the population within single colonies were genetically identical. Prokaryotic antibiotic resistance genes within expression vectors ensured only bacteria expressing this gene could grow on antibiotic-containing agar plates. This isolated populations of transformed *E. coli* that successfully incorporated the plasmid DNA. Agar plates containing bacterial colonies were stored at 4°C for up to 1-2 months.

2.3.9 Small-Scale DNA Purification ('Miniprep')

Selecting multiple isolated colonies that grew in the presence of selection antibiotic, colonies were picked using a sterile pipette tip in proximity to a lit Bunsen burner. This colony-containing tip was aseptically dropped into 5 ml LB Broth containing their respective antibiotic at concentrations described in *Methods 2.3.8*. These 'starter' bacterial cultures were shaken overnight at 225 pm at 37°C.

To isolate DNA propagated in dividing competent *E. coli* cells during this process, a column-based extraction method was used with the Pureyield™ Plasmid Miniprep System (A1223; Promega Corporation, UK). 3 ml of starter bacterial culture was first pelleted at 13,300 x g for 30 seconds using a microcentrifuge (Heraeus Pico 17, Thermo Fisher Scientific) to maximise the yield. These bacteria were resuspended in 600 µl ddH_2O. Alkaline solution was added to lyse cells and denature chromosomal DNA and proteins. This was then neutralised in order to precipitate denatured DNA and protein, which left plasmid DNA in solution as its supercoiled nature was resistant to acid-base manipulation. The precipitate and cell debris were pelleted using a centrifugation step at 13,300 x g for 3 minutes. Plasmid DNA-containing supernatant was then carefully transferred to a spin column positioned within a collection tube and briefly centrifuged for 15 seconds. Having collected DNA on the column filter, this column was washed twice with an ethanol-containing solution to dissolve residual contaminants. This was span for a further 60 seconds for remove residual ethanol. DNA was eluted in 40 µl nuclease-free water into a fresh, sterile 1.5 ml tube, obtaining approximate DNA yields of 200 ng/µl with a 260/280 ratio of ~1.88.

2.3.10 Large-Scale DNA Purification ('Maxiprep')

Purifying plasmid DNA on a larger scale, *E. coli* were transformed (*Methods 2.3.8*) and a colony was picked to establish a starter culture (*Methods 2.3.9*). This was shaken in 5 ml LB broth containing antibiotic at 225 rpm (37°C). Following 8 hours, starter cultures were transferred into a 500 ml conical flask containing sterile 120 ml LB broth and antibiotic (30 µg/ml kanamycin or 50 µg/ml ampicillin). These were shaken overnight at 225 rpm at 37°C. The following day, DNA was extracted and purified using the Pureyield™ Plasmid Maxiprep System (A2393; Promega Corporation, UK). Along similar lines to the miniprep process, 120 ml bacterial cells were pelleted in 250 ml plastic bottles by spinning at 4,000 x g for 10 minutes at room temperature (Eppendorf T5810R). This pellet was resuspended thoroughly, followed by lysis of bacterial cells and neutralisation. This was transferred into containers suitable for the superspeed centrifuge (Sigma 3K30) for centrifugation at 14,000 x g for 20 minutes. This separated the plasmid DNA in the supernatant from the precipitate in the pellet. Using a vacuum pump manifold (Vac-Man, A7231; Promega Corporation, US), columns were assembled such that plasmid DNA would adhere to the silica-based binding column. Waste was removed via a clearing column into the vacuum pump for disposal. The lower clearing column was removed to leave the DNA-bound binding column, which was then washed to remove endotoxins. Contaminants were removed by subsequent ethanol-based wash steps. Having applied the vacuum for an additional 5 minutes to dry the binding column from excess ethanol, this binding column was assembled in an elution device that positioned a sterile 1.5 ml tube beneath. This assembly was placed onto the vacuum manifold. Plasmid DNA was eluted in 1 ml nuclease-free ddH_2O using the vacuum. The maxiprep procedure typically resulted in a 600-700 µl DNA preparation with a yield of 150-500 ng/µl DNA and a 260/280 ratio of between 1.8-1.9. As with DNA obtained from small-scale purification or any other cloning steps, all DNA was stored at -20°C.

2.4 RECOMBINANT CELL LINES

2.4.1 Stable Cell Lines

HEK293T cells were seeded in a 25 cm^2 flask to minimise reagent volumes required for transfection. Cells were grown to 50-60% confluency in DMEM/10% FBS. This culture medium was replaced with 8 ml fresh medium on the day of transfection. Cells were transfected using a non-viral approach. FuGENE® HD (E2312; Promega Corporation, USA) is a non-liposomal transfection technique. This utilises a synthetic lipid-based nanoparticle composed of lipids and other non-disclosed proprietary components. As DNA is hydrophilic, plasmid DNA is encapsulated in these artificial liposomes that can permeate hydrophobic membranes. FuGENE® HD was selected as an effective transfection reagent compared to other reagents (Yamano et al., 2010). Unlike other approaches (Chan et al., 2014), this transfection approach can be performed in the presence of serum to maintain cell health during the transfection process.

Having warmed reagents to room temperature, 8.8 µg plasmid DNA was diluted to a final volume of 414 µl serum-free DMEM in a sterile 1.5 ml tube. Using a 3:1 ratio of FuGENE HD reagent to plasmid DNA, 26 µl FuGENE was added to the tube. The transfection solution was mixed thoroughly by flicking the tube and pipetting to ensure a homogenous solution, then incubated at room temperature for 5-10 minutes. Having allowed the plasmid DNA to incorporate into the lipid-based nanoparticles, 400 µl transfection solution was added to the 25 cm^2 flask and incubated for 24 hours at 37°C/5% CO_2. Expression vectors encode the neomycin resistance gene, therefore 1 mg/ml G418 (Geneticin, Invitrogen) was added to select for cells successfully transfected. Culture medium containing G418 was replaced daily as cells died, until a lower concentration of 0.1 mg/ml G418 was added for maintenance. Once cell lines were screened to ensure plasmid expression (ideally over 50% cell population), G418 was no longer necessary. Novel cell lines were used at this stage as a mixed population, however some previous cell lines obtained from colleagues at Promega and Dr Laura Kilpatrick were dilution cloned to generate a clonal HEK293T cell line (NanoLuc-VEGFR2 V297I; RE-Luc2P).

2.4.2 Transient Transfection

Unlike stable transfections, transient transfections do not integrate DNA into the genome and are only suited to single experimental replicates. FuGENE® HD reagent delivers plasmid DNA to the cytoplasm, after which the plasmid is subject to transcription into mRNA and subsequent translation. HEK293T cells were grown for 24 hours in FBS-containing DMEM until 50-60% confluent. These were seeded in 96-well plates for

plate-based assays or 8-well plates for confocal microscopy, unless stated otherwise. On the day of transfection, seeding medium in 8-well plates was replaced with 200 µl/well serum-free DMEM. In 96-well plates, transfection solutions were added directly into serum-containing seeding medium. In a sterile tube, plasmid DNA was diluted to 10 or 20 ng/µl in serum-free DMEM in sterile conditions. Amended from manufacturer instructions, transient transfections also used FuGENE® HD at a reagent to cDNA ratio of 3:1. Transfection solutions were incubated for 5-10 minutes at room temperature. 5 µl (96-well plates) or 11 µl (8-well plates) was added to each well with a total 50 or 100 ng cDNA per well. Cells were then incubated for 20-24 hours at 37°C/5% CO_2 prior to the assay.

2.4.3 Membrane Preparations

For binding experiments performed using NanoBRET (*Methods 2.8.1*), crude membranes were prepared from stable cell lines. HEK293T cells stably expressing NanoLuc-VEGFR2 (WT or TPD) were grown in DMEM/10% FBS to 80-90% confluency in 148 mm^2 culture dishes (Corning, USA). Having replaced the medium with PBS, cells were removed from the dish by scraping and then transferred into a 50 ml Falcon tube. Cells were centrifuged at 378 x g for 12 minutes at 4°C (Eppendorf T5810R), the supernatant was removed and the remaining pellet was stored at -80°C. Thawed pellets resuspended in PBS were homogenised using an electronic handheld IKA T10 Ultra Turrax homogeniser in 10 x 3 second bursts at 15,000 rpm. Extracts from cell homogenates could then be separated using centrifugation due to the distinct charge and density of cell organelles. Larger components - including unbroken cells, nuclei and the cytoskeleton - were removed by centrifugation at 1,500 x g for 20 minutes (4°C). The supernatant was then centrifuged at 41,415 x g using the superspeed centrifuge (Sigma 3K30) for 30 minutes at 4°C to remove other organelles and pellet the remaining membranes. The pellet was resuspended in 1 ml PBS, transferred to a borosilicate glass homogeniser mortar and homogenised 15 times using an IKA RW16 overhead stirrer attached to a serrated pestle (Kartell) at 1,000 rpm. Protein concentration was determined using a bicinchoninic acid assay (PierceTM BCA Protein Assay, Thermo Fisher Scientific) and absorbance was measured using a Dynex Technologies 4.25 platereader. Membrane preparations were stored at -80°C in PBS.

As membrane preparations can reform vesicles due to phospholipid hydrophobicity, some experiments were performed in the presence of detergent to disrupt vesicles. Saponin is a glycoside and non-ionic surfactant that interacts with membrane cholesterol to cause holes in the membrane (Seeman et al., 1973). In these assays, 0.25 mg/ml saponin (84510; Sigma-Aldrich) was added to the assay buffer.

2.5 FLUORESCENT LIGAND PREPARATION

$VEGF_{165}$a-TMR, $VEGF_{165}$b-TMR and $VEGF_{121}$a-TMR were prepared by Promega Corporation funded by a collaborative link grant from the Biotechnology and Biological Sciences Research Council (grant number BB/L019418/1). This included synthesis of 6-TMR-PEG-CBT (Friedman Ohana et al., 2015), purification steps and preliminary characterisation using mass spectrometry and SDS-PAGE analysis (*Appendix 7.1*).
I would like to thank Rachel Friedman-Ohana, Kris Zimmerman, Matthew Robers, Keith Wood, Mike Rosenblatt, Dave Good and Sergy Levin from Promega Corporation.

2.5.1 $VEGF_{xxx}$x-TMR Purification and Synthesis

In brief, $VEGF_{xxx}$x proteins were labelled at a single N-terminal Cys residue using the HaloTag mammalian protein detection and purification system (G6795; Promega Corporation, USA). $VEGF_{165}$a, $VEGF_{165}$b and $VEGF_{121}$a were genetically fused with an N-terminal HaloTag using the pFN21A vector with an IL-6 signal peptide and recombinant $VEGF_{xxx}$x DNA obtained from Gene Dynamics LLC (Oregon, USA). The sequences of VEGF-A isoforms lacked the endogenous signal peptide that is ordinarily cleaved off following secretion. HaloTag-$VEGF_{xxx}$x was transiently transfected into 1 L HEK293T cells using polyethylenimine (PEI) and incubated in a spinner flask at 70 rpm at 37°C/5% CO_2 (*Figure 2.5a*). Following incubation for 72 hours, the secreted fusion protein was collected and applied onto 1.8 ml HaloLink beads overnight with constant end-over-end rotation (4°C). This allowed the beads to form covalent interactions with secreted HaloTag-$VEGF_{xxx}$x (*Figure 2.5b*). Ligand-bound HaloLink beads were centrifuged for 5 minutes at 1000 x g. These were initially washed in ligand purification buffer containing: 50 mM HEPES buffer; 150 mM NaCl; 0.005% IGEPAL® CA-630 (v/v in purification buffer). IGEPAL CA-630 was used throughout the purification process as a non-ionic, non-denaturing detergent that prevented protein adhesion to plasticware. Ligand-bound beads were then washed in the presence of 100 µM tris(2-carboxyethyl)phosphine (TCEP), a reducing agent for disrupting disulphide bonds. Protein was released from beads by proteolytic cleavage using HaloTEV protease (*Figure 2.5c*). This Cys protease cleaved at the ENLYFQ/C sequence present in the linker region between HaloTag and $VEGF_{xxx}$x, as described in Ohana et al. (2011). Proteolytic release was carried out in the presence of 100 µM TCEP and a 4-fold molar excess of 6-TMR-PEG-CBT (*Figure 2.5c*), synthesised as in Friedman Ohana et al. (2015). This Click Chemistry approach generated an N-terminal Cys that served as single point of conjugation with 6-TMR-PEG-CBT. Unlabelled counterparts were synthesised in an identical protocol but lacked 6-TMR-PEG-CBT. Following mixing overnight at 4°C, dialysis in purification buffer was performed for 24 hours at 4°C using a Slide-A-Lyzer cassette with a molecular weight cut off of 10 kDa. As

the cassette membrane allows the diffusion of molecules <10,000 Da, this removed unconjugated 6-TMR-PEG-CBT (817 Da) and TCEP (250 Da). Removal of this reducing agent enabled $VEGF_{xxx}x$ to reform a disulphide-linked dimer. Modified $VEGF_{xxx}x$ peptides were stored in 2.5 mg/ml protease-free BSA. Ligands were flash frozen in liquid nitrogen and stored long-term at -80°C.

2.5.2 Liquid Chromatography-Tandem Mass Spectrometry (LC-MS/MS)

To determine labelling specificity and efficiency, colleagues performed liquid chromatography-tandem mass spectrometry. As described in Kilpatrick et al. (2017), VEGF-TMR and their unlabelled analogues were suspended in 50 mM ammonium bicarbonate and reduced with 25 mM TCEP (50°C, 1 hour). Reduced proteins were digested with trypsin/LysC, LysC or GluC proteases (1:20 enzyme/substrate ratio; Promega Corporation, USA). These digestes after Lys/Asp/Glu/Asn/Gln (LysC and GluC) or Lys/Arg (trypsin). Fragments obtained from protease digestions had sufficient coverage of both $VEGF_{165}b$ and $VEGF_{121}a$ amino acid sequences (*Appendix 7.1*). Following shaking for 3 hours (400 rpm, 37°C; Eppendorf Thermomixer), reactions were quenched using 1% formic acid (Sigma Aldrich, USA). LC-MS/MS analysis used a Q Exactive Hybrid Quadrople-Orbitrap Mass Spectrometer (Thermo Fisher, USA), with MS resolution of 70,000. The MS product component was then analysed by colleagues using Protein Prospector software (University of California, USA), calculating mono-isotropic masses at different charge states (z = 2-5) to extract ion chromatograms. Labelling efficiencies could then be determined through comparing the integrated peak area of unmodified peptide samples as equimolar amounts of samples were loaded for LC-MS/MS. Data are shown in *Appendix 7.1*.

2.5.3 SDS-PAGE Analysis

Dimerisation and glycosylation status were determined by colleagues using sodium dodecyl sulphate (SDS)-polyacrylamide gel (PAGE) electrophoresis to separate purified protein preparations by mass. $VEGF_{165}b$-TMR or $VEGF_{121}a$-TMR were compared in the presence and absence of 100 mM dithiothreitol (DTT; Sigma-Aldrich, UK) to determine dimerisation status, as a redox reagent that reduces disulphide interactions. Alternatively, glycosylation status was investigated using PNGase F (Promega Corporation, USA) as a recombinant glycosidase that cleaves N-linked oligosaccharides. Gels were scanned on an Amersham Typhoon 9400 Biomolecular Imager (GE Healthcare, USA), exciting the TMR fluorophore at 532 nm and recording emissions at 580 nm. Data are shown in *Appendix 7.1*.

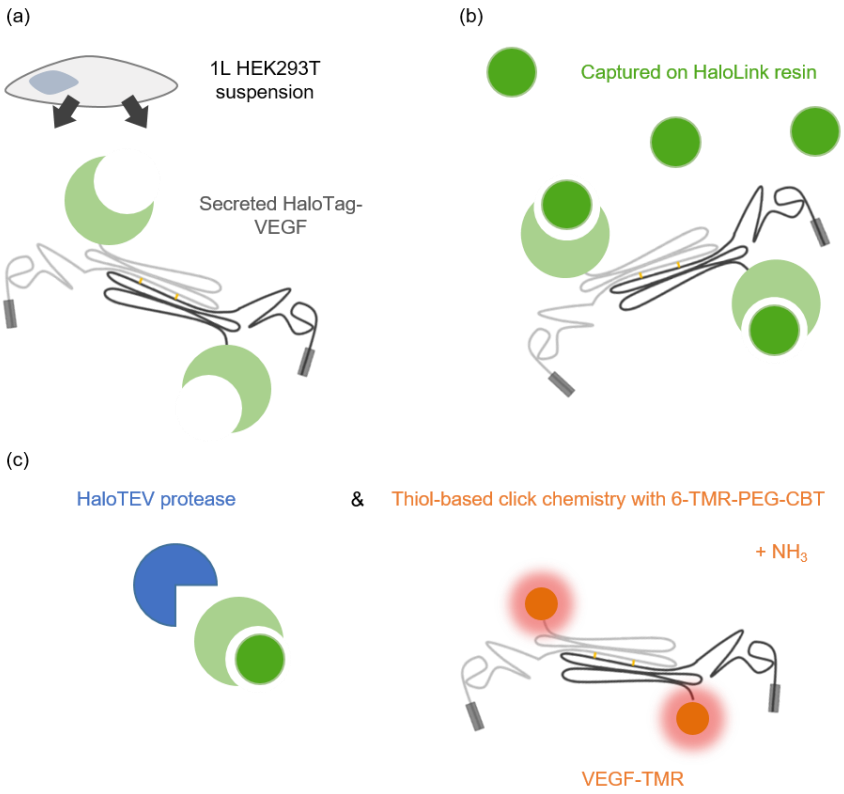


Figure 2.5 ***Workflow of fluorescent VEGF$_{xxx}$x synthesis using HaloTag protein purification***. *(a) HEK293T cells were transfected in suspension for 72 hours to secrete VEGF$_{165}$a, VEGF$_{165}$b or VEGF$_{121}$a fused with an N-terminal HaloTag. (b) Secreted fusion protein was applied onto HaloLink beads and rotated overnight. (c) The linker connecting HaloTag and the VEGF isoforms contained a modified tobacco etch virus (TEV) recognition site (EDLYFQC). Upon proteolytic cleavage, this released VEGF has an N-terminal cysteine residue that can be specifically labelled via 2-cyanobenzothiazole (CBT) condensation. Protein was released from beads by proteolytic cleavage using HaloTEV. The HaloTag moiety on the enzyme also enabled its capture onto HaloLink beads to prevent enzyme contamination. The enzymatic reaction was performed in the presence of reducing agent TCEP and excess 6-TMR-PEG-CBT. Purified isoforms were subsequently dialyzed and stored in BSA at -80°C. Each VEGF$_{xxx}$x monomer is appended to tetramethylrhodamine (TMR; excitation/emission spectra in* Appendix 7.4*). This was conjugated to the N-terminus of VEGF$_{xxx}$x at a single site using Click Chemistry.*

2.6 FLUORESCENCE MICROSCOPY

2.6.1 Live Cell Confocal Microscopy

Receptors were visualised in living cells using interchangable fluorophores with distinct wavelength excitation/emission spectra (*Appendix 7.4*). This used receptors that were genetically fused to a HaloTag and SnapTag moiety for the exogenous addition of a fluorophore. HaloTag® (Promega Corporation, US) is a 33 kDa catalytically inactive derivative of a bacterial haloalkane dehalogenase (Los et al., 2008). SNAP-tag® is a 20 kDa mutant of O^6-alkylguanine-DNA alkyltransferase, a human DNA repair protein (Keppler et al., 2003, 2004). Whereas HaloTag forms covalent bonds with a chloroalkane moiety, SNAP-tag® (New England Biolabs, US) uses a similar approach but reacts with benzylguanine moieties (*Figure 2.6a*). Substrates to these enzymes can be conjugated to a fluorophore, such as HaloTag-AlexaFluor488. Conjugated substrates that are impermeable to the membrane only visualises receptors successfully trafficked from the Golgi apparatus to the plasma membrane where receptors are exposed to added ligand.

Imaging HaloTag-VEGFR2 or HaloTag-NRP1 with $VEGF_{xxx}$x-TMR (Chapter 3)

HEK293T-ReLuc2P cells stably expressing HaloTag-VEGFR2, HaloTag-NRP1 or SnapTag-NRP1 were seeded 48 hours prior to imaging at 20,000 cells/well in 8-well plates pre-coated with poly-D-lysine. Medium was replaced following 24 hours with serum-free DMEM. On the day of the experiment, cells were treated with 0.5 µM membrane impermeant HaloTag-AlexaFluor488 substrate (G1002; Promega Corporation, USA), 0.5 µM membrane permeant HaloTag-TMR substrate (G8251; Promega Corporation, USA) or 0.5 µM membrane impermeant SNAP-Surface AlexaFluor488 substrate (S9129S; New England Biolabs, USA) in serum-free DMEM/0.1% BSA for 30 minutes (37°C/5% CO_2). Cells were washed twice with 200 µl/well HBSS/0.1% BSA and replaced with a final volume of 225 µl/well HBSS/0.1% BSA. Cells expressing HaloTag-VEGFR2 or HaloTag-NRP1 were incubated with 10 nM $VEGF_{165}$a-TMR, $VEGF_{165}$b-TMR or $VEGF_{121}$a-TMR in the dark at 37°C for up to 60 minutes, adding 25 µl to a total volume of 250 µl. SnapTag-NRP1 was only imaged with $VEGF_{165}$a-TMR. Cells were imaged live using a temperature-controlled LSM710 confocal microscope fit with a 40X water objective (Pan Apochromat objective, numerical aperture (NA) 1.2). Having aligned the Köhler illumination by adjusting the diaphragm and condenser and left the lasers to warm up, ddH_2O was applied before placing the sample on the objective. Fluorophores were excited according to their excitation/emission spectra (*Appendix 7.4*) with a DPSS 561 nm laser (2% power) and an Argon 488 nm laser (3-5% power) using a 488/561 beamsplitter. Additional wavelengths monitoring red-shifted fluorophores were excited

with a HeNe 633 nm laser (5% power) using a 488/561/633 beamsplitter. Pinhole diameters were adjusted to 1 Airy Unit to reduce out of focus emissions. Detector gains were adjusted by using the Zeiss Zen 2010 software according to a control well, then settings were constant for subsequent experiments. Transmitted light images of cells were obtained using the condenser in H phase. All images were taken as 12 bit images with 1024x1024 pixels per frame with 8 averages.

Imaging HaloTag-VEGFR2 in the Absence of Tyrosine Phosphorylation (Chapter 4)

HEK293T-ReLuc2P cells were seeded 48 hours prior to imaging at 15,000 cells/well in 8-well plates pre-coated with poly-D-lysine. Cells were transiently transfected with HaloTag-VEGFR2 or HaloTag-VEGFR2 tyrosine phosphorylation deficient (TPD). Following 24 hours, cells were transiently transfected using FuGENE® HD at a 3:1 ratio of reagent to cDNA with 100 ng cDNA/well for another 24 hours. On the day of the experiment, cells were treated with 0.5 µM membrane impermeant HaloTag-AlexaFluor488 substrate (G1002; Promega Corporation, USA). For experiments comparing pharmacological inhibition of VEGFR2 phosphorylation, cells expressing wild type HaloTag-VEGFR2 were incubated in medium containing 1 µM cediranib (S1017, Selleckchem) or 0.01% dimethyl sulfoxide (DMSO). Cells were washed twice with 200 µl/well HBSS/0.1% BSA and replaced with a final volume of 225 µl/well HBSS/0.1% BSA. Cells were imaged in vehicle only using the LSM710 confocal microscope fit with the 40X water objective (Pan Apochromat, NA 1.2), as above.

HaloTag-VEGFR2/SnapTag-NRP1 Colocalisation (Chapter 5)

HEK293T-ReLuc2P cells were plated in 8-well plates pre-coated with poly-D-lysine at 30,000 cells per well in DMEM/10% FBS. Following incubation for 24 hours, cells were transfected with a mixture of HaloTag-VEGFR2 and SnapTag-NRP1. Control wells were also transfected with a single construct and empty vector, such as SnapTag-NRP1 and pcDNA3.1/Neo. Transient transfections used FuGENE® HD at a 3:1 ratio of reagent to cDNA with a total 100 ng cDNA/well, with receptors transfected at equal amounts of 50 ng cDNA/well. Transfection solutions were made up in serum-free DMEM and added as 11 µl/well. Cells were incubated for a further 24 hours at 37°C/5% CO_2. Receptors were then labelled with a solution of serum-free DMEM/0.1% BSA containing both 0.5 µM membrane impermeant HaloTag-AlexaFluor488 substrate (G1002; Promega Corporation, USA) and 0.5 µM membrane impermeant SNAP-Surface AlexaFluor647 (S9136S; New England BioLabs). These were incubated for 30 minutes (37°C/5% CO_2). Cells were washed twice with 200 µl/well HBSS/0.1% BSA, then

replaced with a final volume of 225 µl/well. Cells were incubated with vehicle, 10 nM unlabelled $VEGF_{165}b$ or 10 nM unlabelled $VEGF_{165}a$ for 60 minutes at 37°C, adding 25 µl to a total volume of 250 µl. Cells were imaged live using a temperature-controlled LSM710 confocal microscope fit with a 40X water objective (Pan Apochromat objective, NA 1.2). Wavelengths were imaged simultaneous using the 488/561/633 beamsplitter. HaloTag-VEGFR2 AlexaFluor488 was imaged using an Argon 488 nm laser (493-628 nm bandpass; 2.5% power); SnapTag-NRP1 AlexaFluor647 was imaged with a HeNe633 nm laser (638-747 nm; 2.5% power). All images were taken as 12 bit images with 1024x1024 pixels per frame with 4 averages and similar gains per replicate.

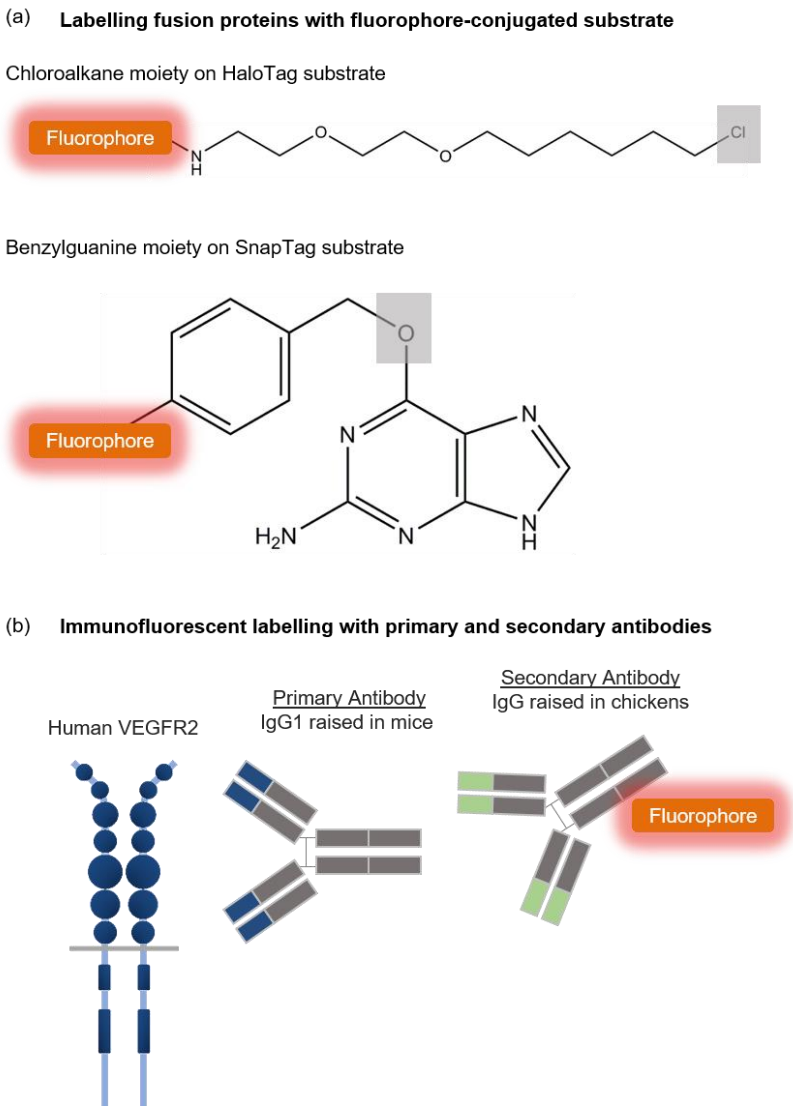


Figure 2.6 ***Labelling proteins using fluorescence-based technologies****. (a) HaloTag and SnapTag substrates are conjugated to a fluorophore. Covalent bonds are formed with the enzyme moiety via the highlighted region (grey). This enzyme portion was genetically fused to our protein of interest. HaloTag substrates undergo nucleophilic displacement with the chloroalkane moiety by displacing Cl (Los et al., 2008). In contrast, SnapTag forms a covalent bond via benzylguanine by releasing the guanine moiety (Keppler et al., 2004). (b) Immunofluorescent labelling uses a primary antibody raised against the protein of interest or antigen, such as the extracellular domain of VEGFR2. Secondary antibodies conjugated to a fluorophore can bind to the primary antibody. These are raised in different species to enable immunoreactivity.*

2.6.2 Immunofluorescent Labelling

Proteins were visualised using immunocytochemistry as a technique that does not require overexpression of a fluorescent receptor. Primary antibodies were raised against our protein of interest, the antigen, in a separate species. This antigen-bound antibody was then detected using a secondary antibody conjugated to a fluorophore (*Figure 2.6b*). This process can lead to high fluorescence background due to non-specific binding of the fluorophore-conjugated secondary antibody to various cell components; this was minimised throughout the protocol, such as pre-incubating with serum collected from the same species as the secondary antibody.

Table 2.5 ***Antibodies used for immunofluorescent labelling***.

Target	Primary Antibody	Secondary Antibody	Serum
VEGFR2	Mouse, monoclonal (V9134, Sigma-Aldrich)	Chicken anti-mouse Alexa Fluor 488 (A21463, Invitrogen)	Chick (C5405, Sigma-Aldrich)
VEGFR1	Mouse, monoclonal (V4742, Sigma-Aldrich)		
Synectin	Mouse, monoclonal (OTI4C11, OriGene)		
Rab5	Rabbit, monoclonal (C8B1, Cell Signalling)	Chicken anti-rabbit Alexa Fluor 488 (A-21441, ThermoFisher Scientific)	
NRP1	Goat, polyclonal (#7239, Santa Cruz)	Donkey anti-goat Alexa Fluor 546 (A11056, Invitrogen)	Donkey (D9663, Sigma-Aldrich)

VEGFR2, NRP1 and VEGFR1 Expression for Confocal Microscopy (Chapter 3)

For immunolabelling experiments visualising receptor expression using confocal microscopy, cells were plated on 18 mm x 18 mm square coverslips (#0107032, Zeiss, Germany). HUVECs, wild type HEK293T cells or recombinant HEK293T cell lines expressing NanoLuc-VEGFR2, NanoLuc-NRP1 were seeded on a poly-D-lysine coated coverslip using 6-well culture plates containing 300,000 cells/well. Cells were grown in culture medium for 24 hours at 37°C/5% CO_2. On the day of the assay, coverslips were transferred to humidified wells lined with parafilm squares and PBS to avoid drying out. Cells were washed with 1-2 ml per well of PBS. Cells were fixed with 3% paraformaldehyde or polymeric formaldehyde (PFA) diluted in PBS from 4% PFA (10% formalin; F8775, Sigma Aldrich). This chemical fixation approach stabilises tissues by reacting with basic amino acids to form methylene crosslinked bridges and coagulate proteins. Having incubated at room temperature for 20 minutes, cells were washed 3 times in PBS leaving 5 minute intervals between each wash to ensure thorough wash steps. All subsequent wash steps were performed using these intervals. To reduce non-specific binding, cells were incubated with 3% BSA/1% glycine in PBS for 30 minutes at room temperature. After washing three times with PBS, cells were blocked with 4% chick serum for VEGFR2 and VEGFR1 conditions or donkey serum for NRP1 staining. Having left in serum for 30 minutes at room temperature, this was immediately replaced with primary antibody diluted 1:200 in 4% serum/PBS and incubated overnight at 4°C (*Table 2.5*). The following day, cells were washed and incubated in the dark with secondary antibody diluted 1:500 in 4% serum/PBS for 1 hour at room temperature (*Table 2.5*). Coverslips were washed, mounted onto slides using ProLong Gold Antifade Mountant (P10144; Thermo Fisher Scientific), sealed with transparent nail varnish and stored in the dark at 4°C for up to 3 months. Coverslips were imaged using a Zeiss LSM880 confocal microscope fit with a 63X oil objective (Pan Apochromat objective, NA 1.4). Fluorophores were excited with an Argon 488 nm laser (2% power) or a DPSS 561 nm laser (2% power). Pinhole diameters were adjusted to 1 Airy Unit and images were taken as a 12 bit image at 1024x1024 pixels per frame with 8 averages.

VEGFR2 and NRP1 Expression for High Content Imaging (Chapter 3)

Applying the previous approach to compare tagged receptor expression in recombinant cell lines, a widefield platereader was used to quantify receptor expression in high throughput. HUVECs, wild type HEK293T cells or HEK293T cells expressing NanoLuc- and HaloTag- labelled VEGFR2 or NRP1 were seeded at 25,000 cells/well in black 96-well plates pre-coated with poly-D-lysine. Following 24 hours at 37°C/5% CO_2, cells were washed with 100 µl/well PBS. Cells were fixed with 3% PFA/PBS for 20 minutes at room temperature, then subsequent steps for washing and reducing non-specific binding were performed as above using volumes of 100 µl/well. To minimise the volume of antibody required, the corresponding primary antibody for VEGFR2 or NRP1 was added to each well as 50 µl/well then incubated overnight at 4°C (*Table 2.5*); this was surrounded in parafilm to reduce evaporation. The following morning, this was washed 3 times in 100 µl/well PBS at 5 minute intervals and replaced with 50 µl/well secondary antibody (*Table 2.5*) for 60 minutes at room temperature. Cells were then washed with PBS and nuclei were stained with 2 mg/ml bisBenzimide H33342 trihydrochloride (B2241; Sigma-Aldrich) diluted in PBS. Following 15 minutes at room temperature, cells were washed and stored in PBS at 4°C in the dark. Cells were imaged using an ImageXpress Micro XLS widefield platereader fit with a Plan Fluor extra-long working distance (ELWD) 20X objective. Images were taken at 4 sites per well, with a FITC (excitation 482/35 nm, emission 536/40 nm) or TRITC filter (excitation 543/22 nm, emission 593/40 nm) for VEGFR2 or NRP1 respectively. A 500 ms exposure time was used for TRITC or FITC measurements, whereas a 25 ms exposure time was used for the DAPI filter imaging nuclei (excitation 377/50 nm, emission 447/60 nm). The platereader is equipped to capture images at 4 different sites per well within 1 mm of the centre of each well.

Synectin Localisation for Confocal Microscopy (Chapter 3)

Immunofluorescent labelling was also used to visualise synectin, a cytoplasmic protein that interacts with NRP1 (*Introduction* *1.5.2*). This may be required for appropriate NRP1 activity, therefore preliminary experiments confirmed this was endogenously expressed in wild type HEK293T cells. As an intracellular protein, immunofluorescent labelling was performed used permeabilised cells. HUVECs or wild type HEK293T cells were plated on 18 mm x 18 mm square coverslips in 6-well culture plates containing a coverslip pre-coated with poly-D-lysine. Cells were grown in culture media for 24 hours at 37°C/5% CO_2, then coverslips were transferred to humidified wells. Cells were washed with PBS then fixed with 3% PFA/PBS for 20 minutes at room temperature. Having washed cells 3 times in PBS at 5 minute intervals, cells were permeabilised using the detergent Triton-X-100 (0.025% in PBS; X100, Sigma-Aldrich). This is a non-ionic surfactant containing both a hydrophilic but uncharged polyethylene oxide chain and a hydrophobic hydrocarbon-phenyl group. This detergent disrupts hydrophobic associations in the membrane bilayer and enables antibodies to permeate the plasma membrane to label intracellular proteins. Following 3 further wash steps in PBS, cells were incubated with 3% BSA/1% glycine in PBS for 30 minutes at room temperature to reduce non-specific binding. After washing three times with PBS, cells were blocked with 4% chick serum. Having left in serum for 30 minutes at room temperature, this was immediately replaced with primary antibody diluted 1:200 in 4% serum/PBS and incubated overnight at 4°C (*Table* 2.5). The following day, cells were washed and incubated in the dark with secondary antibody diluted 1:500 in 4% serum/PBS for 1 hour at room temperature (*Table* 2.5). Coverslips were washed, mounted onto slides using ProLong Gold Antifade Mountant, sealed with transparent nail varnish and stored in the dark at 4°C. Coverslips were imaged using a Zeiss LSM880 confocal microscope as above, using the 63X oil objective (Pan Apochromat NA 1.4). Fluorophores were excited with an Argon 488 nm laser (2% power), using a pinhole diameter adjusted to 1 Airy Unit. Images were taken in 12 bit at 1024x1024 pixels per frame with 8 averages.

Receptor/Ligand Colocalisation with Rab5 for Confocal Microscopy (Chapter 4)

Cellular compartments were imaged using confocal microscopy by immunofluorescent labelling of Rab5, a GTPase present in early endosomes (Rink et al., 2005). HEK293T-ReLuc2P cells stably expressing wild type or tyrosine phosphorylation deficient HaloTag-VEGFR2 were seeded at 300,000 cells/well onto poly-D-lysine coated 18 x 18 mm coverslips in 6-well plates. Following 24 hours at 37ºC/5% CO2, coverslips were transferred to humidified wells of a 6-well plate lined with parafilm and maintained in PBS to retain moisture. Receptors were labelled with 0.5 µM membrane-impermeant HaloTag-AlexaFluor647 (Promega Corporation, USA) in assay buffer (serum-free DMEM containing 0.1% BSA) in the dark. To minimise the volumes required, coverslips were inverted directly onto the parafilm coating each well in the 6-well plate. As such, adding 150-200 µl volumes to upside down coverslips was sufficient to expose all cells and avoid drying out. Following 30 minutes at 37ºC/5% CO_2, coverslips were washed twice with assay buffer, then incubated with 10 nM $VEGF_{121}$a-TMR for 5 minutes or 60 minutes (37ºC/5% CO_2). Cells were washed with PBS and fixed with 3% PFA in PBS for 20 minutes at room temperature. Following numerous wash steps in PBS (3 x 5 minutes), cells were permeabilised with Triton-X-100 (0.025% in PBS). To minimise non-specific antibody labelling, cells were washed (3 x 5 min PBS), incubated with 3% BSA/1% glycine (30 minutes at room temperature), washed (3 x 5 minutes PBS) and blocked with 10% chick serum in PBS (30 minutes at room temperature). This was replaced with the primary monoclonal antibody against Rab5 raised in rabbit (C8B1; Cell Signalling Technologies) diluted 1:200 in 10% chick serum and incubated overnight at 4ºC. Cells were then washed in PBS (3 x 5 minutes) and incubated with the secondary antibody, chick anti-rabbit AlexaFluor488, in 10% chick serum (1 hour, room temperature). To determine non-specific immunofluorescent labelling, this was repeated using secondary antibody only in the absence of primary antibody. Cells were then washed (3 x 5 minutes PBS), nuclei were stained with 2 mg/ml H33342 in PBS (15 minutes, RT) and washed (2 x 5 minutes PBS) before mounting the coverslips onto slides using ProLong Diamond (Thermo Fisher Scientific) and sealing for storage at 4ºC. Coverslips were imaged using a Zeiss LSM880 confocal microscope fit with a 63X oil objective (Pan Apochromat NA 1.4). Wavelengths were imaged in separate tracks with Rab5 immunolabelling imaged with an Argon 488 nm laser (491-571 nm bandpass; 3% power); $VEGF_{121}$a-TMR was imaged with a DPSS 561 nm laser (571-615 nm, 3% power); HaloTag-AlexaFluor647 was imaged using a HeNe633 nm laser (638-747 nm; 15% power). Pinhole diameters were adjusted to 1 Airy Unit. Images were obtained in 8 bit at 1024x1024 pixels per frame with 8 averages and similar gains per replicate.

2.6.3 Bioluminescent Imaging

Using a 4 day protocol, HEK293T-ReLuc2P cells were plated in 6-well plates at 400,000 cells/well in DMEM/10% FBS. On day 2, cells were transfected using FuGENE® HD at a 3:1 ratio of reagent to cDNA with a total 1500 ng cDNA/well made up in serum-free DMEM. Cells were transfected with equal amounts of LgBiT-VEGFR2 (750 ng cDNA/well) and HiBiT-NRP1 WT (750 ng cDNA/well). Alternatively, NanoLuc-VEGFR2 or NanoLuc-NRP1 were transfected at 750 ng cDNA/well with an equal amount of pcDNA3.1/Zeo (750 ng cDNA/well). On day 3, transfected cells were transferred to a 4-compartment 35/10 mm glass bottomed dish. Dishes were pre-coated with poly-D-lysine and cells were plated at 75,000 cells/well in DMEM containing 0.1% FBS. On the day of experimentation (day 4), medium was replaced with HBSS/0.1% BSA. For cells expressing full-length NanoLuc, furimazine was added at 26 µM. In contrast, cells expressing the NanoBiT complex were incubated with a higher furimazine concentration (104 µM). Following incubation for 10 minutes, cells were imaged live at 37°C using the inverted Olympus LV200 Bioluminescence Imaging System. This was fit with a 60X oil immersion objective (super apochromat UPLSAPO 60xO objective; NA 1.35) with a 0.5X tube lens to focus the image, therefore images had a final magnification of 30X. Luminescence was collected using a Hammamatsu Image EMx2 EMCCD (electron multiplying charge coupled device) camera. Transmitted light images were collected using the camera in conventional CCD mode with a 200 ms exposure time. Luminescence emissions from the full-length NanoLuc or NanoBiT complex were measured for 5 second exposure with a gain of 200. Images were taken as 8 bit images with 512x512 pixels per frame.

2.7 FUNCTIONAL ASSAYS

2.7.1 NFAT Reporter Gene Signalling

A reporter gene assay was used to monitor signalling downstream of calcium, as described in Carter et al. (2015). The Firefly luciferase reporter gene ReLuc2P was inserted downstream of the NFAT promoter and used to monitor NFAT-induced gene transcription following VEGFR2 activation (*Figure 2.7*). As this measured luminescence emissions, outer wells of the plate were not used to avoid evaporation of media from the 48 hour total incubation that could compromise cell viability. These assays also relied on cells not being overly confluent. In each assay, luminescence emissions was measured following a 5 minute delay to allow reagent to react with luciferase and background luminescence to subside.

Characterising Fluorescent $VEGF_{xxx}$x-TMR (Chapter 3)

HEK293T-ReLuc2P cells stably expressing untagged VEGFR2 (V297I) were used as a suspension cell line. On the day of experimentation, cells grown to 95-100% confluency were plated in white 96-well plates at 44,000 cells/well. Cells were incubated for 1 hour in 100 µl/well serum-free DMEM/0.1% BSA (37°C/5% CO_2). Cells were stimulated in duplicate wells with increasing concentrations of $VEGF_{121}$a-TMR, $VEGF_{165}$b-TMR or equivalent unlabelled VEGF isoforms synthesised in an identical manner to the fluorescent variant. Cells were then incubated for 5 hours at 37°C/5% CO_2. ONE-Glo Luciferase reagent (Promega Corporation, USA) was added at 100 µl/well. Following a 5 minute delay, luminescence was measured using a TopCount platereader (Perkin Elmer, UK).

Alternatively, adherent HEK293T-ReLuc2P cells stably expressed NanoLuc-VEGFR2 (WT) or NanoLuc-VEGFR2 (V297I). Cells were grown to 70-80% confluency and seeded in DMEM containing 10% FBS. Cells were seeded at 25,000 cells/well in white 96-well plates pre-coated with poly-D-lysine. Following 24 hours of cell growth at 37°C/5% CO_2, plating medium was replaced with serum-free DMEM for a further 24 hours. Cells were stimulated in duplicate wells with increasing concentrations of $VEGF_{xxx}$x (R&D Systems) or vehicle (serum-free DMEM containing 0.1% BSA). Following stimulation for 5 hours at 37%/5% CO_2, medium was replaced with 50 µl/well assay buffer and 50 µl/well ONE-Glo Luciferase reagent (Promega Corporation, USA). Cells were incubated for 5 minutes, then luminescence emissions were measured using a TopCount platereader (Perkin Elmer, UK).

Functional Characterisation of Un-Transfected HEK293T Cells (Chapter 3)

HEK293T-ReLuc2P cells stably expressed HaloTag-VEGFR2 (WT), or only expressed ReLuc2P in the absence or transfected receptors. Cells were plated at 25,000 cells/well in white 96-well plates pre-coated with poly-D-lysine. Cells were seeded in DMEM containing 10% FBS at incubated at 37°C/5% CO_2. Following 24 hours, medium was replaced with serum-free DMEM for a further 24 hours. On the day of experimentation, medium was replaced with DMEM containing 0.1% BSA. Cells were stimulated with increasing concentrations of $VEGF_{165}$a (R&D Systems) for 5 hours at 37°C/5% CO_2. Medium was then replaced with 50 µl/well serum-free DMEM/0.1% BSA and 50 µl/well ONE-Glo Luciferase reagent (Promega Corporation, USA). Cells were incubated with reagent for 5 minutes, then luminescence emissions were measured using a TopCount platereader (Perkin Elmer, UK).

Pharmacological Inhibition of VEGFR2 Phosphorylation (Chapter 4)

HEK293T-ReLuc2P cells stably expressing NanoLuc-VEGFR2 (WT) were plated at 25,000 cells/well in white 96-well plates pre-coated with poly-D-lysine. Cells were seeded in DMEM containing 10% FBS at incubated at 37°C/5% CO_2. Following 24 hours, medium was replaced with serum-free DMEM for a further 24 hours. On the day of experimentation, medium was replaced with DMEM containing 0.1% BSA. Cells were pre-incubated with increasing concentrations of cediranib (S1017, SelleckChem) or 0.01% DMSO at 37°C/5% CO_2. Following 30 minutes, cells were stimulated with 10 nM $VEGF_{165}$a (R&D Systems) for 5 hours at 37°C/5% CO_2. Medium was then replaced with 50 µl/well serum-free DMEM/0.1% BSA and 50 µl/well ONE-Glo Luciferase reagent. Cells were incubated with this reagent for 5 minutes, then luminescence emissions were measured using a TopCount platereader (Perkin Elmer, UK).

Characterising Tyrosine Phosphorylation Deficient Mutants of VEGFR2 (Chapter 4)

HEK293T-ReLuc2P cells were plated at 15,000 cells/well in white 96-well plates pre-coated with poly-D-lysine. Cells were incubated for 24 hours in DMEM containing 10% FBS. This medium was then replaced with serum-free DMEM. At this point, cells were transiently transfected using FuGENE® HD at a 3:1 ratio of reagent to cDNA with a total 50 ng cDNA/well. Cells were transfected with wild type HaloTag-VEGFR2, single HaloTag-VEGFR2 mutants (Y951F, Y1175F, Y1214F), the double mutant in the activation loop (HaloTag-VEGFR2 Y1054/1059F) or the complete HaloTag-VEGFR2 tyrosine phosphorylation deficient (TPD) mutant (Y951F, Y1175F, Y1214F, Y1054F and Y1059F). Transfections were made up in serum-free DMEM and added directly to the 96-well plate at 5 µl/well. Cells were incubated for a further 24 hours. On the day of the experiment, medium was replaced with serum-free DMEM containing 0.1% BSA. In separate control wells with the same transfection conditions, receptors were labelled with 0.5 µM membrane impermeant HaloTag-AlexaFluor488 substrate. Cells were incubated for 30 minutes at 37°C/5% CO_2, then washed twice with 100 µl/well HBSS/0.1% BSA. Fluorescence emissions were quantified using the PHERAstar FS platereader (BMG Labtech) using filters for excitation at 485 nm and emission at 520 nm. This ensured that receptor mutants were successfully transfected and exported to the cell surface. Remaining wells were then treated with increasing concentrations of unlabelled $VEGF_{165}$a (R&D Systems). Cells were stimulated for 5 hours at 37%/5% CO_2. As above, medium was replaced with 50 µl/well serum-free DMEM/0.1% BSA and 50 µl/well ONE-Glo Luciferase reagent. Following 5 minutes, luminescence emissions were measured using a TopCount platereader (Perkin Elmer, UK).

Characterisation of NanoBiT-Tagged VEGFR2 Constructs (Chapter 5)

HEK293T-ReLuc2P cells stably expressed LgBiT-VEGFR2, HiBiT-VEGFR2 or SmBiT-VEGFR2. Cells were seeded at 25,000 cells/well in white 96-well plates pre-coated with poly-D-lysine in DMEM containing 10% FBS. Following incubation for 24 hours at 37%/5% CO_2, medium was replaced with serum-free DMEM and cells were incubated for a further 24 hours. On the day of experimentation, medium was replaced with serum-free DMEM containing 0.1% BSA. Cells were stimulated with increasing concentrations of $VEGF_{165}$a (R&D Systems) for 5 hours at 37%/5% CO_2. As above, medium was replaced with 50 µl/well serum-free DMEM/0.1% BSA and 50 µl/well ONE-Glo Luciferase reagent. Following 5 minutes, luminescence emissions were measured using a TopCount platereader (Perkin Elmer, UK).

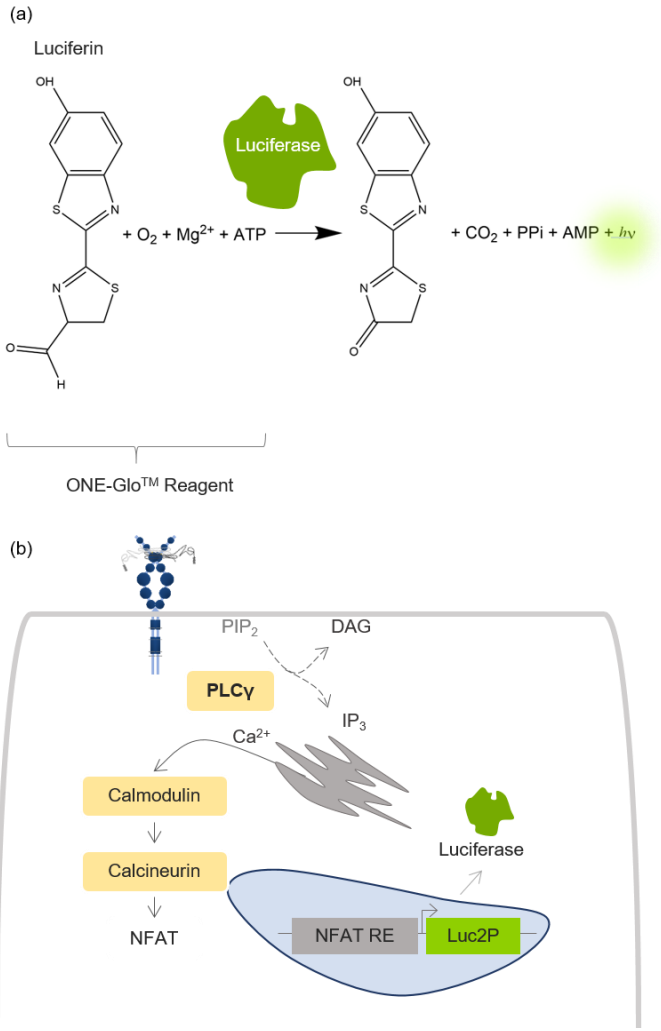


Figure 2.7 ***NFAT reporter gene assay methodology****. (a) Luciferin, a substrate present in the assay reagent ONE-Glo™, is oxidised by a luciferase engineered from the firefly* Phonitus pyralis*. This leads to the emission of light (hv), in addition to pyrophosphate (PPi) as an ATP-dependent reaction. (b) VEGFR2 activation leads to phosphorylation of intracellular tyrosine residues and recruitment of adaptor proteins. This initiates a Phospholipase C γ- (PLCγ) and calcium-mediated signalling cascade. Calcineurin dephosphorylates NFAT, enabling the NFAT transcription factor to translocate into the nucleus and bind to its response element (RE). HEK293T-ReLuc2P cells express a luciferase gene inserted downstream of the NFAT promoter (Carter et al., 2015), NFAT binding its RE leads to transcription and translation of this modified luciferase. Addition of ONE-Glo™ reagent following 5 hour stimulation causes this luciferase to emit luminescence via reaction* (a).

2.7.2 HUVEC Proliferation

As an indication of endothelial cell proliferation, we used high content imaging of nuclei stained with H33342 to monitor HUVEC proliferation in response to VEGF-A stimulation. HUVECs were seeded at 5,000 cells/well in black 96-well plates in Medium 200 containing 10% LVES. Following 24 hours of cell growth at 37°C/5% CO_2, plating medium was replaced with Medium 200 containing 0.1% serum for 24 hours. Cells were then stimulated with 0.3 nM, 3 nM or 30 nM $VEGF_{121}$a-TMR or $VEGF_{165}$b-TMR or commercially available $VEGF_{121}$a or $VEGF_{165}$b (R&D Systems). Ligands were diluted in Medium 200 containing 0.1% serum with 0.1% BSA. Cells were also stimulated with the positive control, 3 nM $VEGF_{165}$a (R&D Systems). Following stimulation for 24 or 48 hours at 37°C/5% CO_2, cells were washed with 100 µl/well PBS and fixed with 3% PFA/PBS for 20 minutes at room temperature. Having washed with PBS, nuclei were stained with 2 mg/ml H33342 for 15 minutes at room temperature. Nuclei were imaged the following day using an ImageXpress Micro widefield platereader (Molecular Devices, USA) with a 4X objective using a DAPI filter (4 sites per well, 25 ms exposure time).

2.7.3 Fluorescent Ligand Internalisation

High content imaging was used to monitor the localisation of fluorescent $VEGF_{xxx}$x-TMR isoforms. HEK293T-ReLuc2P cells stably expressing HaloTag-VEGFR2, NanoLuc-VEGFR2 or un-transfected HEK293T cells were seeded at 25,000 cells/well in DMEM/10% FBS on black 96-well plates pre-coated with poly-D-lysine. Following incubation for 24 hours at 37°C/5% CO_2, the medium was replaced with serum-free DMEM/0.1% BSA. To compare un-transfected HEK293T cells with cells expressing HaloTag-VEGFR2, cells were stimulated with 10 nM $VEGF_{165}$a-TMR, $VEGF_{165}$b-TMR or $VEGF_{121}$a-TMR for 60 minutes (37°C). All other widefield imaging assays used cells expressing NanoLuc-VEGFR2 (WT). For concentration-response experiments, increasing concentrations of $VEGF_{165}$a-TMR, $VEGF_{165}$b-TMR or $VEGF_{121}$a-TMR were added in duplicate wells (60 minutes; 37°C/5% CO_2). Alternatively, cells were stimulated with 10 nM $VEGF_{165}$a-TMR, $VEGF_{165}$b-TMR or $VEGF_{121}$a-TMR for 5-120 minutes as a retrospective timecourse. This ensured that all cells were fixed simultaneously. Cells were washed with 100 µl/well PBS and fixed with 3% PFA in PBS for 15 minutes at room temperature. Following another PBS wash, nuclei were stained with 2 mg/ml H33342 in PBS for 15 minutes at room temperature, then washed and stored in PBS at 4°C. The following day, cells were imaged using an ImageXpress Micro widefield platereader (Molecular Devices, USA). Plates were imaged at 4 sites per well using a 20X Extra Long Working Distance (ELWD) objective, with a TRITC filter to image $VEGF_{xxx}$x-TMR (560 nm excitation, 607-634 nm emission; 2000 ms exposure time) and a DAPI filter for nuclei (405 nm excitation, 447-460 nm emission; 25 ms exposure time).

2.8 BINDING ASSAYS

Bioluminescence resonance energy transfer (BRET) has been previously used to investigate ligand binding to GPCRs using fluorescent ligands (Stoddart et al., 2015a). This proximity-based technique uses a bioluminescent energy donor that excites a nearby fluorophore within a distance of 10 nm (*Appendix 7.5*). NanoLuc is a small, bright luciferase engineered from a deep-sea shrimp luciferase which oxidises its substrate, furimazine, and leads to the emission of luminescence (*Figure 2.8a*). Energy transfer can take place from the NanoLuc fused at the receptor N-terminus to a fluorescent ligand bound at its orthosteric ligand binding site (*Figure 2.8b*). The donor and acceptor spectra require spectral compatibility with sufficient overlap to enable excitation (*Figure 2.8c)*.

For experiments using intact cells, HEK293T cells stably expressed full-length wild type VEGFR2 or NRP1 tagged at their N-terminus with NanoLuc. Cells were seeded at 30,000 cells/well in white 96-well plates pre-coated with poly-D-lysine. Cells were incubated for 24 hours at 37°C/5% CO_2. On the day of experimentation, medium was replaced with HBSS containing 0.1% BSA. For saturation experiments, increasing concentrations of $VEGF_{165}$a–TMR, $VEGF_{165}$b-TMR or $VEGF_{121}$a-TMR (0.5-20 nM) were added in the presence or absence of a high concentration of corresponding unlabelled ligand (100nM, ~100-fold greater than the estimated K_d value). For displacement experiments, cells were co-incubated with vehicle (HBSS/0.1% BSA) or increasing concentrations of unlabelled ligand (0.03 nM-30 nM; R&D Systems), as well as fixed concentrations of fluorescently labelled $VEGF_{165}$a-TMR, $VEGF_{165}$b-TMR or $VEGF_{121}$a-TMR in duplicate wells (0.25 nM-5 nM). Following incubation for 60 minutes in the dark at 37°C, the NanoLuc substrate furimazine (10 μM) was added to each well and equilibrated for 5 minutes to enable NanoLuc-mediated furimazine oxidation and resulting luminescence emissions. Emissions were recorded using the PHERAstar FS platereader (BMG Labtech), predominantly using a filter simultaneously measuring NanoLuc emissions at 450 nm (30 nm bandpass) and TMR emissions using a longpass filter at 550 nm. Experiments in Chapters 3 and 4 investigated ligand binding at NanoLuc-NRP1 using a separate filter for consistency with Dr Kilpatrick's earlier work (NanoLuc emissions 460-480 nm; TMR emissions 610 nm longpass). BRET ratios were calculated as fluorescence over luminescence emissions from the second of three cycles. For kinetic experiments, cells were pre-treated with furimazine (10 μM) for 5 minutes to enable NanoLuc-mediated furimazine oxidation and resulting luminescence emissions. BRET ratios were then measured per well using the PHERAstar FS platereader using the filters above. Following 4 initial measurements, intact cells were stimulated with 1-20 nM $VEGF_{165}$a-TMR, $VEGF_{165}$b-TMR or $VEGF_{121}$a-TMR. Emissions were recorded every 30 seconds for 20 minutes or 90 minutes, using the temperature control function of the PHERAstar FS platereader to maintain conditions at 37°C.

2.8.1 Effect of Membrane Preparations

Ligand binding experiments were repeated in membrane preparations obtained from the same parent cell line (*Methods 2.4.3*), notably from HEK293T cells expressing NanoLuc-VEGFR2 or NanoLuc-NRP1. To first determine the effect of membrane concentration, increasing concentrations of membranes (2.5-20 µg/well) were diluted in HBSS/0.1% BSA in the presence and absence of 0.25 mg/ml saponin. Membranes were incubated with vehicle, 5 nM $VEGF_{165}$b-TMR (NanoLuc-VEGFR2 membranes) or 5 nM $VEGF_{165}$a-TMR (NanoLuc-NRP1 membranes). Following incubation for 60 minutes, 10 µM furimazine was added to each well and equilibrated for 5 minutes to enable NanoLuc-mediated furimazine oxidation and luminescence emissions. Emissions were recorded using the PHERAstar FS platereader and BRET ratios were calculated as fluorescence over luminescence emissions from the second of three cycles. Based on the data presented in *Figure 4.10*, membrane concentrations were used at 5 µg/well for equilibrium binding studies and 10 µg/well for kinetic binding. Membranes were incubated at 37°C for 30 minutes prior to assay, then the same protocol was followed in cells or membrane preparations in a final volume of 50 µl in duplicate wells.

2.8.2 Influence of Inhibiting VEGFR2 Phosphorylation

To pharmacologically interfere with VEGFR2 phosphorylation, cells or membranes expressing NanoLuc-VEGFR2 were pre-incubated with 1 µM cediranib (S1017, Selleckchem) or 0.01% dimethyl sulfoxide (DMSO) in HBSS/0.1% BSA (30 minutes, 37°C). Alternatively, tyrosine phosphorylation deficient VEGFR2 was tagged at the N-terminus with NanoLuc (NanoLuc-VEGFR2 TPD). For whole cell experiments, HEK293T cells were plated at 15,000 cells/well in white 96-well plates pre-coated with poly-D-lysine. Following 24 hours, cells were transiently transfected with 100 ng cDNA/well NanoLuc-VEGFR2 WT or NanoLuc-VEGFR2 TPD using FuGENE® HD (3:1 ratio of reagent:cDNA). For assays using membrane preparations, a stable cell line of NanoLuc-VEGFR2 TPD was established for homogenising membranes. Kinetic experiments were performed with 4 concentrations of $VEGF_{165}$b-TMR (cediranib experiments) or $VEGF_{121}$a-TMR (VEGFR2 TPD experiments) for 90 minutes (3-20 nM). Kinetic binding experiments were performed as described above.

2.8.3 Effect of Buffer pH

Membranes expressing NanoLuc-VEGFR2 (WT) were used to investigate the effect of pH on ligand binding. This used $VEGF_{165}$b-TMR as a representative fluorescent VEGF-A isoform. The pH of HBSS/0.1% BSA (pH 7.4), was lowered to 5.8-6.2 using concentrated hydrochloric acid on the day of the experiment and measured using a pH

Meter PB-11 (Sartorius, Germany). Although HEPES buffer has a pK_a suited to physiological pH (6.8-8.2), control experiments confirmed that the assay buffer remained within 0.2 of the initial pH in conditions replicating the experimental setup (50 µl at 37°C for 2 hours). Saturation and kinetic binding experiments were performed, as above.

2.8.4 Binding at LgBiT-VEGFR2 or HiBiT-VEGFR2

HiBiT and LgBiT are available as purified proteins fused to a recombinant 36 kDa HaloTag protein. These can be used to exogenously complement the NanoBiT complex. HEK293T-ReLuc2P cells stably expressed LgBiT-VEGFR2 or HiBiT-VEGFR2. Cells were seeded at 30,000 cells/well in white 96-well plates pre-coated with poly-D-lysine. Cells were incubated in DMEM/10% FBS for 24 hours at 37°C/5% CO_2. Following 24 hours, medium was replaced with assay buffer (HBSS/0.1% BSA). Cells expressing LgBiT-VEGFR2 were incubated with assay buffer containing 20 nM exogenous HiBiT (N301A). Cells expressing HiBiT-VEGFR2 were simultaneously incubated with purified LgBiT (N401B). Saturation binding experiments were performed with $VEGF_{121}$a-TMR as a representative ligand, whereby cells were simultaneously incubated with their respective purified NanoBiT protein and ligand.

2.8.5 Binding at a Recomplemented VEGFR2/NRP1 NanoBiT Complex

Following a 4 day protocol, HEK293T-ReLuc2P cells were plated in 6-well plates at 400,000 cells/well in DMEM containing 10% FBS. On day 2, cells were transfected using FuGENE® HD at a 3:1 ratio of reagent to cDNA with a total 1500 ng cDNA/well made up in serum-free DMEM. Cells were transfected with equal amounts of LgBiT-VEGFR2 (750 ng cDNA/well) and HiBiT-NRP1 WT (750 ng cDNA/well), or equal amounts of LgBiT-VEGFR2 (750 ng cDNA/well) with SmBiT-NRP1 WT (750 ng cDNA/well). For experiments monitoring kinetics at HiBiT complexes, matched controls were performed alongside in which cells were transfected with single receptors conjugated to full-length NanoLuc. NanoLuc-VEGFR2 or NanoLuc-NRP1 were transfected at 750 ng cDNA/well, made up to 1500 ng cDNA/well with empty pcDNA3.1/Zeo vector (750 ng cDNA/well). On day 3, cells were transferred from 6-well plates using a similar protocol to passaging cells (*Methods* *2.2.*1). Cells were washed with 1 ml/well PBS, detached with 500 µl/well trypsin and resuspended in 2 ml DMEM containing 10% FBS. Cells were seeded in white 96-well plates pre-coated with poly-D-lysine at 30,000 cells/well. On the day of experimentation (day 4), medium was replaced with HBSS/0.1% BSA. Saturation and kinetic binding experiments were then performed for $VEGF_{165}$b-TMR and $VEGF_{165}$a-TMR.

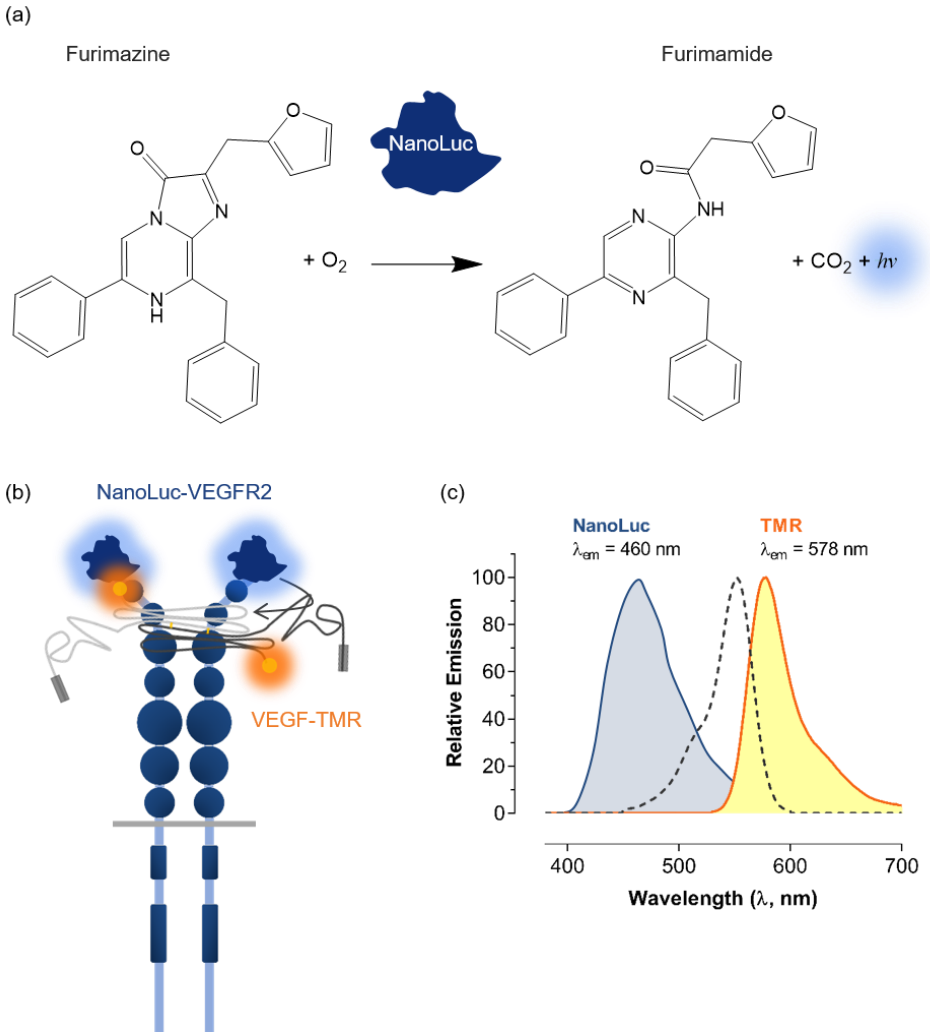


Figure 2.8 ***Using bioluminescent resonance energy transfer (BRET) to monitor ligand binding****. (a) NanoLuc, an engineered luciferase modified from* Oplophorus gracilirostris*, oxidises its substrate furimazine. This results in the emission of bioluminescent light (*hν*; Hall et al., 2012). (b) Using the example of VEGFR2, receptors were tagged at their N-terminus with NanoLuc. NanoLuc-VEGFR2 emits luminescence following addition of furimazine, acting as an energy donor that can excite a nearby fluorophore when VEGF$_{xxx}$x-TMR is bound. (c) NanoLuc emission spectra (blue region) and TMR excitation spectra (dashed line) are sufficiently overlapping to enable energy transfer. The Stokes shift between the NanoLuc emission spectra and the TMR emission spectra (orange region) is sufficient for simultaneous measurement of distinct emissions. The wavelength of peak emission (λ_{Em}) is noted.*

2.9 RECEPTOR-RECEPTOR COMPLEX ASSAYS

2.9.1 BRET between Receptors

HEK293T-ReLuc2P cells were plated in white 96-well plates pre-coated with poly-D-lyine at 25,000 cells per well in DMEM containing 10% FBS. Following 24 hours, cells were transiently transfected with a total 125 ng cDNA/well using FuGENE® HD at a 3:1 ratio of reagent to cDNA. Cells were transfected with a constant amount of NanoLuc-VEGFR2 (25 ng cDNA/well). Cells were also simultaneously transfected with increasing concentrations of HaloTag-NRP1 or SnapTag-NRP1 (2.5-100 ng cDNA/well). Additional wells only contained NanoLuc-VEGFR2. These transfection solutions were made up to equivalent to 125 ng per well using empty pcDNA3.1/Zeo vector in serum-free DMEM. Cells were incubated for another 24 hours at 37°C/5% CO_2. On the day of the experiment, cells were treated with 0.2 µM membrane impermeant HaloTag-AlexaFluor488 substrate or 0.2 µM SNAP-Surface AlexaFluor488 substrate in serum-free-DMEM/0.1% BSA. Cells were incubated for 30 minutes at 37°C/5% CO_2. They were then washed twice with 100 µl/well HBSS/0.1% BSA and replaced with a final volume of 50 µl/well HBSS/0.1% BSA. At this stage, fluorescence emissions were quantified using the PHERAstar FS platereader using filters for excitation at 485 nm and emission at 520 nm. Cells were then incubated with the NanoLuc substrate furimazine (10 µM) for 5 minutes. Emissions were recorded using the PHERAstar FS platereader using filters simultaneously measuring NanoLuc emissions at 475 nm (30 nm bandpass) and AlexaFluor488 emissions at 535 nm (30 nm bandpass). BRET ratios were calculated as fluorescence over luminescence emissions from the second of three cycles.

2.9.2 NanoBiT Complementation

To characterise luminescence emissions from a NanoBiT complex, HEK293T-ReLuc2P cells were plated as 25,000 cells/well in white 96-well plates in DMEM containing 10% FBS. Following 24 hours, cells were transiently transfected using FuGENE® HD at a 3:1 ratio of reagent to cDNA with a total 100 ng cDNA/well. Cells were transfected with a combination of LgBiT (50 ng cDNA/well) and HiBiT/SmBiT (50 ng cDNA/well). Alternatively, cells were transfected with single constructs (50 ng cDNA/well) with empty pcDNA3.1/Zeo vector (50 ng cDNA/well). Transfection mixtures were made up in serum-free DMEM and added as 5 µl/well without replacing DMEM/10% FBS on cells. Cells were incubated at 37°C/5% CO_2 for a further 24 hours. Medium was replaced with HBSS/0.1% BSA containing 10 µM furimazine, in the absence or presence of purified LgBiT protein (N401B, Promega Corporation) or HiBiT protein (N301A, Promega Corporation). Cells were incubated at 37°C for 10 minutes to allow NanoBiT complementation and the oxidation of furimazine. To prevent the loss of signal through

the bottom of the plate, an adhesive plate BackSeal was added at this point. Luminescence emissions were measured on the PHERAstar platereader using the filter settings measuring emissions between 475-505 nm. Experiments investigating tag orientation and background luminescence were performed on the same 96-well plate.

Additional experiments aimed to disrupt the recomplemented NanoBiT complex using increasing concentrations of competing receptor. HEK293T-ReLuc2P cells were plated as 25,000 cells/well in white 96-well plates in DMEM containing 10% FBS. Following 24 hours, cells were transiently transfected using FuGENE® HD at a 3:1 ratio of reagent to cDNA. This used a high amount of cDNA (total 300 ng cDNA/well) as 3-4 DNA constructs were transfected into cells. Cells were transfected with a constant amount of LgBiT-VEGFR2 (50 ng cDNA/well) and either HiBiT-NRP1 or SmBiT-NRP1 (50 ng cDNA/well). Cells were also transfected with increasing concentrations of either HaloTag-VEGFR2 or HaloTag-NRP1 (25-200 ng cDNA/well). This was made up to 300 ng cDNA/well with empty pcDNA3.1/Zeo vector. Additional wells only contained the LgBiT-VEGFR2 and HiBiT/SmBiT-NRP1 complex. Cells were incubated with transfection solution for 24 hours at 37°C/5% CO_2. On the day of the experiment, cells were treated with 0.2 µM membrane impermeant HaloTag-AlexaFluor488 substrate in serum-free-DMEM/0.1% BSA (30 minutes, 37°C/5% CO_2). They were then washed twice with 100 µl/well HBSS/0.1% BSA and replaced with a final volume of 50 µl/well HBSS/0.1% BSA. Fluorescence emissions were quantified using the PHERAstar FS platereader using filters for excitation at 485 nm and emission at 520 nm. Cells were incubated with 10 µM furimazine for 10 minutes, then luminescence and fluorescence emissions were recorded using PHERAstar FS platereader. Emissions were simultaneously measured for NanoLuc at 475 nm (30 nm bandpass) and AlexaFluor488 at 535 nm (30 nm bandpass).

2.10 DATA ANALYSIS

2.10.1 Software

Data are presented as mean ± S.E.M., unless stated otherwise. Experimental data were analysed and presented using GraphPad Prism 7.02 (GraphPad Software, La Jolla). Confocal images were collected using Zen 2010 software (Zeiss, Germany). Confocal images were then processed and analysed using ImageJ Fiji 1.52 software (National Institutes of Health, US). Images from high-content imaging were obtained, processed and analysed using MetaXpress 2.0 software (Molecular Devices, USA). Plasmid sequences were viewed and edited using SnapGene Viewer 4.3 (GSL Biotech, USA). Sequences were aligned to public databases using BLAST® (NCBI NIH, Bethesda, US), accessible from *blast.ncbi.nlm.nih.gov/Blast.cgi*. Primers for mutagenesis were designed using the web-based programme PrimerX (Bioinformatics, Phillipines), accessible from *www.bioinformatics.org/primerx/*. Molecular structures were drawn using ChemBioDraw (v14.0.0; Cambridge BioSoft), while 3D structures obtained from Protein Data Bank (PDB) codes were visualised using UCSF Chimera (San Francisco, US).

2.10.2 Statistics

All statistical tests were performed using GraphPad Prism 7.02 (GraphPad Software, La Jolla). Statistical significance was defined as $P<0.05$. Results from statistical tests are noted in figures, tables and/or in the Results text. Parametric tests were only performed on data corrected for the lognormal distribution, such as pK_d values obtained from equilibrium dissociation constants ($pK_d = -\log K_d$). Parametric two-way ANOVA tests were performed in the absence of a non-parametric equivalent. In all other cases, non-parametric tests were performed. Details of the statistical test used are provided in Chapters 3-5. Significance from parametric tests were displayed in tables and text as $^{\$,}$ whereas results from non-parametric tests were shown as *. According to traditional nomenclature, significant figures were represented as: * $P<0.05$, ** $P<0.01$, *** $P<0.001$, **** $P<0.0001$.

2.10.3 Imaging Quantification

High Content Imaging

Automated image analysis used algorithms on MetaXpress 2.0 software (Molecular Devices, USA). These were performed on images obtained from 96-well plates, imaged at 4 sites per well. Nuclei were quantified using a mask to define nuclei. This was either applied to a basic algorithm counting nuclei or used for quantification on a per cell basis by applying nuclei masks to other acquired images for automated image segmentation. Nuclei were defined by diameter 5-25 μm and 100 grey level intensity above background (*Figure 2.9a*).

To quantify granules indicative of endosomes, images were analysed using a granularity algorithm. Fluorescent granules were defined based upon size (2-15 μm diameter). Pixel depth in grey levels were consistent between replicates, as determined by vehicle and positive control. Granules were then assigned to specific nuclei based upon proximity using the aforementioned segmented image (*Figure 2.9b*).

Fluorescence intensity was quantified using a multiwavelength cell scoring algorithm for high content imaging of VEGFR2 and NRP1 expression (*Figure 2.9c*). Due to differences between antibodies, VEGFR2 (FITC) containing particles were defined as those with an intensity over 200 grey levels and NRP1 (TRITC) particles with an intensity over 50 grey levels. Fluorescence was quantified as integrated intensity per cell. Relative fluorescence units were also baseline-corrected per experiment to non-specific fluorescence observed using secondary antibody only.

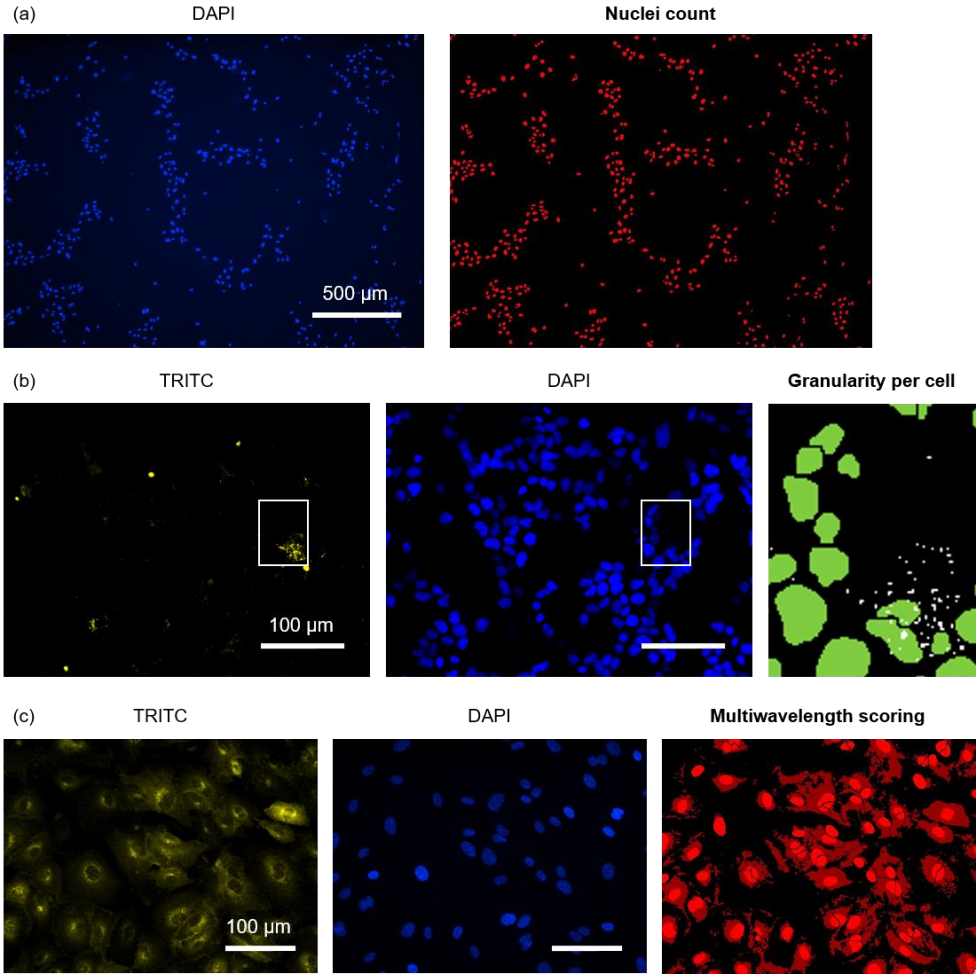


Figure 2.9 ***Representative images for quantifying high content imaging****. (a) HUVECs were stimulated with 30 nM $VEGF_{165}$a for 48 hours, then fixed with 3% PFA/PBS. Nuclei were stained using H33342 and plates were imaged using the IX Micro widefield platereader (10X objective). The nuclei count algorithm applied a mask (5-25 µm diameter). (b) NanoLuc-VEGFR2 cells were stimulated with 10 nM $VEGF_{165}$a-TMR for 60 minutes, then fixed and stained with H33342. Cells were imaged using the IX Micro (20X objective) using filter settings for TRITC (ligand) and DAPI (nuclei). A granularity algorithm detected granules in the TRITC channel (2-15 µm diameter) and quantified this on a per cell basis from nuclei. (c) HUVECs were fixed and an immunofluorescent labelling protocol was used to localise NRP1. Cells were imaged using the IX Micro (20X objective) with filter settings for TRITC (antibody labelling) and DAPI (nuclei). Multiwavelength cell scoring algorithms detected the fluorescence intensity above 50 grey levels, assigned to nuclei per field.*

Colocalisation analysis of Rab5, receptor and ligand from confocal microscopy

Confocal images were processed for colocalization analysis using ImageJ Fiji 1.52 software (National Institutes of Health, US). For colocalisation analysis, images were corrected to the background fluorescence intensity from each experimental replicate. These were determined using the non-specific secondary antibody only (Rab5, 488 nm) or un-transfected cells in each field of view (TMR, 546 nm; HaloTag-VEGFR2, 647 nm). The mean background intensity was calculated for each experimental replicate (n=5) and subtracted from each image for manual thresholding. To quantify colocalization, regions of interest (ROIs) were drawn around each cell expressing HaloTag-VEGFR2 using the nuclei stain and phase contrast image. Following subtraction of the region outside the ROI, colocalisation was determined using pixel-based measures between Rab5/TMR, Rab5/HaloTag and TMR/HaloTag using the ImageJ plugin Coloc 2. Images with saturated pixels were excluded from analyses. Mander's Overlap Coefficients measure co-occurrence as the proportion of Rab5 pixels (green) overlapping with VEGF-TMR (yellow) or HaloTag-VEGFR2 (red). Pearson's Correlation Coefficients measure whether there is a correlation between these channels. These were calculated on a per cell basis, with a total number of 64 cells (5 minute stimulation) and 68 cells (60 minute stimulation) pooled from 5 independent experiments.

Colocalisation analysis of VEGFR2 and NRP1 from live cell confocal microscopy

As above, confocal images were processed for colocalization analysis using ImageJ Fiji 1.52 software (National Institutes of Health). Images were corrected to the background fluorescence intensity from each experimental replicate determined using un-transfected cells in each field of view (HaloTag-VEGFR2, 488 nm; SnapTag-NRP1, 647 nm). The mean background intensity was calculated for each experimental replicate (n=4) and subtracted from each image for manual thresholding. To quantify colocalization, regions of interest (ROIs) were drawn around each cell that co-expressed HaloTag-VEGFR2 and SnapTag-NRP1. Following subtraction of the region outside the ROI, colocalisation was determined using pixel-based measures between HaloTag-VEGFR2 and SnapTag-NRP1 using the ImageJ plugin Coloc 2. Mander's Overlap Coefficients measure co-occurrence as the proportion of SnapTag-NRP1 pixels (red) overlapping with HaloTag-VEGFR2 (green). Pearson's Correlation Coefficients measure whether there is a correlation between these channels. Colocalisation parameters were calculated on a per cell basis, with a total number of 97 cells (vehicle) and 54 cells ($VEGF_{165}$a stimulation) and 68 cells ($VEGF_{165}$b stimulation), pooled from 4 independent experiments.

2.10.4 Functional Assays

Logarithmic concentration-response agonist curves were fit using a non-linear regression equation that fit the data to a sigmoidal function (*Appendix 7.6*). This was used to derive the effective concentration (EC_{50}), or potency. This is defined as the molar ligand concentration, [L], which stimulates 50% of the maximal response (Y_{max}).

Equation 2.2

$$Response = \frac{y_{max}}{1 + 10^{logEC_{50} - [L]}}$$

Equation 2.2 describes: molar ligand concentration, [L] plotted on the x axis; maximal response, Y_{max}; and molar concentration of ligand required to stimulate 50% of the maximal response, EC_{50}.

GraphPad Prism fit data to this sigmoidal format of the logistic function, however this equation can be rearranged to Equation 2.3 to describe the relationship between ligand concentration and EC_{50}.

Equation 2.3

$$Response = y_{max} \cdot \frac{[L]}{[L] + EC_{50}}$$

These data assumed the gradient of the sigmoidal curve, or Hill slope, was equal to 1. The Hill slope can be used to indicate cooperativity according to the law of mass action, from the additional power of $[L]^n$, however this was not considered due to insufficient data points.

Studies monitoring ligand/receptor endocytosis over time were fit using a monoexponential association function (*Appendix 7.6*).

Equation 2.4

$$Response = y_{max} \cdot (1 - e^{-k_{obs} \cdot t})$$

Equation 2.4 describes: time, t, plotted on the x axis; maximum response at infinite time, Y_{max}; and the rate constant observed, k_{obs}.

2.10.5 Binding Assays

In relation to the equilibrium between ligand (L) and receptor (R) described in *Introduction 1.6.2*, ligand binding assays can either assume the system has reached equilibrium or quantify the kinetic rates of binding over time.

Equilibrium Binding

Saturation binding experiments determined affinity using increasing concentrations of labelled ligand. At the assumed point of equilibrium, the rate of the forward (association) and reverse (dissociation) reactions are equal, such that:

Equation 2.5

$$k_{on} \,.[L].[R] = \; k_{off} \,.\; [LR]$$

To determine the affinity of the labelled ligand, saturation binding curves were fit using a non-linear equation that incorporates both specific and non-specific binding elements. Non-specific binding was determined as a linear component in Equation 2.6.

Equation 2.6

$$Non\ Specific\ Binding = M.[L] + c$$

Equation 2.6 describes: nanomolar ligand concentration, [L] plotted on the x axis; the linear slope of the line, M; and the y intercept, c.

Saturation binding experiments ertr plotted on a linear x axis to display whether ligand saturates within this concentration range and to compare non-specific binding. The specific binding component (in the absence of competitor) was fit using a non-linear exponential function (*Appendix 7.6*). This enabled derivation of the equilibrium dissociation constant (K_d), defined as the molar ligand concentration of labelled ligand, [L], which occupies 50% of the total receptors. This is a measure of affinity that is inversely related to the equilibrium association constant. The observed binding curve incorporates both the specific component with the linear, non-specific component in Equation 2.7.

Equation 2.7

$$Total\ Binding = \; B_{max}.\frac{[L]}{[L] + \; K_d} + M.[L] + c$$

This has additional terms to Equation 2.6, describing: maximal binding, B_{max}; the equilibrium dissociation constant of the labelled ligand, K_d, in the same units as [L]. Non-specific binding was determined using a high concentration of corresponding unlabelled $VEGF_{xxx}x$ which was approximately 100-fold higher than the estimated K_d.

Displacement experiments were performed to determine the affinities of unlabelled ligands. This used increasing concentrations of unlabelled ligand which competed with the binding of a fixed concentration of labelled ligand. These affinities, also assuming equilibrium, were calculated in two steps.

First, the molar ligand concentration that inhibits 50% of binding is calculated using a non-linear regression equation that fit data to a sigmoidal function (*Appendix 7.6*).

Equation 2.8

$$Binding = \frac{y_{max}}{1 + 10^{[L] - logIC_{50}}}$$

Equation 2.8 describes: molar unlabelled ligand concentration, [L], plotted on the x axis; maximal binding, Y_{max}; and molar concentration of unlabelled ligand required to inhibit 50% of the specific binding of the fixed concentration of labelled ligand, IC_{50}.

This can be rearranged to provide more information about the relationship between the IC_{50} and ligand concentration. This described the uninhibited, specific binding of the fluorescent ligand.

Equation 2.9

$$Binding = y_{max} \cdot \frac{IC_{50}}{IC_{50} + [L]}$$

Subsequently, the Cheng-Prusoff equation was used to derive the affinity of unlabelled ligands independently of labelled ligand concentration. Calculating the affinity of the unlabelled ligand, K_i, utilised the affinity of the labelled ligand calculated by saturation binding experiments.

Equation 2.10

$$K_i = \frac{IC_{50}}{1 + \frac{[L]}{K_d}}$$

Equation 2.10 describes: molar labelled ligand concentration, [L], used in the displacement experiment; equilibrium dissociation constant of the labelled ligand, K_D; the concentration of unlabelled ligand required to inhibit the specific binding of [L] by 50%, IC_{50}; and the affinity of the unlabelled ligand, K_i.

Kinetic Binding

Kinetic studies of fluorescent ligand binding were measured over time were fit to a monoexponential association function (*Appendix 7.6*).

Equation 2.11

$$Binding = y_{max} . (1 - e^{-k_{obs} . t})$$

Equation 2.11 describes: time, t, plotted on the x axis; maximum response at infinite time, Y_{max}; and the rate constant observed, k_{obs}.

In conjunction with Equation 2.11, k_{on} and k_{off} values were determined simultaneously using different known concentrations of fluorescent ligand ([L]). This utilised the following relationship with k_{obs}:

Equation 2.12

$$k_{obs} = k_{on}.[L] + k_{off}$$

Equation 2.12 further describes: association rate, k_{on}, in units of $min^{-1} M^{-1}$; and dissociation rate, k_{off}, in min^{-1}. This demonstrates that the association rate between ligand and receptor are concentration-dependent. These kinetic data were also used to estimate the binding affinities, due to the relationship between dissociation and association rates within an equilibrium described in Equation 2.13.

Equation 2.13

$$K_d = \frac{k_{off}}{k_{on}}$$

Residence time was calculated as the reciprocal of k_{off}. Additionally, assuming a first order reaction, half life ($t_{1/2}$) was calculated for a given concentration.

Equation 2.14

$$t_{1/2} = \frac{ln\,2}{k_{on}.[L] + k_{off}}$$

$$t_{1/2} = \frac{0.693}{k_{obs}}$$

Chapter 3.
Discriminating between fluorescent VEGF-A isoforms binding VEGFR2 or NRP1

3.1 INTRODUCTION

VEGF-A is a large dimeric protein (~40 kDa) linked by disulphide bonds (*Introduction 1.3.1*). VEGF-A proteins bind to both their cognate RTK, VEGFR2, and the co-receptor NRP1 (Koch et al., 2011; Simons et al., 2016). While signalling cascades are mediated by VEGFR2, interactions with NRP1 enhance signalling induced by VEGF-A (Djordjevic and Driscoll, 2013; Guo and Vander Kooi, 2015). Interactions with each receptor occur via distinct regions of the peptide ligand (*Introduction Figure 1.3*). VEGF-A interacts with the Ig-like D2 and D3 of VEGFR2 via residues encoded at the N-terminus of VEGF-A (Leppanen et al., 2010; Brozzo et al., 2011). In contrast, the C-terminus of VEGF-A interacts with the b1 domain of NRP1 (Mamluk et al., 2002; Vander Kooi et al., 2007; Parker et al., 2012). Residues in the C-terminal region of VEGF-A differ amongst VEGF-A isoforms due to alternative splicing (Woolard et al., 2009). This determines whether ligands interact with other molecules, such as co-receptor NRP1 or components of the ECM (Harper and Bates, 2008). $VEGF_{165}$a is considered the prototypical 'pro-angiogenic' isoform (Woolard et al., 2004; Hervé et al., 2005; Cébe Suarez et al., 2006; Krilleke et al., 2007; Pan et al., 2007; Kawamura et al., 2008b; Catena et al., 2010; Delcombel et al., 2013; Fearnley et al., 2015, 2016; Pang et al., 2017; Shiying et al., 2017; Ourradi et al., 2017). $VEGF_{165}$b and recently identified VEGF-Ax, on the other hand, have reported anti-angiogenic activity *in vivo* (Woolard et al., 2004; Cébe Suarez et al., 2006; Eswarappa et al., 2014). $VEGF_{121}$a is another key isoform. This shorter isoform is considered freely diffusible as it lacks residues that bind heparan sulphate in the ECM (Houck et al., 1992; Krilleke et al., 2007). VEGF-A isoforms have distinct physiological signalling outcomes (*Introduction Table 1.1*), however it is largely unknown how these ligands differ in terms of their receptor pharmacology.

Interactions between an endogenous ligand and its cognate receptor are a fundamental step preceding any ligand-induced signalling or phenotypic response (Kenakin, 2014). Ligand binding interactions are often described by the strength of this interaction (affinity) or the duration of ligand/receptor interactions (kinetics). Experimental approaches that measure ligand binding traditionally used radioactive ligands labelled with a radioisotope (Bylund and Toews, 1993). VEGF-A binding was first investigated using radiolabelled [^{125}I]-$VEGF_{165}$a in intact primary endothelial cells (*Table 3.1*). This cannot distinguish between ligand binding at other receptors that interact with VEGF-A expressed by endothelial cells. Biochemical techniques have also been used to investigate VEGF-A binding affinities using purified receptor domains (*Table 3.1*). Approaches include surface plasmon resonance (SPR; Leppanen et al., 2010), solid-phase enzyme-linked assays (Eswarappa et al., 2014; Nieminen et al., 2014) and isothermal calorimetry (Leppanen et al., 2010; Brozzo et al., 2011). These truncated receptor domains are immobilised on a surface that do not enable receptors to form

oligomers in their native lipid bilayer. There is therefore limited quantitative understanding of VEGF-A binding isolated at full-length receptors in living cells. Additionally, few studies have directly compared the binding properties of numerous VEGF-A isoforms.

To further probe the quantitative pharmacology of VEGF-A and its receptors, technologies can be applied from those developed for other families of cell surface receptors. Significant advances in understanding GPCRs have come from fluorescent ligand technologies (Sridharan et al., 2014; Stoddart et al., 2015b). In contrast to radioligands, fluorescent ligands are a safer and cheaper alternative (Stoddart et al., 2016). Fluorescent GPCR ligands were first developed for microscopy (Melamed et al., 1976; Atlas and Levitzki, 1977). Their advantages in monitoring ligand/receptor interactions were evident by the 1980s as studies observed ligand binding with spatial resolution (Niedel et al., 1979) and temporal resolution (Sklar et al., 1984). Experimental approaches were later developed to exploit fluorescent ligands to monitor protein-protein interactions based on the close proximity of ligand binding interactions. Proximity-based assays were developed using Resonance Energy Transfer (RET; *Appendix 7.5*). These were applied to monitor fluorescent ligand binding in real-time at 37°C isolated at a specified GPCR (Ilien et al., 2003; Castro et al., 2005). This applied Fluorescence RET (FRET) to monitor interactions between a target GPCR tagged with a fluorophore and a fluorescent ligand. FRET relies on the selection of two compatible fluorophores. If these fluorophores are in close proximity within 10 nm (*Appendix 7.5*), an excited donor fluorophore can excite a nearby acceptor fluorophore via non-radiative energy transfer (Lohse et al., 2012). The spectrum of each fluorophore must have spectral overlap between the wavelengths of donor emission and acceptor excitation, in addition to orientation constraints, for energy transfer to take place (Lakowicz, 2006).

Proximity-based RET assays were further developed to monitor protein-protein interactions using bioluminescence RET (BRET). Rather than using a fluorophore as an energy donor, a bioluminescent enzyme can emit photons upon an enzymatic reaction with its substrate (Pfleger and Eidne, 2006). This has advantages over FRET, in which the fluorescent donor is illuminated by an external light source. As such, FRET donors are subject to fluorophore photobleaching. This limits quantification over longer timecourses. Furthermore, there is high background due to cellular autofluorescence in FRET (Lohse et al., 2012). Luciferase enzymes are naturally occurring proteins, such as the Firefly luciferase (61 kDa) and Renilla luciferase (36 kDa). More recently, NanoLuciferase (NanoLuc, 19 kDa) was derived from the deep sea shrimp *Oplophorus gracilirostris* (Hall et al., 2012; Machleidt et al., 2015). NanoLuc has optimal properties in terms of its luminescence emissions and small size. Upon addition of the substrate furimazine, NanoLuc produces extremely bright luminescence during an ATP-independent reaction (*Methods Figure 2.8*). This acts as a bioluminescent energy

donor to a nearby, compatible fluorophore acceptor. Emissions from the luminescent donor and fluorescent acceptor can be quantified by a platereader. BRET approaches using N-terminal NanoLuc-tagged receptors were applied to monitor fluorescent ligand binding at GPCRs (Stoddart et al., 2015a). At the outset of this project, BRET approaches for ligand binding had not been applied to other classes of membrane protein.

Growth factors are large, complex proteins with post-translational modifications. This makes them difficult to label with a fluorophore using techniques applied to other small molecules. In collaboration with Promega, VEGF-A isoforms were labelled at a single amino acid residue with the red-shifted fluorophore, tetramethylrhodamine (TMR). This approach was first used to synthesise $VEGF_{165}$a-TMR (Kilpatrick et al., 2017). Here, we extended this to investigate distinct VEGF-A isoforms by developing fluorescent variants of 'anti-angiogenic' $VEGF_{165}$b and freely diffusible $VEGF_{121}$a. These were synthesised using Click Chemistry for stoichiometric labelling (Friedman Ohana et al., 2015). HaloTag® technologies were also exploited for protein purification (Friedman Ohana et al., 2011), in addition to their use in live cell microscopy (*Methods 2.6.1*). Proteins secreted from mammalian cells were appended to the HaloTag moiety modified from bacterial haloalkane dehalogenase (Los et al., 2008). As HaloTag enzymes form a covalent bond with its substrate (*Methods Figure 2.6*), chemical bonds formed in this enzymatic reaction were used to covalently capture secreted proteins onto beads conjugated to the substrate (*Methods Figure 2.5*). This protocol labelled each $VEGF_{xxx}$x monomer with a fluorophore at a single N-terminal Cys residue. Captured ligand was proteolytically cleaved from beads using a HaloTEV protease, a Cys protease cleaving the ENLYFQ/C sequence (Friedman Ohana et al., 2011). This amino acid sequence was present in the linker region between HaloTag and $VEGF_{xxx}$x. This proteolytic reaction therefore exposed a single N-terminal Cys for stoichiometric labelling with Click Chemistry, while releasing $VEGF_{xxx}$x from the beads. A conjugation reaction was performed simultaneously to enable the formation of a thiazole structure between the free Cys and a TMR fluorophore. Despite ligand production in mammalian cells, modifying any ligand or receptor can disrupt their structure or pharmacophore. Fluorescent ligands, for example, can have markedly different pharmacological properties to their unlabelled counterparts (Stoddart et al., 2016). Single-site fluorescent VEGF-A isoforms will be therefore be characterised as novel entities, prior to using these as fluorescent ligands in proximity-based BRET assays to quantify the pharmacology of distinct VEGF-A isoforms at NanoLuc-tagged VEGFR2 and NRP1.

Table 3.1 ***Published binding affinities of VEGF-A isoforms****.*

Technique	Expression system	Equilibrium dissociation constant (nM)
$VEGF_{165}a$: VEGFR2		
Radioligand binding	Human kidney tissue *in situ* (Simon et al., 1998)	0.01-0.04
	HUVECs (Whitaker et al., 2001)	0.17
	PAE cells expressing VEGFR2 (Waltenberger et al., 1994)	0.76
	PAE cells expressing VEGFR2 (Gille et al., 2001)	0.097
	Balb/c expressing VEGFR2 (Whitaker et al., 2001)	0.29
	COS-1 cells expressing VEGFR2 (Whitaker et al., 2001)	0.34
	Immobilised VEGFR2 (Krilleke et al., 2007)	0.081
SPR	VEGFR2 D2/D3 (Leppanen et al., 2010)	36.7
	VEGFR2 ECD (D1-D7) (Huang et al., 1998)	0.3
	VEGFR2 ECD (D1-D7) (Yamazaki et al., 2009)	0.26
	VEGFR2 ECD (Teran and Nugent, 2018)	8.6
ITC	VEGFR2 D2/D3 (Leppanen et al., 2010)	18
	VEGFR2 D2/D3 (Brozzo et al., 2011)	170
	VEGFR2 ECD (D1-D7) (Brozzo et al., 2011)	2670
HTRF	HEK293T cells expressing SnapTag-VEGFR2 (Auriau et al., 2018)	6-11
$VEGF_{165}a$: NRP1		
Radioligand binding	PAE cells expressing NRP1 (Soker et al., 1998)	0.32
	COS-1 cells expressing NRP1 (Gu et al., 2002)	0.93
	PAE cells expressing NRP1 (Prahst et al., 2008)	3.0
	Immobilised NRP1 (Krilleke et al., 2007)	0.128
SPR	NRP1 ECD (Fuh et al., 2000)	113-2000
	NRP1 ECD (Pan et al., 2007)	120
	NRP1 ECD (Yamazaki et al., 2009)	14.4
	NRP1 ECD (Teran and Nugent, 2018)	25
HTRF	HEK293T cells expressing SnapTag-NRP1 (Auriau et al., 2018)	5-8
$VEGF_{121}a$: VEGFR2		
SPR	VEGFR2 ECD (Teran and Nugent, 2018)	5.5
ITC	VEGFR2 ECD (D1-D7) (Brozzo et al., 2011)	1120
	VEGFR2 ECD (D2/D3) (Brozzo et al., 2011)	93

Equilibrium dissociation constants are estimates of affinity, as the reciprocal of the equilibrium association constant. These were derived experimentally for the labelled ligand (K_d) or competing ligand (K_i). Techniques quantifying the ligand binding of VEGF-A isoforms used radioligand binding, surface plasmon resonance (SPR), isothermal calorimetry (ITC) and Homogenous Time-Resolved Fluorescence (HTRF).

3.2 CHAPTER 3 AIMS

The work described in Chapter 3 aimed to:

(a) Characterise novel fluorescent variants of $VEGF_{165}$b and $VEGF_{121}$a stoichiometrically labelled with TMR;
(b) Characterise model HEK293T cell lines and receptors tagged at the N-terminus with NanoLuc or HaloTag for use in subsequent studies;
(c) Quantify the binding affinities and kinetics of $VEGF_{165}$a-TMR, $VEGF_{165}$b-TMR and $VEGF_{121}$a-TMR to full-length VEGFR2 or NRP1 using BRET;
(d) Image the localisation of full-length VEGFR2 and NRP1 in living cells, in the absence and presence of fluorescent VEGF-A isoforms.

3.3 RESULTS

Characterisation of novel fluorescent VEGF-A isoforms in HUVECs and HEK293T cells

The TMR fluorophore was appended to $VEGF_{165}b$ and $VEGF_{121}a$ at a single N-terminal Cys residue via a PEG linker (*Figure 3.1*). This has been performed previously for $VEGF_{165}a$-TMR (Kilpatrick et al., 2017). Preliminary characterisation therefore focussed on $VEGF_{165}b$-TMR and $VEGF_{121}a$-TMR as novel ligands.

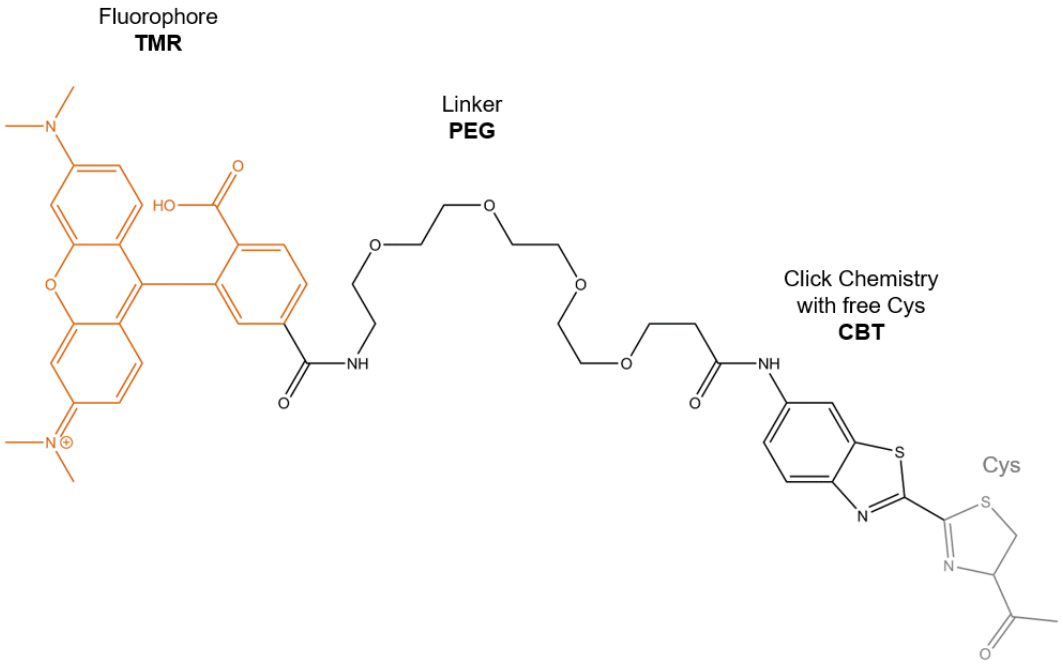


Figure 3.1 ***Structure appended to each VEGF-A monomer****. The red-shifted fluorophore tetramethylrhodamine (TMR) was attached to a polyethylene glycol (PEG) linker and 2-cyanobenzothiazole (CBT). CBT forms a thiazole structure with the free cysteine (Cys) at the N-terminus of purified VEGF-A, such that this can only conjugate at this single site using Click Chemistry upon proteolytic cleavage with HaloTEV. This is detailed in* Methods 2.5*.*

$VEGF_{165}$b-TMR and $VEGF_{121}$a-TMR, were biochemically characterised by colleagues at Promega Corporation (*Appendix 7.1*). Labelling specificities of $VEGF_{165}$b-TMR and $VEGF_{121}$a-TMR were determined by liquid chromatography-tandem mass spectrometry performed on labelled and unlabelled VEGF-A isoforms that had been digested with proteases. This indicated highly selective and efficient labelling of the N-terminal Cys residue of each VEGF-A isoform with the chemical modification in *Figure 3.1*. We did not observe non-specific labelling of other Cys residues present in either $VEGF_{165}$b-TMR or $VEGF_{121}$a-TMR (*Figure 7.1, Figure 7.2*). The labelling efficiency was 97% ($VEGF_{165}$b-TMR) and 94%–99% ($VEGF_{121}$a-TMR; *Table 7.1*). Fluorescence SDS-PAGE analysis of $VEGF_{165}$b-TMR and $VEGF_{121}$a-TMR in the presence or absence of 100 mM DTT confirmed that, in non-reducing conditions, both VEGF-A isoforms were largely present as homodimers (*Figure 7.3*). Deglycosylation by PNGase provided evidence that purified $VEGF_{165}$b-TMR was glycosylated (*Figure 7.3*). However, for $VEGF_{121}$a-TMR, treatment with PNGase suggested that it may be present in both glycosylated and non-glycosylated forms under normal conditions. These data confirmed that novel fluorescent VEGF-A isoforms were stoichiometrically labelled with appropriate post-translational modifications.

To determine whether adding a fluorescent tag influenced their agonist activity, we monitored the proliferation of human umbilical vein endothelial cells (HUVECs) in response to $VEGF_{165}$b-TMR and $VEGF_{121}$a-TMR (*Methods 2.7.2*). Having stained nuclei with Hoechst stain (referred to herein as H33342), high-content imaging was used to quantify the number of nuclei. Analysis was performed on images obtained at four different sites per well (*Methods Figure 2.9a)*. All VEGF-A isoforms stimulated a concentration-dependent increase in HUVEC nuclei (*Figure 3.2*). Both fluorescent ligands, however, evoked a lower maximal response than their unlabelled counterparts. Cells stimulated for 48 hours with VEGF-A isoforms had a higher nuclei count compared to cells stimulated for 24 hours. For both VEGF-A isoforms, there was a lower response of unlabelled VEGF-A isoforms compared to 3 nM $VEGF_{165}$a following 48 hour stimulation (49.9 ± 7.2% for 3 nM $VEGF_{165}$b; 68.3 ± 8.1 % for 3 nM $VEGF_{121}$a; n=6 per group). The highest concentration of unlabelled $VEGF_{121}$a reached a similar maximal response to that obtained with 3 nM $VEGF_{165}$a (96.1 ± 7.0 % for 30 nM $VEGF_{121}$a). In contrast, $VEGF_{165}$b produced a lower maximal response than the positive control 3 nM $VEGF_{165}$a following 48 hour stimulation (58.2 ± 8.6 % for 30 nM $VEGF_{165}$b).

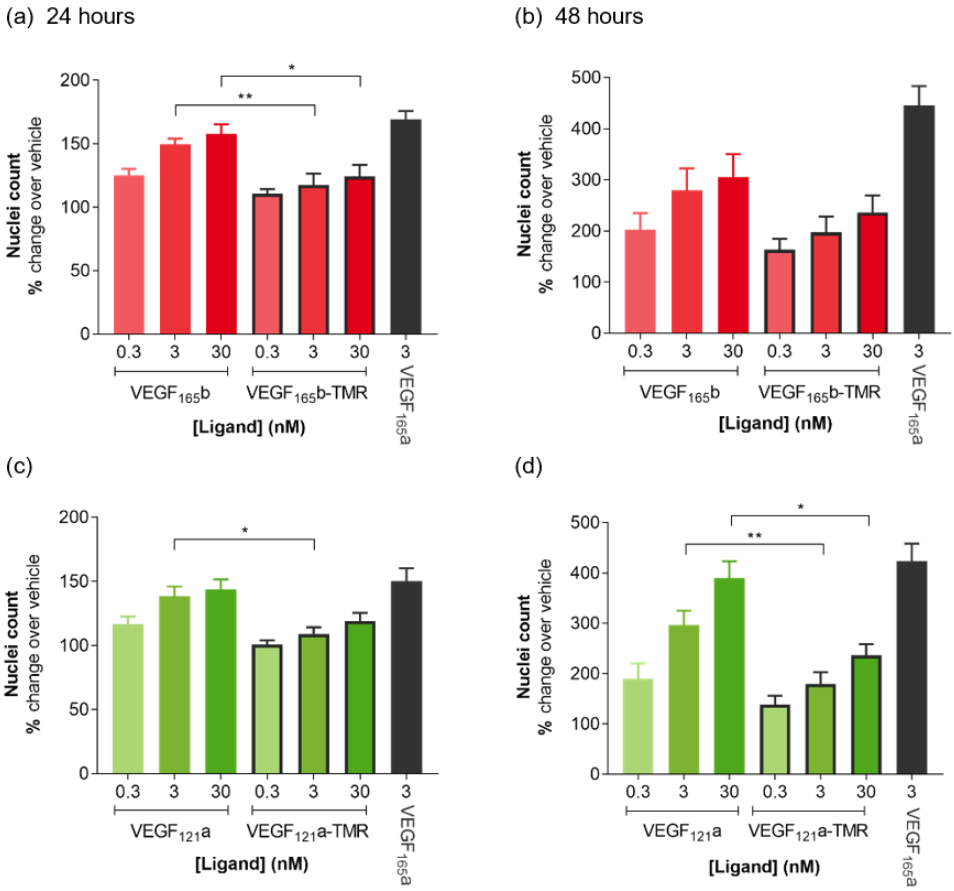


Figure 3.2 ***HUVEC proliferation in response to unlabelled and TMR-labelled VEGF****. Following serum deprivation for 24 hours, HUVECs were incubated with VEGF-A isoforms for 24 or 48 hours. Cells were fixed using 3% PFA/PBS and nuclei stained with 2 mg/ml H33342 for 15 minutes. Plates were imaged the following day on the IX Micro widefield platereader (4X objective). From these images, nuclei were counted using a granularity algorithm (*Methods Figure 2.9a*, MetaXpress, Molecular Devices). (a,b) Cells were stimulated with VEGF$_{165}$b or VEGF$_{165}$b-TMR for 24 hours or 48 hours. (c,d) HUVECs were stimulated with VEGF$_{121}$a or VEGF$_{121}$a-TMR for (c) 24 or (d) 48 hours. Responses to 3 nM VEGF$_{165}$a were included on each plate as a positive control, although not included in statistical comparisons. Data were normalised as percentage change over vehicle (100%) representing mean ± S.E.M. from 6 independent experiments (duplicate wells, imaged 4 sites per well). Statistical analyses were performed using a Kruskal-Wallis test with post-Hoc Dunn's multiple comparisons (* P<0.05, ** P<0.01).*

To quantify agonist potencies in response to VEGFR2 activation, we also monitored signalling using a Ca^{2+}-based reporter gene assay downstream of NFAT (Carter et al., 2015). HEK293T cells expressed an NFAT response element-luciferase (ReLuc2P; *Methods 2.7.1*). This inserted the gene encoding Renilla luciferase downstream of an NFAT response element, such that luminescence emissions were proportional to downstream Ca^{2+}-induced NFAT signalling (*Methods Figure 2.7*). HEK293T cells also stably expressed VEGFR2. Cells were stimulated for 5 hours to enable signalling and luciferase synthesis. There was a concentration-dependent increase in NFAT luminescence in response to $VEGF_{165}$a, $VEGF_{165}$b and $VEGF_{121}$a (*Figure 3.3*). Concentration-response curves were fit using a non-linear regression. This sigmoidal relationship was used to determine the potency (EC_{50}, effective concentration required to stimulate 50% of the maximal response).

Experiments performed in Kilpatrick et al. (2017) used a VEGFR2 construct with a natural VEGFR2 polymorphism (V297I; Rogers and D'Amato, 2012). As such, experiments initially investigated HEK293T-ReLuc2P cells expressing wild type NanoLuc-VEGFR2 (*Figure 3.3a*). $VEGF_{165}$a-TMR had a similar potency to unlabelled $VEGF_{165}$a that was prepared in an identical manner (*Table 3.2*). Compared to published values at NanoLuc-VEGFR2 V297I (Kilpatrick et al., 2017), potencies were also in the nanomolar range with the same rank order of EC_{50} values (*Table 3.2*). This confirmed the V297I point mutation had minimal effect on the pharmacology of VEGFR2. Subsequent NFAT reporter gene assays in Chapter 3 utilised this cell line, having been dilution cloned by Promega Corporation and for consistency with previous characterisation of fluorescent VEGF-A variants by Dr Kilpatrick. Comparing the NFAT response of fluorescent VEGF-A variants to their unlabelled equivalents, there was a rightward shift for $VEGF_{165}$b-TMR and $VEGF_{121}$a-TMR in cells expressing untagged VEGFR2 (*Figure 3.3b-c*) or NanoLuc-tagged VEGFR2 (*Figure 3.3d-f*). Novel fluorescent variants $VEGF_{165}$b-TMR and $VEGF_{121}$a-TMR had pEC_{50} values that were significantly lower, therefore less potent, by an order of magnitude than their unlabelled counterparts (ordinary one-way ANOVA $P<0.05$, post-Hoc Šidák's multiple comparisons $P<0.0001$, n=5-6 per group). In contrast, $VEGF_{165}$a-TMR and its unlabelled analogues had the same potencies (*Figure 3.3a,d, Table 3.2*). Regarding the maximal response with respect to 10 nM $VEGF_{165}$a as positive control, $VEGF_{165}$b and $VEGF_{121}$a evoked a sub-maximal response in all experiments. This was consistent with previous work with unlabelled $VEGF_{165}$b and $VEGF_{121}$a (Carter et al., 2015; Kilpatrick et al., 2017). In each case, the TMR-labelled VEGF-A isoform produced a similar maximal response to that obtained with their unlabelled counterparts.

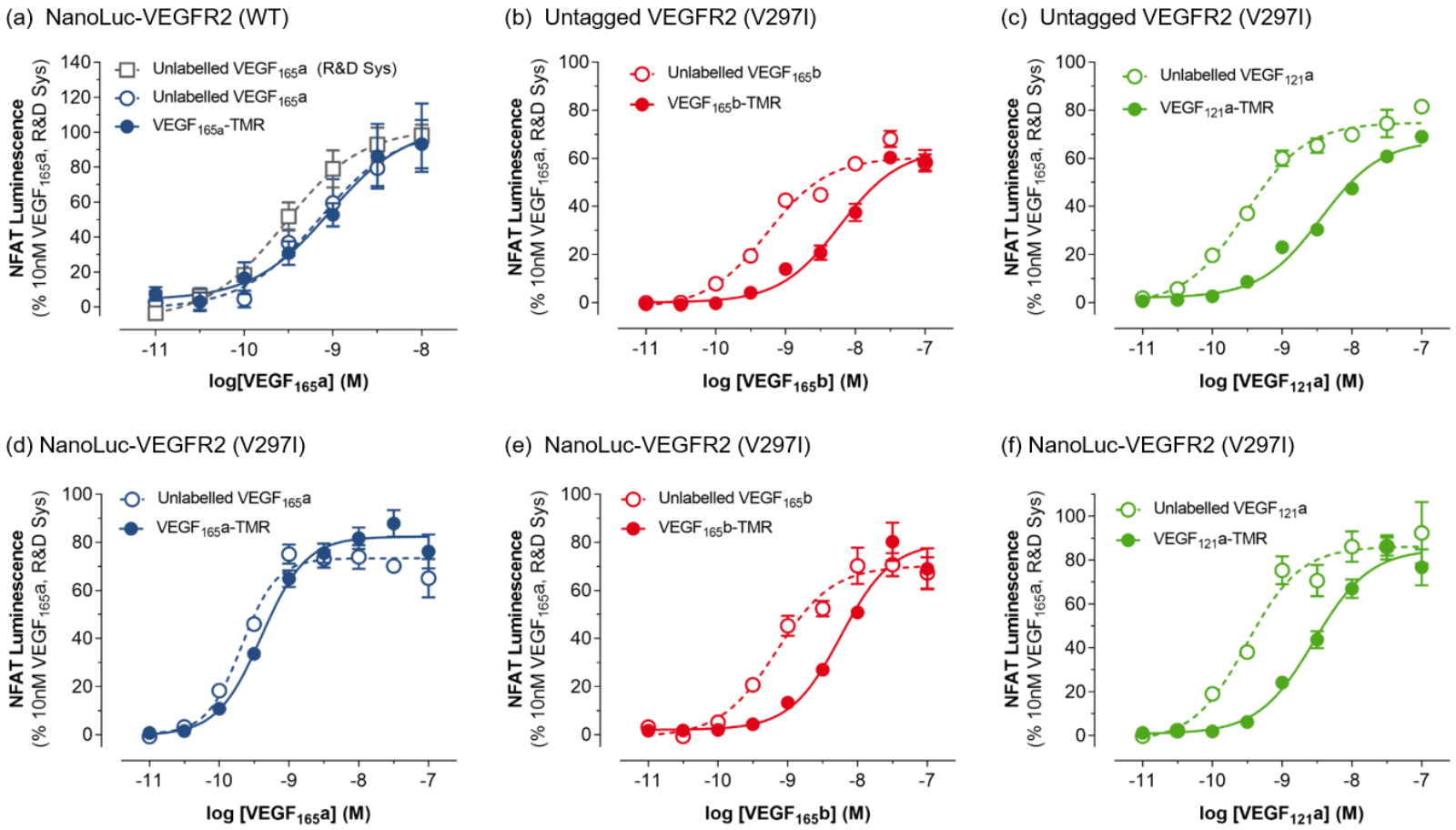


Figure 3.3 ***NFAT signalling in response to VEGF$_{xxx}$x-TMR relative to the unlabelled analogue****. See next page.*

Figure 3.3 Ctd. ***NFAT signalling in response to VEGF$_{xxx}$x-TMR relative to the unlabelled analogue****. HEK293T cells expressing NFAT-ReLuc2P were stimulated with increasing concentrations of unlabelled or TMR-labelled VEGF-A isoforms for 5 hours (37°C incubator with an atmosphere of 5% CO_2 and air). (a) Cells in a monolayer stably expressed NanoLuc-VEGFR2 (WT). These were stimulated with VEGF$_{165}$a-TMR or unlabelled VEGF$_{165}$a obtained either from a commercial source (R&D Systems) or purified in an identical manner (6 independent experiments, each with duplicate wells). (b-c) Suspension cells expressed untagged VEGFR2 with the natural polymorphism V297I, as in* Kilpatrick et al. (2017)*. Cells were stimulated with (b) VEGF$_{165}$b-TMR or (c) VEGF$_{121}$a-TMR, or their unlabelled counterpart prepared in an identical manner (5 independent experiments, duplicate wells). (d-f) Cells stably expressing NanoLuc-VEGFR2 V297I in a monolayer were stimulated with (d) VEGF$_{165}$a-TMR, (e) VEGF$_{165}$b-TMR or (f) VEGF$_{121}$a-TMR, or the unlabelled equivalent purified in an identical manner (5 independent experiments, duplicate wells). All data were normalised per experiment to mean vehicle (0%) or 10 nM unlabelled VEGF$_{165}$a (R&D Systems; 100%). Data are expressed as mean ± S.E.M. Derived potency (EC$_{50}$) and maximal response are shown in* Table 3.2*.*

Table 3.2 ***Summary of pharmacological parameters quantified from a concentration-response NFAT reporter gene assay****.*

Ligand	Potency (pEC_{50})		Maximum response (%)	
	Unlabelled	$VEGF_{xxx}$x-TMR	Unlabelled	$VEGF_{xxx}$x-TMR
NanoLuc-VEGFR2 (WT)				
$VEGF_{165}$a	9.44 ± 0.13 (R&D Systems)	9.24 ± 0.25	107.4 ± 2.9 (R&D Systems)	102.7 ± 21.7
	9.05 ± 0.18		109.1 ± 22.4	
NanoLuc-VEGFR2 (V297I)				
$VEGF_{165}$a	9.79 ± 0.05	9.42 ± 0.05	76.1 ± 4.0	85.5 ± 3.5
$VEGF_{165}$b	9.15 ± 0.11	8.12 ± 0.12 ****	71.9 ± 4.9	94.3 ± 14.1
$VEGF_{121}$a	9.52 ± 0.04	8.49 ± 0.10 ****	87.6 ± 7.9	89.7 ± 8.5
Untagged VEGFR2 (V297I)				
$VEGF_{165}$a	*10.14 ± 0.07*	*9.78 ± 0.07*	*100*	*100*
	9.72 ± 0.09			
$VEGF_{165}$b	9.25 ± 0.07	8.15 ± 0.11 ****	60.6 ± 1.8	66.6 ± 3.7
$VEGF_{121}$a	9.51 ± 0.06	8.45 ± 0.06 ****	75.2 ± 3.2	68.0 ± 1.7

Data represent mean ± S.E.M. from 5-6 independent experiments with duplicate wells. *Italicised values* were published in Kilpatrick et al. (2017), using the same cell line. Maximal responses were normalised per experiment to vehicle (0%) and 10 nM $VEGF_{165}$a from R&D Systems (100%). Unless stated that ligands were purchased from R&D Systems, unlabelled ligands were purified in an identical manner to $VEGF_{xxx}$x-TMR. Statistical analyses for pEC_{50} parameters were performed using a parametric ordinary one-way ANOVA (P<0.05) with post-Hoc Šidák's multiple comparisons comparing unlabelled and labelled isoforms ($^{\$\$\$\$}$ P<0.0001, n=5-6 per group). Statistical analyses for maximum responses, excluding the maximum response from Kilpatrick et al. (2017), were compared using a non-parametric Kruskal-Wallis test (P<0.05) with a post-Hoc Dunn's multiple comparisons test between unlabelled and labelled isoforms (not significant). As described in *Methods 2.10.2*, parametric tests were only performed on data corrected for the lognormal distribution (pEC_{50} = -log EC_{50}).

To investigate the endogenous expression of NRP1, VEGFR1 or VEGFR2 in HEK293T cells, immunofluorescent antibody labelling was used to image cells with confocal microscopy (*Methods 2.6.2*). We compared native HUVECs, un-transfected HEK293T cells and HEK293T cell lines expressing NanoLuc-tagged receptors. Non-specific antibody binding was determined using secondary antibody only in the absence of primary antibody (*Methods Table 2.5*). First, NRP1 expression was investigated using a polyclonal antibody labelled with donkey anti-rabbit AlexaFluor546 (*Figure 3.4*). In HUVECs, NRP1 expression was both membrane-associated and inside the cell. In contrast, wild type HEK293T cells had minimal immunostaining for NRP1 while stably expressing NanoLuc-NRP1 cell lines had positive staining in some cells. This reflects that not all HEK293T cells were successfully transfected with the receptor in a mixed population. Second, VEGFR1 expression was investigated using a monoclonal antibody against the extracellular domain and a secondary anti-mouse AlexaFluor488 antibody (*Figure 3.5*). There was no immunofluorescent labelling for VEGFR1 detected in HUVECs or wild type HEK293T cells. This was repeated in permeabilised HUVECs and wild type HEK293T cells using a separate polyclonal C-terminal antibody against VEGFR1 (Santa Cruz 316-G; a kind gift from Prof. David Bates). This polyclonal antibody was labelled with the same donkey anti-goat AlexaFluor546 secondary antibody as NRP1 studies. Likewise, there was no immunofluorescent signal detected compared to non-specific binding, despite using the highest gains possible on the LSM880 Confocal for both antibodies (data not shown). Third, VEGFR2 was labelled with a monoclonal antibody against the extracellular domain and secondary anti-mouse AlexaFluor488 antibody (*Figure 3.6*). This therefore used the same secondary antibody as VEGFR1 labelling. HUVECs showed high endogenous VEGFR2 expression with both intracellular and membrane localisation. A proportion of un-transfected HEK293T cells were positive for VEGFR2 (25.0 ± 3.8 % cells, from 34 images across 5 independent experiments). Staining was largely present in intracellular sites. Endogenous expression in HEK293T cells was also evident from cells overexpressing NanoLuc-NRP1 only. Compared to wild type HEK293T cells, there was increased VEGFR2 expression in those expressing NanoLuc-VEGFR2.

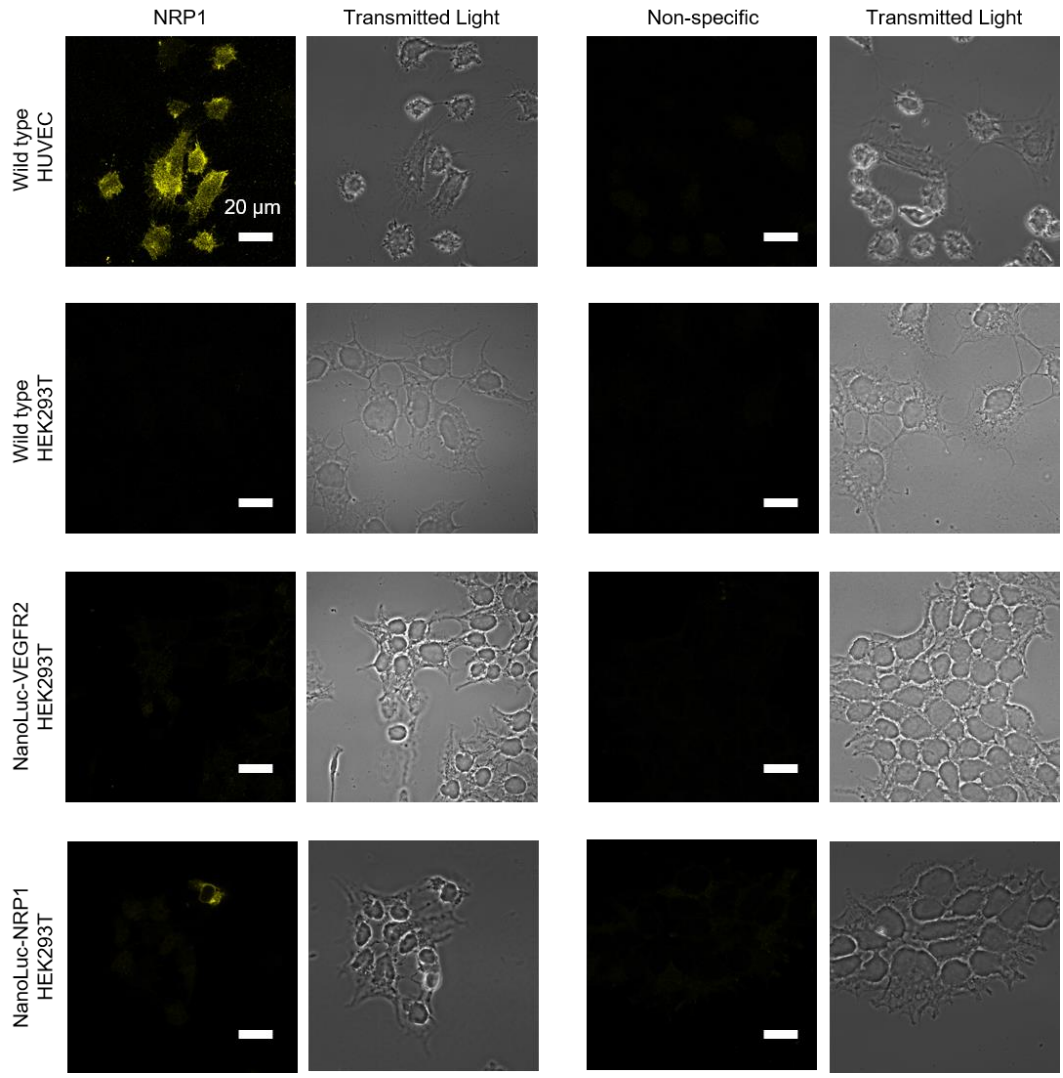


Figure 3.4 ***Immunofluorescent labelling of NRP1****. Cell lines were plated 24 hours prior on glass coverslips. Un-stimulated cells were fixed (3% PFA/PBS), blocked for non-specific binding and incubated overnight in the presence or absence of a polyclonal antibody against the C-terminus of NRP1 (Santa Cruz #7239). This was labelled with an AlexaFluor546-conjugated secondary antibody. Non-specific binding was determined by incubation with secondary antibody only (right panel). Images were obtained with the Zeiss LSM880 Confocal (63X magnification), using the DPSS 561 nm laser. Images are displayed alongside the corresponding transmitted light image. Images are representative of 3 independent experiments.*

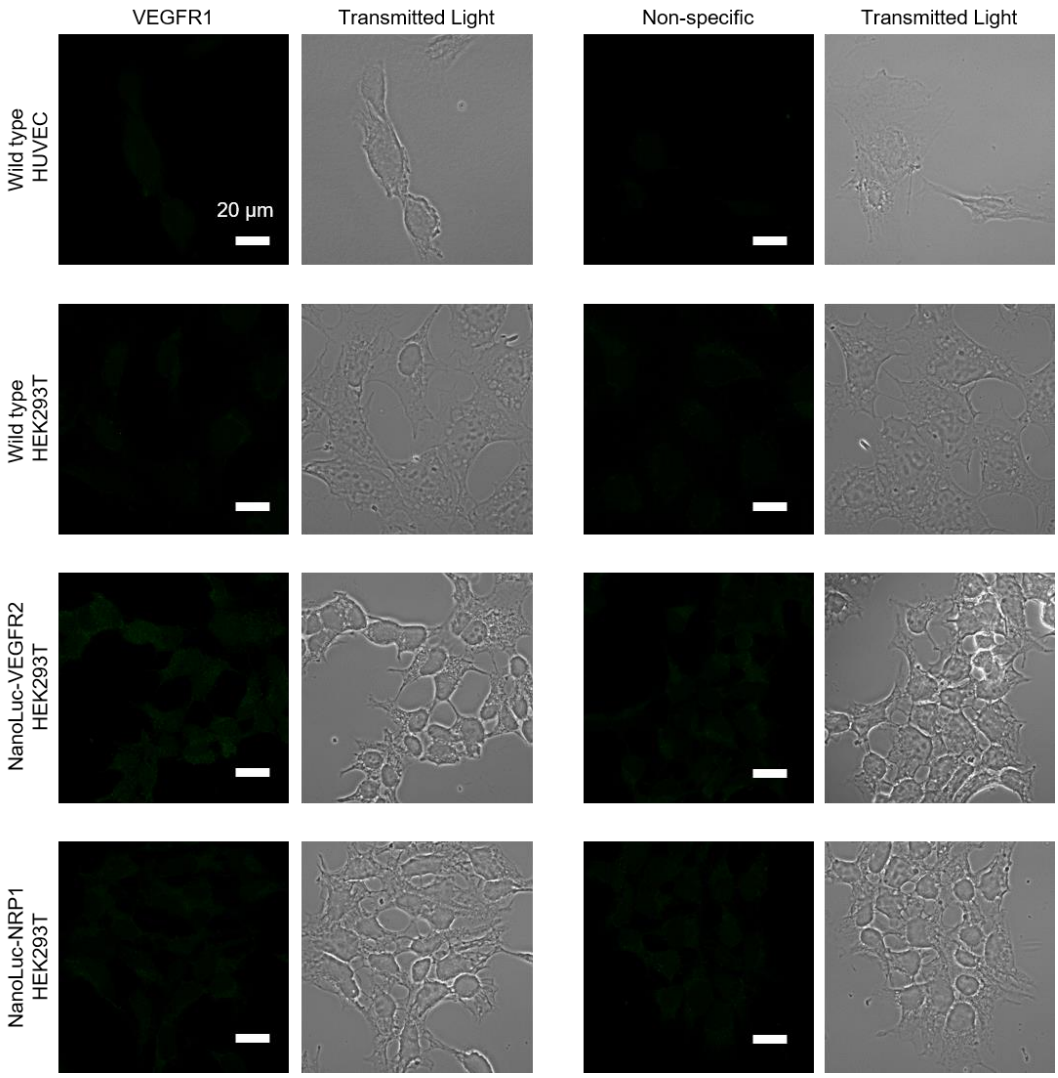


Figure 3.5 ***Lack of immunofluorescent labelling of VEGFR1****. HUVECs or HEK293T cell lines were plated on glass coverslips. Following 24 hours, cells were fixed (3% PFA/PBS) and blocked for non-specific binding. Cells were then incubated overnight in the presence or absence of a polyclonal antibody against the extracellular domain of VEGFR1 (Sigma V4762). This was labelled with a secondary antibody conjugated to AlexaFluor488, which was used in isolation to determine non-specific (right panel). Images were obtained by using the Zeiss LSM880 Confocal (63X magnification), on the same day as VEGFR2 immunolabelling in* Figure 3.6*. Images are representative of 3 independent experiments.*

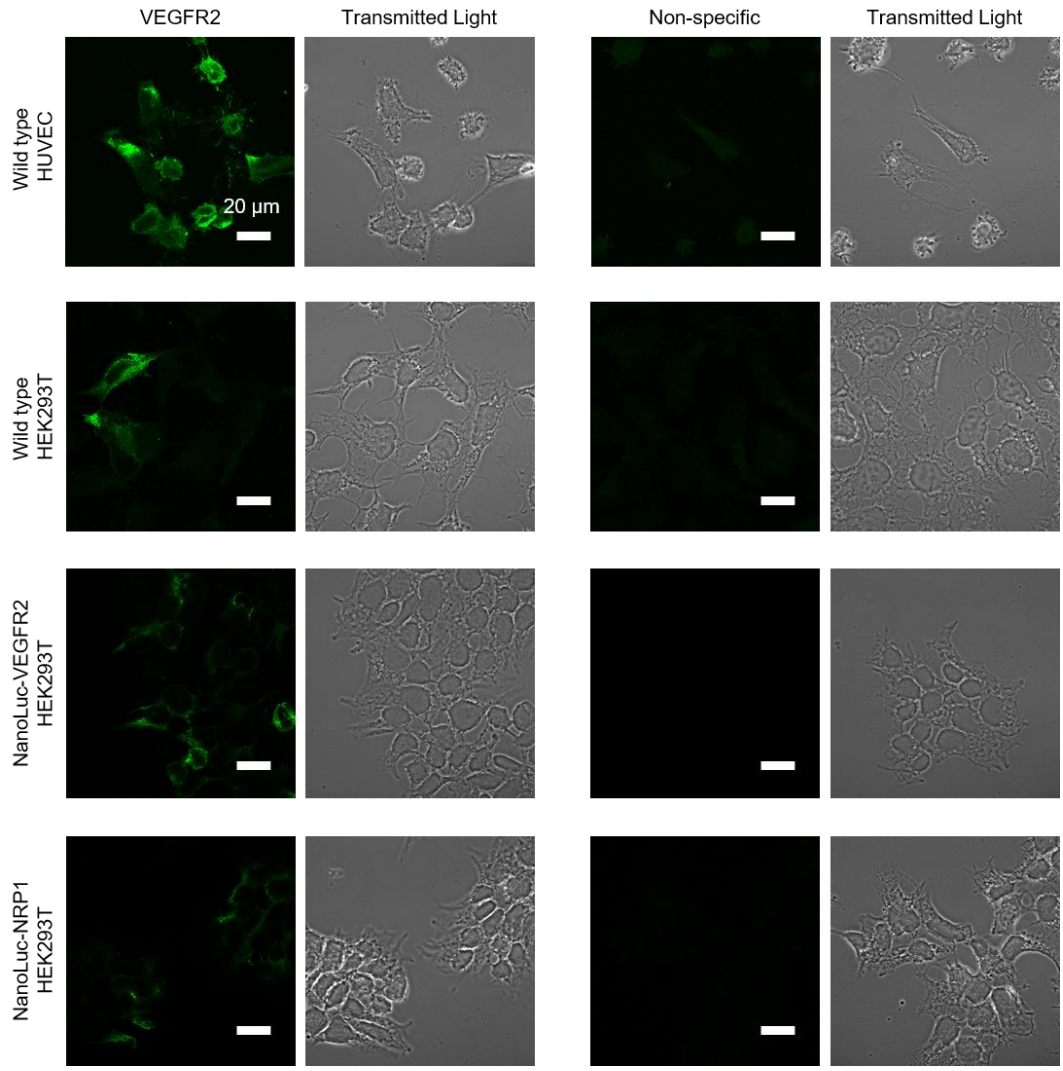


Figure 3.6 ***Immunofluorescent labelling of VEGFR2****. HUVECs, wild type HEK293T cells or stable cell lines were plated on glass coverslips 24 hours prior to experimentation. Cells were fixed (3% PFA/PBS), blocked for non-specific binding then incubated overnight in with an antibody raised against for the extracellular domain of VEGFR2 (Sigma-Aldrich V9134). This was labelled with an AlexaFluor488-conjugated secondary antibody. Non-specific antibody binding was determined using secondary antibody only (right panel). Images were obtained by Zeiss LSM880 Confocal (63X magnification) using a 488 nm laser. Transmitted light images are displayed alongside. Images are representative of 5 independent experiments.*

We then investigated whether endogenous VEGFR2 expression compromised the use of HEK293T cells in subsequent studies. First, un-transfected HEK293T cells were incubated with 10 nM $VEGF_{165}$a-TMR, $VEGF_{165}$b-TMR and $VEGF_{121}$a-TMR for 60 minutes at 37°C (*Methods 2.7.3*). These compared the localisation of fluorescent VEGF-A variants to HEK293T cells stably expressing HaloTag-VEGFR2. There was minimal fluorescence detected upon incubation of un-transfected HEK293T cells with fluorescent VEGF-A isoforms (*Figure 3.7a*). This was quantified using a granularity analysis algorithm (*Figure 3.7b*), showing a clear distinction in the ability of fluorescent VEGF-A to localise with cells expressing HaloTag-VEGFR2. This also confirmed that fluorescent VEGF-A isoforms did not have non-specific interactions with the phospholipid bilayer in un-transfected HEK293T cells. Second, we investigated whether the NFAT reporter gene assay would detect signalling from endogenous VEGFR2 (*Figure 3.7d*). HEK293T cells expressed *ReLuc2P* in the absence or presence of HaloTag-VEGFR2 (*Methods 2.7.1*). Cells overexpressing HaloTag-VEGFR2 had a concentration-dependent increase in NFAT luminescence in response to commercially available $VEGF_{165}$a (pEC_{50} = 9.92 ± 0.12, n=5). In comparison, there was no signalling response to increasing concentrations of $VEGF_{165}$a in un-transfected HEK293T-ReLuc2P cells.

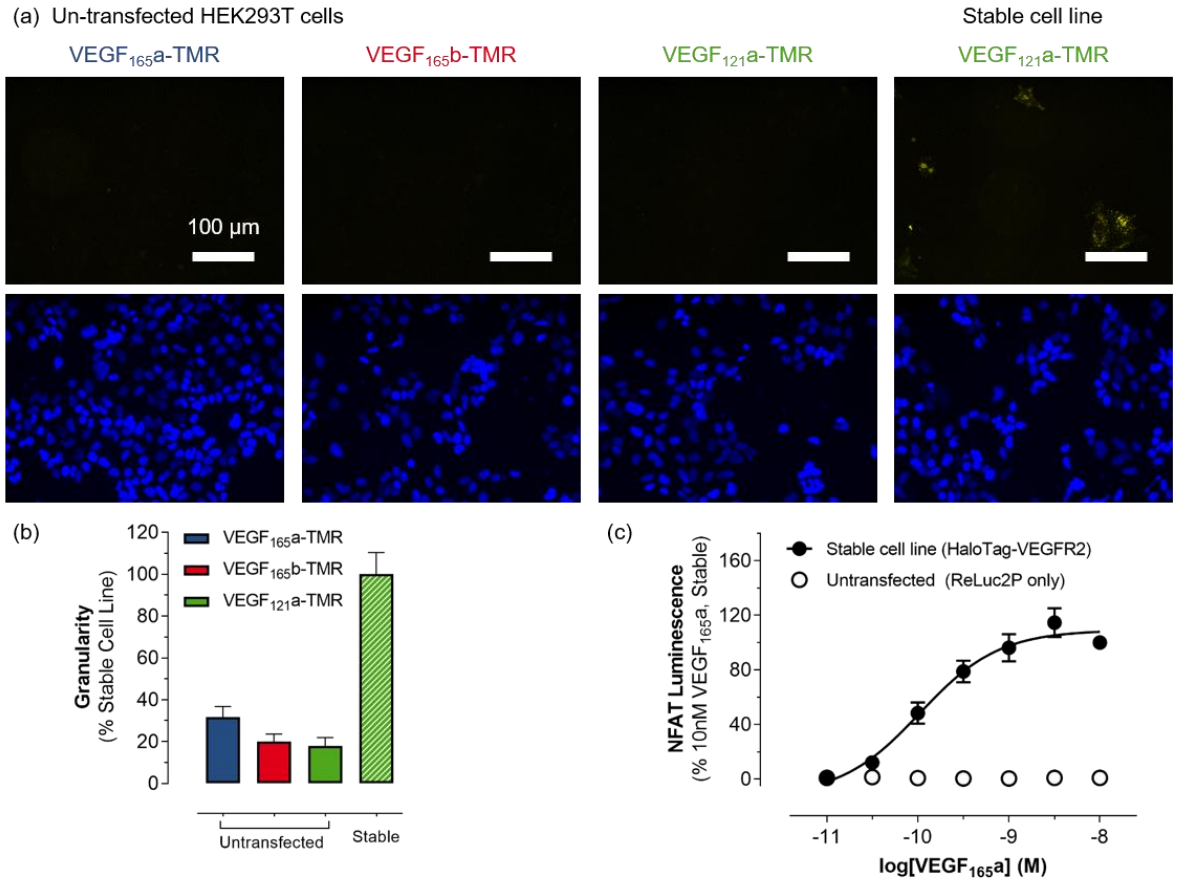


Figure 3.7 ***Functional characterisation of endogenous VEGFR2 expression in HEK293T cells.*** *See next page.*

Figure 3.7 Ctd. (a) Un-transfected HEK293T cells or HEK293T cells stably expressing HaloTag-VEGFR2 were seeded in 96-well plates. Following 24 hours, cells were incubated with 10 nM fluorescent $VEGF_{xxx}$x-TMR (60 minutes, 37°C/5% CO_2). Cells were fixed (3% PFA/PBS), nuclei were stained (2 mg/ml H33342) and cells were imaged with an IX Micro widefield platereader (20X objective). (b) Images were analysed using a granularity algorithm (Molecular Devices, Methods Figure 2.9b*). Fluorescent granules (2-15 µm diameter) and nuclei (5-25 µm diameter) were quantified by size. Granules were assigned to nuclei based upon proximity using the segmented image and quantified on a per cell basis. Data were normalised to mean vehicle (0%) or $VEGF_{121}$a-TMR stimulation in HaloTag-VEGFR2 cells (100%) per experiment. Data are shown as mean ± S.E.M. from 5 independent experiments with duplicate wells imaged at 4 sites per well. (c) HEK293T cells expressed ReLuc2P in the absence or presence of HaloTag-VEGFR2. Following 24 hours, cells were serum starved. The following day, NFAT luciferase production was monitored in response to 5 hour stimulation with increasing concentrations of $VEGF_{165}$a. Data were normalised per experiment to vehicle (0%) or 10 nM $VEGF_{165}$a at HaloTag-VEGFR2 (100%). Data are shown as mean ± S.E.M. from 5 independent experiments with duplicate wells.*

To gain insight into whether transfected receptors used in subsequent studies were markedly overexpressed in HEK293T cells, we compared the expression between native levels in HEK293T and HUVECs using immunofluorescent antibody labelling (*Figure 3.8, Figure 3.9*). Labelling cells in a 96-well plate format for high-content imaging enabled an unbiased algorithm to quantify relative fluorescence intensity above background on a per cell basis (*Methods 2.6.2*). Despite prior VEGFR2-positive immunolabelling in HEK293T cells, there was lower fluorescence intensity per cell in wild type HEK293T cells compared to native HUVECs (*Figure 3.8*). There was increased fluorescence in stable cell lines expressing NanoLuc-VEGFR2 and HaloTag-VEGFR2 compared to wild type HEK293T cells, however this was lower than native HUVECs (*Figure 3.8b*). We also quantified the relative expression of NRP1. There was higher fluorescence per cell in HEK293T cell lines expressing NanoLuc-NRP1 or HaloTag-NRP1 compared to un-transfected HEK293T cells (*Figure 3.9*). These data also suggested that the expression levels of the tagged NRP1 variants were low and below the native expression level of NRP1 in HUVECs.

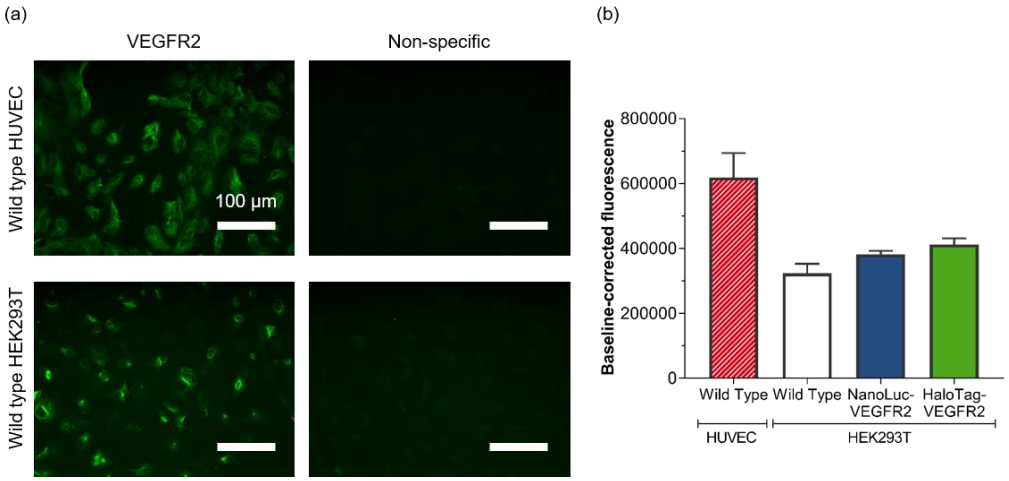


Figure 3.8 ***Quantifying relative VEGFR2 expression in cell lines****.*

(a) HUVECs or HEK293T cells were seeded in black 96-well plates. Following 24 hours, cells were fixed (3% PFA/PBS), blocked for non-specific binding and incubated overnight with a monoclonal antibody against VEGFR2 (as in Figure 3.6*). This was labelled with an AlexaFluor488 secondary (left panel), for which non-specific binding was determined the absence of primary antibody (right panel). Cells were washed in PBS, nuclei stained with H33342 and stored in PBS (4°C). Plates were imaged using the IX Micro widefield platereader (20X objective) with a FITC filter (500 ms exposure time) and a DAPI filter imaging nuclei (25 ms exposure time). Images are shown for HUVECs and wild type HEK293T cells, but this was also performed for HEK293T cells stably expressing NanoLuc-VEGFR2 or HaloTag-VEGFR2 for quantitative analysis. (b) Fluorescence intensity was quantified from images in* (a) *using a multi-wavelength cell scoring algorithm to quantify the fluorescence intensity over background (*Methods Figure 2.9c*). FITC channel signals were defined as intensity over 200 grey levels. The integrated intensity per cell was baseline-corrected per experiment to non-specific fluorescence (secondary antibody only). Data are shown as mean ± S.E.M. from 5 independent experiments with duplicate wells imaged at 4 sites per well.*

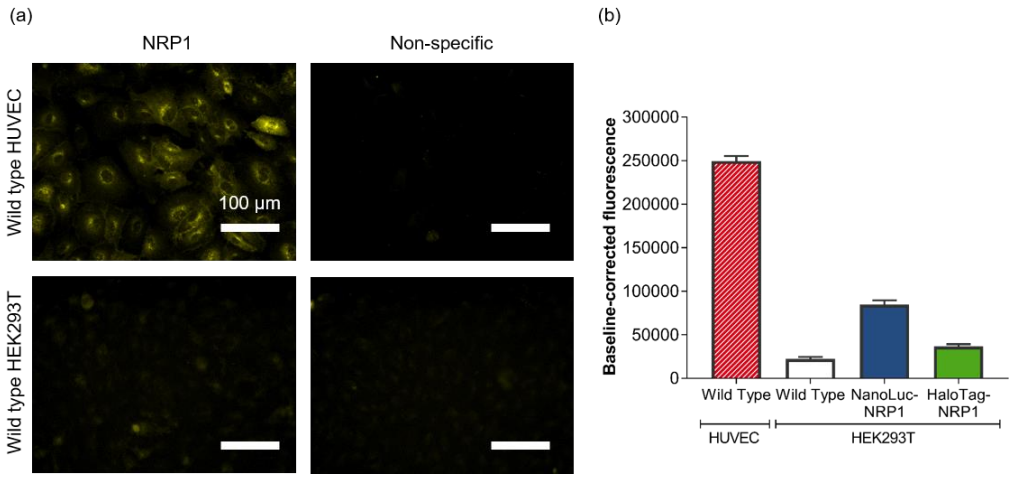


Figure 3.9 ***Relative NRP1 expression in cell lines****. (a) HUVECs or wild type HEK293T cells were seeded in black 96-well plates 24 hours prior to experiments. Cells were then fixed (3% PFA/PBS), blocked for non-specific binding and incubated overnight with a polyclonal antibody for NRP1 (as in* Figure 3.4*). This was labelled with an AlexaFluor546 secondary antibody (left panel), for which non-specific binding was determined for each cell line in the absence of primary antibody (right panel). Cells were washed in PBS, nuclei labelled with H33342 and stored in PBS (4°C). Plates were imaged using the IX Micro widefield platereader (20X objective) with a TRITC filter (500ms exposure time) and a DAPI filter imaging nuclei (25ms exposure time). Representative images are shown for HUVECs and wild type HEK293T cells, but this was also performed with HEK293T cells expressing NanoLuc-NRP1 or HaloTag-NRP1 for quantification. (b) Fluorescence intensity was quantified from high-content images in* (a) *using a multi-wavelength cell scoring algorithm to quantify the fluorescence intensity over background (*Methods Figure 2.9c*). TRITC channel signals were defined as intensity over 50 grey levels due to a lower signal for NRP1 immunofluorescent labelling than for VEGFR2. The integrated intensity per cell was baseline-corrected per experiment to non-specific fluorescence (secondary antibody only). Data are shown as mean ± S.E.M. from 5 independent experiments with duplicate wells imaged at 4 sites per well.*

Finally, we characterised whether tagging the receptors themselves would compromise receptor signalling. We used the reporter gene NFAT assay in HEK293T-ReLuc2P cells expressing VEGFR2 tagged at the N-terminus with NanoLuc or HaloTag. This monitored downstream signalling in response to $VEGF_{165}a$ stimulation. Each cell line had a concentration-dependent increase in NFAT luminescence in response to increasing concentrations of $VEGF_{165}a$ (*Figure 3.10*). $VEGF_{165}a$ had similar potencies in cells expressing HaloTag- and NanoLuc-tagged VEGFR2 (HaloTag-VEGFR2 pEC_{50} = 9.96 ± 0.10; NanoLuc-VEGFR2 pEC_{50} = 9.49 ± 0.06; n=5 per group). These were comparable to those obtained at wild type VEGFR2 in response to $VEGF_{165}a$ ($VEGF_{165}a$ pEC_{50} 10.14 ± 0.06, n=4).

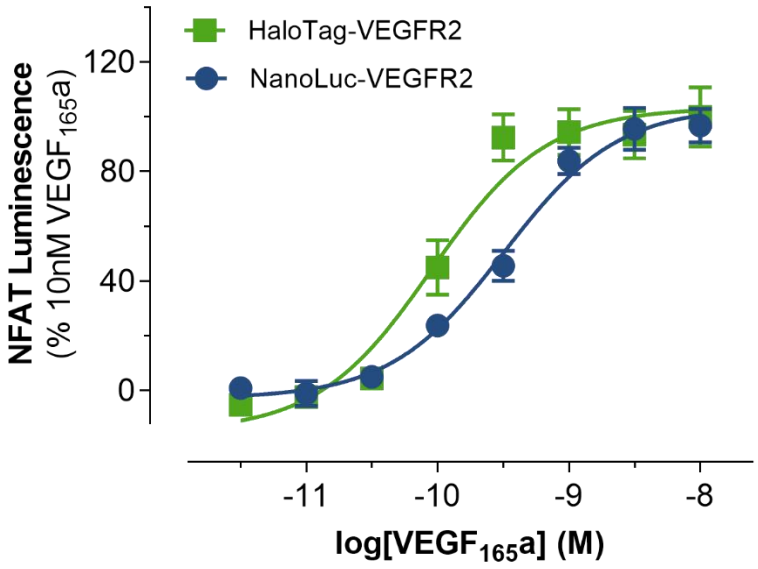


Figure 3.10 ***Receptor tags had minimal effects on downstream VEGFR2 signalling****. HEK293T cells stably expressing HaloTag-VEGFR2 or NanoLuc-VEGFR2, as well as ReLuc2P, were serum-starved 24 hours prior to experimentation. Cells were stimulated with increasing concentrations of commercially available $VEGF_{165}a$ (5 hours, 37°C/5% CO_2). Data were normalised as a percentage of vehicle (0%) or 10 nM $VEGF_{165}a$ (100%) in each individual experiment. Data are expressed as mean ± S.E.M. (5 independent experiments, duplicate wells).*

High affinity binding of $VEGF_{165}$a-TMR, $VEGF_{165}$b-TMR, and $VEGF_{121}$a-TMR to VEGFR2

Live cell imaging studies were performed to visualise the localisation of fluorescent VEGF-A isoforms with HaloTag-labelled VEGFR2 expressed in isolation in HEK293T cells (*Methods 2.6.1*). HaloTag® technologies can tag receptors with interchangeable fluorophores that have optimal properties for the experimental setup (Los et al., 2008). Receptors were labelled with membrane-impermeant HaloTag-AlexaFluor488 substrate (*Figure 3.11*). Thus, only receptors successfully exported to the plasma membrane were labelled with a fluorophore. Under basal conditions, VEGFR2 was located on both the cell membrane and within intracellular sites. Due to the HaloTag labelling approach, this was indicative of constitutive internalisation. Following 60 minute stimulation with 10 nM $VEGF_{165}$a-TMR, $VEGF_{165}$b-TMR or $VEGF_{121}$a-TMR, both receptor and ligand was localised in the same regions at both the cell membrane and intracellular sites. This is displayed as white regions in the overlay images (*Figure 3.11*).

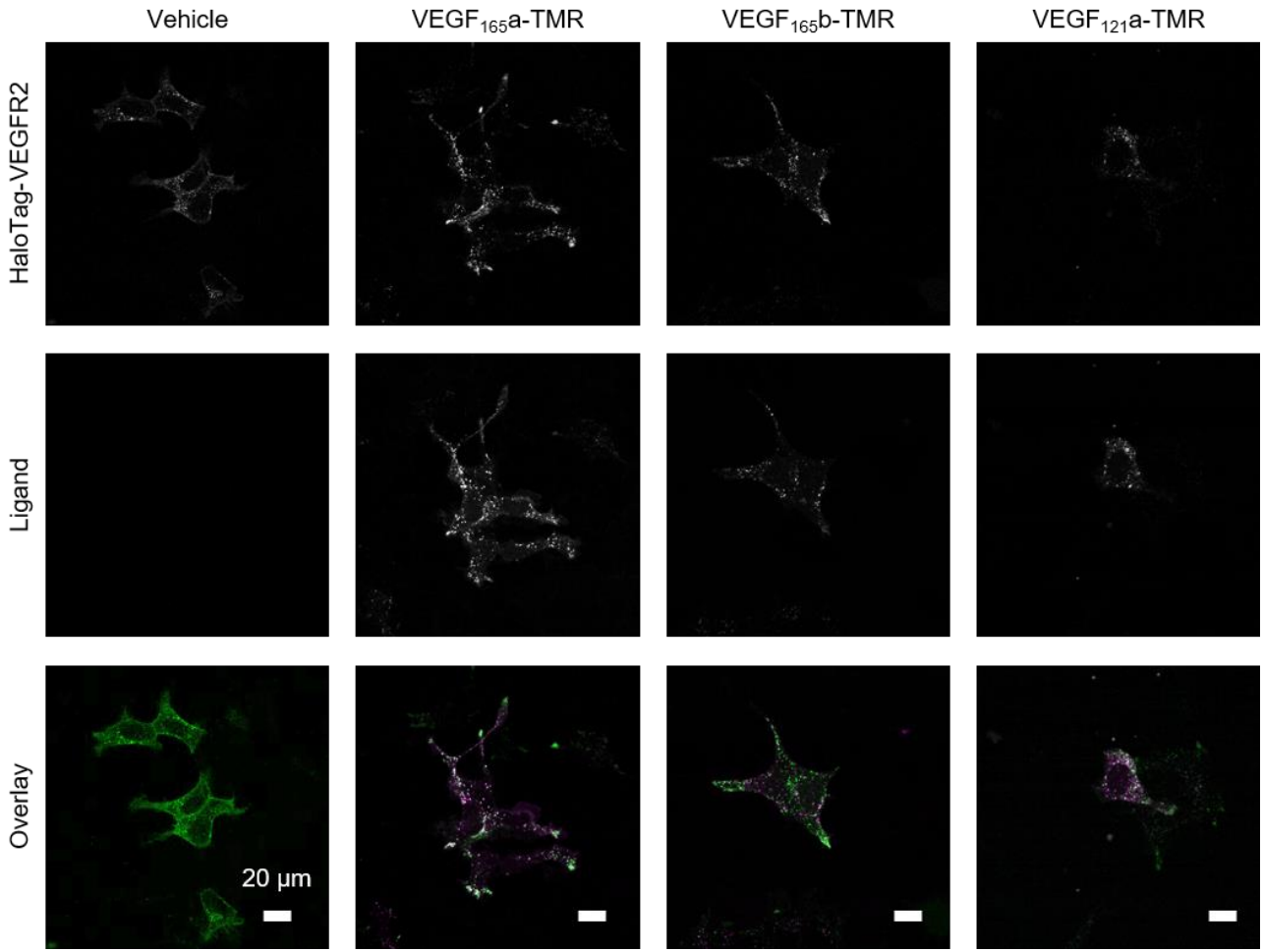


Figure 3.11 ***Imaging fluorescent VEGF-A isoforms at HaloTag-VEGFR2.*** *HEK293T-ReLuc2P cells stably expressing HaloTag-VEGFR2 were serum starved 24 hours prior. On the day of the assay, receptors were labelled with membrane-impermeant HaloTag-AlexaFluor488 substrate (0.5 µM) for 30 minutes (37°C). Cells were washed in serum-free DMEM then replaced with HBSS/0.1% BSA. Cells were stimulated with vehicle or ligand (10 nM $VEGF_{165}$a-TMR, $VEGF_{165}$b-TMR or $VEGF_{121}$a-TMR) for 1 hour at 37°C. Cells were imaged live using a Zeiss LSM710 Confocal Microscope (40X objective). The overlay shows HaloTag-VEGFR2 (green) and ligand (magenta). Images are representative of those obtained in 3 independent experiments.*

BRET was used to quantify the binding of fluorescent VEGF-A isoforms to NanoLuc-tagged VEGFR2 expressed in living HEK293T cells (*Figure 3.12a; Methods 2.8*). This assay relies on the close proximity required for RET between a bioluminescent donor and a fluorescent acceptor (<10 nm, *Appendix 7.5*). Here, BRET occurred between the N-terminal NanoLuc-tagged receptor to the fluorophore of receptor-bound VEGF-TMR (*Figure 3.12a*). Emissions were simultaneously measured from NanoLuc (450-480 nm) and TMR (550 long pass, unless stated otherwise) using the PHERAstar FS platereader. Calculated BRET ratios are considered proportional to fluorescent ligand binding. There was saturable total binding of $VEGF_{165}$a-TMR, $VEGF_{165}$b-TMR and $VEGF_{121}$a-TMR to NanoLuc-VEGFR2 following incubation for 60 minutes (*Figure 3.12b-d*). There was low, linear non-specific binding as the BRET signal was largely prevented in the presence of 100 nM unlabelled competitor (*Figure 3.12b-d*). Derived equilibrium dissociation binding constants revealed that each isoform bound with nanomolar affinity (*Table 3.3*; $VEGF_{165}$a-TMR K_d = 2.03 ± 0.51 nM; $VEGF_{165}$b-TMR K_d = 9.53 ± 1.36 nM; $VEGF_{121}$a-TMR K_d = 5.54 ± 1.34 nM; n=5 for each isoform). The rank order of fluorescent VEGF-A isoform affinities at NanoLuc-VEGFR2 was $VEGF_{165}$a-TMR > $VEGF_{121}$a-TMR > $VEGF_{165}$b-TMR. These affinities were compared using a parametric one-way ANOVA between fluorescent VEGF-A isoforms as these were converted to a negative logarithm for comparisons (pK_d = -log K_d). This transformation allows for the assumption of a Gaussian distribution. Novel fluorescent VEGF-A isoforms had a significantly lower affinity than $VEGF_{165}$a-TMR (*Table 3.3*; one-way ANOVA $P<0.05$; post-Hoc Tukey's multiple comparisons test, $VEGF_{165}$a-TMR vs. $VEGF_{165}$b-TMR $P<0.001$; $VEGF_{165}$a-TMR vs. $VEGF_{121}$a-TMR $P<0.01$; $VEGF_{165}$b-TMR vs. $VEGF_{121}$a-TMR $P>0.05$; n=5 per group).

To estimate the affinity of a panel of unlabelled VEGF-A isoforms, we used $VEGF_{165}$a-TMR, $VEGF_{165}$b-TMR and $VEGF_{121}$a-TMR as three distinct fluorescent probes (*Figure 3.13*). Increasing concentrations of unlabelled VEGF-A, such as $VEGF_{165}$a or VEGF-Ax, were used to inhibit the binding of multiple concentrations of fluorescent ligand to NanoLuc-VEGFR2 (0.25-3 nM). These data were used to derive pK_i values assuming law of mass action interactions (*Table 3.4*). Binding affinities were derived from similar studies with a comprehensive panel of unlabelled VEGF-A isoforms at NanoLuc-VEGFR2 (*Table 3.4*). pK_i values obtained for each competing ligand were not significantly different between the fluorescent VEGF-A probe used (one-way ANOVA, $P>0.05$, n=5 per group). There was a significant difference between pK_i values obtained for each unlabelled VEGF-A isoform (one-way ANOVA, $P<0.05$, n=5 per group). Compared to prototypical $VEGF_{165}$a, the pK_i values for $VEGF_{145}$a and $VEGF_{189}$a had a significantly lower affinity when comparing data from each fluorescent VEGF-A probe (Dunnett's multiple comparisons test, $VEGF_{165}$a vs. $VEGF_{145}$a $P<0.001$, $VEGF_{165}$a vs. $VEGF_{189}$a $P<0.01$). All other isoform comparisons had no significant difference to $VEGF_{165}$a (*Table 3.4*; $P>0.05$).

Fluorescent VEGF-TMR probes were also used to investigate whether other VEGF proteins were able to compete for binding at NanoLuc-VEGFR2. Encoded by separate genes, these included commercially available VEGF-B (Chromosome *11q13*) and VEGF-C (Chromosome *4q34*). Following incubation for 60 minutes, 30 nM VEGF-B was unable to displace any fluorescent VEGF-A isoform from NanoLuc-VEGFR2 (3 nM) (*Figure 3.14a*). VEGF-C largely displaced $VEGF_{165}$b-TMR and $VEGF_{121}$a-TMR from NanoLuc-VEGFR2 (*Figure 3.14b-c*). Despite this incomplete displacement of fluorescent VEGF-A by 30 nM VEGF-C, binding affinities were estimated for VEGF-C ($VEGF_{165}$b-TMR $pK_i = 7.65 \pm 0.12$; $VEGF_{121}$a-TMR $pK_i = 8.01 \pm 0.15$; n=5 per group)

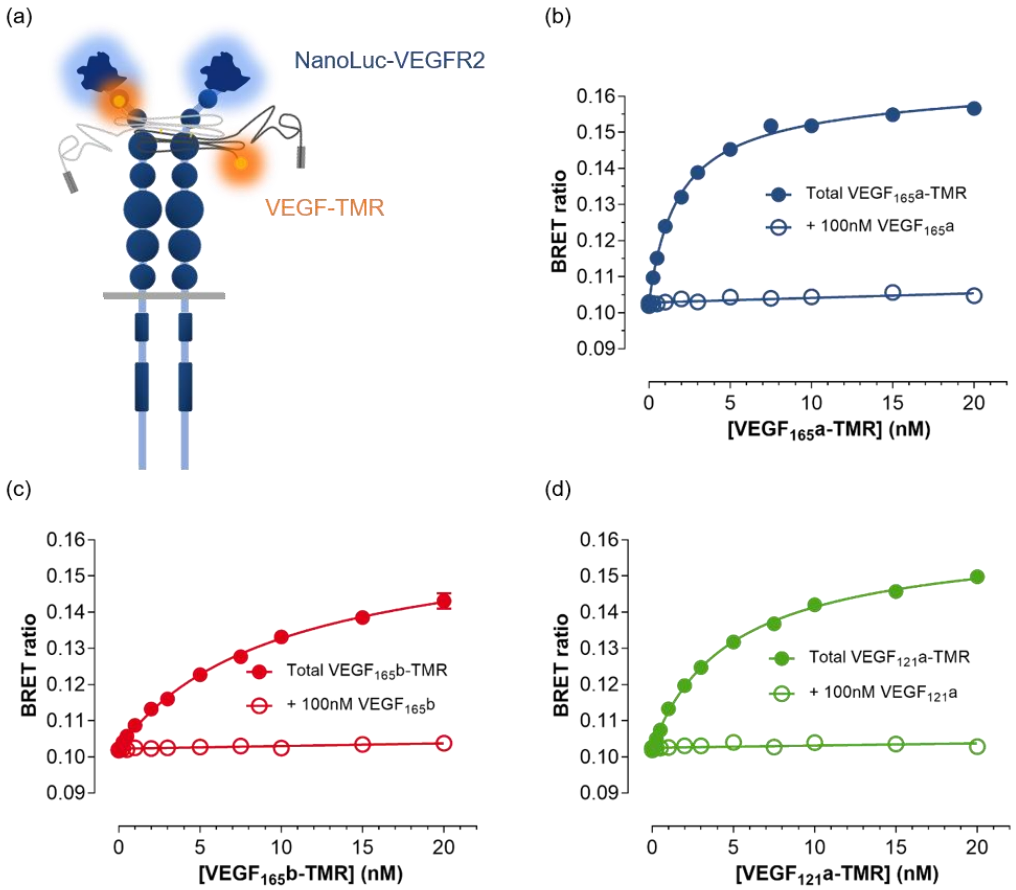


Figure 3.12 ***Monitoring binding of novel fluorescent VEGF-A isoforms to NanoLuc-VEGFR2 expressed in HEK293T cells using BRET.***

(a) HEK293T-ReLuc2P cells stably expressed N-terminal NanoLuc-VEGFR2. Upon addition of the NanoLuc substrate furimazine, emitted luminescence acts as a BRET donor to VEGF-TMR interacting with its orthosteric site at Ig-like D2 and D3. This excites the TMR fluorophore as a BRET acceptor, leads to fluorescence emissions. (b-d) Cells were incubated with increasing concentrations of (b) VEGF$_{165}$a-TMR, (c) VEGF$_{165}$b-TMR or (d) VEGF$_{121}$a-TMR. This was performed in the absence or presence of 100 nM of its unlabelled counterpart. This was added simultaneously to define non-specific binding. Following 60 minutes at 37°C, 10 µM furimazine was added for 5 minutes. Emissions were measured on the PHERAstar platereader (NanoLuc emissions at 450-480nm; TMR emissions above 550 nm). BRET ratios are expressed as mean ± S.E.M. from 5 independent experiments with duplicate wells. Where not shown, error bars are within the size of the symbol. Derived affinities of fluorescent VEGF-A isoforms (K_d) are in Table 3.3.

Table 3.3 ***Summary of binding affinities (K_d) or kinetic parameters of fluorescent VEGF-A isoforms at NanoLuc-VEGFR2****.*

Fluorescent ligand	Saturation assays		Kinetic assays			
	K_d (nM)	pK_d	K_d (nM)	pK_d	k_{on} ($min^{-1}M^{-1}$)	k_{off} (min^{-1})
$VEGF_{165}$a-TMR	2.03 ± 0.51	8.75 ± 0.25	6.64 ± 4.37	8.47 ± 0.23	$1.54x10^7 \pm 0.38x10^7$	0.055 ± 0.017
$VEGF_{165}$b-TMR	9.53 ± 1.36	8.04 ± 0.06 $^{\$\$\$}$	11.3 ± 3.54	8.07 ± 0.18	$7.29x10^6 \pm 1.84x10^6$	0.060 ± 0.011
$VEGF_{121}$a-TMR	5.54 ± 1.34	8.30 ± 0.08 $^{\$\$}$	5.75 ± 0.46	8.24 ± 0.03	$8.51x10^6 \pm 0.81x10^6$	0.048 ± 0.002

Data are expressed as mean ± S.E.M. from 5 independent experiments with duplicate wells. Equilibrium binding parameters were first derived from saturation experiments (*Figure 3.12*). Equilibrium association rate constants (k_{on}) and dissociation rate constants (k_{off}) were also used to estimate the K_d from each kinetic experiment (*Figure 3.16*; $K_d = k_{off}/k_{on}$). pK_d values, the negative log of the K_d, were compared using a one-way ANOVA and a Tukey's multiple comparisons test ($^{\$\$}$ $P<0.01$, $^{\$\$\$}$ $P<0.001$). k_{on} and k_{off} parameters were compared using a Kruskal-Wallis test (not significant).

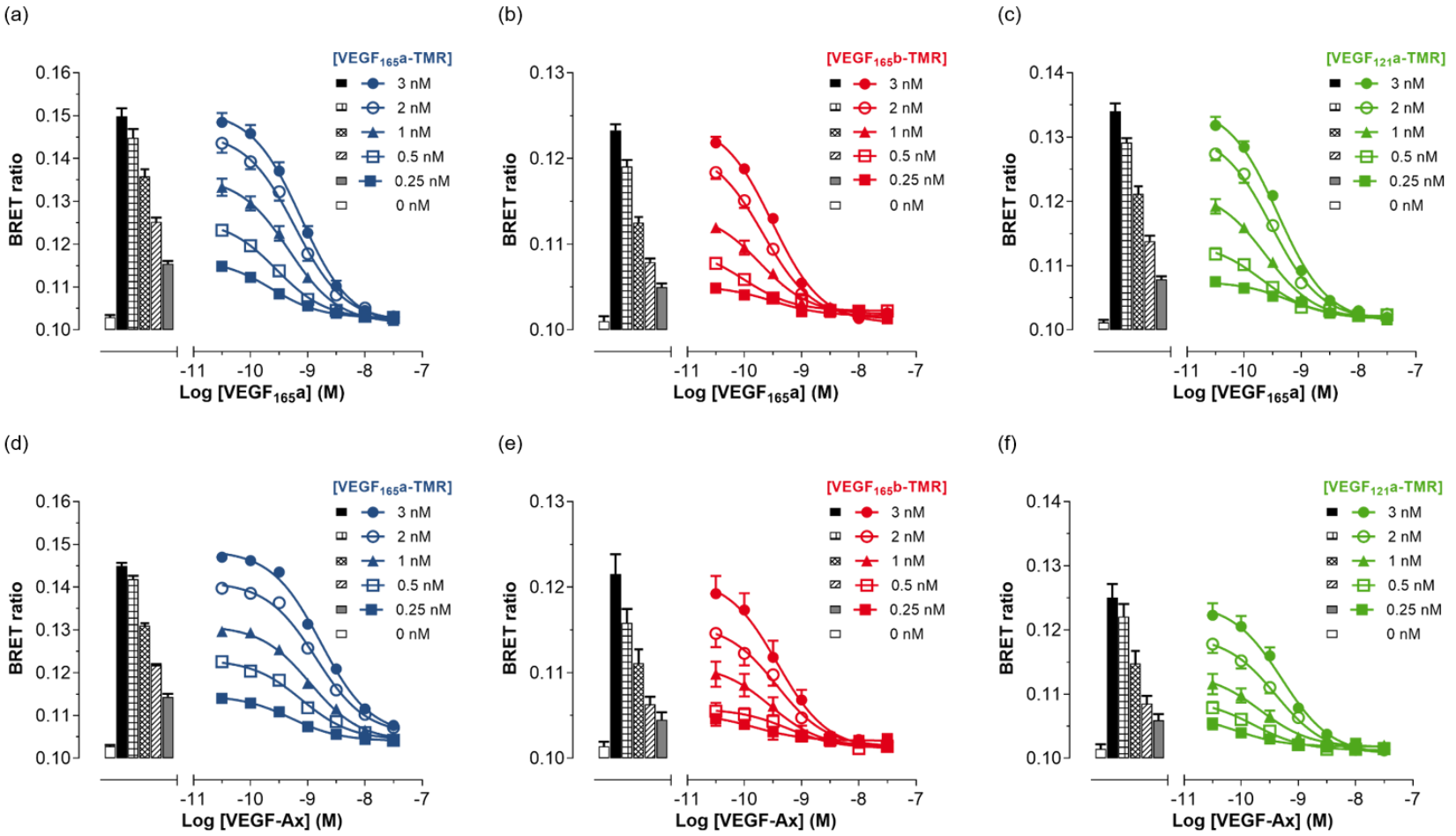


Figure 3.13 ***Displacement of fluorescent VEGF-A probes by unlabelled VEGF$_{165}$a or VEGF-Ax NanoLuc-VEGFR2.*** *See next page.*

Figure 3.13 Ctd. HEK293T-ReLuc2P cells stably expressed NanoLuc-VEGFR2. Cells were incubated with increasing concentrations of unlabelled (a-c) $VEGF_{165}$a or (d-f) VEGF-Ax. These were added simultaneously to 5 separate fixed concentrations of (a,d) $VEGF_{165}$a-TMR, (b,e) $VEGF_{165}$b-TMR or (c,f) $VEGF_{121}$a-TMR. Cells were incubated for 60 minutes at 37°C in the dark. Bars represent vehicle only (white bars) or incubation with fluorescent $VEGF_{xxx}$x-TMR alone (filled bars). Raw BRET ratios are shown as mean ± S.E.M. from 5 independent experiments, each with duplicate wells. Derived affinities of competing unlabelled VEGF-A isoforms (pK_i) are shown in Table 3.4.

Table 3.4 ***Binding affinities (pK_i) of unlabelled VEGF-A isoforms determined from inhibition of $VEGF_{165}$a-TMR, $VEGF_{165}$b-TMR or $VEGF_{121}$a-TMR binding to NanoLuc-VEGFR2****.*

Unlabelled VEGF-A isoform	Fluorescent VEGF-A probe		
	$VEGF_{165}$a-TMR	$VEGF_{165}$b-TMR	$VEGF_{121}$a-TMR
$VEGF_{165}$a	9.57 ± 0.04	9.73 ± 0.09	9.54 ± 0.05
$VEGF_{165}$b (NS)	9.07 ± 0.02	9.61 ± 0.06	9.28 ± 0.10
$VEGF_{121}$a (NS)	9.30 ± 0.06	9.58 ± 0.18	9.31 ± 0.08
$VEGF_{145}$a ($^{\$\$\$}$)	8.83 ± 0.03	8.92 ± 0.08	8.82 ± 0.08
$VEGF_{189}$a ($^{\$\$}$)	9.13 ± 0.03	8.92 ± 0.03	9.06 ± 0.09
$VEGF_{111}$a (NS)	9.66 ± 0.13	9.89 ± 0.15	9.98 ± 0.05
VEGF-Ax (NS)	9.20 ± 0.02	9.57 ± 0.03	9.65 ± 0.06

Data are expressed as mean ± S.E.M. from 5 independent experiments with duplicate wells. Competition experiments were fit to a non-linear regression for each concentration of fluorescent probe, as shown for $VEGF_{165}$a and VEGF-Ax in *Figure 3.13*. Using equations described in *Methods 2.10.5*, competition curves were used to determine the pK_i for each unlabelled VEGF-A isoform. Statistical analyses between unlabelled VEGF-A isoforms were performed using a one-way ANOVA, with post-Hoc Dunnett's multiple comparisons relative to $VEGF_{165}$a (NS Not significant, $^{\$\$}$ $P<0.01$; $^{\$\$\$}$ $P<0.001$).

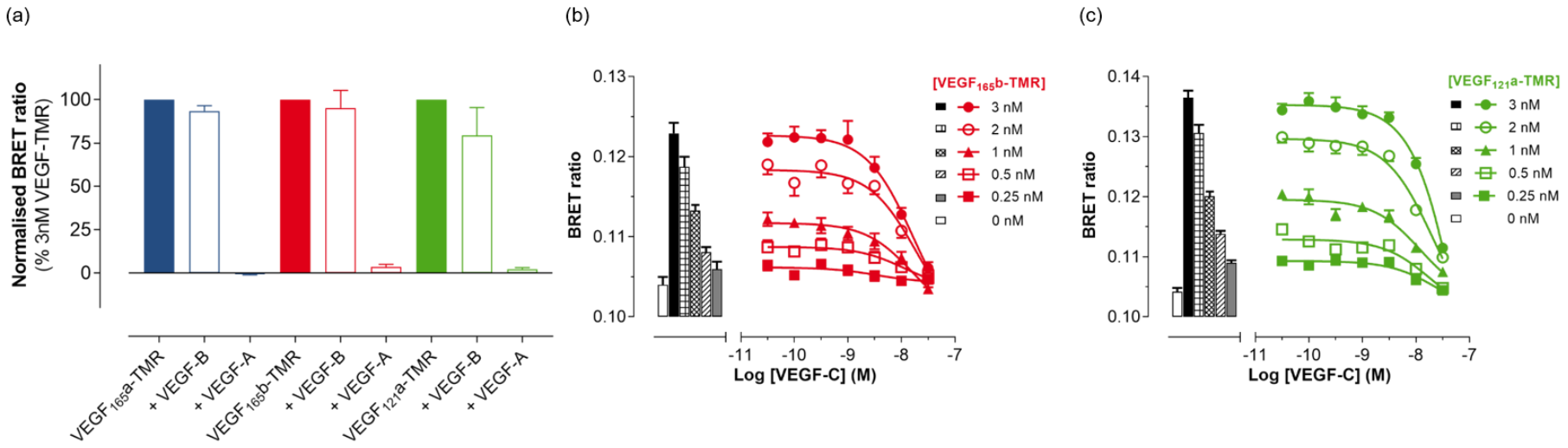


Figure 3.14 ***Inhibition of fluorescent VEGF-TMR binding by VEGF proteins encoded by separate genes.*** *(a) HEK293T-ReLuc2P cells stably expressing NanoLuc-VEGFR2 were stimulated with 3 nM $VEGF_{165}$a-TMR, $VEGF_{165}$b-TMR or $VEGF_{121}$a-TMR (solid bars). Cells were simultaneously incubated with 30 nM VEGF-B or prototypical $VEGF_{165}$a (open bars). BRET ratios were normalised to vehicle (0%) or 3 nM $VEGF_{xxx}$x-TMR (100%) per experiment. (b,c) Increasing concentrations of VEGF-C were added simultaneously with 5 concentrations of (b) $VEGF_{165}$b-TMR or (c) $VEGF_{121}$a-TMR (60 minutes, 37°C). Bars represent vehicle only (white bars) or incubation with fluorescent VEGF-TMR alone (filled bars). BRET ratios are shown as mean ± S.E.M. from 5 independent experiments with duplicate wells.*

BRET can also be used as a real-time technique to quantify the dynamics of protein-protein interactions at 37°C. To monitor ligand binding over time, cells expressing NanoLuc-tagged receptors were pre-incubated with the substrate furimazine for 5 minutes. Following four initial reads, fluorescent VEGF-A ligand was added. The PHERAstar FS platereader maintained temperature conditions at 37°C. Emissions were simultaneously measured every 30 seconds for NanoLuc (450-480 nm) and TMR (550 long pass, unless stated otherwise). We first monitored how emissions change over time in the presence of vehicle only (*Figure 3.15a*). There was an exponential decay over time in luminescence emissions from NanoLuc (luminescence, left y axis) and TMR emissions (fluorescence, right y axis). NanoLuc-mediated luminescence results from an enzymatic reaction, therefore furimazine substrate depletion causes a decrease in luminescence. In this example, luminescence emissions had a half life ($t_{1/2}$) of 21.3 minutes ($k = 0.0326min^{-1}$). Due to the nature of RET, the emissions from the acceptor channel had a similar exponential decay ($t_{1/2}$ = 21.0 minutes; $k = 0.0331min^{-1}$). BRET is quantified by the calculation of ratios from each emission obtained simultaneously (NanoLuc/TMR emissions). The ratiometric nature of this calculation led to a constant BRET signal over time despite the exponential decay resulting from furimazine depletion (*Figure 3.15b*). In subsequent kinetic experiments, the BRET ratio obtained at vehicle over time was routinely subtracted as 'baseline-corrected BRET'.

The ligand binding kinetics of each fluorescent VEGF-A variant was monitored using BRET at 37°C for 20 minutes. At higher concentrations, each $VEGF_{xxx}$x-TMR isoform reached a peak within 20 minutes (*Figure 3.16*). Kinetic binding experiments were conducted with five separate concentrations of fluorescent $VEGF_{xxx}$x-TMR to enable data to be globally fit to kinetic association curves. This can be used to quantify association rate (k_{on}) and dissociation rate (k_{off}) constants for each fluorescent ligand. These data showed that $VEGF_{165}$a-TMR had a slightly faster k_{on} than $VEGF_{121}$a-TMR and $VEGF_{165}$b-TMR, however each isoform had similar k_{off} rates (*Table 3.3*). There was no significant difference between fluorescent VEGF-A isoforms in terms of their k_{on} or k_{off} (Kruskal-Wallis test, $P>0.05$, n=5). The ratio of k_{off}/k_{on} also provided an estimate of the kinetically derived K_d values. These were similar to those obtained from equilibrium measurements, however there was no significant difference between kinetically derived pK_d values (one-way ANOVA, $P>0.05$, n=5).

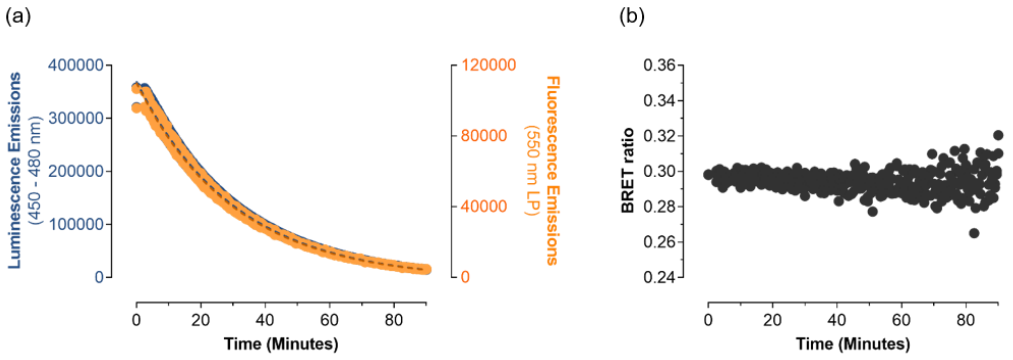


Figure 3.15 ***Monitoring the BRET signal over time in control conditions****. HEK293T-ReLuc2P cells expressing NanoLuc-VEGFR2 were plated for 24 hours in white 96-well plates. Cells were pre-incubated for 5 minutes in assay buffer (HBSS/0.1% BSA) containing 10 µM furimazine. Cells were maintained at 37°C throughout the experiment. Experiments were performed in the absence of ligand. (a) Emissions were simultaneously measured by the PHERAstar FS platereader every 30 seconds for 90 minutes. These were quantified as NanoLuc emissions (blue, left y axis) or TMR emissions (orange, right y axis). Dotted lines represent the exponential decay fit to the data. (b) Emissions from BRET experiments are expressed as a BRET ratio (NanoLuc emissions/TMR emissions). This was performed for data in* (a) *monitored in presence of vehicle only. BRET ratios remained constant throughout the 90 minute timecourse as the exponential decay was proportional for each emission. Individual replicates are displayed from duplicate wells. Data are shown from 1 representative experiment, however similar data were obtained in 9 further experiments monitoring ligand binding kinetics.*

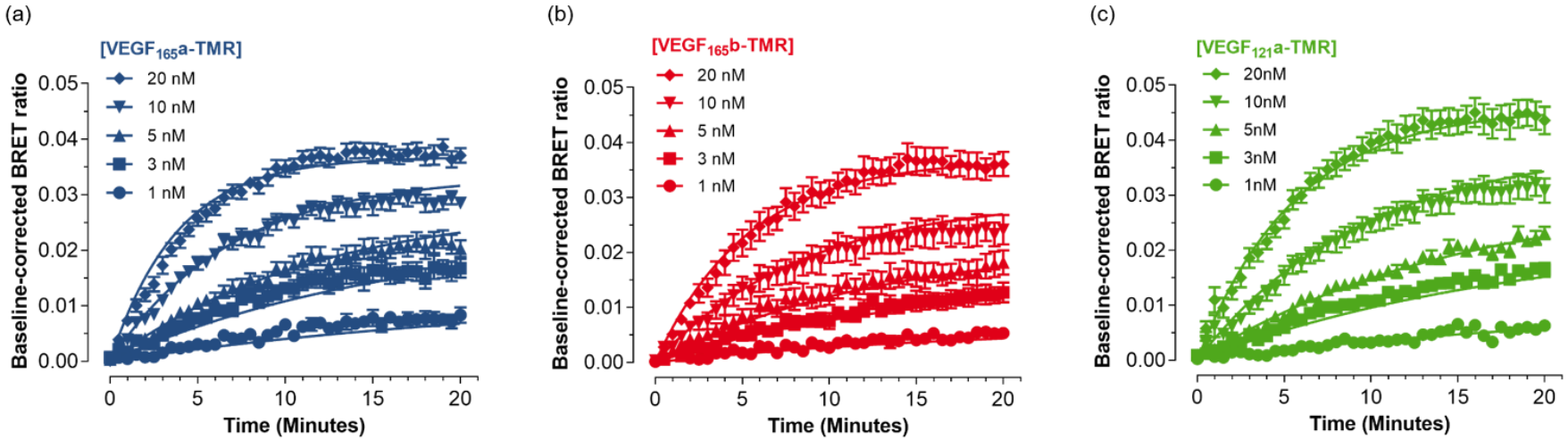


Figure 3.16 ***Association binding kinetics of fluorescent VEGF-A variants to NanoLuc-VEGFR2.*** *HEK293T-ReLuc2P cells stably expressed NanoLuc-VEGFR2. Cells treated with furimazine (10 μM) were left to equilibrate for 5 minutes. Subsequently, vehicle or 5 separate concentrations of (a) $VEGF_{165}$a-TMR, (b) $VEGF_{165}$b-TMR or (c) $VEGF_{121}$a-TMR were added. Measurements were taken every 30 seconds for 20 minutes (37°C). BRET ratios were baseline-corrected to vehicle at each time point. Data represent mean ± S.E.M from 5 independent experiments with duplicate wells. Individual kinetic curves were fit with a simple exponential association model as a global fit to each concentration of fluorescent VEGF-TMR. Derived kinetic parameters of association rate (k_{on}) and dissociation rate (k_{off}) are shown in* Table 3.3.

Real-time binding of $VEGF_{165}$a-TMR to NRP1 using BRET

To investigate how distinct fluorescent VEGF-A isoforms were able to interact with NRP1, we monitored fluorescent ligand binding using live cell confocal microscopy. HEK293T cells stably expressing HaloTag-NRP1 were labelled with membrane-impermeant HaloTag-AlexaFluor488 (*Methods 2.6.1*). Cells were stimulated with vehicle or 10 nM $VEGF_{165}$a-TMR, $VEGF_{165}$b-TMR or $VEGF_{121}$a-TMR for 60 minutes at 37°C (*Figure 3.17*). Firstly, not all fluorescent VEGF-A isoforms were observed to bind HaloTag-NRP1. While 10 nM $VEGF_{165}$a-TMR was observed in identical regions to HaloTag-NRP1 (*Figure 3.17,* white regions in overlay), we detected no binding of $VEGF_{165}$b-TMR and $VEGF_{121}$a-TMR to HaloTag-NRP1. Secondly, HaloTag-NRP1 remained at the cell surface upon incubation with both vehicle or fluorescent VEGF-A.

The C-terminus of NRP1 interacts with synectin (*GIPC1*), a cytoplasmic protein that interacts with the cytoskeleton (Cai and Reed, 1999; Wang et al., 2006; Prahst et al., 2008). In the absence of $VEGF_{165}$a-induced NRP1 internalisation (*Figure 3.17*), we used immunofluorescent labelling to confirm HEK293T cells expressed synectin. HUVECs and un-transfected HEK293T cells were fixed and permeabilised for labelling with a monoclonal antibody against synectin labelled with a secondary anti-mouse AlexaFluor488 antibody (*Methods 2.6.2*). There was intracellular distribution of the cytoplasmic protein in both cell lines (*Figure 3.18*).

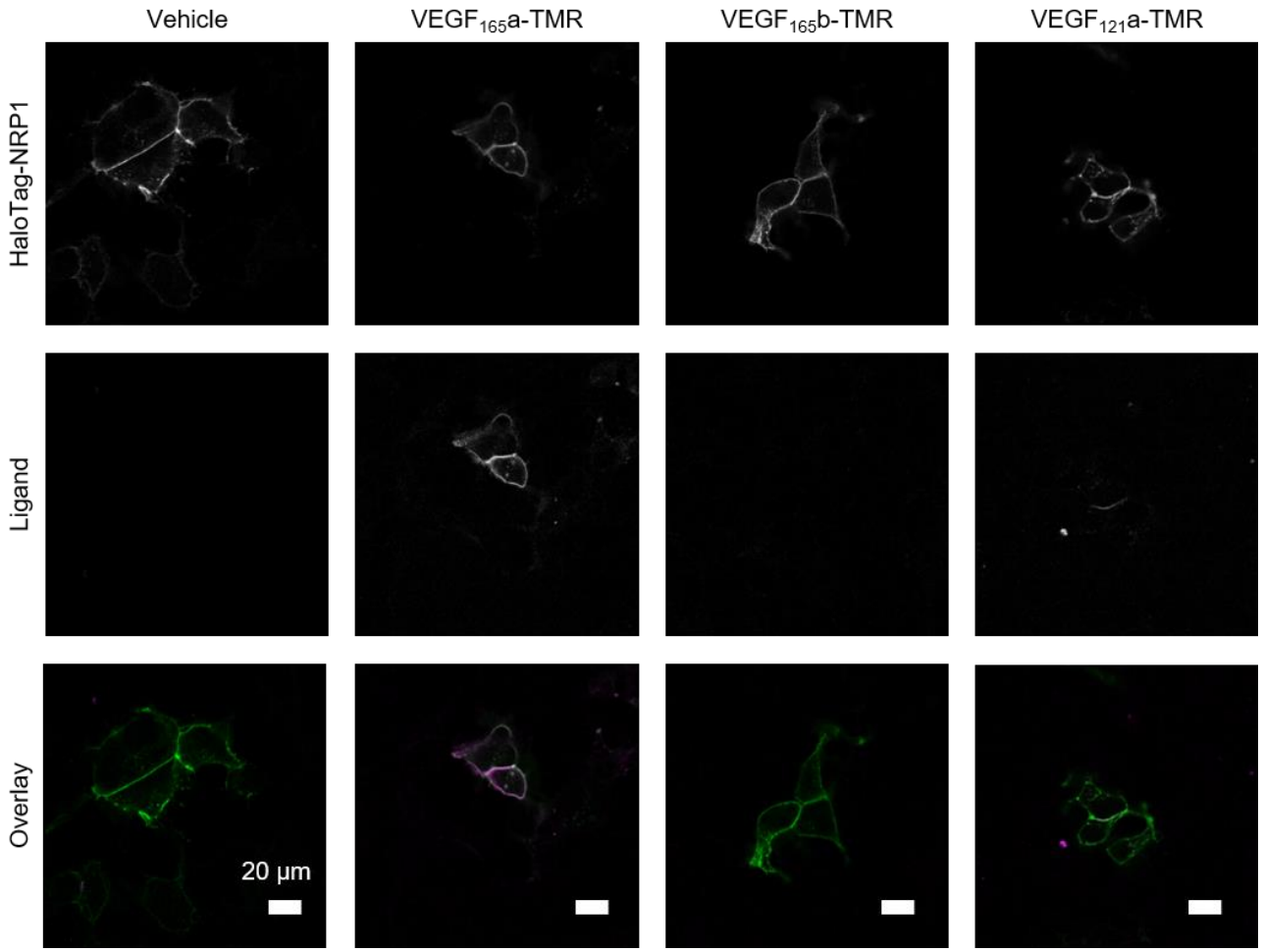


Figure 3.17 ***Imaging fluorescent VEGF-A isoforms at HaloTag-NRP1.*** *HEK293T-ReLuc2P cells stably expressed HaloTag-NRP1. Receptors were labelled with membrane-impermeant HaloTag-AlexaFluor488 substrate (0.5 µM) for 30 minutes (37°C). Cells were washed in serum-free DMEM and medium was replaced with HBSS/0.1% BSA. Cells were then stimulated with vehicle or ligand (10 nM $VEGF_{165}$a-TMR, $VEGF_{165}$b-TMR or $VEGF_{121}$a-TMR) for 1 hour at 37°C. Cells were imaged live using a Zeiss LSM710 Confocal Microscope (40X objective). The overlay shows HaloTag-NRP1 (green) and ligand (magenta). Images are representative from 3 independent experiments.*

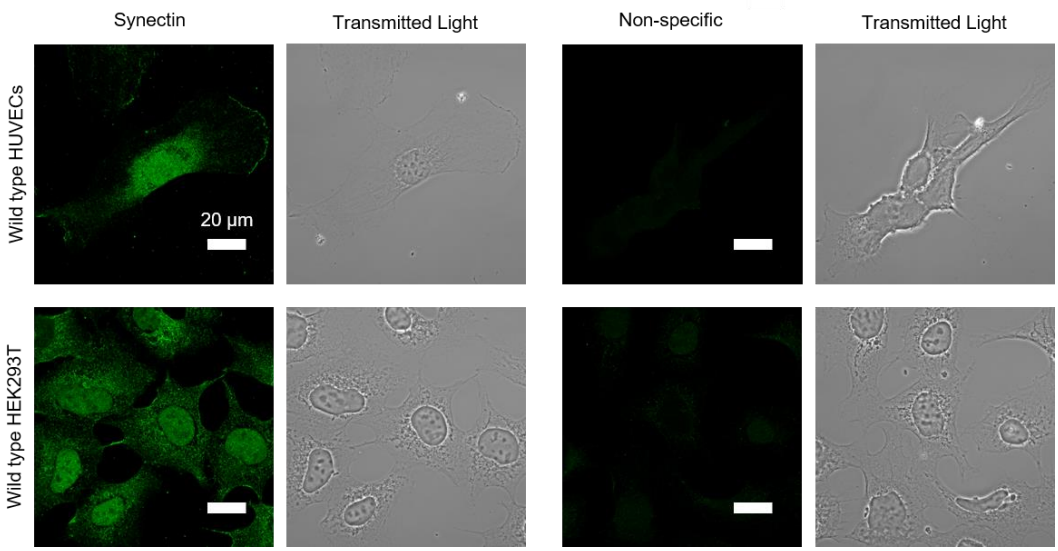


Figure 3.18 ***Immunofluorescent labelling of synectin.*** *Wild type HUVEC or wild type HEK293T cells were plated 24 hours prior to experimentation on glass coverslips. Un-stimulated cells were fixed (3% PFA/PBS), permeablised (0.025% Triton-X-100 in PBS) and blocked for non-specific binding (4% chick serum). These were incubated overnight in the presence or absence of a monoclonal antibody against synectin (OriGene, OTI4C11). This was labelled with an AlexaFluor488-conjugated secondary antibody. Non-specific binding was determined by incubation with secondary antibody only (right panel). Images were obtained by Zeiss LSM880 Confocal (63X magnification) using a 488 nm laser. Images were displayed alongside the corresponding transmitted light image. Images are representative from 3 independent experiments.*

We then applied BRET technology to monitor ligand binding at the Type I transmembrane protein, NRP1, for the first time. NanoLuc was fused to the extracellular N-terminus of full-length NRP1 and receptors were expressed in HEK293T cells (*Figure 3.19a*). Increasing concentrations of $VEGF_{165}$a-TMR led to a saturable BRET signal. In contrast, there was no saturable binding detected between $VEGF_{165}$b-TMR or $VEGF_{121}$a-TMR and NanoLuc-NRP1 (*Figure 3.19b*). This corroborated data from confocal imaging, whereby these fluorescent VEGF-A isoforms were unable to interact with NRP1 (*Figure 3.17*). Saturable binding of $VEGF_{165}$a-TMR for NanoLuc-NRP1 was largely displaced by a high concentration of unlabelled $VEGF_{165}$a, showing minimal non-specific binding (*Figure 3.19c*). $VEGF_{165}$a-TMR had a nanomolar affinity for NanoLuc-NRP1 expressed in HEK293T cells (K_d = 4.41 ± 1.34 nM, n=6). This was similar to the affinity of $VEGF_{165}$a-TMR derived in HEK293T cells expressing NanoLuc-VEGFR2 (*Table 3.5*). There was no significant difference between the pK_d for $VEGF_{165}$a-TMR derived at VEGFR2 or NRP1 (unpaired t-test, P>0.05, n=5-6 per group).

Monitoring ligand binding kinetics revealed that maximal $VEGF_{165}$a-TMR binding to NanoLuc-NRP1 reached equilibrium within 5 minutes (*Figure 3.19d*). Quantifying the kinetic binding parameters demonstrated that binding at NanoLuc-NRP1 exhibited faster k_{on} (7.11 ± 2.33 $x10^7$ $min^{-1}.M^{-1}$) and k_{off} (0.26 ± 0.05 min^{-1}) rate constants than those achieved with this ligand at NanoLuc-VEGFR2. For each kinetic parameter in *Table 3.5*, kinetic parameters derived at NanoLuc-NRP1 were significantly faster than those at NanoLuc-VEGFR2 (Mann-Whitney test, P<0.01, n=5 per group). Half times of association between the ligand/receptor complex ($t_{1/2}$) were estimated from the k_{obs} values determined for each experimental replicate. Distinctions in ligand binding kinetics were evident from comparing both the estimated residence time or half time at NanoLuc-VEGFR2 and NanoLuc-NRP1 (*Table 3.5*). However, the pK_d equilibrium dissociation constants were very similar for $VEGF_{165}$a-TMR between VEGFR2 and NRP1 from both saturation binding experiments and those derived from kinetic assays (unpaired t-test, P>0.05, n=5-6 per group).

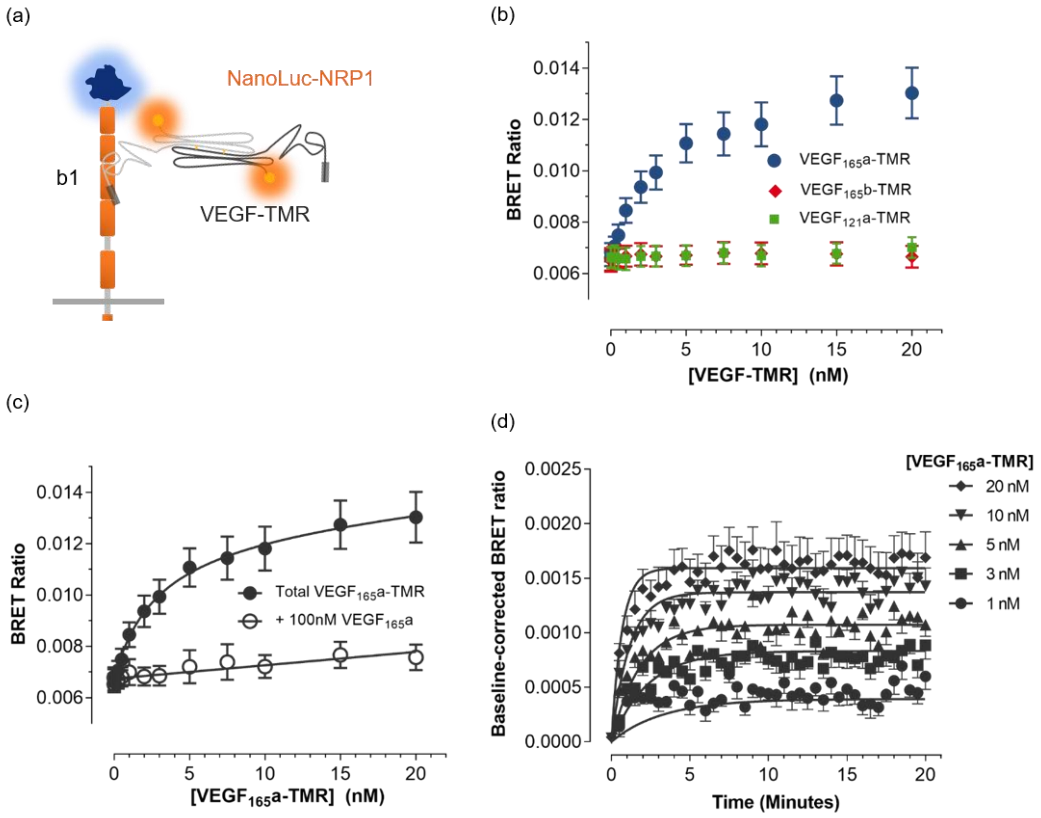


Figure 3.19 ***Binding characteristics of VEGF$_{165}$a binding to NanoLuc-NRP1 in HEK293T cells.*** *(a) HEK293T-ReLuc2P cells stably expressed N-terminal tagged NanoLuc-NRP1. In the presence of furimazine, emissions from NanoLuc-NRP1 can excite VEGF-TMR interacting with its orthosteric site at the b1 domain. (b) Cells were incubated with increasing concentrations of VEGF$_{165}$a-TMR, VEGF$_{165}$b-TMR or VEGF$_{121}$a-TMR. (c) Increasing concentrations of VEGF$_{165}$a-TMR were added in the absence and presence of 100 nM unlabelled VEGF$_{165}$a to determine non-specific binding. In* (b) *and* (c)*, cells were incubated for 60 minutes at 37°C. Data are expressed as mean ± S.E.M. from 6 independent experiments. (d) Timecourse of the binding of 5 concentrations of VEGF$_{165}$a-TMR binding to NanoLuc-NRP1. Furimazine was added 5 minutes prior to the addition of VEGF$_{165}$a-TMR at x=0. BRET ratios were baseline-corrected to vehicle over time. Kinetics were globally fit to a simple exponential association model. Unlike NanoLuc-VEGFR2, emissions were measured on the PHERAstar platereader using a 630-LP filter. BRET ratios are expressed as mean ± S.E.M. from 5 independent experiments with duplicate wells. Derived parameters are shown in* Table 3.5*.*

Table 3.5 ***Comparison of binding parameters determined at NanoLuc-VEGFR2 or NanoLuc-NRP1 for VEGF$_{165}$a-TMR****.*

Parameters		NanoLuc-VEGFR2	NanoLuc-NRP1
Saturation binding assay			
Saturation K_d (nM)		2.03 ± 0.51 nM	4.41 ± 1.34 nM (n=6)
Saturation pK_d		8.75 ± 0.11	8.45 ± 0.13 (n=6)
Kinetic binding assay			
Kinetic K_d (nM)		6.64 ± 4.37 nM	4.95 ± 1.25 nM
Kinetic pK_d		8.47 ± 0.23	8.40 ± 0.17
k_{on} ($min^{-1}M^{-1}$)		$1.54x10^7 \pm 0.38x10^7$	$7.11x10^7 \pm 2.33x10^7$ **
k_{off} (min^{-1})		0.06 ± 0.02	0.26 ± 0.05 **
Residence time (min)		28.49 ± 9.15	4.40 ± 0.74 **
Half time, $t_{1/2}$ (min)	20 nM	2.20 ± 0.39	0.50 ± 0.08 **
	10 nM	3.64 ± 0.45	0.82 ± 0.13 **
	5 nM	5.73 ± 0.74	1.24 ± 0.18 **
	3 nM	7.71 ± 1.25	1.58 ± 0.22 **
	1 nM	12.54 ± 3.01	2.24 ± 0.28 **

Data are expressed as mean ± S.E.M. from 5 independent experiments (unless stated otherwise) with duplicate wells. Equilibrium association rate constants (k_{on}) and dissociation rate constants (k_{off}) were used to estimate the K_d from each kinetic experiment. Equilibrium binding parameters derived from saturation experiments are also shown. Residence time was calculated as $1/k_{off}$. Half times were calculated assuming a first order rate reaction, calculated as $0.693/(k_{on}.[ligand] + k_{off})$. Unlike in Peach et al. (2018a), residence times and half times were calculated for each experimental replicate rather than the pooled k_{on} and k_{off} parameters. Kinetic parameters were compared between VEGFR2 and NRP1 using a Mann-Whitney test (** P<0.01). Alternatively, pK_d values were compared between VEGFR2 and NRP1 using an unpaired t-test (P>0.05, n=5-6 per group).

3.4 DISCUSSION

This Chapter evaluated the ability of fluorescent analogues of VEGF-A ($VEGF_{165}$a, $VEGF_{165}$b and $VEGF_{121}$a) to discriminate between VEGFR2 and NRP1 receptors in living cells in real-time. Considering the importance of temperature on the dynamics of biological processes, assay conditions were maintained at 37°C to reflect physiological conditions. To enable the application of BRET technologies to monitor ligand binding, VEGF-A isoforms were single-site labelled with TMR using a Click Chemistry approach. $VEGF_{165}$b and $VEGF_{121}$a were labelled at an N-terminal Cys, prepared as described previously for $VEGF_{165}$a (Kilpatrick et al., 2017). The site of TMR conjugation was distant from VEGF-A residues responsible for intermolecular disulphide bonds or receptor interactions (*Introduction Figure 1.4)*. VEGF-A is a large, glycosylated dimeric peptide, therefore protein expression and purification utilised mammalian cells (Friedman Ohana et al., 2011; *Methods 2.5*). Appropriate glycosylation and dimerisation of fluorescent VEGF-A variants was confirmed using SDS-PAGE gels in the presence of modifying enzymes (Kilpatrick et al., 2017; *Appendix 7.1*). Mass spectrometry confirmed stoichiometric labelling of >94% sample. Recent work demonstrated the importance of single-site labelling for VEGF-A binding and signalling, as additional moieties increasingly hindered the pharmacophore (Friedman Ohana et al., 2019). Stoichiometric labelling was also important for subsequent studies monitoring ligand binding using BRET, thus enabling us to quantify the pharmacology of VEGF-A isoforms at VEGFR2 or NRP1.

Fluorescent ligands can have different pharmacological properties to their unlabelled counterparts, thus requiring evaluation as new chemical entities. Kilpatrick et al. (2017) previously demonstrated that $VEGF_{165}$a-TMR behaved similarly to $VEGF_{165}$a in its ability to (1) stimulate NFAT reporter gene signalling in HEK293T cells expressing VEGFR2 and (2) stimulate the proliferation of HUVECs (Kilpatrick et al., 2017). Here, both $VEGF_{165}$b-TMR and $VEGF_{121}$a-TMR differed from their unlabelled counterparts in these functional assays. The EC_{50} values obtained using the NFAT reporter gene assay demonstrated that both $VEGF_{165}$b-TMR (pEC_{50} = 8.2) and $VEGF_{121}$a-TMR (pEC_{50} = 8.5) were an order of magnitude higher, thus less potent, than unlabelled versions ($VEGF_{165}$b pEC_{50} = 9.3; $VEGF_{121}$a pEC_{50} = 9.5). These EC_{50} values were very similar to pK_d values obtained from BRET saturation binding studies (7.9-8.1 for $VEGF_{165}$b-TMR and 8.2-8.4 for $VEGF_{121}$a-TMR) and from competition binding studies (9.1-9.6 for $VEGF_{165}$b and 9.3-9.6 for $VEGF_{121}$a). This suggested that there was little signal amplification in the NFAT assay. Monitoring HUVEC proliferation similarly demonstrated both $VEGF_{165}$b-TMR and $VEGF_{121}$a-TMR were lower efficacy than non-fluorescent ligands. These data also highlighted that $VEGF_{165}$b and $VEGF_{121}$a induced a lower response than prototypical $VEGF_{165}$a in stimulating HUVEC proliferation, acting as a partial agonist at endogenously expressed receptors. This agreed with published studies

using phenotypic assays on HUVECs comparing $VEGF_{165}a$ to $VEGF_{165}b$ (Kawamura et al., 2008b; Catena et al., 2010; Delcombel et al., 2013; Hueso et al., 2017) and $VEGF_{121}a$ (Pan et al., 2007; Delcombel et al., 2013; Fearnley et al., 2016; Shiying et al., 2017). Comparing the number of HUVECs may not distinguish between cell proliferation and survival, however this phenotypic assay measures the net effect of VEGF-A stimulation in endothelial cells. Partial agonism was also seen to a lesser extent with $VEGF_{165}b$ and $VEGF_{121}a$ relative to $VEGF_{165}a$ in NFAT experiments, as observed in previous studies (Carter et al., 2015; Kilpatrick et al., 2017). While addition of the TMR moiety resulted in decreased potency for $VEGF_{165}b$ and $VEGF_{121}a$, fluorescent VEGF-A variants retained agonist activity in all assays.

BRET was used to evaluate the selectivity of VEGF-A isoform binding at VEGFR2 or NRP1 in living HEK293T cells. This technology isolated ligand binding at NanoLuc-tagged receptors only, regardless of the extent of endogenous receptor expression. This is demonstrated by the low non-specific binding observed in saturation binding assays. Close proximity is required for BRET to occur (<10 nm), such as between a fluorescent ligand and its receptor, thus ensuring a high specificity of interaction. This enabled the quantification of ligand binding dynamics at specified tagged receptors. Unlike radioligand binding techniques, RET techniques cannot typically quantify the absolute concentration of receptors expressed (Stoddart et al., 2015b). Although HEK293T did not express endogenous VEGFR1 or NRP1, endogenous VEGFR2 was detected in a subpopulation of wild type HEK293T cells. Expression was insufficient to compromise ligand binding or signalling in un-transfected cells. Immunofluorescent antibody labelling also does not label proteins with 1:1 stoichiometry (*Methods* *Figure 2.6*), therefore cannot quantify the absolute number of VEGFR2 receptors expressed using these methods. HUVECs are a primary endothelial cell line that expressed VEGFR2 and NRP1. They lacked VEGFR1 expression, in agreement with previous studies comparing endothelial cell lines (Imoukhuede and Popel, 2011; Lee-Montiel et al., 2015). Considering HEK293T cells as a model cell line in further studies, semi-quantitative imaging analysis suggested receptors were not largely overexpressed relative to their native expression in HUVECs. A functional NFAT reporter gene assay also confirmed that adding a NanoLuc (19.1 kDa) or HaloTag (33 kDa) moiety to VEGFR2 had minimal effect on $VEGF_{165}a$-induced signalling.

At full-length NanoLuc-VEGFR2 expressed in living cells, saturable binding was observed for $VEGF_{165}$a-TMR, $VEGF_{165}$b-TMR and $VEGF_{121}$a-TMR with nanomolar affinities. There was minimal non-specific binding detected with each fluorescent VEGF-A ligand monitored using BRET. The real-time binding kinetic parameters derived for each fluorescent VEGF-A ligand indicated that all three fluorescent VEGF variants had similar association (k_{on}) and dissociation (k_{off}) rate constants, with relatively slow dissociation rate constants (k_{off} = 0.05-0.06 min^{-1}). From competition experiments using these fluorescent ligands as probes, pK_i values were obtained for a panel of seven unlabelled VEGF-A isoforms. This was the first comprehensive quantification of VEGF-A isoform binding affinities compared in the same study, including recently described VEGF-Ax (Eswarappa et al., 2014). Despite nuances of signalling described in the literature, unlabelled VEGF-A isoforms had comparable nanomolar binding affinities at NanoLuc-VEGFR2 ranging between 0.1-1.5 nM. In line with these findings, all VEGF-A isoforms contain residues that interact with VEGFR2. Affinities for unlabelled $VEGF_{165}$a at VEGFR2 derived using BRET were similar to those determined with radioligand binding (*Table 3.1*). Cébe Suarez et al. (2006) also showed $VEGF_{165}$b and $VEGF_{165}$a had similar binding affinities using radioligand binding in PAE cells expressing VEGFR2, however this was not quantified in terms of their pharmacological equilibrium dissociation constant. VEGF-C had a lower affinity than all VEGF-A isoforms at NanoLuc-VEGFR2 (~6 nM), while VEGF-B was unable to compete with fluorescent VEGF-A for the same binding site. There was also no evidence of probe dependence in the measurement of these equilibrium constants. As these studies demonstrated that all isoforms were able to bind VEGFR2 with a similar nanomolar affinity, this suggests that VEGF-A/VEGFR2 binding alone is insufficient to explain the functional distinctions between VEGF-A isoforms in terms of their signalling downstream of VEGFR2.

$VEGF_{165}$a-TMR bound to NanoLuc-NRP1 in living cells with a similar high affinity (4.41 nM) to that observed at NanoLuc-VEGFR2 (2.03 nM). This agrees with prior radioligand binding studies (*Table 3.1*). In marked contrast, $VEGF_{165}$b-TMR and $VEGF_{121}$a-TMR did not interact with NanoLuc-NRP1 at concentrations up to 20 nM. This observation was corroborated by live cell confocal imaging, as $VEGF_{165}$b-TMR (10 nM) and $VEGF_{121}$a-TMR (10 nM) bound to HaloTag-VEGFR2 but not to HaloTag-NRP1. Published in Peach et al. (2018a), this finding was confirmed with unlabelled VEGF-A isoforms as Dr Kilpatrick performed competition binding experiments at NanoLuc-NRP1. Published studies yielded a rank order of pK_i values $VEGF_{165}$a (pK_i = 9.54 ± 0.21, n=5) > $VEGF_{189}$a (pK_i = 8.60 ± 0.14, n=5) > $VEGF_{145}$a (pK_i = 7.82 ± 0.15, n=5). Unlabelled $VEGF_{165}$b, VEGF-Ax, $VEGF_{121}$a and $VEGF_{111}$a were unable to displace 3 nM $VEGF_{165}$a-TMR from NanoLuc-NRP1 at concentrations up to 30 nM (Peach et al., 2018a). There have been conflicting reports regarding $VEGF_{121}$a binding to NRP1 (Sarabipour and Mac Gabhann, 2017). In agreement with our data, radioligand binding

and solid-phase biotinylation assays have shown no interaction between $VEGF_{121}$a and NRP1 (Cébe Suarez et al., 2006; Kawamura et al., 2008a; Xin et al., 2016), as well as recent SPR data (Teran and Nugent, 2018). Conversely, low affinity binding was detected using immobilised monomeric NRP1 with SPR or isolated NRP1 b1/b2 domains (Pan et al., 2007; Parker et al., 2012; Delcombel et al., 2013). No BRET was detected between NanoLuc-NRP1 and $VEGF_{121}$a-TMR up to 20 nM. These concentrations are in excess of physiological levels of these ligands, predicted as <1 nM by computational modelling (Clegg and Mac Gabhann, 2017). These data therefore suggest that $VEGF_{165}$b-TMR and $VEGF_{121}$a-TMR can be used as selective fluorescent probes for VEGFR2, even if used in cells that also express NRP1.

A key feature of this technique is the ability to study the binding dynamics of VEGF-A to full length VEGFR2 or NRP1 in living cells. Monitoring interactions in real-time has more physiological relevance than experiments taking a 'snapshot' after 60 minutes that assume equilibrium. Despite comparable affinities determined by saturation and kinetic binding experiments, $VEGF_{165}$a-TMR had faster binding kinetics at NanoLuc-NRP1 compared to NanoLuc-VEGFR2. Maximal binding to NanoLuc-NRP1 was achieved within 5 minutes, largely as a consequence of its fast dissociation rate constant (k_{off} = 0.26 min^{-1}). As there was a proportional increase relative to the association rate constant (k_{on} = $7.11x10^7 \pm 2.33x10^7$ M^{-1} min^{-1}), this led to an unchanged K_d relative to VEGFR2 estimated from kinetic experiments ($K_d = k_{off}/k_{on}$). This striking distinction in ligand binding kinetics is demonstrated by considering the half time ($t_{1/2}$) of the $VEGF_{165}$a-TMR at the receptors. For example, 10 nM $VEGF_{165}$a-TMR is estimated to associate with VEGFR2 for 4 minutes compared to 1 minute at NRP1. Teran & Nugent (2018) recently quantified $VEGF_{165}$a binding kinetics using SPR at immobilised receptors. Comparing VEGFR2 and NRP1, they also showed faster binding at NRP1 than VEGFR2. Kinetic rate constants determined using BRET were slower at both receptors than those quantified using SPR at purified receptors (*Table 3.6*). Unlike SPR, BRET quantified binding kinetics at full-length receptors expressed in their native membrane microenvironment that enable dynamic receptor oligomerisation. However, they were able to directly monitor dissociation rate constants by switching injectors to flow buffer alone. These data suggested a greater difference in k_{off} parameters than those estimated from our BRET association binding experiments. Both approaches quantified the kinetics of ligand binding at each receptor alone. It is unknown whether, in cells expressing both VEGFR2 and NRP1, $VEGF_{165}$a could bind more quickly to NRP1 than to VEGFR2. This may have important implications for the dynamics of VEGF-A-induced VEGFR2 signalling or trafficking, emphasising the need to understand the kinetic aspects of VEGF-A pharmacology at VEGFR2 and its co-receptors.

Table 3.6. ***Comparing kinetic binding data determined using BRET with surface plasmon resonance (SPR) on purified receptors****.*

	SPR	BRET	Comparison to SPR
VEGFR2			
k_{on} (M^{-1} sec^{-1})	$1.76x10^6 \pm 0.04x10^6$	$2.56x10^5 \pm 0.63x10^5$	6.9-fold slower
k_{off} (sec^{-1})	0.0151 ± 0.0007	0.001 ± 0.00003	15.1-fold slower
K_d (nM)	8.6 ± 0.5	6.63 ± 4.37	Similar affinity
NRP1			
k_{on} (M^{-1} sec^{-1})	$3.6x10^6 \pm 0.02x10^6$	$1.19x10^6 \pm 0.39x10^6$	3.0-fold slower
k_{off} (sec^{-1})	0.090 ± 0.004	0.00434 ± 0.0008	22.5-fold slower
K_d (nM)	25 ± 2	4.95 ± 1.25	Higher affinity

Kinetic parameters were obtained from surface plasmon resonance (SPR) studies in Teran and Nugent (2018). Bioluminescence Resonance Energy Transfer (BRET) studies performed in this Chapter were also published in Peach et al. (2018a). Compared to *Table 3.5*, parameters have been converted into units per second.

Imaging ligand/receptor interactions using a membrane-impermeant HaloTag substrate also highlighted differences in the subcellular distribution of VEGFR2 and NRP1. VEGFR2 was constitutively internalised in the absence of ligand stimulation. These data agree with previous antibody-based imaging in endothelial cells (Gampel et al., 2006; Basagiannis and Christoforidis, 2016; Basagiannis et al., 2016) and Dr Kilpatrick's prior studies with VEGFR2 stably expressed in HEK293T cells (Kilpatrick et al., 2017). Comparing distinct fluorescent VEGF-A isoforms, there were no distinctions in HaloTag-VEGFR2 localisation. $VEGF_{165}$a-TMR, $VEGF_{165}$b-TMR and $VEGF_{121}$a-TMR internalised with VEGFR2 receptors by 60 minutes. In contrast, HaloTag-NRP1 largely remained on the cell membrane, despite confirmation that HEK293T cells endogenously express the cytoskeleton-associated adaptor protein synectin. This cell surface expression persisted despite stimulation for 60 minutes with a saturating concentration of $VEGF_{165}$a-TMR. Other groups have shown an intracellular distribution of NRP1 using immunofluorescent antibody labelling in permeabilised cells (Narazaki and Tosato, 2006; Ballmer-Hofer et al., 2011). However, labelling with a membrane-impermeant HaloTag substrate isolated NRP1 receptors that were successfully exported to the plasma membrane for exposure to extracellular ligand. These data therefore monitored the direct consequences of $VEGF_{165}$a stimulation on NRP1 localisation in living cells. The spatial resolution possible with fluorescent VEGF-A isoforms revealed novel distinctions between the localisation of VEGFR2 and NRP1.

3.5 CHAPTER 3 CONCLUSIONS

In summary, we applied BRET to two different classes of membrane protein. This real-time approach was able to quantify the ligand binding pharmacology of the complex dimeric VEGF-A protein. Novel fluorescent VEGF-A isoforms were labelled at a single site with TMR using Click Chemistry. While $VEGF_{165}$a-TMR was published previously, $VEGF_{165}$b-TMR and $VEGF_{121}$a-TMR were characterised as novel ligands. They retained their agonist activity, albeit with reduced potency than unlabelled counterparts. HEK293T cells were also characterised as a cell line to isolate the pharmacology of tagged VEGFR2 or NRP1 receptors.

Having established this assay system, fluorescent VEGF-A variants were used to monitor the dynamics of ligand binding at VEGFR2 or co-receptor NRP1 at 37°C. This selective approach isolated interactions at full-length receptors tagged at their N-terminus with NanoLuc. As the first comprehensive ligand binding study across a range of VEGF-A isoforms, all isoforms had a similar nanomolar affinity at NanoLuc-VEGFR2. $VEGF_{165}$a-TMR was able to interact with NanoLuc-NRP1 with a similar equilibrium dissociation constant compared to NanoLuc-VEGFR2. Despite these similar affinities, the real-time sensitivity of this BRET assay revealed clear differences in the kinetics of $VEGF_{165}$a-TMR for VEGFR2 and NRP1. As well as highlighting differences in ligand binding dynamics, this work emphasised distinctions in the spatial localisation of VEGFR2 and NRP1 when expressed alone in living cells. Additionally, $VEGF_{165}$b-TMR and $VEGF_{121}$a-TMR were unable with NanoLuc-NRP1. These two novel fluorescent VEGF-A isoforms therefore act as selective, fluorescent probes that bind VEGFR2 but not NRP1.

Chapter 4.
Influence of VEGFR2 endocytosis and phosphorylation on VEGF-A ligand binding

4.1 INTRODUCTION

VEGF-A primarily stimulates angiogenesis via the activation of VEGFR2, a Class IV RTK (*Introduction 1.4*). Ligand binding across the VEGFR2 dimer leads to conformational changes that enable intrinsic ATP-dependent kinase activity in the cytoplasmic catalytic domain (Tao et al., 2001; Ruch et al., 2007; Dosch and Ballmer-Hofer, 2010; Leppanen et al., 2010; Brozzo et al., 2011; Kisko et al., 2011). This leads to the auto- and trans-phosphorylation of intracellular tyrosine residues, including Y1054, Y1059, Y951, Y1175 and Y1214 (Manni et al., 2014a). Adaptor proteins, such as PLCγ, are recruited to these phosphorylated VEGFR2 residues. This initiates signalling cascades that lead to endothelial cell proliferation, migration and vascular permeability (Koch et al., 2011; Simons et al., 2016). VEGFR2 is subject to complex trafficking via clathrin-dependent (Ewan et al., 2006; Lampugnani et al., 2006) and clathrin-independent endocytosis (Labrecque et al., 2003; Basagiannis and Christoforidis, 2016; Basagiannis et al., 2016). It internalises in both the presence and absence of VEGF-A (Ewan et al., 2006; Jopling et al., 2009; Jopling et al., 2011), as demonstrated in *Chapter 3*. Following the onset of endocytosis, VEGFR2 first accumulates in $Rab5^+$ endosomes (Gampel et al., 2006). VEGFR2 can then recycle back to the plasma membrane. This occurs via a short loop recycling route in $Rab4^+$ endosomes or long loop recycling via $Rab11^+$ endosomes (Jopling et al., 2014; *Introduction Figure 1.8*). Alternatively, receptor ubiquitination can initiate lysosomal degradation (Smith et al., 2016). VEGFR2 trafficking has primarily been investigated using immunofluorescent antibody labelling in fixed, permeabilised cells (Ewan et al., 2006; Gampel et al., 2006; Lampugnani et al., 2006; Jopling et al., 2009; Fearnley et al., 2016). As such, receptor trafficking has not been monitored in real-time in living cells that isolate receptors successfully exported to the cell surface to interact with ligand. Alternatively, biotinylation can be used to label cell surface proteins (Volz et al., 1995). Biotinylation was used with subsequent VEGFR2-specific Western blot and pull-down assays (Gampel et al., 2006; Lampugnani et al., 2006; Basagiannis and Christoforidis, 2016; Basagiannis et al., 2016; Fearnley et al., 2016). Due to the constitutive internalisation of VEGFR2, it can be difficult to isolate the ligand-driven component of endocytosis using these approaches.

Numerous clinically approved anti-angiogenic drugs, such as RTKIs, target VEGF-A/VEGFR2 signalling (*Introduction Table 1.2*). These small molecule inhibitors prevent tyrosine phosphorylation through directly or indirectly inhibiting ATP binding at the kinase domain. As this catalytic domain is highly conserved amongst kinases, RTKIs are relatively non-specific (Davis et al., 2011). Previous work demonstrated that pre-incubation with RTKIs led to the inhibition of VEGFR2 endocytosis (Kilpatrick et al., 2017). While the non-selective nature of RTKIs are advantageous as a cancer therapeutic, their ability to inhibit other intracellular kinases can make it difficult to isolate their molecular mechanism at VEGFR2. As a consequence, it remains largely unknown

whether VEGFR2 phosphorylation is an essential prerequisite for ligand-dependent or ligand-independent endocytosis. A more selective means is required to isolate the role of VEGFR2 phosphorylation on its subcellular localisation.

Chapter 3 characterised fluorescent variants of $VEGF_{165}$a, $VEGF_{165}$b and $VEGF_{121}$a that were stoichiometrically labelled with tetramethylrhodamine (TMR). Using a proximity-based BRET assay, we monitored the real-time ligand binding of fluorescent VEGF-A isoforms at 37°C in living cells. This approach was specific to receptors tagged with NanoLuciferase (NanoLuc). NanoLuc acts as a luminescent donor that can excite a nearby fluorophore via BRET; as such, BRET occurs when $VEGF_{xxx}$x-TMR binds at NanoLuc-VEGFR2. Kilpatrick et al. (2017) identified a striking feature of $VEGF_{165}$a-TMR binding at VEGFR2 in living cells using a retrospective timecourse, whereby the BRET signal declined after 20 minutes of incubation with the fluorescent ligand. This was hypothesised to be a consequence of ligand/receptor endocytosis (Kilpatrick et al., 2017), however it is unknown how this differs between VEGF-A isoforms. Live cell imaging demonstrated that each fluorescent VEGF-A isoform internalised with VEGFR2 into intracellular endosomes within 60 minutes (*Figure 3.11*). The BRET signal between $VEGF_{xxx}$x-TMR and NanoLuc-VEGFR2 could therefore originate from ligand/receptor interactions at the cell surface or within intracellular endosomes. Endosomes have a unique microenvironment that could impact the stability of ligand/receptor complexes, such as an increasingly acidic pH as they mature along the vesicular pathway (Maxfield and Yamashiro, 1987). It is unknown how the complex trafficking of VEGFR2 in space and time influences the ligand binding of distinct VEGF-A isoforms in living cells.

Homogenised membrane preparations are the most common approach used for radioligand binding experiments (Bylund and Toews, 1993). Having established BRET to monitor ligand/receptor interactions in intact cells, membrane preparations were used as an alternative approach to isolate the kinetics of ligand-receptor interactions in the absence of agonist-induced receptor endocytosis. This assay was also amenable to directly probe the influence of biochemical factors, such as how an acidic pH that reflects endosomes influenced ligand binding. Due to the complexities in VEGFR2 trafficking, we set out to probe the interplay between VEGFR2 localisation, phosphorylation and the ligand binding of VEGF-A.

4.2 CHAPTER 4 AIMS

The work described in Chapter 4 aimed to:

(a) Develop approaches to quantify the concentration-dependence and temporal profile of VEGF-A/VEGFR2 endocytosis using fluorescent VEGF-A isoforms;
(b) Investigate the influence of VEGFR2 phosphorylation inhibition on receptor endocytosis and ligand binding;
(c) Use isolated membrane preparations to probe the kinetics of ligand-receptor interactions in the absence of parallel receptor endocytosis.

4.3 RESULTS

Agonist-mediated endocytosis of VEGFR2 in HEK293T cells

We previously used BRET to distinguish between the association kinetics of ligand binding at NanoLuc-VEGFR2 and NanoLuc-NRP1 in HEK293T cells. Here, we extended the timecourse of binding beyond the initial 20 minutes. For each fluorescent VEGF-A isoform, binding to NanoLuc-VEGFR2 reached a peak in BRET ratio at 20 minutes (*Figure 4.1a-c*). At higher ligand concentrations (10-20 nM), the BRET signal then declined substantially towards baseline over the remaining 70 minutes. With non-saturating concentrations close to their respective K_d values, the binding of each ligand was relatively well maintained over the course of the experiment. These data recapitulated previous findings for $VEGF_{165}$a-TMR (Kilpatrick et al., 2017), with similar BRET profiles observed for $VEGF_{165}$b-TMR and $VEGF_{121}$a-TMR. In contrast, this decline in BRET ratio for $VEGF_{165}$a-TMR was absent in HEK293T cells expressing NanoLuc-NRP1 (*Figure 4.1d*). We previously showed evidence for ligand/receptor internalisation at HaloTag-VEGFR2 (*Figure 3.11*), not HaloTag-NRP1 (*Figure 3.17*). These distinctions in long-term BRET binding profiles therefore support the hypothesis that the decline in BRET signal at NanoLuc-VEGFR2 reflects local changes resulting from ligand/receptor endocytosis. While Chapter 3 presented qualitative data showing fluorescent VEGF-A isoforms internalised with VEGFR2, there is limited quantitative understanding of this process.

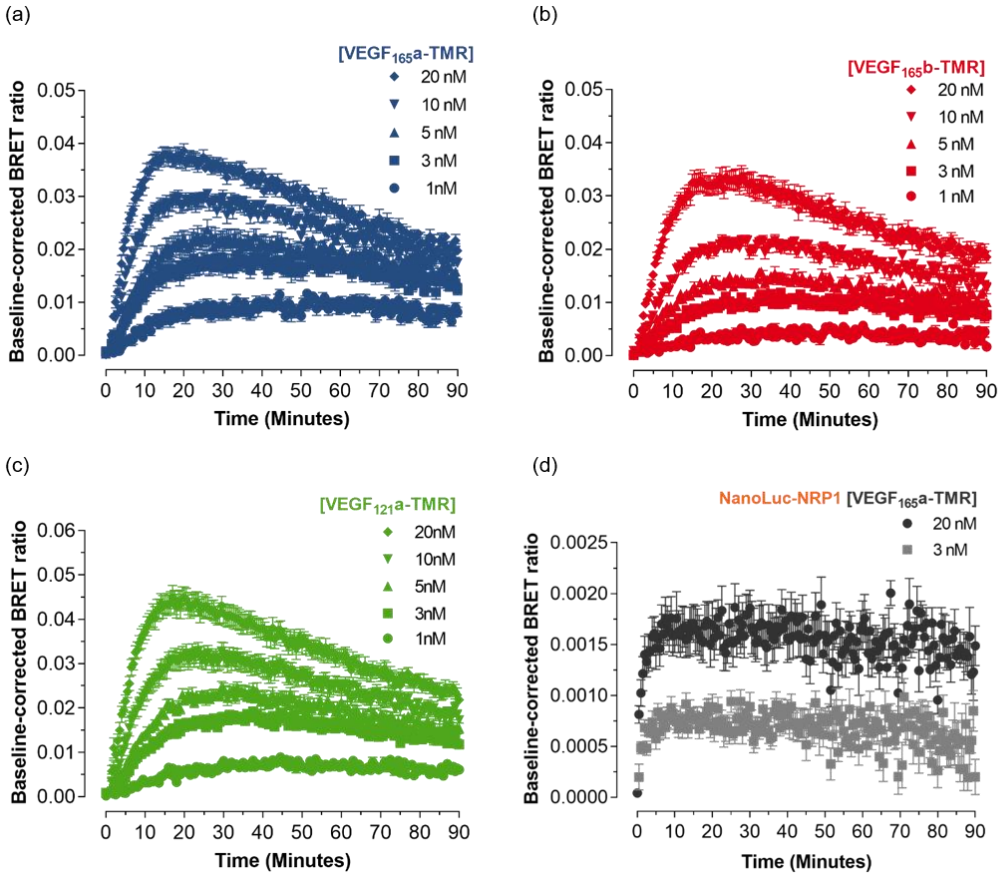


Figure 4.1 ***Long-term kinetic binding profiles of fluorescent VEGF-A isoforms at NanoLuc-VEGFR2 or NanoLuc-NRP1 in living cells.***

(a-c) HEK293T-ReLuc2P cells stably expressed NanoLuc-VEGFR2. Following 5 minutes pre-treatment with the NanoLuc substrate furimazine, 5 concentrations (a) $VEGF_{165}$a-TMR, (b) $VEGF_{165}$b-TMR or (c) $VEGF_{121}$a-TMR were added at x=0. BRET ratios were monitored on the PHERAstar FS platereader at 37°C using a 550-LP/450-480 nm filter. (d) HEK293T cells stably expressed NanoLuc-NRP1. Cells were stimulated with $VEGF_{165}$a-TMR at a saturating (20 nM) concentration and a concentration approximately equal to its K_d value (3 nM). Emissions at NanoLuc-NRP1 were quantified using a 610-LP/460-480 nm filter, in line with previous work. BRET ratios were calculated every 30 seconds for 90 minutes. These data are also shown in Figure 3.16 *and* Figure 3.19d, *but extended here to a longer timecourse. Data were baseline-corrected to vehicle at each time point to adjust for background. Data are shown as mean ± S.E.M. from 5 independent experiments, each with duplicate wells.*

Fluorescent VEGF-A isoforms were used to follow the internalisation of ligand-occupied VEGFR2 using unbiased automated high-content imaging. Ligand/receptor internalisation was quantified in terms of its timecourse and potency (*Methods 2.7.3*). VEGFR2-driven endocytosis of fluorescent VEGF-A in HEK293T cells was monitored by quantifying the appearance of fluorescent ligand in intracellular endosomes. A granularity algorithm was used to detect the presence of fluorescent VEGF-A within granules (2-15 µm; *Figure 4.2a, Methods Figure 2.9b*). While individual endosomes range in size from 50 nm to 400 nm (Mukherjee et al., 1997), this is beyond the detection limit of conventional light microscopy. As such, intracellular fluorescent granules likely represent clusters of endosomes. Although experiments were performed on a widefield imaging platereader with limited axial (Z) resolution, these granules were considered as intracellular vesicles due to their distribution away from the plasma membrane (*Figure 4.2a*). Previous work demonstrated that the timecourse of $VEGF_{165}$a-TMR granularity analysis reflected the endocytosis of HaloTag-VEGFR2 (Kilpatrick et al., 2017). Minimal intracellular granules were detected in un-transfected HEK293T cells incubated with the same ligand concentration (*Figure 3.7*). This process was therefore dependent on transfected VEGFR2. Thus, granularity analysis will be considered a representative measure of $VEGF_{xxx}$x-TMR/VEGFR2 endocytosis.

All three fluorescent VEGF-A isoforms stimulated the concentration-dependent internalisation of VEGFR2 (*Figure 4.2b; Table 4.1*). $VEGF_{165}$b-TMR had a lower potency than $VEGF_{165}$a-TMR (one-way ANOVA, $P<0.05$; Šidák's multiple comparisons, $P<0.05$, n=5 per group). In the presence of 10 nM of $VEGF_{165}$a-TMR, $VEGF_{165}$b-TMR or $VEGF_{121}$a-TMR, the appearance of ligand/receptor complexes in endosomes was rapid (*Figure 4.2c*). Timecourse data were fit to a one-phase exponential association, from which a rate constant (k_{obs}) was estimated (*Table 4.1*). This was also used to estimate that the half time ($t_{1/2}$) for the appearance on intracellular fluorescent VEGF-A granules was between 15 and 20 minutes. There was no significant difference between the rate constants or derived half times for each fluorescent VEGF-A isoform (Kruskal-Wallis test, $P>0.05$, n=5 per group). Calculated half times can be directly compared with those estimated from binding kinetics using NanoLuc-tagged receptors in HEK293T cells (*Table 3.3*). For example, the binding interaction between 10 nM $VEGF_{165}$a-TMR and NanoLuc-VEGFR2 had a $t_{1/2}$ ~4 minutes, while internalisation $t_{1/2}$ was ~18 minutes. Fluorescent VEGF-A isoforms were also consistently less potent in stimulating internalisation compared to ligand binding or NFAT signalling (40-50 -fold lower EC_{50} than ligand binding K_i; 40-70 -fold lower than NFAT signalling EC_{50}).

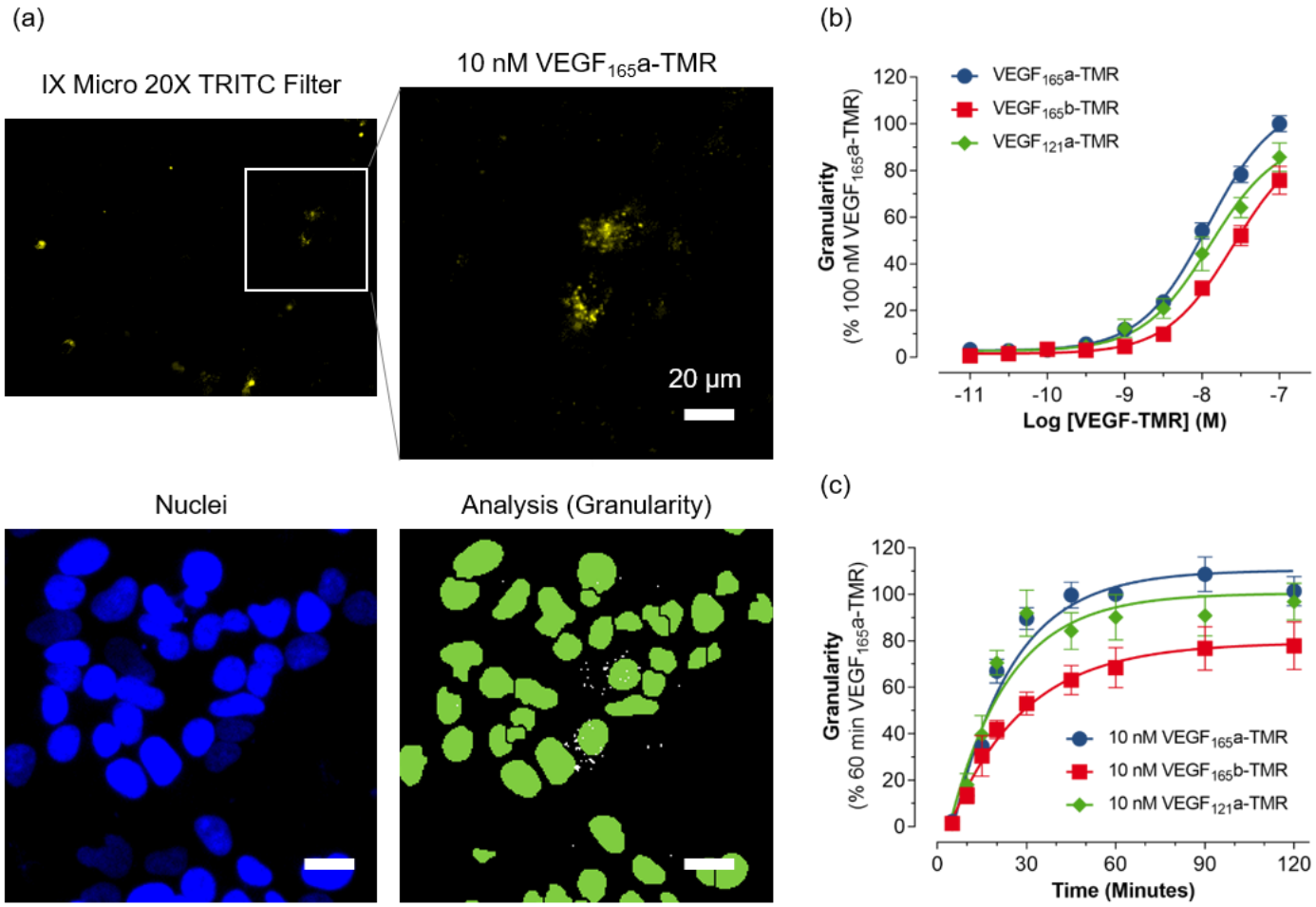


Figure 4.2 ***Using high-content imaging to quantify endocytosis of fluorescent ligand-receptor complexes****. See next page.*

Figure 4.2 Ctd. (a) HEK293T cells stably expressing NanoLuc-VEGFR2 were stimulated with 10 nM fluorescent $VEGF_{165}$a-TMR for 60 minutes at 37°C. Cells were fixed in 3% PFA in PBS and incubated with nuclear stain (H33342). The following day, cells were imaged at 4 sites per well with an ImageXpress Micro widefield platereader (20X objective). This used filter settings for TRITC (10 nM $VEGF_{165}$a-TMR) and DAPI (nuclei). Images were analysed using a granularity algorithm (Molecular Devices; Methods Figure 2.9b*). Nuclei were identified based upon their size (5-25 µm diameter) and pixel depth in grey levels (Analysis image, green). Fluorescent granules detected in the TRITC channel were defined based upon size (2-15 µm diameter) and pixel depth in grey levels (Analysis image, white spots). (b) Cells expressing NanoLuc-VEGFR2 were stimulated with increasing concentrations of fluorescent VEGF-A variants (60 minutes, 37°C). Data were normalised to the mean response per experiment to vehicle (0%) and 100 nM $VEGF_{165}$a-TMR (100%). (c) Timecourse of the appearance of $VEGF_{xxx}$x-TMR granules using the same cell lines. Cells were stimulated with 10 nM $VEGF_{165}$a-TMR, $VEGF_{165}$b-TMR, or $VEGF_{121}$a-TMR for 0-120 minutes at 37°C. Data were normalised to vehicle (0%) and 60 minute $VEGF_{165}$a-TMR stimulation (100%). Data are expressed as mean ± S.E.M. Data are pooled from 5 independent experiments with duplicate wells per replicate, each imaged at 4 sites per well.*

Table 4.1 ***Parameters for VEGFR2-mediated endocytosis of fluorescent VEGF-A-isoforms in HEK293T cells expressing NanoLuc-VEGFR2****.*

Ligand	pEC_{50}	Rate constant (k_{obs}, min^{-1})	Half time ($t_{1/2}$, min)
$VEGF_{165}$a-TMR	7.92 ± 0.07	0.04 ± 0.01	17.5 ± 1.87
$VEGF_{165}$b-TMR	7.54 ± 0.08 $^{\$}$	0.04 ± 0.01	19.8 ± 3.53
$VEGF_{121}$a-TMR	7.84 ± 0.14	0.05 ± 0.01	14.8 ± 2.11

Data represent mean ± S.E.M. from 5 separate experiments with duplicate wells and images obtained from 4 sites per well. Potency (pEC_{50}) values were derived from concentration-response data in *Figure 4.2b*. Kinetic parameters of k_{obs} were fit from *Figure 4.2c*. Half times ($t_{1/2}$) were fit assuming a first order reaction, calculated per experiment as $0.693/k_{obs}$. Statistical analysis for potencies were compared using a one-way ANOVA and Šidák's multiple comparisons test comparing pEC_{50} values to $VEGF_{165}$a-TMR ($^{\$}$ $P<0.05$). Statistical analysis for kinetic parameters were compared using a Kruskal-Wallis test (not significant).

We used confocal microscopy to further investigate the localisation of fluorescent VEGF-TMR in HEK293T cells expressing VEGFR2. Confocal imaging has better axial resolution through the central equatorial Z plane of the cell compared to widefield imaging. To identify whether fluorescent ligand was localised in early endosomes, immunofluorescent antibody labelling was used to localise endogenous Rab5 (*Methods 2.6.2*). HaloTag-VEGFR2 was first labelled with membrane-impermeant HaloTag-AlexaFluor647. Cells were then stimulated with 10 nM $VEGF_{121}$a-TMR as a representative fluorescent VEGF-A ligand. This was a saturating concentration sufficient to stimulate ligand/receptor internalisation (*Figure 4.2b*) and the decline in BRET signal (*Figure 4.1c*). These low-throughput studies monitored endocytosis at 60 minutes. As a negative control, cells were also incubated with ligand for 5 minutes. This time point was earlier than the time taken for $VEGF_{xxx}$x-TMR/NanoLuc-VEGFR2 ligand binding to reach equilibrium (*Figure 4.1*). This also preceded the appearance of intracellular granules of fluorescent VEGF-A in HEK293T cells expressing NanoLuc-VEGFR2 (*Figure 4.2)*, therefore allowing quantification of background colocalisation. Following ligand stimulation, cells were fixed and permeabilised. Rab5 was labelled with a monoclonal antibody and a secondary anti-rabbit AlexaFluor488 antibody. Control imaging experiments confirmed there was no spectral bleedthrough between these channels. Receptors were labelled with membrane-impermeant HaloTag substrate, showing further evidence of constitutive receptor internalisation (*Figure 4.3*). Representative images also show that $VEGF_{121}$a-TMR and HaloTag-VEGFR2 were localised at intracellular sites following incubation with VEGF-A for 60 minutes (*Figure 4.3*).

Qualitative fluorescence-based images were used for quantitative analysis to allow objective comparisons. The probability of whether two fluorophores cluster in the same region was determined by their degree of colocalisation. Pixel-based colocalisation analysis was used to investigate the presence of $VEGF_{121}$a-TMR and VEGFR2 in $Rab5^{+}$ endosomes (*Figure 4.4*). Colocalisation analysis was performed using the Coloc 2 plugin for ImageJ/Fiji (*Methods 2.10.3*). Two measures of pixel-based analyses can indicate either correlation or co-occurrence. Pearson's Correlation Coefficients measure the extent of the relationship between two fluorophores (Manders et al., 1992). This ranges between -1 (negative correlation) and 1 (positive correlation), while 0 denotes no colocalisation. As this considers the difference from average intensities, Pearson's Correlation Coefficients are subject to differences in fluorescence intensity. Co-occurrence can also be quantified with split Mander's Overlap Coefficients, quantifying how much signal from each channel overlap in the same region (Manders et al., 1993). Values range from 0 (no colocalisation) to 1 (perfect colocalisation), indicating the absence or presence of co-occurrence, respectively. These are split according to how much Channel A is in Channel B (M1), or how much Channel B is in Channel A (M2). M1 and M2 parameters are independent of fluorescence intensity.

Regions of Interest (ROIs) were drawn around cells positive for HaloTag-VEGFR2 expression. For clarity, only M1 values are shown to denote (i) the amount of Rab5 in ligand-positive regions, (ii) the amount of Rab5 in receptor-positive regions and (iii) the amount of receptor in ligand-positive regions. This accounts for there being increased non-specific signal in Channel A, such as the widespread endogenous expression of Rab5. Statistical tests compared Pearson's Correlation Coefficients or Mander's Overlap Coefficients using a two-way ANOVA (n=64 cells for 5 minute stimulation, n=68 cells for 60 minute stimulation). For each comparison, there was significant variation between both channel and time point variables (P<0.0001, n=64-68 per group). A post-Hoc Šidák's multiple comparisons test then compared each time point per channel (*Figure 4.4b,c*). This tested the null hypothesis that there was no difference in colocalisation following stimulation for 60 minutes compared to 5 minutes. There was increased colocalisation between ligand and receptor at 60 minutes for both colocalisation parameters (P<0.0001). The Mander's Overlap Coefficient was significantly increased between ligand and Rab5$^+$ endosomes after 60 minutes (P<0.0001). This suggested increased co-occurrence, but the absence of a correlation between ligand and Rab5$^+$ immunolabelling. There was also a decrease in both colocalisation parameters between receptor and Rab5 after 60 minutes (P<0.05). This could reflect trafficking away from Rab5$^+$ compartments by 60 minutes, thus consistent with VEGFR2 recycling back to the plasma membrane that was previously observed using super resolution imaging after 60 minutes (Kilpatrick et al., 2017).

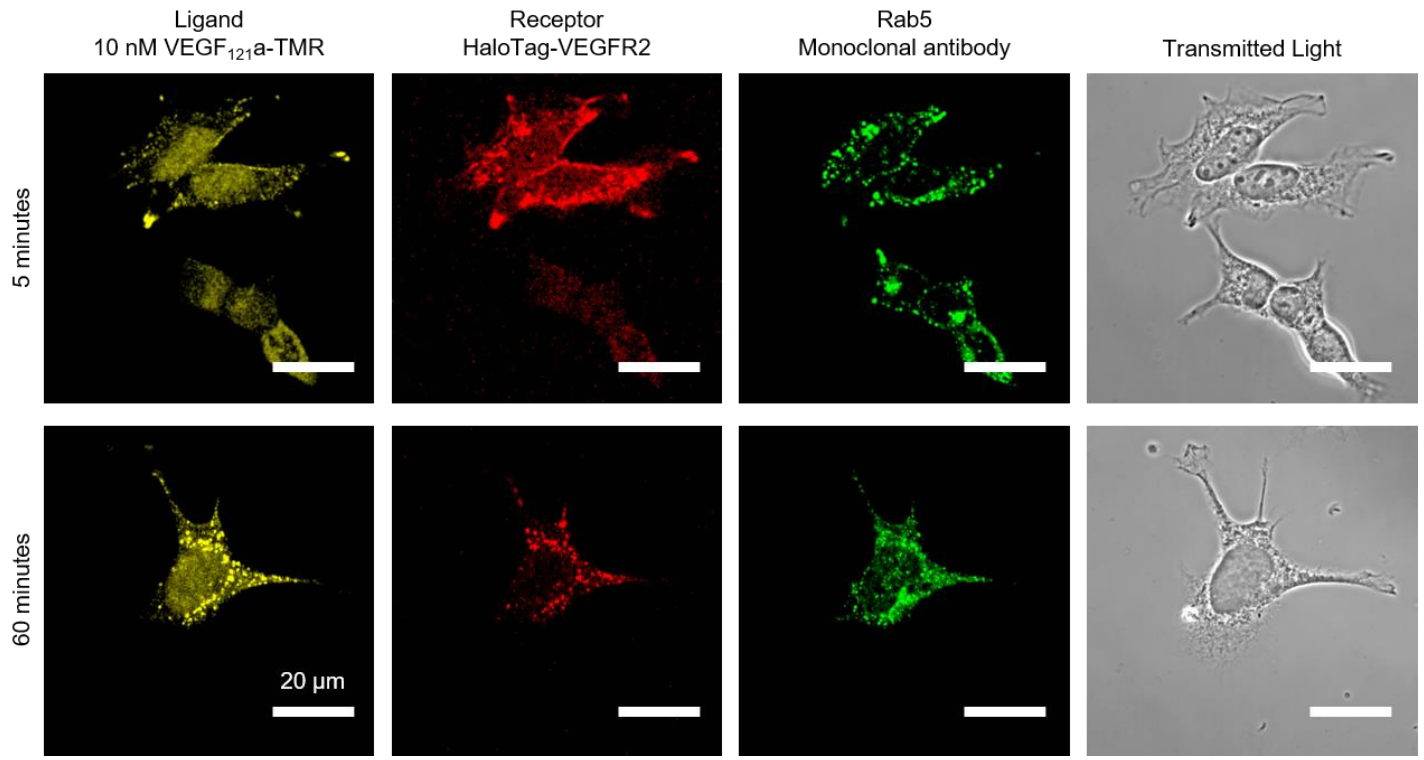


Figure 4.3 ***Localisation of VEGFR2, VEGF$_{121}$a-TMR and Rab5^{+} endosomes.*** *HEK293T cells stably expressed HaloTag-VEGFR2. Receptors were labelled with membrane impermeant HaloTag-AlexaFluor647 (red) for 30 minutes. Cells were washed in HBSS/0.1% BSA and stimulated with 10 nM VEGF$_{121}$a-TMR (yellow) for 5 minutes or 60 minutes at 37ºC. Cells were then fixed (3% PFA in PBS, 20 minutes) and permeabilised (0.025% Triton-X-100 in PBS, 10 minutes). Early endosomes were labelled with a primary monoclonal antibody against Rab5. This was labelled with a secondary AlexaFluor488-conjugated antibody (green). Coverslips were imaged using a Zeiss LSM880 Confocal (63X oil objective), with representative images obtained on the same day.*

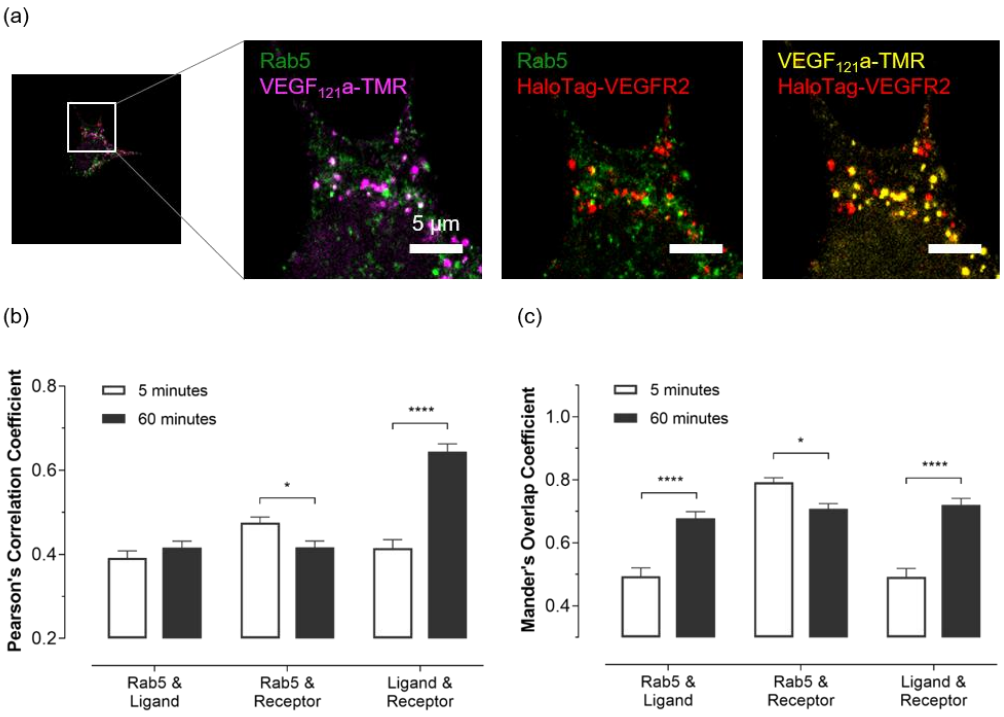


Figure 4.4 ***Colocalisation analysis of VEGFR2 and VEGF$_{121}$a-TMR in Rab5^{+} endosomes****. (a) Images were obtained using the Zeiss LSM880 Confocal, as in* Figure 4.3*. ImageJ software was used to analyse images with channels corresponding to ligand (10 nM VEGF$_{121}$a-TMR), receptor (HaloTag-VEGFR2 AlexaFluor647) and Rab5 (monoclonal antibody indirectly labelled with AlexaFluor488). An example of regions of spatial overlay between ligand and Rab5 are visualised as white regions in the first image. (b,c) Colocalisation parameters were quantified based on regions of interest drawn around cells that expressed HaloTag-VEGFR2. Pearson's Correlation Coefficients (b) and Mander's Overlap Coefficients (c) are pixel-based analyses of colocalisation between 2 fluorophores. Both parameters were compared between 5 minutes and 60 minutes. All coefficient values were pooled from 5 independent experiments, with a total of 68 cells (5 minute stimulation) or 64 cells (60 minute stimulation). Coefficients were compared using a two-way ANOVA (P<0.0001, n=64-68 per group). Each parameter was compared between different time points using a post-Hoc Šidák's multiple comparisons test (* P<0.05; **** P<0.0001).*

Influence of VEGFR2 phosphorylation on endocytosis

Kilpatrick et al. (2017) demonstrated that pre-incubation with RTKIs reduced VEGFR2 endocytosis in HEK293T cells, however inhibitors can have non-specific effects. We used two approaches to probe the effect of tyrosine phosphorylation on the spatiotemporal dynamics of VEGFR2. First, VEGFR2 phosphorylation was inhibited pharmacologically using cediranib, a Class I/IV RTKI (Wedge et al., 2005; McTigue et al., 2012). HEK293T cells expressing HaloTag-VEGFR2 were pre-incubated with 1 µM cediranib for 30 minutes (*Figure 4.5a*). Signalling was monitored using the NFAT reporter gene assay downstream of Ca^{2+} (*Figure 4.5b*; *Methods 2.7.1*). We confirmed that increasing concentrations of cediranib inhibited NFAT reporter gene signalling in response to 10 nM $VEGF_{165}$a (Cediranib pIC_{50} = 8.56 ± 0.34, n=3). To investigate constitutive VEGFR2 endocytosis, HaloTag-VEGFR2 receptors were expressed in HEK293T cells and labelled with a membrane-impermeant substrate (*Methods 2.6.1*). Pre-incubation with 1 µM cediranib prevented the constitutive endocytosis of VEGFR2 (*Figure 4.5c*). This was similar to the effect seen in the presence of $VEGF_{165}$a-TMR (Kilpatrick et al., 2017), in which HEK293T cells expressing VEGFR2 were also pre-incubated with 1 µM cediranib for 30 minutes.

Second, we directly investigated the effect of inhibiting VEGFR2 tyrosine phosphorylation using site-directed mutagenesis (*Methods 2.3.3*). Key tyrosine residues that initiate VEGFR2 signalling were mutated to phenylalanine (Y951F, Y1054F, Y1059F, Y1175F, Y1214F). This mutant is referred to herein as tyrosine phosphorylation deficient VEGFR2 (VEGFR2 TPD; *Figure 4.6a*). Phenylalanine has a similar benzene ring side chain to maintain structural integrity, but lacks the tyrosine hydroxyl group for phosphoryl group attachment (*Introduction Figure 1.2c*). Signalling was monitored using the NFAT reporter gene assay. This compared the ability of mutant receptors to signal in response to increasing concentrations of $VEGF_{165}$a with that of wild type (WT) receptors (*Figure 4.6b*; n=3). HEK293T cells were transiently transfected with either HaloTag-VEGFR2 WT, mutant receptors containing single or double amino acid point mutations (Y1054/1059F, Y951F, Y1175F, Y1214F) or the complete TPD mutant. In each assay, we confirmed receptors were transported to the plasma membrane using the membrane-impermeant HaloTag-AlexaFluor488 substrate (data not shown). $VEGF_{165}$a stimulated NFAT signalling with a similar potency for VEGFR2 WT (pEC_{50} = 10.23 ± 0.15), Y951F (pEC_{50} = 10.06 ± 0.02) and Y1214F (pEC_{50} = 10.40 ± 0.21). There was NFAT reporter gene signalling detected for VEGFR2 receptors with mutations in the activation loop (Y1054/Y1059F), phosphorylated Y1175 or the complete TPD mutant. We also used live cell confocal microscopy to determine the localisation of VEGFR2 TPD compared to WT using membrane-impermeant HaloTag AlexaFluor488 substrate (*Figure 4.6c*). These data illustrate that VEGFR2 TPD receptors were still subject to constitutive endocytosis in the absence of ligand.

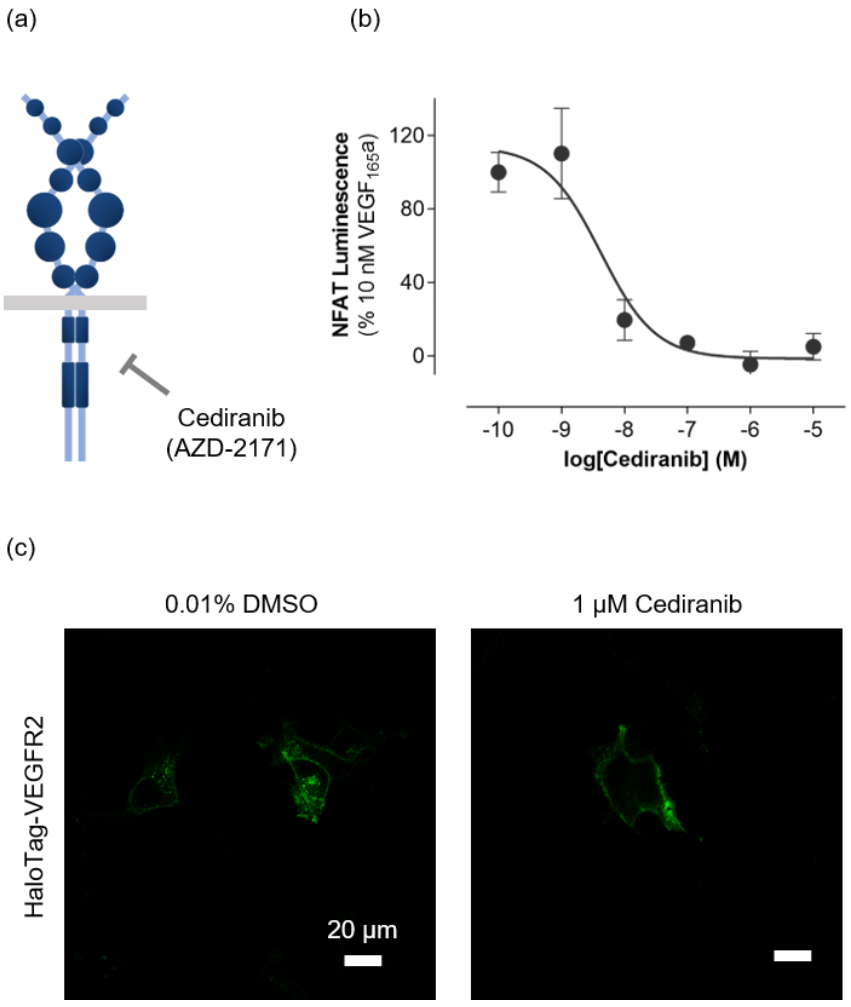


Figure 4.5 ***Cediranib inhibited VEGF$_{165}$a-induced signalling and constitutive VEGFR2 endocytosis****. (a) Schematic representing the mechanism of cediranib, an RTKI binding the intracellular ATP binding site. (b) HEK293T-ReLuc2P cells stably expressed HaloTag-VEGFR2. Cells were pre-incubated for 30 minutes with increasing concentrations of cediranib, then stimulated with 10 nM VEGF$_{165}$a for 5 hours at 37°C. Data were normalised per experiment to vehicle (0%) or 10 nM VEGF$_{165}$a (100%). Data are shown as mean ± S.E.M. pooled from 3 independent experiments with duplicate wells. (c) HEK293T-ReLuc2P cells expressing HaloTag-VEGFR2 were pre-labelled with 0.5 µM HaloTag-AlexaFluor488, in the absence or presence of 1 µM cediranib. Medium was replaced with HBSS/0.1% BSA following 30 minutes, maintaining the absence or presence of 1 µM cediranib. Images were obtained using the Zeiss LSM710 Confocal (40X objective). Images are representative from 3 independent experiments.*

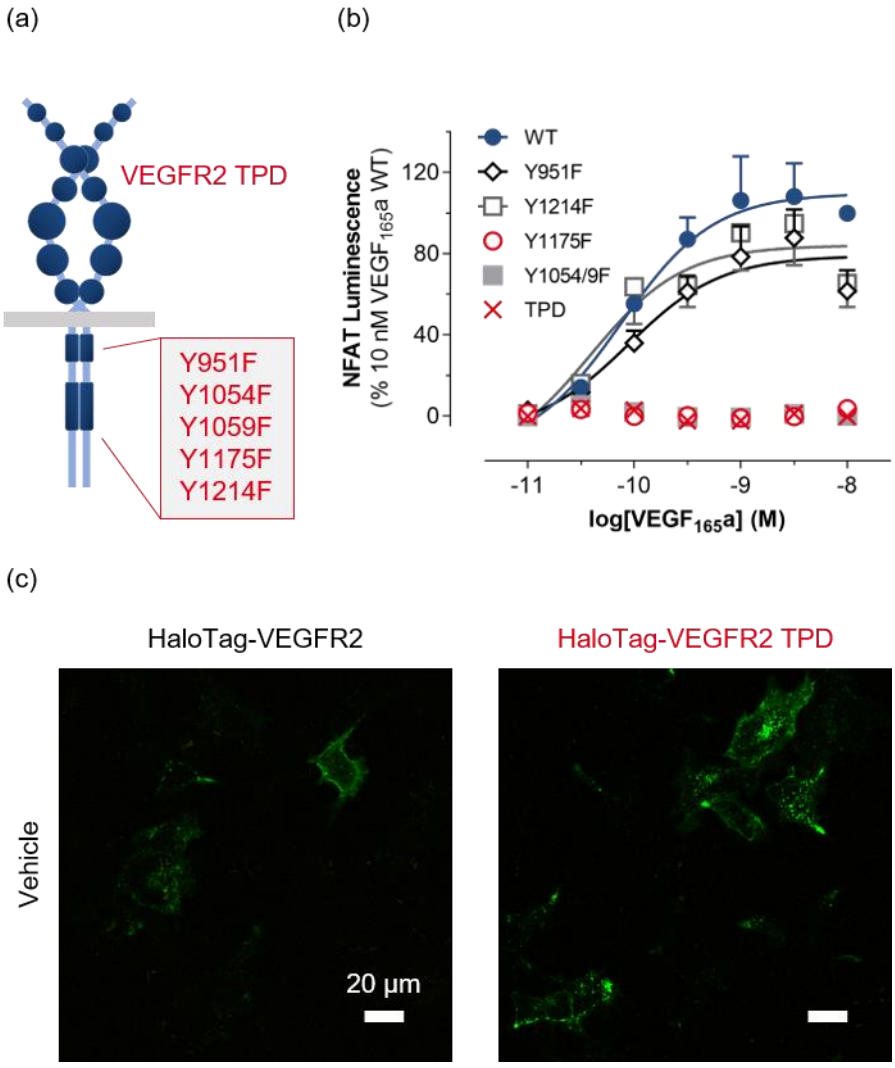


Figure 4.6 ***Characterising novel VEGFR2 mutant receptors that lack tyrosine phosphorylation****. (a) Schematic of the VEGFR2 tyrosine phosphorylation deficient mutant (VEGFR2 TPD). This receptor has 5 single point mutants, however single and double mutants were also made. (b) HEK293T-ReLuc2P cells transiently expressed HaloTag-VEGFR2 mutants or wild type (WT). Cells were stimulated with increasing concentrations VEGF$_{165}$a for 5 hours at 37°C. Data were normalised per experiment to vehicle (0%) or 10 nM VEGF$_{165}$a in cells expressing HaloTag-VEGFR2 WT (100%). Data were pooled from 3 independent experiments with duplicate wells. (c) HEK293T-ReLuc2P cells transiently expressed HaloTag-VEGFR2 WT or TPD. Receptors were labelled with 0.5 µM HaloTag-AlexaFluor488 for 30 minutes. Cells were washed in HBSS/0.1% BSA and imaged using the LSM710 Confocal (40X objective). Images are representative from 3 independent experiments.*

To gain insight into VEGFR2 TPD ligand/receptor endocytosis, colocalisation analysis was performed between the ligand, receptor and immunofluorescent labelling of Rab5. HEK293T cells expressing HaloTag-VEGFR2 TPD were labelled with HaloTag-AlexaFluor647 for confocal microscopy in parallel experiments to WT (*Figure 4.3, Figure 4.4*). Likewise, cells were stimulated for 5 minutes or 60 minutes with 10 nM $VEGF_{121}$a-TMR. Cells were then fixed, permeabilised and $Rab5^+$ compartments were localised using a monoclonal antibody labelled with secondary antibody conjugated to AlexaFluor488 (*Figure 4.7a*). The membrane-impermeant HaloTag substrate demonstrated that this stable HEK293T cell line successfully exported HaloTag-VEGFR2 TPD to the plasma membrane. There was also evidence for constitutive endocytosis at the 5 minute time point. Following 60 minutes, $VEGF_{121}$a-TMR and HaloTag-VEGFR2 TPD were localised to intracellular sites that overlay with Rab5. These data suggested that VEGFR2 receptors lacking key phosphorylation sites continued to internalise fluorescent VEGF-A.

Colocalisation parameters, Pearson's Correlation Coefficients and Mander's Overlap Coefficients, were compared using a two-way ANOVA (n=68 cells for 5 minute stimulation, n=63 cells for 60 minute stimulation). For each comparison, there was significant variation between both the channels and time points (P<0.0001, n=63-68 per group). A post-Hoc Šidák's multiple comparisons test then compared each time point per channel (*Figure 4.7b,c*). There was increased ligand/receptor colocalisation following 60 minute stimulation (P<0.0001). For both colocalisation parameters, there was also increased ligand/Rab5 colocalisation at 60 minutes compared to 5 minutes (P<0.0001). In contrast to HaloTag-VEGFR2 WT (*Figure 4.4b,c*), there was no significant decrease in HaloTag-VEGFR2 TPD localisation in $Rab5^+$ endosomes following 60 minute stimulation for both parameters (P>0.05).

Colocalisation coefficients were directly compared between studies investigating VEGFR2 WT and TPD as immunofluorescent antibody experiments and imaging had been performed at the same time. First, we compared the average fluorescence intensities of the HaloTag-AlexaFluor647 channel to indicate whether cell lines had different expression in stable HEK293T cell lines. There was no statistically significant difference in the average fluorescence intensities of all ROIs (HaloTag-VEGFR2 WT 11.86 ± 1.0 relative fluorescent units (RFU), vs. HaloTag-VEGFR2 TPD 11.28 ± 0.8 RFU; Mann-Whitney test P>0.05, n=147 per condition with no excluded cells). Data were then compared using a two-way ANOVA, with a significant difference between both the channels and experimental conditions (P<0.0001, n=147 per group). A post-Hoc Tukey's multiple comparisons compared colocalisation parameters between WT and TPD cell lines. There were distinctions between VEGFR2 WT and TPD with regards to Pearson's Correlation Coefficients after 60 minutes for Rab5/receptor colocalisation (P<0.05, n=63-64 per group) and ligand/receptor colocalisation (P<0.05).

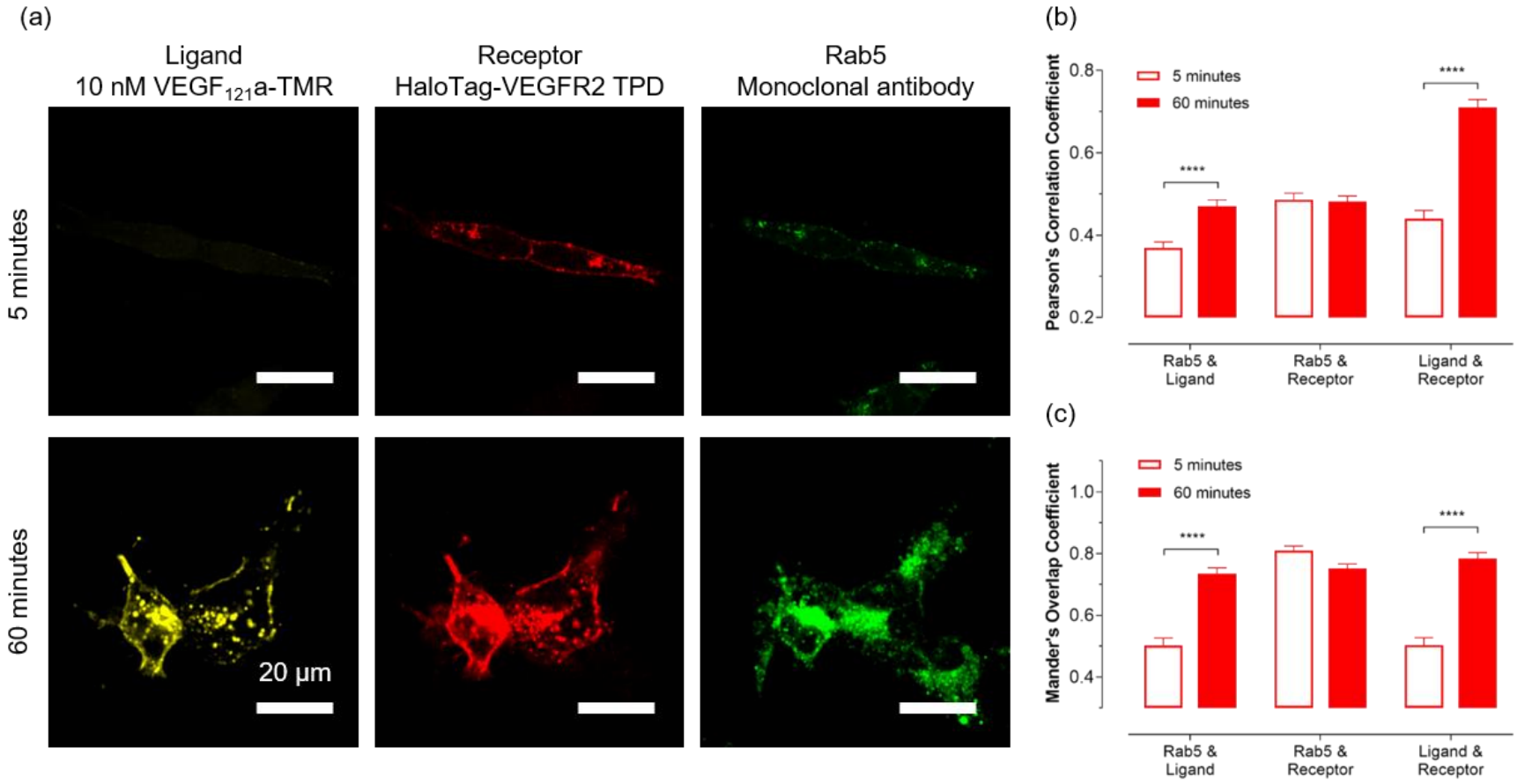


Figure 4.7 ***Colocalisation between VEGFR2 TPD, fluorescent VEGF$_{121}$a-TMR and Rab5****. See next page.*

Figure 4.7 Ctd. (a) HEK293T cells stably expressed HaloTag-VEGFR2-TPD. Receptors were labelled with membrane impermeant HaloTag-AlexaFluorAF647 for 60 minutes then washed in HBSS/0.1% BSA. Cells were then stimulated with 10 nM $VEGF_{121}$a-TMR for 5 minutes or 60 minutes at 37ºC. Following cell fixation and permeabilisation, early endosomes were labelled with a monoclonal primary antibody against Rab5 and a secondary antibody conjugated to AlexaFluor488. Cells were imaged using a Zeiss LSM880 Confocal (63X oil objective). Images are representative from 5 independent experiments. (b) ImageJ software was used for colocalisation analysis, as in Figure 4.4*. These data show the Pearson's Correlation Coefficient (b) and Mander's Overlap Coefficient (c). Data were pooled from 5 independent experiments, with a total of 68 cells (5 minute stimulation) or 63 cells (60 minute stimulation). Coefficients were compared using a two-way ANOVA (P<0.05, n=63-68 per group), using a post-Hoc Šidák's multiple comparisons (**** P<0.0001).*

Monitoring ligand binding in the absence of VEGFR2 phosphorylation using BRET

Ligand binding dynamics were compared in the presence or absence of tyrosine phosphorylation using VEGFR2 TPD tagged at the N-terminus with NanoLuc. NanoLuc-VEGFR2 WT or NanoLuc-VEGFR2 TPD receptors were transiently transfected into HEK293T cells (*Methods 2.8.2*). There was an elevation in BRET signal at NanoLuc-VEGFR2 TPD observed for both 3 nM and 20 nM $VEGF_{121}$a-TMR (*Figure 4.8a,b*, n=8). There was a decline in BRET signal for NanoLuc-VEGFR2 TPD after the initial peak at 20 minutes, with a similar dynamic profile to WT. At the 20 minute peak for 20 nM $VEGF_{121}$a-TMR, BRET ratios were elevated by 1.32 ± 0.06-fold at NanoLuc-VEGFR2 TPD compared to WT (n=8). BRET ratios were significantly elevated at this 20 minute peak comparing VEGFR2 WT and TPD (Wilcoxon matched-pairs signed rank test, $P<0.01$, n=5 per group). An elevated BRET ratio upon inhibition of tyrosine phosphorylation was consistent with previous observations obtained with RTKIs (Kilpatrick et al., 2017). Transient transfections allowed the relative expression of receptors to differ between experimental replicates. This was quantified by comparing emissions from the NanoLuc tag in the presence of furimazine. Luminescence emissions were compared for each experimental replicate, as in *Figure 4.8c* (duplicate wells). The elevated BRET signal of $VEGF_{121}$a-TMR binding did not result from differences in luminescent donor expression, as this was repeated with numerous relative levels of NanoLuc-VEGFR2 WT to NanoLuc-VEGFR2 TPD. Each replicate had an elevated BRET ratio despite similar baseline BRET ratios at x=0, as in *Figure 4.8d* (duplicate wells).

Ligand binding was also monitored in the presence of cediranib as a non-selective approach to inhibit VEGFR2 phosphorylation. Cells stably expressing NanoLuc-VEGFR2 were pre-incubated with 1 μM cediranib, or 0.01% DMSO, for 30 minutes. Cediranib-treated cells had an elevated BRET signal at both 5 nM and 20 nM $VEGF_{165}$b-TMR relative to DMSO (*Figure 4.9a-b*). There was a 1.12 ± 0.03 fold (n=5) elevation at the 20 minute peak. While this was also elevated, the difference in BRET ratios were not statistically significant (Wilcoxon matched-pairs signed rank test, $P>0.05$, n=5 per group). The BRET profile decreased following the peak at 20 minutes in the presence of cediranib. Kinetic parameters were derived using a global fit with four concentrations of $VEGF_{165}$b-TMR from the initial 20 minute association. This approach used matched controls pre-incubated with 0.01% DMSO (*Figure 4.9c*) or 1 μM cediranib (*Figure 4.9d*). There was a similar dissociation rate constant of $VEGF_{165}$b-TMR from NanoLuc-VEGFR2 in both conditions (DMSO k_{off} = 0.081 ± 0.009 min^{-1}; cediranib k_{off} = 0.091 ± 0.015 min^{-1}; n=5). $VEGF_{165}$b-TMR had a slower association rate constant in the presence of cediranib (DMSO k_{on} = $4.26x10^6$ ± $0.50x10^6$ $min^{-1}M^{-1}$; cediranib k_{on} = $2.63x10^6$ ± $0.51x10^6$ $min^{-1}M^{-1}$; n=5), however there was no significant difference using matched statistical analyses (Wilcoxon matched-pairs signed rank test, $P>0.05$, n=5 per group).

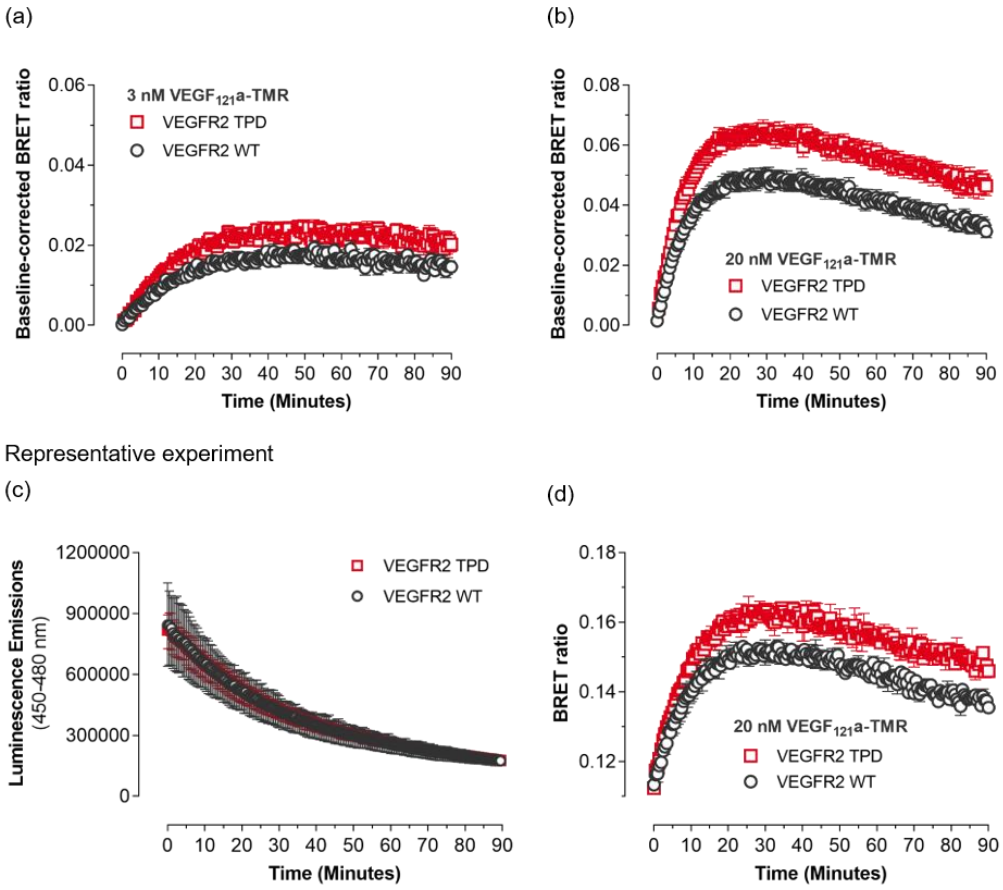


Figure 4.8 ***Timecourse of VEGF$_{121}$a-TMR binding in cells expressing tyrosine phosphorylation deficient NanoLuc-VEGFR2****. HEK293T cells were transiently transfected with NanoLuc-VEGFR2 wild type (WT) or tyrosine phosphorylation deficient VEGFR2 (TPD) at 100 ng cDNA/well. Cells were pre-treated with furimazine for 5 minutes, then (a) 3 nM or (b) 20 nM VEGF$_{121}$a-TMR was added at x=0. BRET ratios were monitored every 30 seconds at 37ºC using a PHERAstar platereader. BRET ratios were baseline-corrected to vehicle at each time point. Data are expressed as mean ± S.E.M. from 8 independent experiments with duplicate wells. (c) In each experiment, luminescence emissions were compared to indicate their relative expression given the variability of transiently transfecting NanoLuc-tagged receptors. In this representative dataset, expression was similar for WT and TPD. (d) In the same example, there was an elevated BRET ratio despite identical luminescent donor emissions. Data from the same representative experiment (c,d) are shown as mean ± range from duplicate wells.*

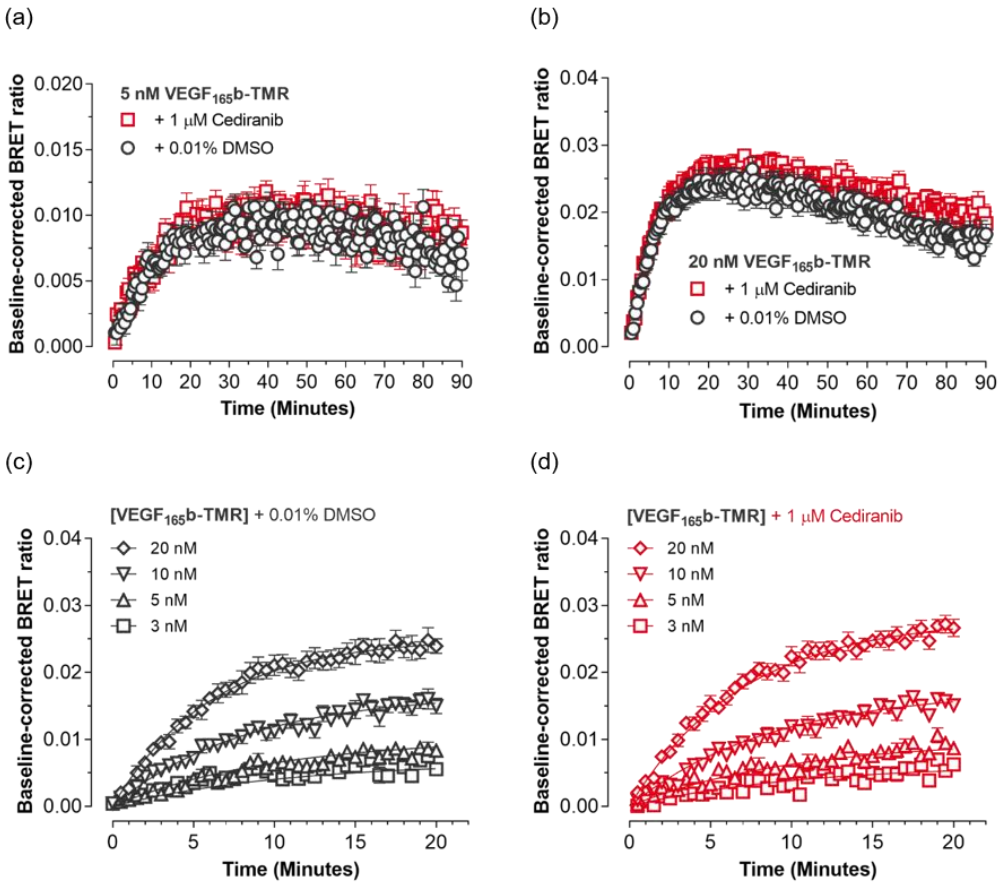


Figure 4.9 ***Timecourse of VEGF$_{165}$b-TMR binding in cells pre-treated with cediranib, an RTKI inhibiting VEGFR2 phosphorylation****. HEK293T cells stably expressed NanoLuc-VEGFR2. Cells were pre-treated with 1 μM cediranib or 0.01% DMSO (negative control) for 30 minutes at 37°C. Having added furimazine for 5 minutes, the real-time binding of (a) 5 nM or (b) 20 nM VEGF$_{165}$b-TMR was monitored every 30 seconds for 90 minutes at 37°C. (c,d) Association binding curves were analysed using a global fit to 4 concentrations of VEGF$_{165}$b-TMR. Curves were fit from data obtained from the initial 20 minutes of incubation with VEGF$_{165}$b-TMR, prior to the decline in BRET signal. The data for 5 nM and 20 nM are plotted in (a) and (b). Data are shown as mean ± S.E.M. from 5 independent experiments with duplicate wells measured in each individual experiment. Kinetic parameters are noted in the text.*

Using membrane preparations to probe ligand binding and the effect of pH

In intact cells, receptors are subject to trafficking (endocytosis, recycling and lysosomal degradation), ligand degradation and interactions with intracellular effectors. Monitoring ligand binding in living cells reflect their native cellular environment, however the resulting decline in BRET between $VEGF_{xxx}$x-TMR and NanoLuc-VEGFR2 prevents the system from reaching equilibrium. The ability for agonists to stimulate receptor endocytosis in living cells led to the development of fluorescent antagonists to probe receptors (Bylund and Toews, 1993), however no orthosteric antagonist has been identified for VEGFR2. To inhibit VEGF-A/VEGFR2 endocytosis using approaches that maintain the system at 37°C for studying dynamics, we prepared homogenised membranes (*Methods 2.4.3*). These were from the same HEK293T cell line stably expressing NanoLuc-VEGFR2 in order to quantify ligand binding pharmacology at equilibrium using BRET. This experimental approach also investigated NanoLuc-NRP1 as a negative control that reached equilibrium in intact cells.

We initially determined the influence of membrane concentration on the BRET signal for both NanoLuc-VEGFR2 and NanoLuc-NRP1 (*Methods 2.8.1*). This was compared in the presence and absence of saponin, a detergent that permeabilises the membrane if vesicles form in the membrane preparations (Seeman et al., 1973). We quantified protein concentrations using a BCA assay and plated membranes at concentrations between 2.5-20 µg protein. Luminescence emissions had a linear relationship with membrane concentration (*Figure 4.10*). This was observed for membranes expressing both NanoLuc-VEGFR2 (*Figure 4.10b*) and NanoLuc-NRP1 (*Figure 4.10e*). No differences were observed in luminescence emissions upon addition of saponin, likely because furimazine is membrane permeable. There was a consistent BRET ratio over different membrane concentrations (*Figure 4.10c, 4.10f*). BRET ratios were higher for both VEGFR2 and NRP1 upon addition of saponin. This effect was less pronounced at higher membrane concentrations. As there was sufficient signal to noise ratio in the absence of saponin, we did not include the detergent in subsequent experiments. We used membranes at 5 µg or 10 µg per well for equilibrium and kinetic experiments, respectively. This ensured there was sufficient membrane for each experiment from the same sample.

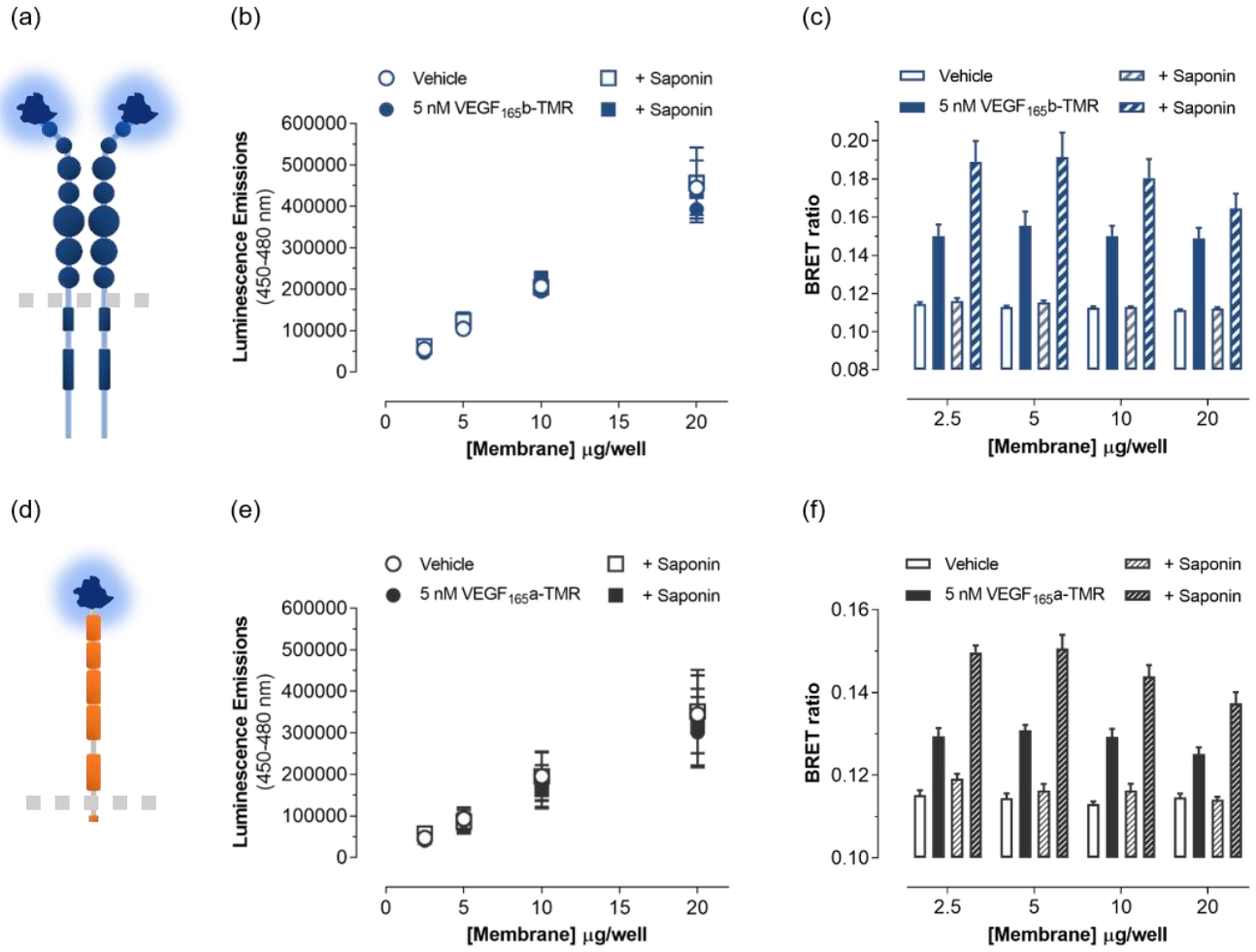


Figure 4.10 ***Influence of membrane concentration on the BRET signal with NanoLuc-VEGFR2 or NanoLuc-NRP1****. See next page.*

Figure 4.10. Ctd. Membranes were homogenised from HEK293T cells stably expressing NanoLuc-VEGFR2 (a) or NanoLuc-NRP1 (d). Upon addition of furimazine, luminescence was emitted from NanoLuc-tagged receptors expressed in membrane preparations (left panel, dotted membrane). Increasing concentrations of membrane were prepared in HBSS/0.1% BSA, in the absence or presence of 0.25 mg/ml saponin. After 10 minutes, membranes were incubated for 60 minutes at 37°C with 5 nM $VEGF_{165}$b-TMR for NanoLuc-VEGFR2 (b,c) or 5 nM $VEGF_{165}$a-TMR for NanoLuc-NRP1 (e,f). The middle panel represents luminescence emissions only, while the right panel illustrates raw BRET ratios. All BRET data were obtained using the same filter for each receptor (550 LP/460-80 nm). Data are expressed as mean ± S.E.M. and pooled from 5 independent experiments with duplicate wells. Independent experiments used separate membrane preparations from a distinct cell passage.

BRET was used to estimate the binding affinities of VEGF-A isoforms in membrane preparations at 60 minutes. Saturation binding experiments used increasing concentrations of fluorescent VEGF-A. There was clear saturable binding for each fluorescent isoform at NanoLuc-VEGFR2 (*Figure 4.11a-c*) and $VEGF_{165}$a-TMR at NanoLuc-NRP1 (*Figure 4.11d*). There was low non-specific binding in each case in the presence of unlabelled competitor. Equilibrium binding experiments in membrane preparations obtained K_d values that were significantly higher affinity than those derived in intact cells in Chapter 3 (*Table 4.2*; unpaired t-test, *P* values in *Table 4.2*).

Competition binding experiments were also performed in membrane preparations to determine the affinity of unlabelled VEGF-A. In membranes expressing NanoLuc-VEGFR2, we used multiple concentrations of $VEGF_{165}$a-TMR, $VEGF_{165}$b-TMR and $VEGF_{121}$a-TMR as fluorescent probes with increasing concentrations of VEGF-Ax (*Figure 4.12a-c*). These experiments yielded similar nanomolar affinities for VEGF-Ax (*Table 4.2*). Affinities were higher in membrane preparations than those derived in intact cells (*Table 4.2*). The affinity of unlabelled $VEGF_{165}$a at NanoLuc-NRP1 was also determined in membranes using $VEGF_{165}$a-TMR as a probe (*Figure 4.12d, Table 4.2*).

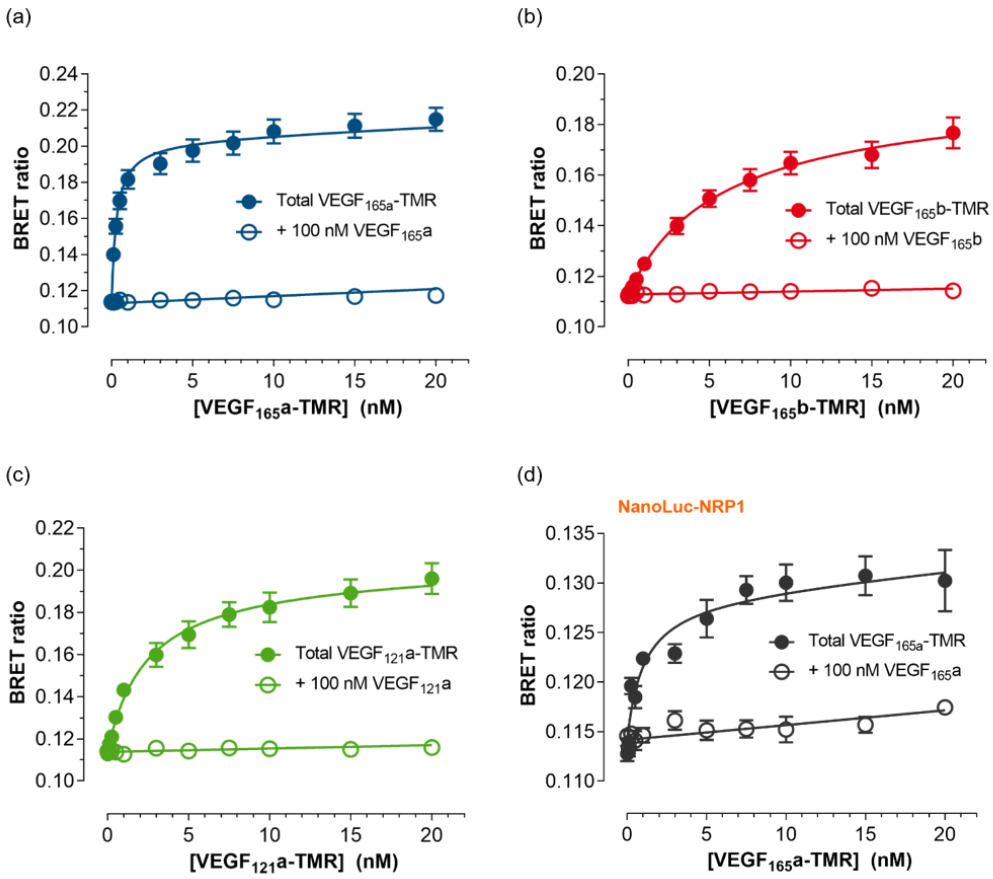


Figure 4.11 ***Saturation binding of fluorescent VEGF-A isoforms in membrane preparations****. Membranes were homogenised from HEK293T cells stably expressing NanoLuc-VEGFR2 (a-c) or NanoLuc-NRP1 (d). Membranes were plated at 5 µg protein/well. Membranes were incubated with increasing concentrations of* $VEGF_{165}$*a-TMR (a,d),* $VEGF_{165}$*b-TMR (b) and* $VEGF_{121}$*a-TMR (c) for 60 minutes at 37°C. Non-specific binding was determined using 100 nM unlabelled* $VEGF_{xxx}$*x (R&D Systems), added simultaneously with the fluorescent ligand. Raw BRET ratios are expressed as mean ± S.E.M. from 5 (NanoLuc-VEGFR2) or 4 (NanoLuc-NRP1) independent experiments, each with duplicate wells. Derived equilibrium dissociation constants (*pK_d*) are shown in* Table 4.2.

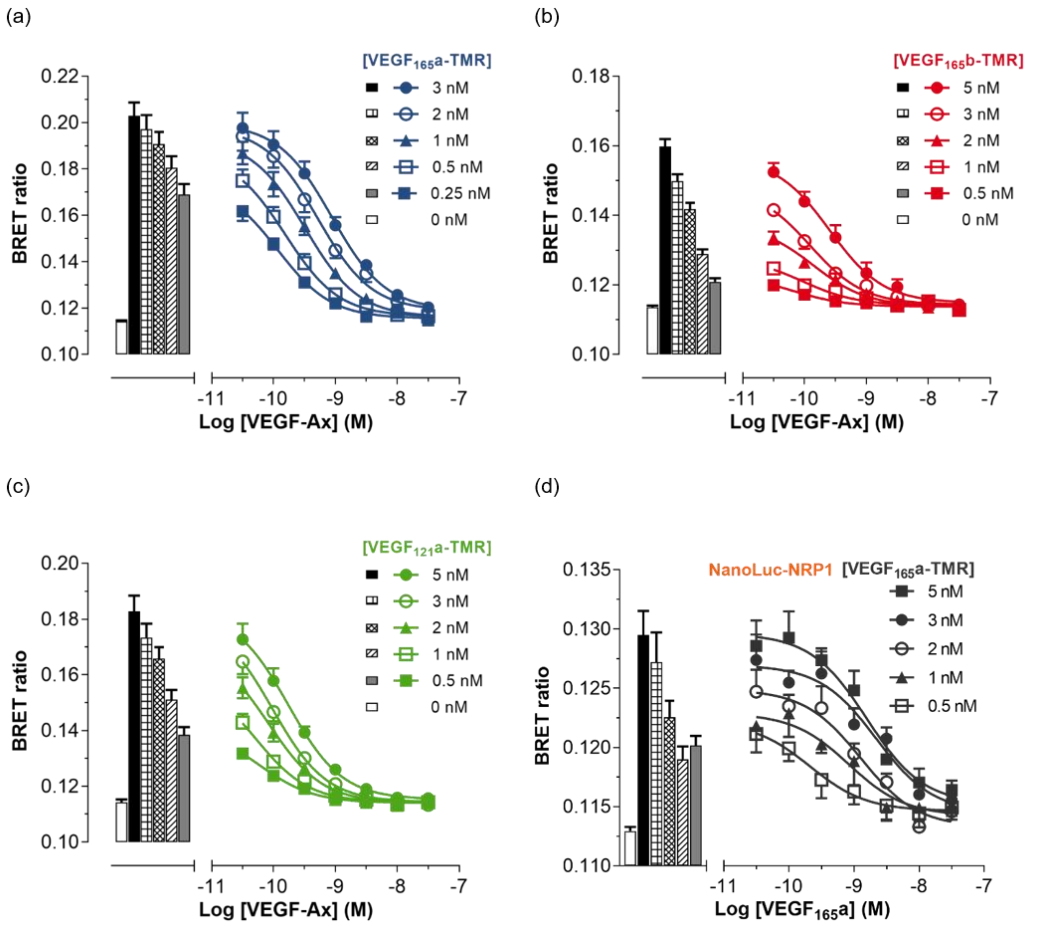


Figure 4.12 ***Displacement of fluorescent VEGF-A isoforms by unlabelled VEGF-A in membrane preparations****. Membranes were homogenised from HEK293T cells stably expressing NanoLuc-VEGFR2 (a-c) or NanoLuc-NRP1 (d). Membranes were plated at 5 µg protein/well. (a-c) Increasing concentrations of VEGF-Ax were used to displace 5 fixed concentrations of (a) $VEGF_{165}$a-TMR, (b) $VEGF_{165}$b-TMR and (c) $VEGF_{121}$a-TMR. (d) In membranes expressing NanoLuc-NRP1, increasing concentrations of unlabelled $VEGF_{165}$a were used to displace 5 concentrations of $VEGF_{165}$a-TMR. Ligands were added simultaneously and incubated for 60 minutes (37°C). Raw BRET ratios are expressed as mean ± S.E.M. from 4-6 independent experiments ((a) n=5, (b) n=6, (c) n=5, (d) n=4), each with duplicate wells. Bars represent vehicle only (white bars) or fluorescent ligand alone (filled bars). Derived equilibrium dissociation constants of unlabelled ligands (pK_i) are shown in* Table 4.2.

Table 4.2 ***Summary of binding affinities derived at equilibrium for fluorescent (pK_d) and unlabelled VEGF-A isoforms (pK_i), comparing membrane preparations and intact cells****.*

	Membranes	Intact Cells	Membranes	Intact Cells	Membranes	Intact Cells
NanoLuc-VEGFR2						
	Saturation K_d (nM)		Saturation pK_d		VEGF-Ax pK_i	
$VEGF_{165}$a-TMR	0.31 ± 0.06 (5)	2.03 ± 0.51 (5)	9.53 ± 0.07 (5)	8.75 ± 0.11 (5) $^{\$\$\$}$	10.18 ± 0.04 (5)	9.20 ± 0.02 (5) $^{\$\$\$\$}$
$VEGF_{165}$b-TMR	5.55 ± 0.47 (5)	9.53 ± 1.36 (5)	8.26 ± 0.04 (5)	8.04 ± 0.06 (5) $^{\$}$	9.96 ± 0.21 (6)	9.57 ± 0.03 (5)
$VEGF_{121}$a-TMR	2.58 ± 0.34 (5)	5.54 ± 1.34 (5)	8.60 ± 0.06 (5)	8.30 ± 0.08 (5) $^{\$}$	10.34 ± 0.08 (5)	9.65 ± 0.06 (5) $^{\$\$\$\$}$
NanoLuc-NRP1						
	Saturation K_d (nM)		Saturation pK_d		$VEGF_{165}$a pK_i	
$VEGF_{165}$a-TMR	1.06 ± 0.13 (3)	4.41 ± 1.34 (6)	8.98 ± 0.05 (3)	8.45 ± 0.13 (6) $^{\$}$	9.52 ± 0.08 (4)	*9.54 ± 0.21 (5)*

The number of independent experiments are given in the parentheses. Parameters were obtained in intact cells in Chapter 3 (NanoLuc-VEGFR2) or in similar experiments for NanoLuc-NRP1 by Dr Kilpatrick (*italicised*; published in Peach et al., 2018a). pK_i values were derived for unlabelled VEGF-Ax (NanoLuc-VEGFR2) or unlabelled $VEGF_{165}$a (NanoLuc-NRP1), both purchased from R&D Systems. pK_d and pK_i values were compared between cells and membranes using an unpaired t-test for each ligand ($^{\$}$ $P<0.05$, $^{\$\$\$}$ $P<0.001$, $^{\$\$\$\$}$ $P<0.0001$).

Membrane preparations were also used to monitor real-time ligand binding at 37°C. BRET binding profiles for a saturating concentration of $VEGF_{xxx}$x-TMR were compared in *Figure 4.13* between intact cells (left y axis) and membrane preparations (right y axis). Compared to intact cells expressing NanoLuc-VEGFR2, there was no decline in BRET ratio in membranes following the peak at 20 minutes (*Figure 4.13a-c*). In contrast, there was no difference in the BRET profile at NanoLuc-NRP1 comparing intact cells and membranes (*Figure 4.13d*). Binding profiles at NanoLuc-VEGFR2 were quantified using the same PHERAstar filter and gain settings, illustrating that BRET ratios were higher in membrane preparations compared to intact cells.

Membrane preparations were then used to quantify the kinetic parameters of fluorescent VEGF-A isoforms binding to NanoLuc-VEGFR2. All three fluorescent VEGF-A isoforms produced classic ligand binding association curves that, in contrast to studies in intact cells, were maintained for 90 minutes for four separate ligand concentrations (*Figure 4.14*). Kinetic association rate (k_{on}) and dissociation rate (k_{off}) constants were derived from a global association fit for the full 90 minute timecourse (*Table 4.3*). Kinetic parameters were compared between fluorescent VEGF-A ligands using a Kruskal-Wallis test. This highlighted differences between VEGF-A isoforms in the k_{on} (P<0.001, n=5 per group), whereby $VEGF_{165}$b-TMR had a significantly slower k_{on} than $VEGF_{165}$a-TMR in membrane preparations (P<0.01, n=5). The ratio of k_{off}/k_{on} provided an estimate of the kinetically derived K_d values ($VEGF_{165}$a-TMR K_d = 2.53 ± 0.28 nM; $VEGF_{165}$b-TMR K_d = 9.21 ± 2.53 nM; $VEGF_{121}$a-TMR K_d = 3.85 ± 0.61 nM; n=5).

Parameters were compared between those derived intact cells and membrane preparations (*Table 4.3).* These compared each fluorescent VEGF-A isoform in terms of their affinities (pK_d, unpaired t-test) or kinetic parameters (k_{on}, k_{off}, Mann-Whitney test). There were consistently slower k_{on} and k_{off} in membrane preparations compared to intact cells. For $VEGF_{121}$a-TMR, each kinetic parameter was significantly slower in membranes than intact cells (Mann-Whitney test, P<0.01, n=5). There was no difference between cells and membranes for kinetic parameters derived for $VEGF_{165}$a-TMR (Mann-Whitney test, P>0.05, n=5). While saturation binding experiments showed consistently higher affinities in membranes than intact cells for each fluorescent VEGF-A isoform, this difference was less pronounced when estimated from kinetic assays.

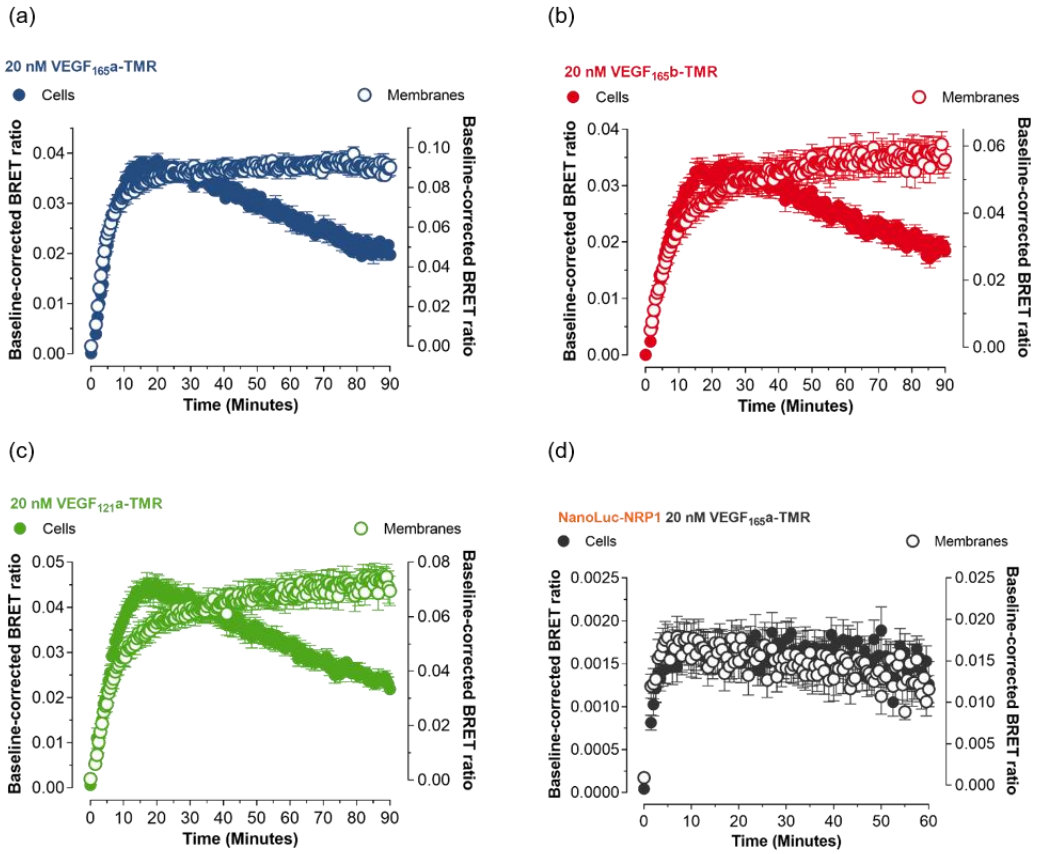


Figure 4.13 ***Comparing real-time BRET profiles between intact cells and membrane preparations.*** *HEK293T cells stably expressed NanoLuc-VEGFR2 (a-c) or NanoLuc-NRP1 (d). Kinetics were monitored in intact cells (left y axes, solid circles) or the same cell line homogenised to isolate crude membrane preparations (right y axes, open circles). Furimazine was added for 5 minutes to enable the NanoLuc to oxidise the substrate. A saturating concentration of (a,d) VEGF$_{165}$a-TMR, (b) VEGF$_{165}$b-TMR or (c) VEGF$_{121}$a-TMR was added at x=0. Cells were incubated for up to 90 minutes at 37°C. This was shown for the initial 60 minutes for NanoLuc-NRP1 due to increased noise. Emissions monitored in intact cells expressing NanoLuc-NRP1 were quantified using a 610-LP/460-480 nm filter for consistency with Dr Kilpatrick's previous work. All other BRET ratios used the 550-LP/450-480 nm filter. BRET ratios were calculated every 30 seconds and baseline-corrected to vehicle at each time point per experimental replicate. Data are shown as mean ± S.E.M. from 5 independent experiments, each with duplicate wells.*

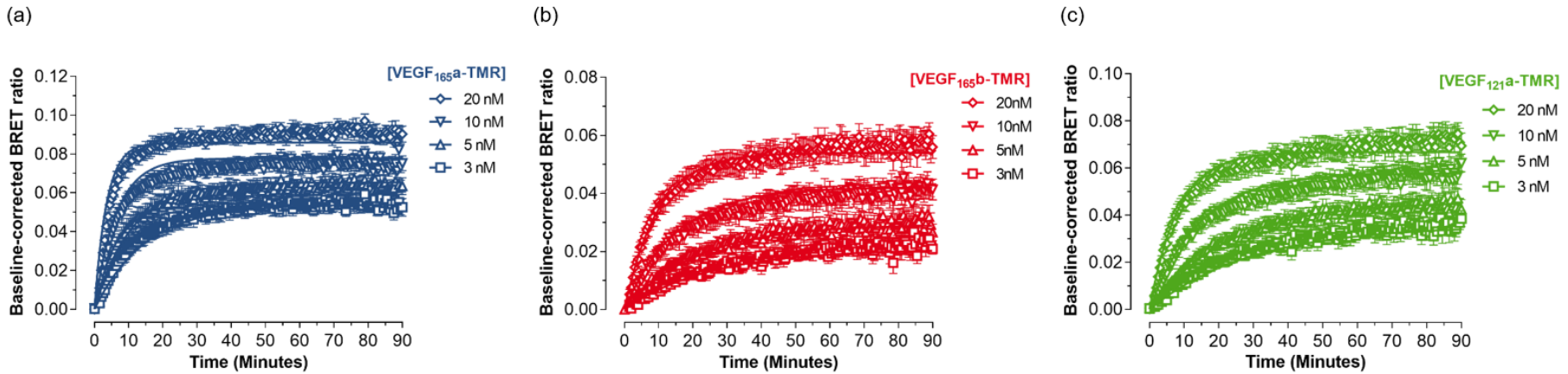


Figure 4.14 ***Kinetics of fluorescent VEGF-A isoforms binding NanoLuc-VEGFR2 in membrane preparations****. Membranes were homogenised from HEK293T cells stably expressing NanoLuc-VEGFR2 and plated at 10 µg protein/well. Membranes were pre-treated with furimazine for 5 minutes. Four concentrations of (a) $VEGF_{165}$a-TMR, (b) $VEGF_{165}$b-TMR or (c) $VEGF_{121}$a-TMR were added at x=0. Measurements were taken every 30 seconds for 90 minutes at 37°C. BRET ratios were baseline-corrected to vehicle at each time point. Data represent mean ± S.E.M. from 5 independent experiments with duplicate wells. Individual curves were fit with a simple association model, with derived kinetic parameters in* Table 4.3*.*

Table 4.3 ***Kinetic binding parameters derived at NanoLuc-VEGFR2 in membrane preparations compared to intact cells****.*

Ligand	Kinetic pK_d		k_{on} ($min^{-1}M^{-1}$)		k_{off} (min^{-1})		Residence time (min)		Half time, $t_{1/2}$ (min) at 10 nM	
	Membranes	Cells	Membranes	Cells	Membranes	Cells	Membranes	Cells	Membranes	Cells
$VEGF_{165}$a-TMR	8.61 ± 0.05	8.47 ± 0.23	$1.27x10^7$ ± $0.24x10^7$	$1.54x10^7$ ± $0.38x10^7$	0.030 ± 0.001	0.055 ± 0.017	33.95 ± 1.13	28.49 ± 9.15	4.76 ± 0.54	3.64 ± 0.45
$VEGF_{165}$b-TMR	8.09 ± 0.10	8.07 ± 0.18	$3.69x10^6$ ± $0.67x10^6$	$7.29x10^6$ ± $1.84x10^6$	0.029 ± 0.004	0.060 ± 0.011	37.38 ± 5.19	19.50 ± 4.16	11.31 ± 1.42	5.34 ± 0.38 **
$VEGF_{121}$a-TMR	8.44 ± 0.07	8.24 ± 0.03 $^{\$}$	$5.13x10^6$ ± $0.48x10^6$	$8.51x10^6$ ± $0.81x10^6$ **	0.019 ± 0.002	0.048 ± 0.002 **	55.70 ± 5.77	21.15 ± 1.09 **	10.10 ± 0.78	5.32 ± 0.35 **

Kinetic binding parameters were derived from association binding kinetics fit to 90 minutes in membrane preparations (*Figure 4.14*) or the initial 20 minutes in intact cells (*Figure 3.16*). Residence times and half times at the receptor were calculated from the k_{obs} derived from each experiment, as opposed to estimates from the pooled k_{on} or k_{off} in Peach et al. (2019). Data are shown as mean ± S.E.M. from 5 independent experiments, each with duplicate wells. Statistical tests comparing fluorescent VEGF-A isofroms are noted in the Results text. Statistical tests displayed in the table compared parameters between membranes and intact cells. pK_d values, the negative log of the K_d, were compared using an unpaired t-test ($^{\$}$ $P<0.05$). All other kinetic parameters were compared using a Mann-Whitney test (** $P<0.01$).

Membrane preparations were used to compare ligand binding kinetics in the absence of VEGFR2 phosphorylation. First, ligand binding kinetics were quantified at NanoLuc-VEGFR2 TPD. A stable cell line was generated for these experiments, although expression was lower than cell lines used for membranes expressing NanoLuc-VEGFR2 WT. BRET binding profiles for 20 nM $VEGF_{121}$a-TMR were crudely compared in membrane preparations between NanoLuc-VEGFR2 TPD (*Figure 4.15a*, left y axis) and NanoLuc-VEGFR2 WT (right y axis). In both preparations, the BRET profile remained elevated for the 90 minute timecourse. Kinetic parameters were derived for NanoLuc-VEGFR2 TPD using four concentrations of $VEGF_{121}$a-TMR for a global association fit (*Figure 4.15b*). These were compared to the kinetics derived in membrane preparations for $VEGF_{121}$a-TMR at NanoLuc-VEGFR2 WT (*Table 4.4a*). Kinetic parameters derived for $VEGF_{121}$a-TMR in membranes were similar comparing NanoLuc-VEGFR2 WT and TPD membranes (Mann-Whitney test, $P>0.05$, n=5).

Second, $VEGF_{165}$b-TMR kinetics in membrane preparations were compared in the presence or absence of RTK phosphorylation using an RTKI (*Figure 4.16*). Membranes expressing NanoLuc-VEGFR2 were pre-incubated for 30 minutes with cediranib (1 µM) or the negative control (0.01% DMSO). Unlike the real-time binding profiles derived in intact cells, there was no elevation in BRET ratio in the presence of cediranib in membrane preparations. Kinetic parameters were derived using four concentrations of $VEGF_{165}$b-TMR for the 90 minute timecourse (*Table 4.4b*). As in *Table 4.3*, there was a slower k_{off} in membrane preparations compared to cells that resulted in a longer estimated residence time. There was no significant difference in affinity (pK_d) upon cediranib pre-treatment (paired t-test, $P>0.05$, n=5 per group). Cediranib treatment also had no effect on kinetic parameters compared to DMSO-treated membranes (Wilcoxon matched-pairs signed rank test, $P>0.05$, n=5). While there was a small decrease in k_{on} upon cediranib pre-treatment in intact cells, this was absent in membrane preparations.

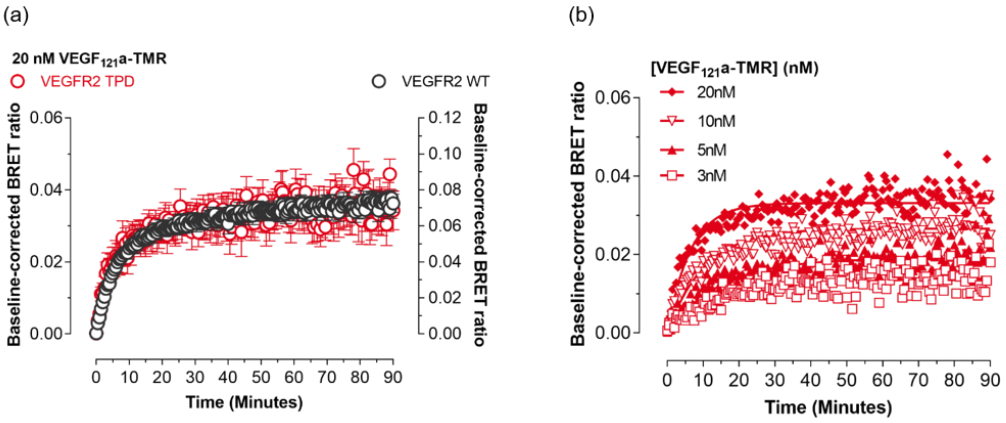


Figure 4.15 ***Kinetics of VEGF$_{121}$a-TMR binding NanoLuc-VEGFR2 tyrosine phosphorylation deficient (TPD) in membrane preparations****. Membranes were homogenised from HEK293T cells stably expressing NanoLuc-VEGFR2 wild type (WT) or NanoLuc-VEGFR2 TPD. Membranes were plated at 10 µg protein/well and pre-treated with furimazine to equilibrate for 5 minutes. (a) Membranes were incubated with saturating concentration of VEGF$_{121}$a-TMR (20 nM). This compared the profile for mutant NanoLuc-VEGFR2 TPD (left y axis, red circles) and NanoLuc-VEGFR2 WT (right y axis, black circles). Data represent mean ± S.E.M. from 5 independent experiments with duplicate wells. (b) Membranes were incubated with 4 concentrations of VEGF$_{121}$a-TMR, showing the 20 nM data from* (a)*. Measurements were taken every 30 seconds for 90 minutes at 37°C. BRET ratios were baseline-corrected to vehicle for each time point. Individual curves in* (b) *were fit with a simple exponential association model. For clarity, error bars are not shown. Derived kinetic parameters are shown in* Table 4.4*.*

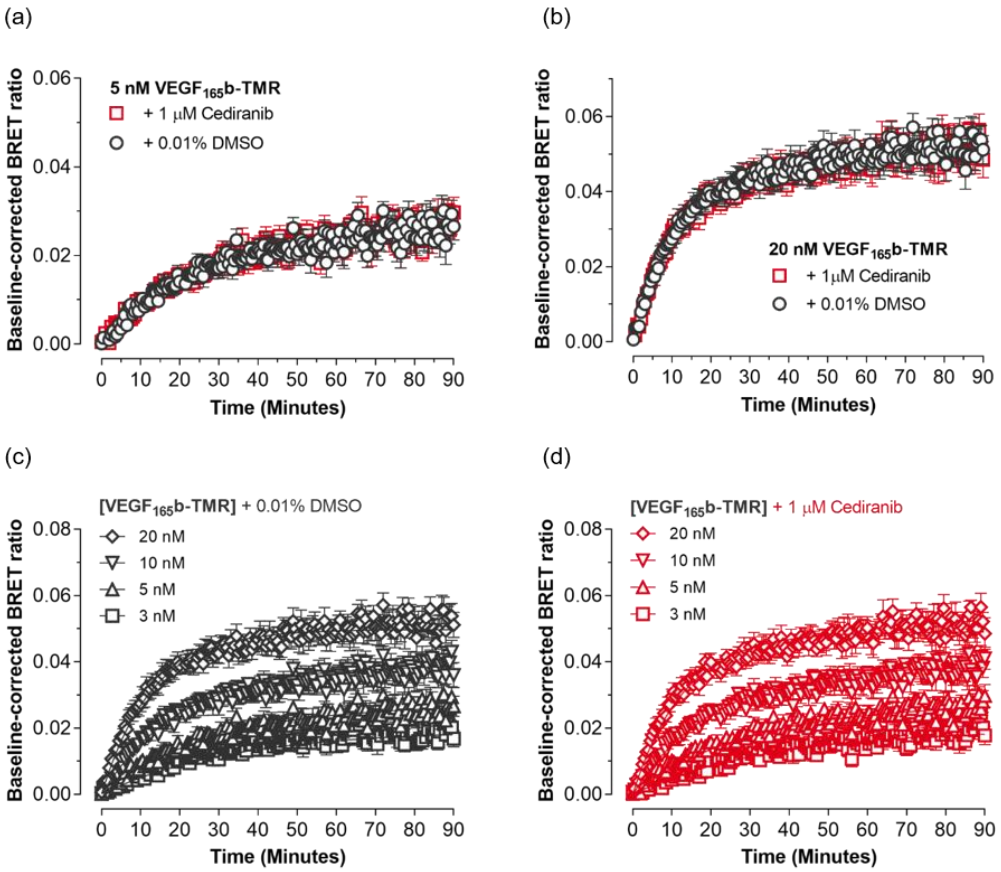


Figure 4.16 ***Kinetics of VEGF$_{165}$b-TMR binding in membrane preparations pre-treated with cediranib****. Membranes were homogenised from HEK293T cells stably expressing wild type NanoLuc-VEGFR2 and plated at 10 µg protein/well. Membranes were pre-treated 0.01% DMSO (control) or 1 µM cediranib (30 minutes, 37°C). Furimazine was added for 5 minutes, before VEGF$_{165}$b-TMR binding was monitored every 30 seconds for 90 minutes at 37°C. (a,b) Membranes were stimulated with 5 nM (a) or 20 nM (b) VEGF$_{165}$b-TMR. Matched experiments compared the profile in the presence of cediranib (red) or DMSO (black). (c,d) Association kinetic binding parameters were fit from the initial 20 minutes using 4 concentrations of VEGF$_{165}$b-TMR. Data are shown as mean ± S.E.M. from 5 independent experiments with duplicate wells. These are the same data for 5 nM and 20 nM as plotted in* (a) *and* (b)*. Derived kinetic parameters are shown in* Table 4.4.

Table 4.4 ***Effect of inhibiting tyrosine phosphorylation on kinetic parameters using (a) genetic or (b) pharmacological interventions.***

Expression system	Ligand	Kinetic pK_d	k_{on} ($min^{-1}M^{-1}$)	k_{off} (min^{-1})	Residence time (min)	Half time, $t_{1/2}$ (min) at 10 nM
(a) Site-directed mutagenesis						
VEGFR2 WT	$VEGF_{121}$a-TMR	8.44 ± 0.07	$5.13x10^6 \pm 0.48x10^6$	0.019 ± 0.002	55.70 ± 5.77	10.10 ± 0.78
VEGFR2 TPD		8.19 ± 0.07 $^{\$}$	$6.21x10^6 \pm 1.61x10^6$	0.037 ± 0.006	31.64 ± 7.13	8.76 ± 2.20
(b) Pre-incubation with an RTKI						
Cells						
0.01% DMSO	$VEGF_{165}$b-TMR	7.72 ± 0.06	$4.26x10^6 \pm 0.50x10^6$	0.081 ± 0.009	13.09 ± 1.67	5.82 ± 0.56
1 µM Cediranib		7.45 ± 0.14	$2.63x10^6 \pm 0.51x10^6$	0.091 ± 0.015	12.23 ± 2.01	6.14 ± 0.60
Membranes						
0.01% DMSO	$VEGF_{165}$b-TMR	8.08 ± 0.11	$2.69x10^6 \pm 0.30x10^6$	0.023 ± 0.003	46.91 ± 6.17	14.0 ± 0.58
1 µM Cediranib		8.12 ± 0.07	$2.74x10^6 \pm 0.28x10^6$	0.021 ± 0.002	50.27 ± 5.31	14.64 ± 0.98

Data represent mean ± S.E.M. from 5 independent experiments with duplicate wells. Parameters derived in intact cells were limited to the initial 20 minutes. Statistical tests probed the hypothesis that inhibiting tyrosine phosphorylation (TPD or 1 µM cediranib, red) altered kinetically derived parameters relative to the respective negative control (WT or 0.01% DMSO, black). pK_d values were compared using a parametric unpaired t-test ($^{\$}$ $P<0.05$). Other parameters were compared using a non-parametric Mann-Whitney test ($P>0.05$).

Membrane preparations enabled the investigation of specific biochemical factors on real-time ligand/receptor interactions at 37°C. We probed how an acidic endosomal microenvironment influenced ligand/receptor interactions monitored using BRET (*Methods 2.8.3*). This compared a pH reflecting early endosomes (pH 6.0; Maxfield and Yamashiro, 1987) with physiological extracellular pH (7.4, as above). Control experiments confirmed that the buffering capacity of HBSS was maintained at this lower pH over a 2 hour period (50 µl per well at 37°C; data not shown). TMR is a pH-insensitive fluorophore, however pH is reported to influence luminescence emissions from NanoLuc (Hall et al., 2012). Indeed, luminescence values decreased at an acidic pH 6.0 in each experiment but BRET ratios were not altered (*Figure 4.17*). Using $VEGF_{165}$b-TMR as a representative ligand in membrane preparations expressing NanoLuc-VEGFR2, there was no difference in BRET ratio between pH 7.4 and pH 6.0 (*Figure 4.17a*). There was comparable saturable binding between pH conditions with similar low non-specific binding. Derived equilibrium dissociation constants for $VEGF_{165}$b-TMR suggested that affinities were similar at pH 7.4 (K_d = 5.29 ± 1.12 nM, n=6) and pH 6.0 (K_d = 4.43 ± 1.25 nM, n=6). The pK_d affinities obtained from saturation binding experiments were compared using a paired t-test, suggesting these were not significantly different (P>0.05, n=6).

Ligand binding kinetics were also compared in matched experiments between pH 7.4 and pH 6.0. Kinetic parameters were derived using four concentrations of $VEGF_{165}$b-TMR, as shown for pH 6.0 (*Figure 4.17b*). The K_d affinity estimated from derived kinetic parameters (k_{off}/k_{on}) yielded a similar binding affinity in both pH conditions (pK_d paired t-test, P>0.05, n=6). There was, however, a faster association and dissociation constant derived for $VEGF_{165}$b-TMR at pH 6.0 compared to pH 7.4 (*Table 4.5*). Association and dissociation rate constants were compared between experiments at pH 7.4 and pH 6.0 using a Wilcoxon matched-pairs signed rank test (P<0.05, n=6 per group). Faster ligand binding kinetics at pH 6.0 can be seen when the BRET profile is directly compared at concentrations around K_d (*Figure 4.17c*) and at saturating concentrations (*Figure 4.17d*). These kinetic data suggest that ligands have faster kinetics, hence a shorter residence time at VEGFR2, at an endosomal pH.

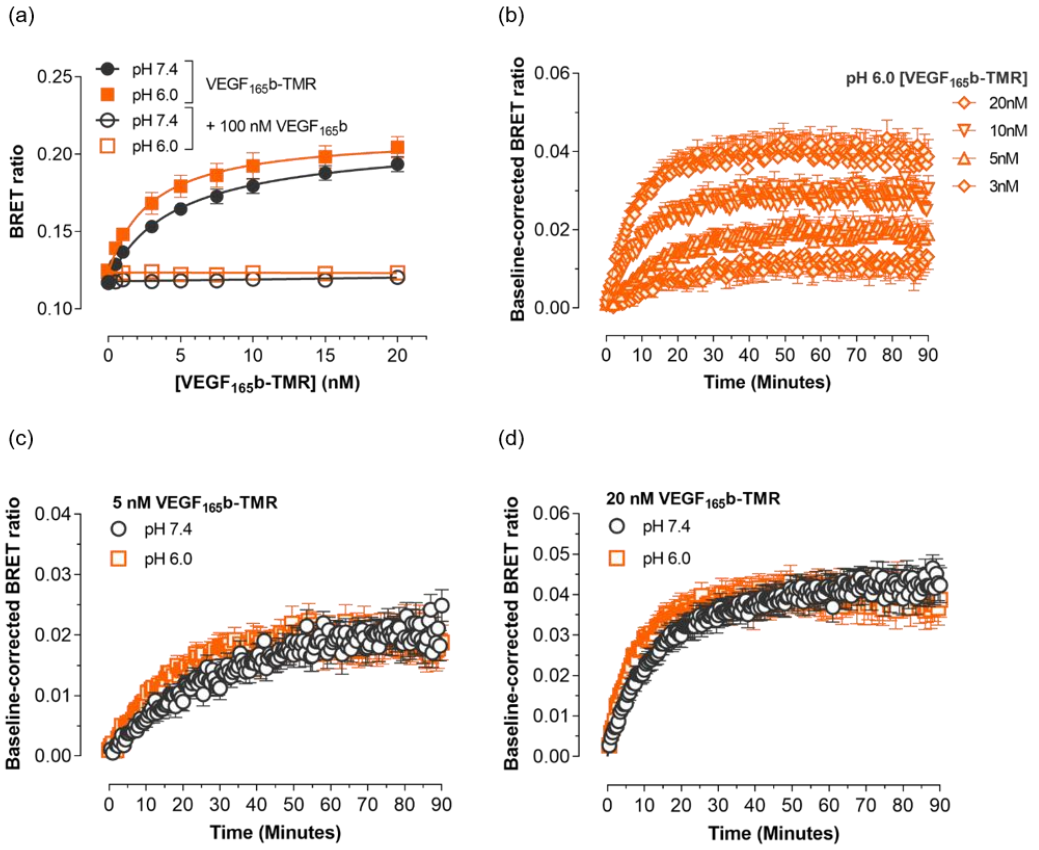


Figure 4.17 ***Effect of acidic pH on ligand binding monitored by BRET****. Membranes were homogenised from HEK293T cells expressing wild type NanoLuc-VEGFR2. Membranes were plated in HBSS/0.1% BSA at pH 7.4 and 6.0. Ligands were also prepared in buffer with the corresponding pH. (a) Membranes for saturation binding assays were plated at 5 µg protein/well. Increasing concentrations of VEGF$_{165}$b-TMR were added (60 minutes, 37°C), in the absence or presence of 100 nM unlabelled VEGF$_{165}$b to determine non-specific binding. Raw BRET ratios are expressed as mean ± S.E.M. from 6 independent experiments with duplicate wells. (b-d) Membranes were plated at 10 µg protein/well, and pre-incubated with furimazine for 5 minutes. Membranes were incubated with 4 concentrations of VEGF$_{165}$b-TMR for a global association fit, as in* (b) *for pH 6.0. Binding profiles for (c) 5 nM and (d) 20 nM VEGF$_{165}$b-TMR were directly compared between assay buffers at pH 7.4 and pH 6.0 (HBSS/0.1% BSA). Data represent mean ± S.E.M. from 6 independent experiments with duplicate wells. Derived kinetic parameters are shown in* Table 4.5.

Table 4.5 ***Effect of pH on VEGF$_{165}$b-TMR kinetics at NanoLuc-VEGFR2****.*

	Saturation pK_d	Kinetic pK_d	k_{on} ($min^{-1}M^{-1}$)	k_{off} (min^{-1})	Residence time (min)	Half time, $t_{1/2}$ (min) at 10 nM
Membrane preparations						
pH 7.4 (n=6)	8.32 ± 0.08	8.01 ± 0.05	$2.34x10^6 \pm 0.19x10^6$	0.023 ± 0.002	44.70 ± 3.73	15.11 ± 0.86
pH 6.0 (n=6)	8.43 ± 0.12 (NS)	7.93 ± 0.09 (NS)	$4.39x10^6 \pm 0.39x10^6$ *	0.059 ± 0.019 *	22.12 ± 3.60 *	7.68 ± 1.06 *
Intact cells						
pH 7.4 (n=5)	8.26 ± 0.04	8.07 ± 0.18	$7.29x10^6 \pm 1.84x10^6$	0.060 ± 0.011	19.50 ± 4.16	5.34 ± 0.38

Data represent 5-6 independent experiments with duplicate wells. Parameters derived in intact cells were limited to the initial 20 minutes. A paired t-test compared pK_d values at pH 7.4 and pH 6.0 (NS Not significant, $P>0.05$). Kinetic parameters were compared between pH 7.4 and pH 6.0 with a Wilcoxon matched-pairs signed rank test (* $P<0.05$).

4.4 DISCUSSION

The spatial dynamics of VEGFR2 are subject to complex regulation in living cells. Monitoring the long-term timecourse of ligand binding using BRET demonstrated further distinctions between VEGFR2 and NRP1. Ligand binding at NanoLuc-NRP1 remained elevated over time with no difference between intact cells and membrane preparations. In contrast, there was a peak in BRET signal at 20 minutes in intact cells for each fluorescent VEGF-A isoform at VEGFR2. This subsequently declined towards baseline over the following 70 minutes, recapitulating previous findings for $VEGF_{165}$a-TMR alone (Kilpatrick et al., 2017). This was particularly apparent at saturating concentrations of $VEGF_{165}$a-TMR, $VEGF_{165}$b-TMR and $VEGF_{121}$a-TMR, whereas BRET profiles at concentrations close to their respective K_d remained elevated over 90 minutes. Kilpatrick et al. (2017) suggested this characteristic BRET profile at VEGFR2 was a consequence of endocytosis, dissociation of ligand/receptor in endosomes and recycling of ligand-free receptor back to the plasma membrane. This feature of ligand binding at NanoLuc-VEGFR2 was absent in homogenised membrane preparations that lacked the ability for parallel agonist-driven endocytosis. Real-time binding at NanoLuc-NRP1 showed no difference in the BRET profile over 90 minutes between membranes and intact cells; this acted as a negative control that did not internalise in HEK293T cells (Chapter 3). This decline in BRET signal observed at VEGFR2 in intact cells suggested a link between ligand/receptor endocytosis and ligand binding dynamics. Understanding this relationship is important for considering receptor pharmacology in living cells that are subject to various degrees of regulation by their local cellular context.

There is limited quantification of the dynamics of ligand-driven VEGFR2 trafficking. Studies in primary endothelial cells using immunofluorescence antibody labelling or biochemical techniques agreed that VEGFR2 internalised within 15-60 minutes of VEGF-A stimulation (Ewan et al., 2006; Lampugnani et al., 2006; Jopling et al., 2009). This is comparable to the timecourse of EGFR trafficking (Goh and Sorkin, 2013). To determine the potency and kinetic profile of agonist-induced VEGFR2 endocytosis, we monitored the appearance of fluorescent ligand-associated receptors in intracellular endosomes using unbiased high-content imaging. This exploited novel fluorescent VEGF-A isoforms to follow the internalisation of VEGF-A itself, as opposed to constitutive VEGFR2 endocytosis (Ewan et al., 2006; Gampel et al., 2006; Jopling et al., 2011; Basagiannis and Christoforidis, 2016). To confirm that intracellular granules of fluorescent VEGF-A isoforms reflected endocytosis, we used confocal microscopy to confirm both $VEGF_{121}$a-TMR and VEGFR2 were colocalised with Rab5 in intracellular endosomes upon addition of the fluorescent ligand. All three fluorescent VEGF-A isoforms stimulated comparable concentration-dependent increase in the internalisation

of VEGF-TMR/VEGFR2 (EC_{50} = 12-30 nM). $VEGF_{165}$a-TMR, $VEGF_{165}$b-TMR and $VEGF_{121}$a-TMR also appeared in intracellular granules with a $t_{1/2}$ between 15 and 20 minutes for 10 nM ligand. This corresponded to the timecourse of BRET ligand binding at NanoLuc-VEGFR2. Fluorescent VEGF-A isoforms were similar in their ability to stimulate VEGFR2 endocytosis in HEK293T cells. This contrasted with Fearnley et al. (2016), whereby $VEGF_{121}$a had a reduced ability to induce VEGFR2 endocytosis compared to $VEGF_{165}$a. This was studied in HUVECs co-expressing NRP1, a co-receptor reported to modulate VEGFR2 trafficking (Ballmer-Hofer et al., 2011). Our technique, on the other hand, isolated trafficking at VEGFR2 alone as HEK293T cells had minimal NRP1 expression (Chapter 3). High-content imaging assays suggested that fluorescent VEGF-A isoforms internalised with VEGFR2 at concentrations at least two-fold greater than their affinities estimated from equilibrium dissociation constants (endocytosis EC_{50} = 12, 29 and 14 nM for $VEGF_{165}$a-TMR, $VEGF_{165}$b-TMR and $VEGF_{121}$a-TMR, respectively). Our data therefore suggest that substantial agonist-induced VEGFR2 endocytosis is occurring in intact HEK293T cells over the concentration range (1-20 nM) and timecourse (20 minutes) used to quantify ligand binding kinetics in live cells in Chapter 3.

Tyrosine phosphorylation initiates intracellular signalling pathways. Upon pre-incubation with RTKIs, Kilpatrick et al. (2017) demonstrated that RTKIs led to a concentration-dependent elevation in the BRET ligand binding between $VEGF_{165}$a-TMR and VEGFR2. Non-specific RTKIs will, however, inhibit numerous kinases in HEK293T cells. To directly explore the influence of RTK phosphorylation on localisation and ligand binding, we generated a tyrosine phosphorylation deficient VEGFR2 mutant (VEGFR2 TPD). Here, key intracellular tyrosine residues were mutated to phenylalanine to prevent their phosphorylation (Y951F, Y1054F, Y1059F, Y1175F, Y1214F). We confirmed that VEGFR2 TPD had no point mutations elsewhere in the receptor by sequencing the full expression vector (*Methods 2.3.1; Appendix Figure 7.11*). Receptors were exported successfully to the plasma membrane. We then used the NFAT reporter gene assay to ensure that this mutant receptor could not signal in response to $VEGF_{165}$a stimulation. We also isolated specific mutants that inhibited NFAT responses upon mutation to phenylalanine. These tyrosine residues, Y1175 and Y1054/1059, agreed with published literature in their involvement with PLCγ and Ca^{2+} signalling (Cunningham et al., 1997; Takahashi et al., 2001). VEGFR2 TPD was still subject to both constitutive and ligand/receptor endocytosis. This suggests that VEGFR2 phosphorylation is not required for these endocytic mechanisms, as seen for EGFR (Goh and Sorkin, 2013). In terms of ligand binding, preventing VEGFR2 phosphorylation in the TPD mutant caused an elevation in the amplitude of the BRET binding signal obtained with 3 nM and 20 nM $VEGF_{121}$a-TMR. This was independent of differences in receptor expression. There are, however, limitations in making conclusions from the magnitude of BRET ratios. Unlike

radioligand binding experiments, this typically provides no information regarding absolute receptor counts. Increased RET efficiency ($k_T(r)$, *Appendix 7.5*), could result from an altered conformation or orientation between the NanoLuc donor and TMR acceptor. Alternatively, the local environment could influence the spectral properties of the donor emission or acceptor fluorophore. While it is unknown why the elevation in BRET signal occurs, this effect was robust across 8 independent experiments. Comparing wild type to tyrosine phosphorylation deficient VEGFR2, both receptors were subject to constitutive endocytosis (live cell imaging and immunofluorescent antibody labelling in fixed cells) and the internalisation of ligand/receptor complexes (live cell imaging in Chapter 3, immunofluorescent antibody labelling in fixed cells and BRET profiles of ligand binding).

To compare these findings with pharmacological inhibition of VEGFR2 phosphorylation, we used cediranib as a representative RTKI (Carter et al., 2015; Kilpatrick et al., 2017). Pre-treating cells with cediranib successfully inhibited $VEGF_{165}a$-stimulated NFAT reporter gene signalling with a pIC_{50} within the range of published values (Carter et al., 2015; Kilpatrick et al., 2017). We also recapitulated the inhibitory effect of cediranib on constitutive VEGFR2 endocytosis. In HEK293T cells, cediranib pre-treatment led to a small elevation in BRET signal upon $VEGF_{165}b$-TMR binding. This was similar to previous findings for $VEGF_{165}a$-TMR with numerous RTKIs (Kilpatrick et al., 2017), albeit less pronounced. This mimicked the effect of inhibiting phosphorylation with VEGFR2 TPD, using distinct fluorescent VEGF-A isoforms to confirm the effects of disrupting VEGFR2 phosphorylation was not isoform-specific. Pre-incubation of intact cells with cediranib was accompanied by a small decrease in the association rate constant (k_{on}) but no change in dissociation rate constant (k_{off}) or residence time. While there were minimal differences in kinetic parameters, there was an elevated amplitude of BRET signal in the presence of cediranib in intact cells only. There were no distinctions in the BRET signal in membrane preparations in the presence of cediranib. While BRET ratios cannot be directly compared between NanoLuc-VEGFR2 WT and TPD membrane preparations, experiments suggested that inhibiting tyrosine phosphorylation influenced the amplitude of ligand binding in intact cells. This could be linked to the subcellular localisation of VEGFR2 in living cells.

We used colocalisation analysis to compare the localisation of wild type and tyrosine phosphorylation deficient VEGFR2 in early endosomes. Quantification is limited by the spatial resolution of conventional confocal microscopy, however it is sufficient to infer whether receptors are at the plasma membrane or in subcellular compartments. There were differences between analyses for correlation (Pearson's Correlation Coefficient) and co-occurrence (Mander's Overlap Coefficient). There was higher colocalisation between ligand/receptor after 60 minutes for cells expressing

HaloTag-VEGFR2 TPD compared to WT. Having confirmed there was no distinction in receptor expression, this suggests a similar effect as the elevated BRET ligand binding profiles. There was also a difference in the correlation between Rab5/receptor, whereby there was no decrease following 60 minute ligand stimulation in the absence of VEGFR2 phosphorylation. Receptors lacking phosphorylation may have different trafficking away from $Rab5^{+}$ endosomes, therefore receptor localisation could be compared in other subcellular compartments. It would also be valuable to develop techniques that directly track the real-time dynamics of VEGFR2 endocytosis and trafficking in living cells.

Ligand binding assays in isolated membrane preparations were used to disrupt the potential for agonist-induced receptor endocytosis or engagement with cytoplasmic signalling complexes. Monitoring $VEGF_{165}$a-TMR, $VEGF_{165}$b-TMR and $VEGF_{121}$a-TMR binding with BRET demonstrated clear saturable binding in membrane preparations with low non-specific binding. Binding affinities estimated in membrane preparations were higher than in living cells. This included derived equilibrium dissociation constants of fluorescent VEGF-A isoforms (K_d) and the pK_i values of VEGF-Ax determined following 60 minutes. At NanoLuc-NRP1, there was also a higher affinity of $VEGF_{165}$a-TMR in membranes compared to intact cells but little difference between the pK_i of $VEGF_{165}$a.

The kinetic binding profile of $VEGF_{165}$a-TMR, $VEGF_{165}$b-TMR and $VEGF_{121}$a-TMR at NanoLuc-VEGFR2 were markedly different in membrane preparations compared to intact living cells. Kinetics from ligand binding association curves were able to reach equilibrium over the 90 minute timecourse. Association (k_{on}) and dissociation (k_{off}) rate constants determined in membrane preparations were of a similar order to those derived in intact cells. Quantifying kinetic parameters in cells was limited to the initial 20 minutes of agonist stimulation to remove the influence of receptor endocytosis. Kinetics quantified in membrane preparations from the full 90 minutes were consistently slower than those derived in cells. Association rate constants (k_{on}) were 1.2 to 2.0-fold smaller than corresponding parameters obtained in intact cells. There was also a 1.8 to 2.5-fold decrease in dissociation rate constants (k_{off}), indicating agonists were slower to dissociate in membrane preparations when reaching equilibrium. The process of receptor endocytosis in intact cells therefore led to an underestimate of the receptor residence time ($1/k_{off}$) on the receptor. Likewise, the estimated $t_{1/2}$ for $VEGF_{165}$b-TMR at VEGFR2 was ~5 minutes in cells whilst membranes preparations was ~11 minutes.

Due to the complex trafficking of VEGFR2, BRET studies of ligand binding in living cells likely contain components of both the initial ligand binding interaction and those that reflect VEGFR2 endocytosis. Endosomes have a unique microenvironment in terms of acidic pH (Maxfield and Yamashiro, 1987) and distinct membrane lipids (Kobayashi et al., 1998). These discrete membrane-enclosed structures could contain

higher localised receptor concentrations (Weddell and Imoukhuede, 2017) and altered local ligand concentrations that influence how ligand rebinding within endosomes. Endosomes also contain proteolytic enzymes, such as endothelial-converting enzyme 1 (Roosterman et al., 2007); proteases could therefore degrade VEGF-A ligand and reduce agonist availability. Using the assay in membrane preparations on isolated ligand/receptor interactions, we manipulated the local environment to study the influence of pH. We used matched experiments to compare physiological extracellular pH (pH 7.4) to an acidic pH reflecting early endosomes (pH 6.0). These data showed that while the overall affinity and amplitude of BRET signal was identical, the k_{on} and k_{off} of $VEGF_{165}$b-TMR at NanoLuc-VEGFR2 were faster at pH 6.0 than those quantified at pH 7.4. Interestingly, these kinetic parameters were comparable to those obtained in intact cells in Chapter 3. These data suggest that a proportion of the ligand binding characteristics observed in intact cells could result from the lower pH environment in endosomes.

4.5 CHAPTER 4 CONCLUSIONS

Receptor localisation can influence ligand binding monitored by BRET. In terms of endocytosis, we demonstrated that VEGFR2 internalised constitutively or with ligand into $Rab5^{+}$ early endosomes. Automated imaging was used as an unbiased, quantitative approach to monitor the internalisation of fluorescent VEGF-A isoforms with VEGFR2 in living cells. $VEGF_{165}$a-TMR, $VEGF_{165}$b-TMR and $VEGF_{121}$a-TMR each produced rapid and potent endocytosis of ligand-bound VEGFR2 into intracellular endosomes. As real-time ligand binding studies at NanoLuc-VEGFR2 in intact cells demonstrated that the BRET signal fell towards baseline after reaching a peak at 20 minutes, this was attributed to a change in its local environment linked to ligand/receptor trafficking. Directly inhibiting VEGFR2 phosphorylation using site-directed mutagenesis did not inhibit ligand-dependent and ligand-independent VEGFR2 endocytosis, suggesting this internalises through mechanisms that do not dependent on RTK phosphorylation. We also demonstrated that inhibiting tyrosine phosphorylation led to an elevation in the BRET signal upon fluorescent VEGF-A binding, using both pharmacological and genetic interventions.

To disrupt the influence of agonist-driven endocytosis on VEGF-A ligand binding kinetics at VEGFR2, we adapted the BRET assay for use in isolated membrane preparations. Monitoring ligand binding kinetics in membrane preparations produced BRET association curves that were maintained for the duration of the 90 minute experiment. Equilibrium binding affinities estimated in membranes were of a similar order to those determined in live cells, allbeit with consistently higher affinity. Kinetic parameters derived in membrane preparations were slower than in intact cells. This suggested VEGFR2 endocytosis in intact cells led to an underestimate in measured residence times of fluorescent ligands on the receptor. Interestingly, manipulating the local pH to mimic acidic endosomes suggested ligand binding kinetics of VEGF-A could differ between the plasma membrane and intracellular endosomes.

Chapter 5.
Dynamics of ligand binding at VEGFR2/NRP1 complexes in living cells

5.1 INTRODUCTION

VEGFR2 signalling is upregulated by the co-receptor NRP1 (Chittenden et al., 2006; Fantin et al., 2011; Lanahan et al., 2013). VEGF-A is a large dimeric peptide ligand that can bind to both VEGFR2 and NRP1 (Soker et al., 1998, 2002). VEGF-A interacts with VEGFR2 via residues encoded at the N-terminus of VEGF-A (Leppanen et al., 2010; Brozzo et al., 2011), while the C-terminus interacts with NRP1 (Mamluk et al., 2002; Vander Kooi et al., 2007; Parker et al., 2012). As VEGF-A binds each receptor via spatially distinct regions (*Introduction Figure 1.3*), ligands are suggested to simultaneously engage both receptors. This could therefore form a higher order macromolecular protein complex that consists of VEGF-A, VEGFR2 and NRP1. Both NRP1 and VEGFR2 are expressed in endothelial cells (Soker et al., 1998; Witmer et al., 2002). NRP1 is also expressed in numerous tumour subtypes (Jubb et al., 2012; Goel and Mercurio, 2013; Lee et al., 2014b) and immune cells in the tumour microenvironment (Roy et al., 2017). NRP1 is already a growing target in drug delivery for uptake around the tumour site (Ruoslahti, 2017). Targeting NRP1-mediated VEGFR2 sensitisation as an anti-angiogenic strategy could reduce the side effects observed for non-selective RTKIs (Davis et al., 2011), however the mechanism by which NRP1 upregulates VEGFR2 is not well understood.

VEGF-A isoforms differ in how they signal in physiological systems (*Introduction Table 1.1*). While $VEGF_{165}$a stimulates angiogenesis as a full agonist, $VEGF_{165}$b is a partial agonist with reported anti-angiogenic activity *in vivo* (Woolard et al., 2004; Cébe Suarez et al., 2006; Qiu et al., 2008). VEGF-A isoforms also have distinct expression profiles in health and disease (Vempati et al., 2014). VEGF-A isoforms have the same residues encoded by the N-terminus, whereas the C-terminus is subject to alternative splicing (Woolard et al., 2009; Peach et al., 2018b). Key residues that differ between VEGF-A isoforms determine the presence or absence of interactions with other components of a higher order macromolecular complex (*Introduction Figure 1.4*). The C-terminal arginine residue encoded by exon 8a interacts with the b1 domain of NRP1 (Mamluk et al., 2002; Vander Kooi et al., 2007; Parker et al., 2012). Unlike $VEGF_{165}$a, 'anti-angiogenic' $VEGF_{165}$b isoforms are unable to interact with NRP1 (Cébe Suarez et al., 2006; Kawamura et al., 2008b; Delcombel et al., 2013). Our previous ligand binding studies quantified interactions at either VEGFR2 or NRP1 expressed alone in HEK293T cells (Chapter 3). These data demonstrated minimal distinctions between the ligand binding of VEGF-A isoforms at NanoLuc-VEGFR2, however $VEGF_{165}$b and $VEGF_{121}$a were unable to bind NanoLuc-NRP1 (Chapter 3). Distinctions between VEGF-A isoforms were observed in systems endogenously co-expressing NRP1 (*Introduction Table 1.1*), therefore the co-expression of NRP1 may be necessary to reveal differences between the pharmacology of VEGF-A isoforms.

In Chapter 3, we collaborated with Promega Corporation to develop VEGF-A isoforms single-site labelled with tetramethylrhodamine (TMR). $VEGF_{165}$b-TMR and $VEGF_{121}$a-TMR were characterised as novel fluorescent probes selective for VEGFR2. In contrast to these isoforms, $VEGF_{165}$a-TMR was able to interact with both VEGFR2 and NRP1. The pharmacology of fluorescent VEGF-A isoforms was quantified at these distinct receptors using technologies selective for a NanoLuc-tagged receptor. Ligand binding was monitored in real-time at 37°C with BRET (Stoddart et al., 2015a), whereby NanoLuc emits luminescence upon oxidation of the furimazine substrate. This can excite a compatible fluorophore in close proximity, such as $VEGF_{xxx}$x-TMR (Kilpatrick et al., 2017; Peach et al., 2018a, 2019). Despite having a similar nanomolar binding affinity for both NanoLuc-VEGFR2 and NanoLuc-NRP1, $VEGF_{165}$a-TMR binding kinetics were significantly faster at NRP1 than VEGFR2 (Chapter 3). We also demonstrated that these receptors were localised in distinct regions of the cell in the absence or presence of ligand. Whereas VEGFR2 was constitutively internalised, NRP1 remained on the plasma membrane regardless of ligand stimulation. Novel distinctions between receptors were highlighted in cells only expressing one tagged receptor in isolation. Endothelial cells and tumour cells endogenously express both VEGFR2 and NRP1 in the same cell (Whitaker et al., 2001; Prahst et al., 2008; Fantin et al., 2013; Koch et al., 2014; Lee-Montiel et al., 2015), however it is unknown how the distinct pharmacology of VEGFR2 and NRP1 modulate one another in co-expressing cells. As these receptors have distinct ligand binding dynamics, novel approaches are required that isolate the pharmacology of VEGF-A ligand binding in cells co-expressing VEGFR2 and NRP1.

Numerous techniques have suggested that heteromeric complexes are formed between VEGFR2 and NRP1 in endothelial cells. Co-immunoprecipitation studies first demonstrated receptor-receptor interactions between VEGFR2 and NRP1 (Whitaker et al., 2001; Prahst et al., 2008; Gelfand et al., 2014). This biochemical approach highlights durable interactions resistant to cell lysis, however solubilisation of receptors away from their native membrane environment can lead to artefacts. Proximity-ligation assays have also been applied to observe VEGFR2/NRP1 complexes using antibodies in tumours (Koch et al., 2014). More recently, FRET was used to demonstrate receptor-receptor complexes between VEGFR2 and NRP1 tagged with fluorophores at their C-termini (King et al., 2018). Here, each receptor was tagged with a complementary fluorophore to monitor FRET between a donor and acceptor fluorophore. BRET can also be applied to monitor energy transfer between receptors tagged with a bioluminescent donor and fluorescent acceptor. Monitoring FRET or BRET between tagged receptors was first used to investigate the oligomerisation of G protein-coupled receptors (McVey et al., 2001; Milligan, 2001). Using BRET to monitor proximity between receptors has already been extended to RTKs, such as monitoring EGFR heterodimers (Ayoub et al., 2013). While there are growing techniques to investigate the presence or absence of interactions

between proteins, techniques are often unable to isolate the resulting functional effect at a defined complex in terms of receptor signalling or ligand binding.

Growing interest in protein-protein interactions, such as receptor oligomerisation, led to the development of technologies that take advantage of reporter tags split into distinct fragments (Hébert et al., 2006). Proteins of interest can be fused to complementary fragments such that tags must complement to emit their reporter signal. These have been developed for both FRET- and BRET-based approaches. For example, bimolecular fluorophore complementation split the N- and C-termini of the donor fluorophore, such as YFP or GFP (Hu et al., 2002; Hu and Kerppola, 2003; Magliery et al., 2005). These have disadvantages as fluorophore fusion is irreversible and chromophore maturation time is slow. A similar strategy was performed modifying the BRET donor *Renilla luciferase* (RLuc) into N- and C- termini (Paulmurugan et al., 2004). As introduced in Chapter 3, bioluminescent donors have been developed due to optimal properties as an energy donor in RET techniques. NanoLuc is a small enzyme engineered from a deep sea shrimp with bright, ATP-independent luminescence emissions (Hall et al., 2012; Chapters 3-4). This was recently engineered into a split tag denoted NanoLuc Binary Technology (NanoBiT; Dixon et al., 2016). These separate moieties require complementation into a complex to emit luminescence. The 10-stranded beta barrel structure of NanoLuc was dissected into (a) a larger protein tag, made up of 156 amino acid residues, and (b) a smaller 11 amino acid tag. NanoBiT complementation is rapid and often reversible (Dixon et al., 2016). Mutations were made throughout each fragment to optimise their structural integrity and intrinsic tag affinity. Interestingly, numerous variants of the smaller tag were developed with different intrinsic affinities for complementation with the LgBiT fragment. This included the 'higher affinity' HiBiT fragment (K_d ~0.7 nM) and the lower affinity SmBiT fragment (K_d ~190 µM). In this Chapter, VEGFR2 and NRP1 were tagged with each combination of LgBiT and either HiBiT or SmBiT in order to investigate this heteromeric receptor complex. Here, NanoBiT technologies were developed for use with fluorescent VEGF-A variants to investigate ligand binding pharmacology isolated at higher order VEGFR2/NRP1 complexes. For the first time, this technology enabled us to monitor ligand binding at a defined heterotypic receptor-receptor complex between an RTK and a single transmembrane co-receptor.

5.2 CHAPTER 5 AIMS

The work described in Chapter 5 aimed to:

(a) Probe the localisation of HaloTag-VEGFR2 and SnapTag-NRP1 when co-expressed in the same cell, in the absence and presence of ligand;
(b) Detect whether VEGFR2 and NRP1 form receptor-receptor complexes when co-expressed in the same cell, extending beyond BRET to implement NanoBiT® complementation technologies;
(c) Monitor ligand binding at a complex of VEGFR2 and NRP1 in real-time, comparing VEGF-A isoforms selective for VEGFR2 ($VEGF_{165}$b-TMR) or a ligand that can interact with both receptors ($VEGF_{165}$a-TMR).

5.3 RESULTS

Localisation of VEGFR2 and NRP1 co-expressed in HEK293T cells

Prior imaging studies in HEK293T cells highlighted that VEGFR2 and NRP1 were localised in distinct subcellular regions when transfected into cells individually (Chapter 3). It is, however, unknown where these receptors are localised when co-expressed in HEK293T cells. Confocal imaging was used to image both VEGFR2 and NRP1 in living cells at 37°C (*Methods 2.6.1*). HaloTag and SnapTag are distinct tags that interact with their respective fluorophore-conjugated substrate via a chloroalkane or benzylguanine moiety (*Methods Figure 2.6*). These distinct tags were exploited to label cell surface receptors with distinct fluorophores in living cells expressing both receptors. For imaging alongside HaloTag-VEGFR2, we cloned NRP1 tagged at the N-terminus with SnapTag (*Methods 2.3.4*). First, SnapTag-NRP1 was characterised as a novel construct to verify localisation was comparable to prior imaging studies with HaloTag-NRP1. HEK293T cells transiently expressing SnapTag-NRP1 receptors were labelled with membrane-impermeant SnapTag-AlexaFluor488 (*Figure 5.1*). This had a similar localisation to HaloTag-NRP1, whereby SnapTag-NRP1 remained at the cell surface in the absence or presence of 10 nM $VEGF_{165}$a-TMR (*Figure 5.1,* bottom panel). SnapTag-NRP1 was also localised in filopodia-like projections, particularly at the basolateral side of HEK293T cells against the glass surface (*Figure 5.1b*). Upon stimulation with 10 nM $VEGF_{165}$a-TMR for 60 minutes, fluorescent VEGF-A and SnapTag-NRP1 were localised in identical regions (*Figure 5.1,* white regions in overlay). This was comparable to previous imaging studies for HaloTag-NRP1 (*Figure 3.17*).

Secondly, control studies were performed to ensure that HaloTag-VEGFR2 and SnapTag-NRP1 could be imaged separately in cells co-expressing both receptors (*Figure 5.2*). HEK293T cells were transiently transfected with HaloTag-VEGFR2 and SnapTag-NRP1. Alternatively, cells were transfected with a single receptor construct (HaloTag-VEGFR2 or SnapTag-NRP1 alone) in the presence of empty pcDNA3.1/Neo vector to maintain the same total amount of DNA. In all conditions, cells were simultaneously labelled with membrane-impermeant HaloTag-AlexaFluor488 and membrane-impermeant SnapTag-AlexaFluor647. Following multiple wash steps in HBSS/0.1% BSA to remove any unconjugated substrate, cells were maintained in imaging buffer for 60 minutes at 37°C. Studies in cells expressing single receptor constructs were used to investigate whether labelling could be performed simultaneously without non-specific binding to the other substrate (*Figure 5.2*). There was no spectral bleedthrough detected in the other channel, verifying that the selected boundaries of emission wavelengths were appropriate for the fluorophore spectra under study. In the

absence or presence of NRP1, there was constitutive internalisation of VEGFR2. In contrast, SnapTag-NRP1 was largely expressed at the plasma membrane with its highest fluorescence intensity at cell-cell junctions. There were also some peri-nuclear intracellular spots of SnapTag-NRP1 in the absence or presence of HaloTag-VEGFR2 co-expression in vehicle conditions.

We then investigated the localisation of HaloTag-VEGFR2 and SnapTag-NRP1 co-expressed in HEK293T cells in response to ligand. These studies compared the same population of cells before and after ligand stimulation. Receptors were labelled as above with membrane-impermeant HaloTag-AlexaFluor488 and SnapTag-AlexaFluor647. The same cell population was imaged prior to ligand addition, then following incubation with 10 nM unlabelled VEGF-A (60 minutes, 37°C). This compared the $VEGF_{165}$b isoform selective for VEGFR2 (*Figure 5.3*) with the non-selective 'prototypical' $VEGF_{165}$a isoform (*Figure 5.4*). In both conditions, there was a heterogeneous distribution of receptors in different cells (*Figure 5.3a, Figure 5.4a*). The sites of spatial overlay between VEGFR2 and NRP1, highlighted in white in the overlay image, were largely intracellular. There were also some discrete regions of VEGFR2 co-localised with NRP1 on the plasma membrane. A larger proportion of NRP1 was localised at the plasma membrane in filopodia-like projections, indicated by magenta in the overlay.

We further probed receptor localisation by quantifying fluorescence intensity from confocal images of the same population of cells pre- and post- ligand stimulation. Fluorescence intensity was quantified across a single cell by drawing a line through the centre of a cell co-expressing HaloTag-VEGFR2 and SnapTag-NRP1 (*Figure 5.3b, Figure 5.4b;* white dashed line on overlay image). This included a region where two co-expressing cells were connected by a cell-cell junction (*Figure 5.3b, Figure 5.4b;* junctions at ~32 nm and ~18 nm respectively). In each condition, HaloTag-VEGFR2 was largely localised in the centre of the cell with minimal receptor localised at the plasma membrane (*Figure 5.3b, Figure 5.4b;* green). Upon stimulation with both isoforms, there was increased intensity of intracellular HaloTag-VEGFR2. Fluorescence intensity profiles also clearly demonstrated a higher NRP1 intensity at cell-cell junctions (*Figure 5.3b, Figure 5.4b;* magenta line). Upon stimulation with $VEGF_{165}$b or $VEGF_{165}$a, there was decreased intensity of NRP1 at this cell-cell junction.

Due to the heterogeneity of receptor localisation, quantitative analysis was performed to investigate the colocalisation between VEGFR2 and NRP1 (*Methods 2.10.3*). Regions of interest were drawn around any cell successfully co-expressing both VEGFR2 and NRP1. Mander's Overlap Coefficients were used to compare the proportion of the total NRP1 fluorescence residing in VEGFR2 positive regions (*Figure 5.5a*). This is independent of fluorescence intensity and ranges between 0 (not colocalised) and 1 (complete co-occurrence). These values were compared using a Kruskal-Wallis test ($P<0.05$, n=219 cells analysed), followed by a post-Hoc Dunn's multiple comparisons test. There was less NRP1 in $VEGFR2^+$ regions following stimulation with $VEGF_{165}b$ ($P<0.01$, n=68 cells), compared to vehicle ($P<0.01$, n=97 cells) or $VEGF_{165}a$ ($P<0.01$, n=54 cells). There was no difference to vehicle upon $VEGF_{165}a$ stimulation ($P>0.05$). This suggested that upon stimulation with a ligand selective for VEGFR2 only, there was less NRP1 in the same location as VEGFR2 compared to colocalisation in presence of vehicle only. Pearson's Correlation Coefficients were then compared between conditions (*Figure 5.5b*). This indicates whether there is a positive correlation (+1), no correlation (0) or a negative correlation (-1) between the intensity of these channels. Similarly, values were compared using a Kruskal-Wallis test ($P<0.05$, n=219 cells) followed by a post-Hoc Dunn's multiple comparisons test. Upon $VEGF_{165}a$ stimulation, there was a higher correlation between VEGFR2 and NRP1 compared to vehicle ($P<0.0001$) or $VEGF_{165}b$ ($P<0.01$). This suggested that a ligand interacting with both receptors increased the extent of colocalisation between VEGFR2 and NRP1.

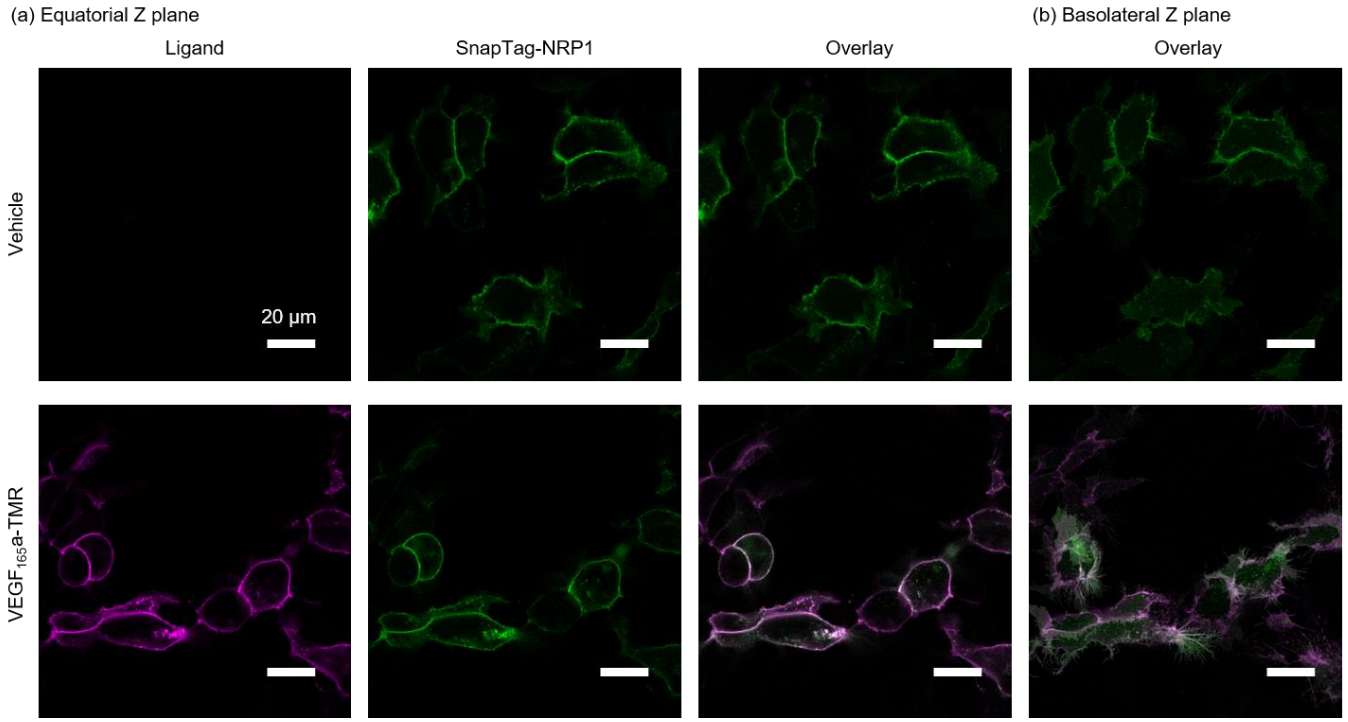


Figure 5.1 ***Imaging VEGF$_{165}$a-TMR at SnapTag-NRP1 in HEK293T cells****. HEK293T cells transiently expressed SnapTag-NRP1 in 8-well plates. Receptors were labelled with membrane-impermeant 0.5 µM SnapTag-AlexaFluor488 (green) for 30 minutes. Cells were washed twice in HBSS/0.1% BSA, then stimulated with either vehicle or 10 nM VEGF$_{165}$a-TMR (magenta) for 1 hour at 37°C. Cells were imaged live using the LSM710 Confocal Microscope (40X objective). Overlay images show both SnapTag-NRP1 (green) and VEGF$_{165}$a-TMR (magenta), therefore regions with fluorophore in the same region are shown in white. Images compare (a) the central Z plane through the cell or (b) the basal surface of the cell at the 8-well plate surface. Images are representative from 3 independent experiments.*

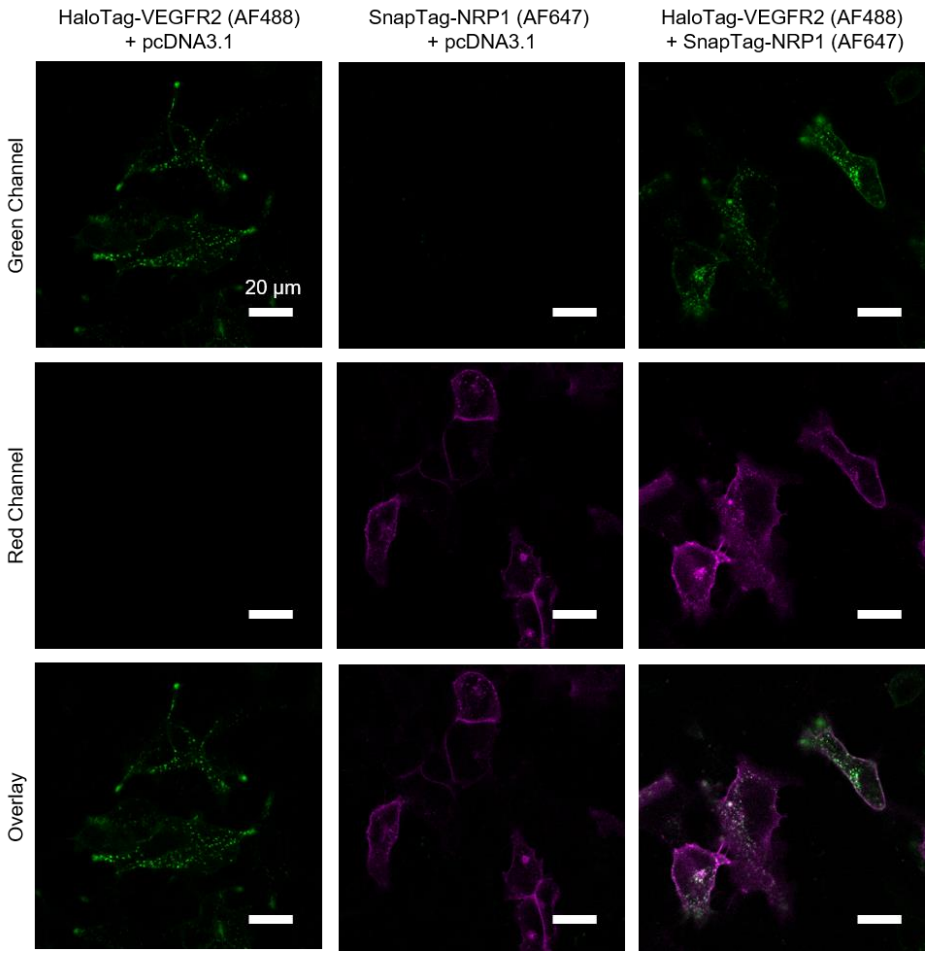


Figure 5.2 ***Control imaging studies of HEK293T cells expressing HaloTag-VEGFR2 and/or SnapTag-NRP1****. HEK293T cells were transiently transfected with equal amounts of HaloTag-VEGFR2, SnapTag-NRP1 and/or empty pcDNA3.1/Neo vector (50 ng cDNA/well per construct). Receptors were simultaneously labelled with membrane-impermeant 0.5 µM HaloTag-AlexaFluor488 and 0.5 µM SnapTag-AlexaFluor647 substrate in serum-free DMEM/0.1% BSA. Following 30 minutes at 37°C, cells were washed in HBSS/0.1% BSA. Cells were incubated in vehicle for 60 minutes at 37°C then imaged live using the LSM710 Confocal Microscope (40X objective). Images were obtained using the green channel (Argon 488 nm laser 2.5% power, emissions 493-628 nm) or red channel (HeNe633 nm laser 2.5% power, emissions 638-747 nm). The overlay shows HaloTag-VEGFR2 (green) and SnapTag-NRP1 (magenta), with regions of spatial overlay highlighted in white. Images are representative from 4 independent experiments.*

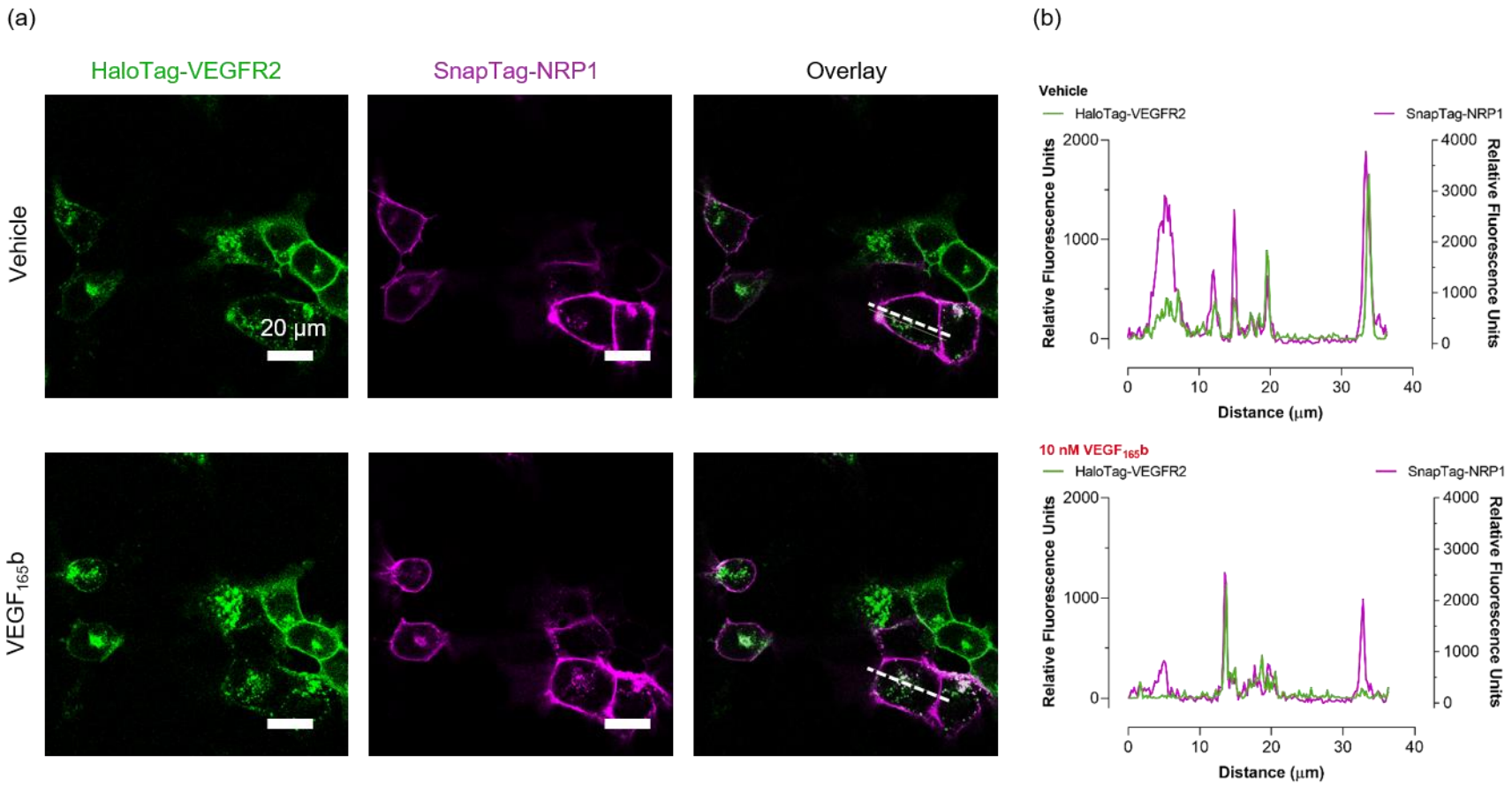


Figure 5.3 ***Localisation of HaloTag-VEGFR2 and SnapTag-NRP1 in response to unlabelled VEGF$_{165}$b****. See next page.*

Figure 5.3 Ctd. HEK293T cells were transiently transfected with HaloTag-VEGFR2 (50 ng cDNA/well) and SnapTag-NRP1 (50 ng cDNA/well). Receptors were simultaneously labelled with membrane-impermeant 0.5 µM HaloTag-AlexaFluor488 and 0.5 µM SnapTag-AlexaFluor647 (30 minutes, 37°C). Cells were then washed twice in vehicle (HBSS/0.1% BSA). The same region was imaged at '0 minutes' and following stimulation with 10 nM unlabelled $VEGF_{165}b$ for 60 minutes. Cells were imaged live at both time points using the LSM710 Confocal Microscope (40X objective).
(a) Each channel is shown separately in grayscale. The overlay of these images show HaloTag-VEGFR2 (green) and SnapTag-NRP1 (magenta), such that any overlapping regions in the overlay are shown in white. Images are representative from 4 independent experiments. The dashed line in the overlay image represents the line drawn across the cell to quantify fluorescence intensity in (b)*. (b) Fluorescence intensities for each channel were plotted across a single cell in absence or presence of $VEGF_{165}b$. The orientation of the fluorescence intensities across the line include a cell-cell junction at the furthest distance (x axis = ~32 nm). These profiles compare relative fluorescence units for HaloTag-VEGFR2 (green, left y axis) and SnapTag-NRP1 (magenta, right y axis), corresponding to the overlay image.*

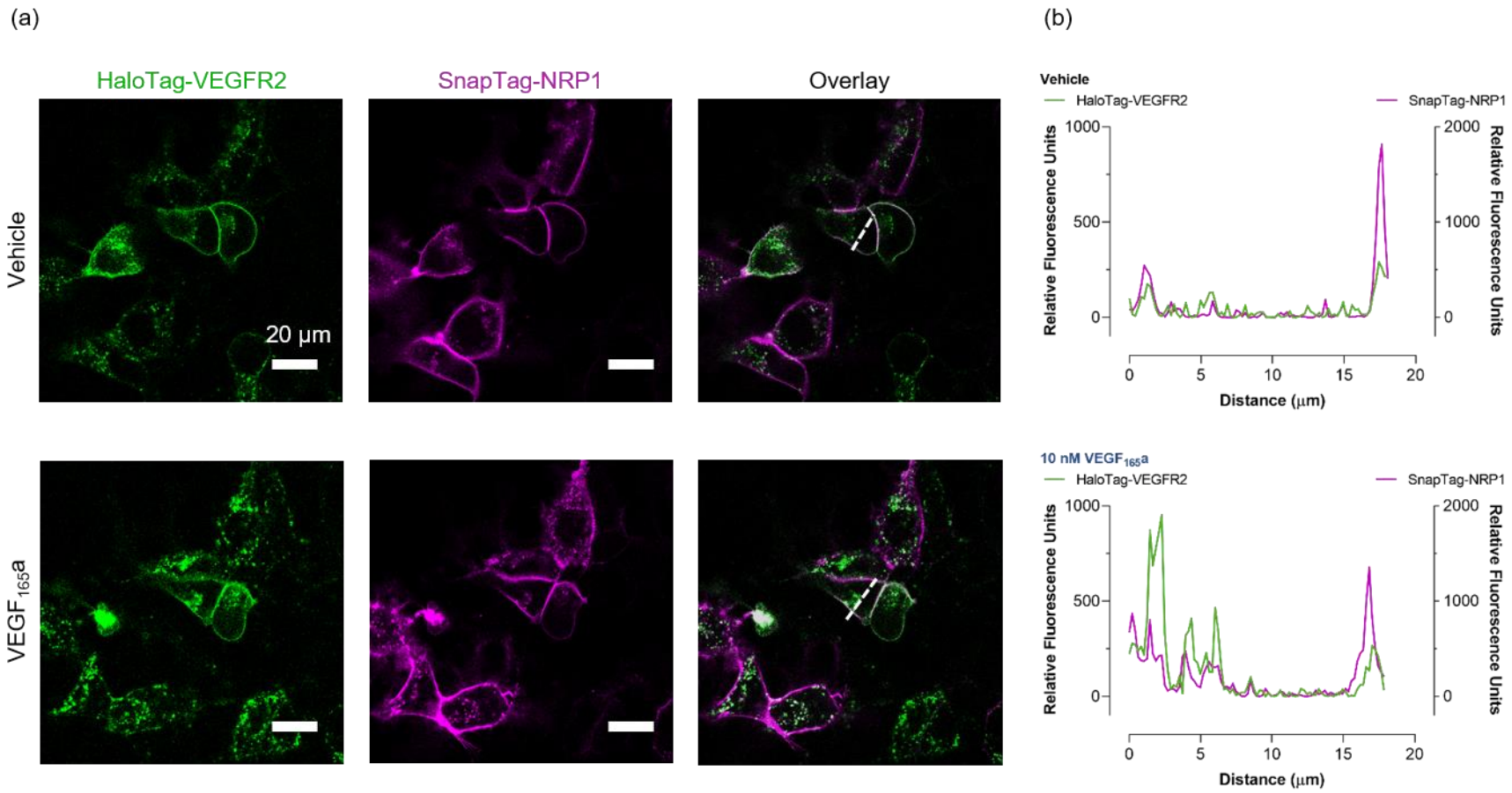


Figure 5.4 ***Localisation of HaloTag-VEGFR2 and SnapTag-NRP1 in response to VEGF$_{165}$a stimulation****. See next page.*

Figure 5.4 Ctd. HEK293T cells were transiently transfected with HaloTag-VEGFR2 (50 ng cDNA/well) and SnapTag-NRP1 (50 ng cDNA/well). Receptors were simultaneously labelled with membrane-impermeant 0.5 µM HaloTag-AlexaFluor488 and 0.5 µM SnapTag-AlexaFluor647 for 30 minutes (37°C). Cells were washed twice in vehicle (HBSS/0.1% BSA). The same site was imaged at 0 minutes and following stimulation with 10 nM unlabelled $VEGF_{165}a$ for 60 minutes. Cells were imaged live at both time points using the LSM710 Confocal Microscope (40X objective).
(a) As in Figure 5.3*, each channel is shown separately in grayscale. The overlay shows HaloTag-VEGFR2 (green) and SnapTag-NRP1 (magenta). Spatially overlapping regions in the overlay image are shown in white. Images are representative from 4 independent experiments. The dashed line in the overlay image represents the line drawn across the cell to quantify fluorescence intensity in* (b)*. (b) Fluorescence intensities for each channel were plotted for a single cell in absence or presence of $VEGF_{165}a$ stimulation. This profile also features a cell-cell junction at the furthest distance (x axis = ~18 nm). These profiles compare relative fluorescence units for HaloTag-VEGFR2 (green, left y axis) and SnapTag-NRP1 (magenta, right y axis), corresponding to the overlay image.*

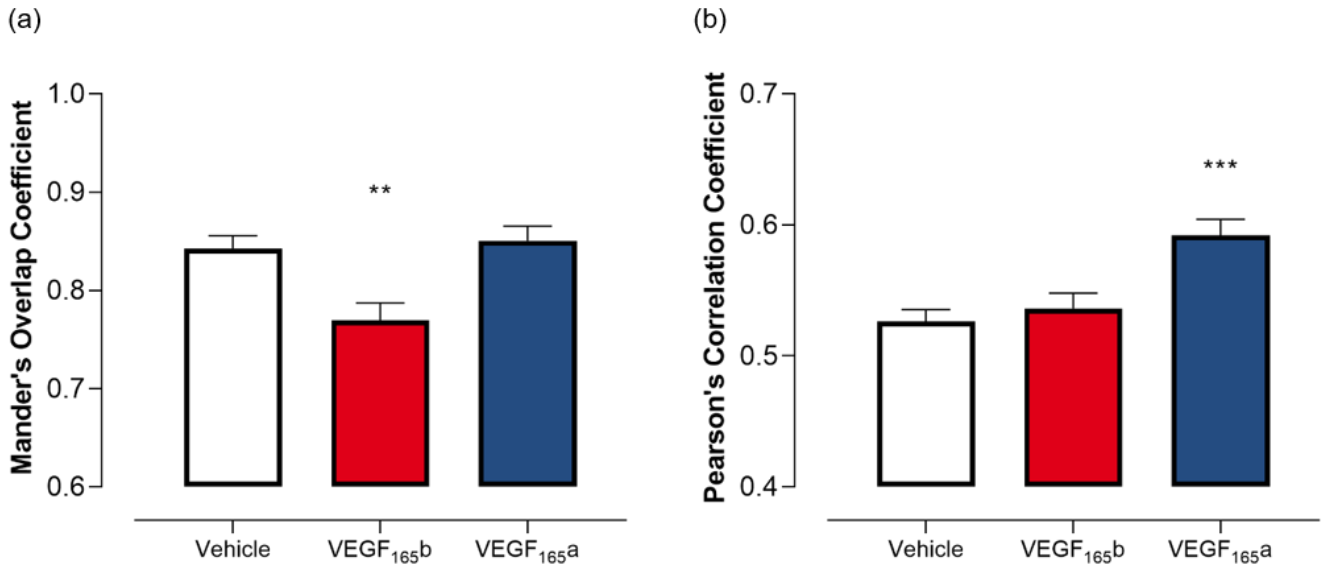


Figure 5.5 ***Colocalisation analysis between HaloTag-VEGFR2 and SnapTag-NRP1****. Images were obtained in living cells using the Zeiss LSM710 Confocal Microscope in experiments shown in* Figure 5.3 *and* Figure 5.4*. ImageJ software was used to analyse images with channels corresponding to HaloTag-VEGFR2 (green channel, HaloTag-AlexaFluor488) and SnapTag-NRP1 (red channel, SnapTag-AlexaFluor647). Cells were incubated with vehicle (HBSS/0.1% BSA), 10 nM $VEGF_{165}b$ or 10 nM $VEGF_{165}a$ (60 minutes, 37°C). Colocalisation parameters were quantified based on regions of interest drawn around cells expressing both HaloTag-VEGFR2 and SnapTag-NRP1. (a) The Mander's Overlap Coefficient represented the proportion of SnapTag-NRP1 in HaloTag-VEGFR2$^+$ regions. (b) Pearson's Correlation Coefficients compared the relationship between the intensity of VEGFR2 and NRP1 pixels. All coefficient values were pooled from 4 independent experiments, with a total of 97 cells (vehicle), 68 cells ($VEGF_{165}b$) or 54 cells ($VEGF_{165}a$). Coefficients were compared between conditions using a Kruskal-Wallis test ($P<0.05$, n=219 total cells) followed by a post-Hoc Dunn's multiple comparisons test between vehicle, $VEGF_{165}b$ or $VEGF_{165}a$ stimulation (** $P<0.01$, *** $P<0.001$).*

Monitoring heteromeric complex formation between VEGFR2/NRP1

We then investigated whether VEGFR2 and NRP1 formed heteromeric complexes when co-expressed in HEK293T cells. Receptor-receptor BRET was used to monitor whether tagged VEGFR2 and NRP1 were in close proximity (<10 nm, *Appendix 7.5*). The bioluminescent donor, NanoLuc-VEGFR2, was transfected into HEK293T at a constant amount (25 ng cDNA/well; (*Methods 2.9.1*). Cells were simultaneously transfected with increasing amounts of NRP1 conjugated to a fluorescent tag (0-100 ng cDNA/well HaloTag or SnapTag). HaloTag-NRP1 and SnapTag-NRP1 were labelled with a membrane-impermeant substrate conjugated to AlexaFluor488. The excitation spectra of AlexaFluor488 (*Appendix 7.4*) overlaps with NanoLuc emissions (*Methods Figure 2.8c*), thus enabling efficient BRET. For both HaloTag-NRP1 and SnapTag-NRP1, there was clear saturation of the BRET signal with NanoLuc-VEGFR2 (*Figure 5.6*). This was observed with pooled BRET ratios plotted against the amount of cDNA added to each well (*Figure 5.6a*). A similar effect was seen plotting BRET ratios against raw fluorescence emissions, confirming increasing amounts of HaloTag-NRP1 and SnapTag-NRP1 were successfully transfected (*Figure 5.6b*). As there was clear saturation of the BRET signal upon increasing HaloTag- or SnapTag- NRP1, it can be inferred that VEGFR2 and NRP1 were in close proximity (<10 nm). These experiments were performed in the absence of ligand, providing evidence for the formation of constitutive heteromers in living HEK293T cells.

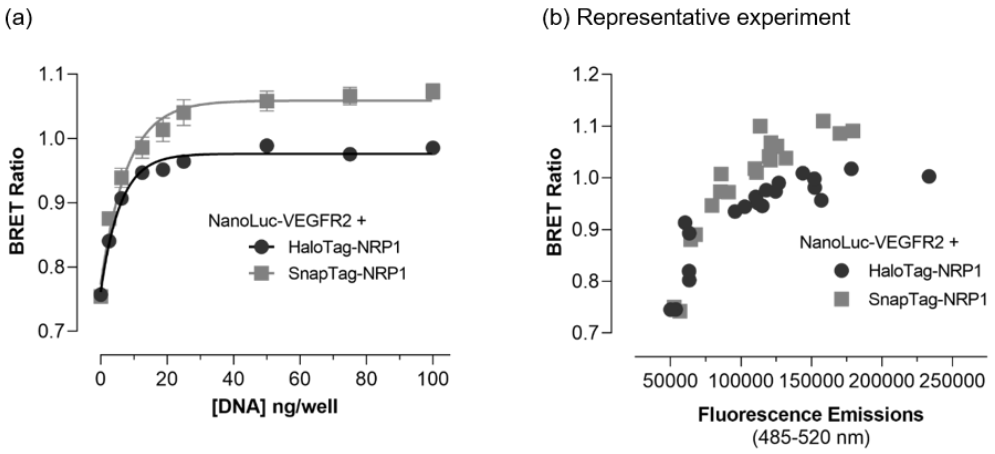


Figure 5.6 ***Using BRET to monitor proximity between NanoLuc-VEGFR2 and either HaloTag-NRP1 or SnapTag-NRP1****. HEK293T cells were transiently transfected in 96-well plates with a fixed concentration of donor (NanoLuc-VEGFR2, 25 ng cDNA/well) and increasing concentrations of fluorescent acceptor (HaloTag-NRP1 or SnapTag-NRP1, 0-100 ng cDNA/well). All wells were transfected with a total 125 ng cDNA/well using empty pcDNA3.1/Zeo vector to make up the difference (0-100 ng cDNA/well). Fluorescent acceptors were labelled with 0.2 µM HaloTag-AlexaFluor488 substrate or 0.2 µM SNAP-Surface AlexaFluor488 substrate for 30 minutes in serum-free DMEM (37°C/5% CO_2). Cells were washed twice with HBSS/0.1% BSA, then incubated in furimazine (10 µM) for 5 minutes (37°C). Emissions from the luminescent donor and fluorescent acceptor receptor were simultaneously monitored by the PHERAstar FS platereader. (a) Data are expressed as mean ± S.E.M. from 5 independent experiments with duplicate wells. (b) A representative experiment plotting individual data points as the BRET ratio (y axis) against fluorescence emissions alone (x axis). This indicated whether receptors were successfully expressed and exported to the plasma membrane, rather than raw cDNA added per well.*

Having confirmed VEGFR2 and NRP1 were in close proximity when co-expressed in HEK293T cells, we applied a split luminescent tag approach to investigate fluorescent VEGF-A ligand binding at a defined higher order VEGFR2/NRP1 complex (*Methods 2.9.2*). NanoBiT complementation was modified from NanoLuc, enabling direct comparisons using the same furimazine substrate (Dixon et al., 2016). Here, LgBiT was appended to the N-terminus of each receptor, while the 11 amino acid HiBiT or SmBiT tag was conjugated to the other receptor (*Figure 5.7a; Methods 2.3*). In the presence of furimazine, tags in isolation would emit minimal luminescence. In contrast, complementation of the NanoBiT complex would enable enzymatic activity to oxidise furimazine and emit luminescence. NanoBiTs must be in close proximity with appropriate orientation for NanoBiT complementation. We first investigated the optimal orientation of tagging VEGFR2 or NRP1 with the LgBiT or 11 amino acid tag (*Figure 5.7b,c*). LgBiT was fused to both receptors via a long, flexible linker (*Methods Figure 2.1*). We also tagged receptors with a HiBiT tag, named according to its higher affinity for LgBiT, or the SmBiT tag with low intrinsic affinity for LgBiT. Luminescence emissions were higher for the combination that appended LgBiT to VEGFR2 and the 11 amino acid tag on NRP1. This was evident from both the pooled data (*Figure 5.7b*) and example luminescence emissions from a single experiment (*Figure 5.7c*). Luminescence emissions from the HiBiT complex were approximately ten-fold higher than for the lower affinity NanoBiT complex (*Figure 5.7b,c*).

We then characterised whether these tag fragments compromised receptor signalling or ligand binding. As described in Chapter 3, we used the reporter gene NFAT assay in HEK293T-ReLuc2P cells to monitor downstream signalling in response to $VEGF_{165}a$ (*Methods* *2.7.1*). Concentration-response curves were compared between cells stably expressing VEGFR2 tagged at the N-terminus with either LgBiT, HiBiT or SmBiT (*Figure* *5.8a*). Each receptor enabled a concentration-dependent increase in NFAT luminescence in response to increasing concentrations of $VEGF_{165}a$. Each cell line had a similar potency derived for $VEGF_{165}a$ (LgBiT-VEGFR2 pEC_{50} = 9.95 ± 0.11; HiBiT-VEGFR2 pEC_{50} = 10.06 ± 0.12; SmBiT-VEGFR2 pEC_{50} = 10.23 ± 0.23; n=5 for each). These were not statistically significant when compared using a one-way ANOVA (P>0.05, n=5 per group). Ligand binding was also characterised at LgBiT-VEGFR2 or HiBiT-VEGFR2 (*Figure* *5.8b,c*). Exogenous purified HiBiT or LgBiT proteins were added, respectively, to complement the NanoBiT complex to act as a luminescent donor to fluorescent VEGF-A (*Methods* *2.8.4*). Saturation binding experiments were performed using increasing concentrations of $VEGF_{121}a$-TMR as a representative ligand. For both receptors, there was saturable binding with minimal non-specific binding at both receptor complexes. Equilibrium dissociation constants for $VEGF_{121}a$-TMR were in the nanomolar range (LgBiT-VEGFR2 K_d 5.13 ± 0.86 nM; HiBiT-VEGFR2 K_d 4.36 ± 0.37 nM; n=3 for each), suggesting there was no effect on heteromeric complex formation on ligand binding affinity. These were similar to affinities derived at full-length NanoLuc-tagged receptors in *Table* *3.3* (one-way ANOVA, P>0.05, n=3-6 per group). Having confirmed the tags themselves did not compromise receptor signalling or ligand binding, subsequent studies focussed on LgBiT-VEGFR2, HiBiT-NRP1 and SmBiT-NRP1 as the optimal orientation of tags.

Luminescence must only be emitted from a complemented NanoBiT complex to enable subsequent BRET studies that isolate binding at a defined VEGFR2/NRP1 complex. To confirm receptor tags did not individually emit luminescence, each receptor construct was expressed alone in HEK293T cells (*Figure 5.9*). First, background luminescence in the presence of furimazine was compared relative to the VEGFR2/NRP1 complex (*Figure 5.9a,b*). Constitutive luminescence emissions were higher for LgBiT-VEGFR2 than HiBiT- or SmBiT-tagged NRP1 (*Figure 5.9a*). Comparing emissions from individual experiments demonstrated that raw luminescence counts were minimal (*Figure 5.9b*). We confirmed individual constructs were expressed in isolation using exogenous, purified NanoBiT fragments (*Figure 5.9c,d*). Purified fragments are membrane-impermeable due to conjugation to a HaloTag linker, therefore this confirmed that VEGFR2 and NRP1 constructs were exported to the cell surface. On a logarithmic scale, luminescence emissions were clearly increased upon re-complementation with exogenous NanoBiTs (*Figure 5.9c*). As observed from raw luminescence counts (*Figure 5.9d*), adding purified LgBiT led to a smaller increase in luminescence emissions from SmBiT-NRP1 compared to HiBiT-NRP1. Overall, these data confirmed minimal background luminescence emissions compared to the complemented NanoBiT complex. We also verified each tagged receptor was exported to the cell surface when expressed alone in HEK293T cells.

Finally, we investigated whether the VEGFR2/NRP1 NanoBiT complex was disrupted by simultaneously transfecting receptor that could compete with this complex. HEK293T cells were transfected with the NanoBiT complex, composed of LgBiT-VEGFR2 and either HiBiT-NRP1 or SmBiT-NRP1 (*Figure 5.10a,b*). These cells were also transfected with increasing concentrations of HaloTag-VEGFR2 (*Figure 5.10a*) or HaloTag-NRP1 (*Figure 5.10b*). Control wells confirmed that these competing receptors were successfully expressed in each experimental replicate by labelling receptors with 0.2 μM membrane-impermeant HaloTag-AlexaFluor488. Luminescence values decreased upon addition of HaloTag-VEGFR2 or HaloTag-NRP1. This suggested that the heteromeric NanoBiT complex between VEGFR2 and NRP1 was disrupted by receptors that were not conjugated to a NanoBiT fragment. There was a greater decrease in luminescence emissions for SmBiT complexes compared to HiBiT complexes. There was greater displacement of the complex by HaloTag-NRP1 compared to HaloTag-VEGFR2. Comparing HaloTag fluorescence emissions suggested that NRP1 was transfected more effectively than VEGFR2 (HaloTag-NRP1 200 ng cDNA = 189208 ± 14002 RFU; HaloTag-VEGFR2 200 ng cDNA/well = 88141 ± 4176 RFU; n=3 for both).

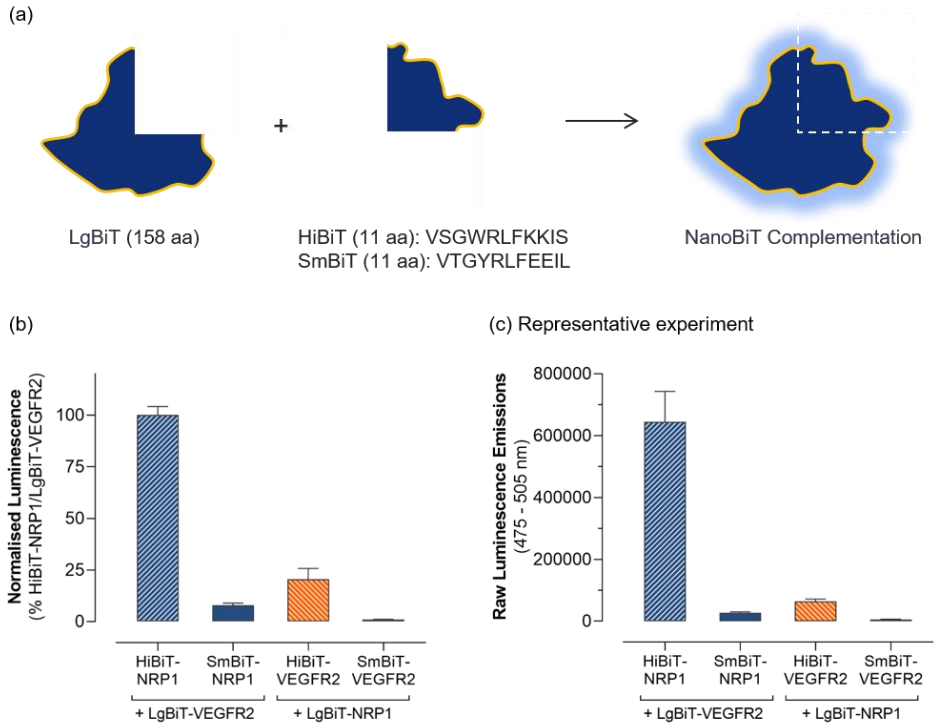


Figure 5.7 ***Complementation of a VEGFR2/NRP1 NanoBiT complex****.*

(a) NanoLuc Binary Technology (NanoBiT) involves an 18 kDa fragment (LgBiT) and a smaller 11 amino acid (aa) fragment (Dixon et al., 2016). Point mutations in the short tag influence the intrinsic affinity for tag complementation, with HiBiT exhibiting higher affinity than SmBiT. In the presence of furimazine, fragments emit minimal luminescence in isolation. When NanoBiTs complement as a complex, enzymatic activity enables furimazine oxidation and the emission of luminescence. (b,c) VEGFR2 and NRP1 were conjugated to each fragment to optimise configuration for NanoBiT complementation. HEK293T-ReLuc2P cells were transiently transfected in 96-well plates with equal amounts of LgBiT-tagged receptor (50 ng cDNA/well) and HiBiT- or SmBiT-tagged receptor (50 ng cDNA/well). Cells were incubated with 10 µM furimazine in HBSS/0.1% BSA for 10 minutes (37°C). Luminescence emissions (475-505 nm) were measured by the PHERAstar FS platereader. (b) Data were normalised to un-transfected cells (0%) and HiBiT-NRP1/LgBiT-VEGFR2 (100%) per experiment. Data are expressed as mean ± S.E.M. from 5 independent experiments (LgBiT-VEGFR2) or 3 independent experiments (LgBiT-NRP1), each with triplicate wells. (b) Raw luminescence emissions were plotted as mean ± S.E.M. from triplicate wells.

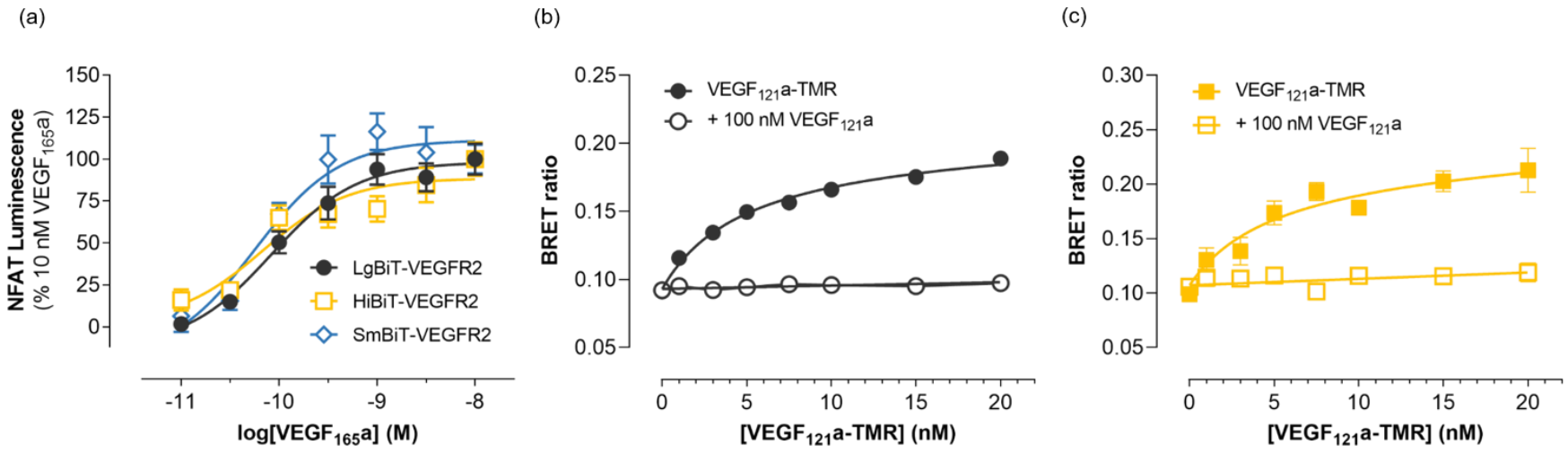


Figure 5.8 ***Characterisation of VEGFR2 tagged with LgBiT, HiBiT or SmBiT moieties****. HEK293T cells stably expressed both ReLuc2P and either LgBiT-VEGFR2, HiBiT-VEGFR2 or SmBiT-VEGFR2. (a) Cells were serum-starved for 24 hours. On the day of experimentation, cells were stimulated with increasing concentrations of $VEGF_{165}a$ for 5 hours and 37°C/5% CO_2. Data were normalised to mean vehicle (0%) or 10 nM unlabelled $VEGF_{165}a$ (100%) per experiment. Data are expressed as mean ± S.E.M. from 5 independent experiments with duplicate wells per experiment. (b,c) HEK293T stably expressed either LgBiT-VEGFR2 (b) or HiBiT-VEGFR2 (c). To complement the NanoBiT complex, 20 nM purified HiBiT (b) or purified LgBiT (c) was added in HBSS/0.1% BSA. Cells were simultaneously incubated with increasing concentrations of $VEGF_{121}a$-TMR, in the presence or absence of 100 nM $VEGF_{121}a$ to determine non-specific binding. Following incubation for 60 minutes at 37°C, furimazine was added for 10 minutes. BRET ratios were measured on the PHERAstar FS platereader. Data are shown as mean ± S.E.M. from 3 independent experiments with duplicate wells. Derived equilibrium dissociation constants are given in the text.*

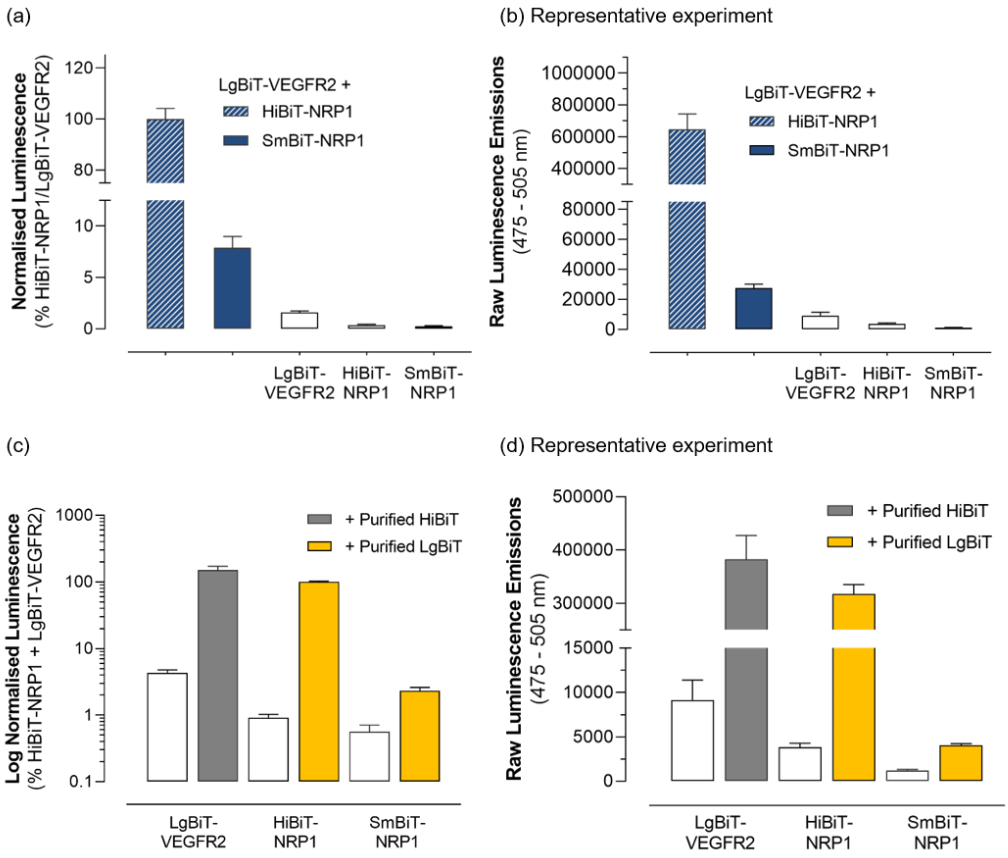


Figure 5.9 ***Emissions from individual NanoBiT-tagged receptors relative to a complemented NanoBiT complex****. HEK293T-ReLuc2P cells were transiently transfected in 96-well plates with LgBiT-VEGFR2, HiBiT-NRP1 or SmBiT-NRP1 (50 ng cDNA/well). Cells expressing single constructs were also transfected with 50 ng cDNA/well empty pcDNA3.1/Zeo vector. (a,b) Background emissions were compared to the complemented NanoBiT complex. Filled bars were transfected with equal amounts of LgBiT-VEGFR2 and either HiBiT-NRP1 or SmBiT-NRP1. (c,d) Cells expressed a single NanoBiT-tagged construct, in the absence (open bars) or presence of 20 nM purified HiBiT or LgBiT (filled bars). In all experiments, cells were incubated with furimazine (10 µM) in HBSS/0.1% BSA for 10 minutes (37°C). Luminescence emissions (475-505 nm) were measured by the PHERAstar FS platereader. (a,c) Data were normalised to un-transfected cells (0%) and HiBiT-NRP1/LgBiT-VEGFR2 (100%) per experiment. Data are expressed as mean ± S.E.M. from 5 independent experiments with triplicate wells per experiment. (b,d) Raw emissions were plotted from the same representative experiment as mean ± S.E.M. from triplicate wells.*

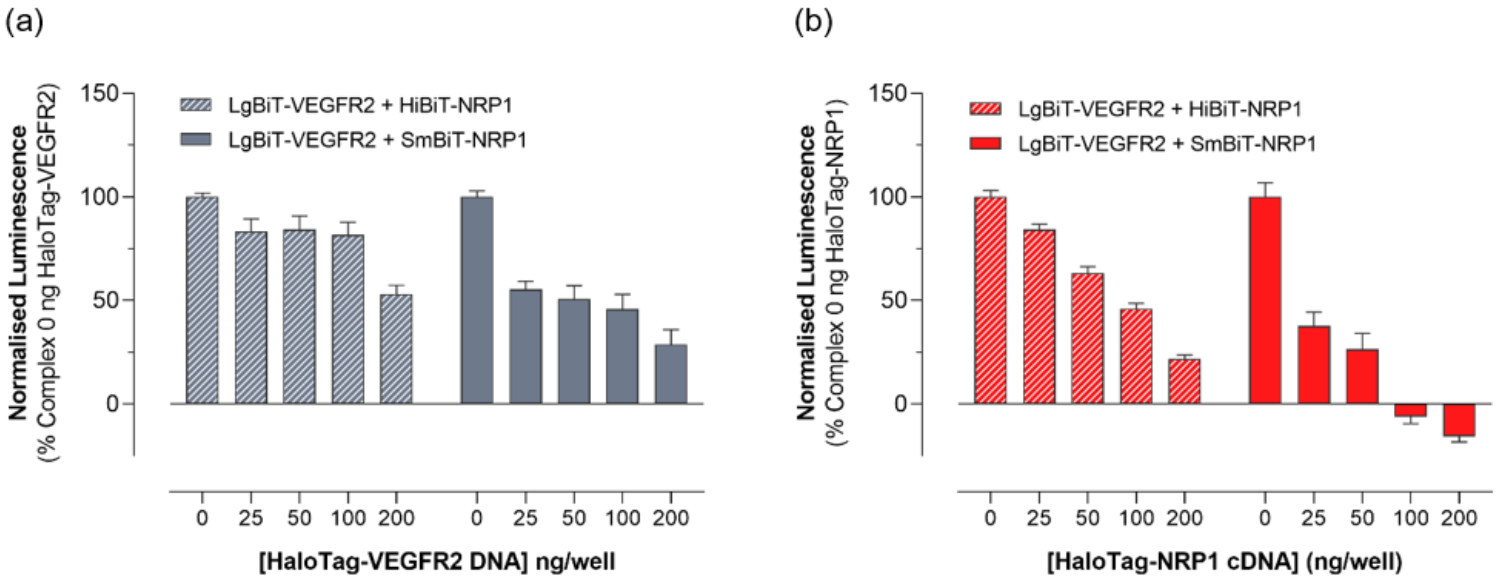


Figure 5.10 ***Prevention of NanoBiT complex formation by co-expression of increasing amounts of competing VEGFR2 or NRP1****. HEK293T-ReLuc2P cells were transiently transfected in 96-well plates. Cells were transfected with equal amounts of LgBiT-VEGFR2 (50 ng cDNA/well) and either HiBiT-NRP1 (lined bars) or SmBiT-NRP1 (solid bars) at 50 ng cDNA/well. Cells were also transfected with increasing amounts (0-200 ng cDNA/well) of HaloTag-VEGFR2 (a) or HaloTag-NRP1 (b), as well as with pcDNA3.1/Zeo empty vector (for 300 ng total cDNA/well). Cells were incubated with 10 µM furimazine in HBSS/0.1% BSA for 10 minutes (37°C). Luminescence emissions were measured by the PHERAstar FS platereader (475-505 nm). Data were normalised to un-transfected cells (0%) and the complemented NanoBiT complex in the absence of competing receptor (100%), per experiment. Data are expressed as mean ± S.E.M. from 3 independent experiments, each with triplicate wells.*

Quantifying ligand binding at a defined VEGFR2/NRP1 complex

We previously demonstrated that $VEGF_{165}$a-TMR had distinct ligand binding kinetics at VEGFR2 and NRP1 when expressed individually. Having demonstrated that co-expressed receptors were able to form a heteromeric complex, we aimed to determine the pharmacological characteristics of this defined complex. To quantify ligand binding at a defined receptor/co-receptor complex, we used LgBiT-VEGFR2/HiBiT-NRP1 as a luminescent donor (*Figure 5.11a; Methods 2.8.5*). When fluorescent VEGF-TMR binds the heteromeric VEGFR2/NRP1 complex, BRET should only occur from the defined NanoBiT complex. Initial ligand binding studies were performed with LgBiT-VEGFR2 and HiBiT-NRP1 due to the higher luminescence signal compared to the SmBiT complex.

At the complemented NanoBiT complex, there was saturable binding in the presence of increasing concentrations of $VEGF_{165}$b-TMR (*Figure 5.11b*) or $VEGF_{165}$a-TMR (*Figure 5.11c*). This was displaced by a high concentration of unlabelled ligand, demonstrating low non-specific binding. Both fluorescent ligands had equilibrium dissociation constants in the nanomolar range at the VEGFR2/NRP1 complex ($VEGF_{165}$b-TMR K_d = 16.26 ± 3.81 nM; $VEGF_{165}$a-TMR K_d = 2.53 ± 0.49; n=3 for both). Estimated ligand binding affinities were similar to those derived at isolated receptors tagged with full-length NanoLuc (*Table 5.1,* Saturation pK_d). There was no significant difference in the affinity of $VEGF_{165}$b-TMR at the complex compared to NanoLuc-VEGFR2 alone (unpaired t-test P>0.05, n=3-5 per group). Affinities were also similar for $VEGF_{165}$a-TMR at the NanoBiT complex compared to NanoLuc-VEGFR2 (unpaired t-test P>0.05, n=3-5 per group) or NanoLuc-NRP1 (unpaired t-test P>0.05, n=3-6 per group). $VEGF_{165}$b-TMR did, however, have a significantly lower affinity (pK_d) than $VEGF_{165}$a-TMR for the NanoBiT complex (unpaired t-test P<0.01, n=3).

Ligand binding kinetics for $VEGF_{165}$b-TMR and $VEGF_{165}$a-TMR were monitored at the complemented LgBiT-VEGFR2/HiBiT-NRP1 complex (*Figure 5.12*). Four ligand concentrations were used to quantify kinetic parameters at the NanoBiT complex. First, $VEGF_{165}$b-TMR kinetics were characterised as a selective ligand that can only interact with VEGFR2 within the complex. The profile continued to increase over the full 90 minute timecourse in intact cells (*Figure 5.12a*). This produced a classic ligand binding association curve maintained for each concentration of $VEGF_{165}$b-TMR. This was comparable to the ligand binding kinetic profile monitored in membrane preparations (*Figure 4.14*). These kinetic data were fit to a simple exponential association to individually estimate the k_{obs} for each ligand concentration (*Figure 5.12b*). These data demonstrated a linear relationship for $VEGF_{165}$b-TMR ($y = 0.0023x + 0.034$, $R^2 = 0.46$), suggesting this interaction with the NanoBiT complex can be defined as a first order reaction. Association binding curves were analysed globally over the 90 minute timecourse with $VEGF_{165}$b-TMR at the constrained VEGFR2/NRP1 complex (*Table 5.1*). For all kinetic data in this Chapter, data were fit to a global association without constraining the association rate (k_{on}). $VEGF_{165}$b-TMR demonstrated a significantly slower association rate for the NanoBiT complex compared to NanoLuc-VEGFR2 alone (Mann-Whitney test, $P<0.01$, n=5 per group). There was a similar binding affinity derived from saturation and kinetic assays (unpaired t-test, $P>0.05$).

Kinetic experiments were repeated with four concentrations of $VEGF_{165}$a-TMR (*Figure 5.12c*), using 10 nM as a saturating concentration based on previous endpoint assays (*Figure 5.11c*). Unlike $VEGF_{165}$b-TMR, there was a small decline in BRET ratio between 30-60 minutes for $VEGF_{165}$a-TMR. As such, association binding curves were fit to kinetic data from the initial 20 minutes. Plotting the k_{obs} calculated for each $VEGF_{165}$a-TMR concentration, there was a linear relationship between kinetic constants and $VEGF_{165}$a-TMR concentration (*Figure 5.12d;* $y = 0.0024x + 0.10$, $R^2 = 0.72$). This suggested that despite binding both receptors within the complex, the interaction between $VEGF_{165}$a-TMR and the NanoBiT complex could also be defined by a first order reaction (Pollard and De La Cruz, 2013). Kinetic parameters were fit using a global association fit (*Table 5.1*). There was a significantly slower dissociation rate constant derived for $VEGF_{165}$a-TMR at the NanoBiT complex compared to NanoLuc-NRP1 (one-way ANOVA $P<0.05$; post-Hoc Dunn's multiple comparisons test, $P<0.05$, n=5).

Real-time ligand binding profiles were directly compared between the HiBiT complex (LgBiT-VEGFR2 + HiBiT-NRP1) with cells expressing NanoLuc-tagged receptors alone. First, raw luminescence emissions were compared in the presence of vehicle (HiBiT complex emissions = 159695 ± 26097 RFU; NanoLuc-VEGFR2 emissions = 300835 ± 40997 RFU; NanoLuc-NRP1 566140 ± 76973 RFU; n=5 for each). Compared using a repeated measures ANOVA (P<0.05, n=5 per group) and Holm-Šidák's multiple comparisons test, cells expressing the HiBiT complex had significantly lower luminescence emissions than NanoLuc-VEGFR2 (P<0.01) or NanoLuc-NRP1 (P<0.001). Saturating concentrations of $VEGF_{165}$b-TMR and $VEGF_{165}$a-TMR were then added to cells expressing the complemented NanoBiT complex, NanoLuc-VEGFR2 or NanoLuc-NRP1 on the same plate (*Figure 5.13*). $VEGF_{165}$b-TMR had a similar association binding profile at the NanoBiT complex compared to NanoLuc-VEGFR2 *(Figure 5.13a*). The small decline in BRET signal after a peak at 20 minutes at NanoLuc-VEGFR2 in intact cells was absent at the NanoBiT complex for $VEGF_{165}$b-TMR. There was no BRET detected between $VEGF_{165}$b-TMR and NanoLuc-NRP1 (*Figure 5.13b*). As such, $VEGF_{165}$b-TMR ligand binding at the NanoBiT complex arises from interactions with VEGFR2 alone. A one-phase exponential association model was fit to compare the k_{obs} between the complex and NanoLuc-tagged receptors at this saturating ligand concentration (*Table 5.2*). Having demonstrated that these were defined by a first order rate reaction, the k_{obs} was used to estimate $t_{1/2}$ ($t_{1/2} = 0.693/k_{obs}$). This was defined as the time taken for half of the ligand/receptor complexes to associate at that concentration. $VEGF_{165}$b-TMR had similar kinetics at the NanoBiT complex compared to NanoLuc-VEGFR2 (Wilcoxon matched-pairs signed rank test, P>0.05, n=5 per group).

Ligand binding kinetics of 10 nM $VEGF_{165}$a-TMR were also compared between the NanoBiT complex and NanoLuc-VEGFR2 (*Figure 5.13c*) or NanoLuc-NRP1 (*Figure 5.13d*). Compared to full-length NanoLuc-VEGFR2 in intact cells, $VEGF_{165}$a-TMR had a lesser decline in BRET ratio after the peak at the VEGFR2/NRP1 NanoBiT complex. $VEGF_{165}$a-TMR kinetics at the NanoBiT complex in the initial 20 minutes had a closer overlay to NanoLuc-VEGFR2 compared to NanoLuc-NRP1. Derived kinetic parameters from these initial 20 minutes also suggested that the dynamics of binding at the NanoBiT complex had a comparable rate constant and half time for ligand/receptor association to NanoLuc-VEGFR2 (*Table 5.2*). $VEGF_{165}$a-TMR kinetic parameters were significantly slower at the NanoBiT complex than at NanoLuc-NRP1 (repeated-measures ANOVA, Holm-Šidák's multiple comparisons; P<0.05, n=5).

Initial publication of NanoBiT complementation technologies demonstrated that the HiBiT tag itself had an intrinsic affinity to complement with LgBiT (Dixon et al., 2016). In contrast, SmBiT had a lower intrinsic affinity for NanoBiT complementation. This reduced the likelihood for the tag itself to drive heteromeric receptor-receptor interactions. As such, ligand binding kinetics were monitored at the NanoBiT complex formed between SmBiT-NRP1 and LgBiT-VEGFR2 (*Figure 5.14*). Using four concentrations of $VEGF_{165}$b-TMR or $VEGF_{165}$a-TMR, binding was monitored over 90 minutes (*Figure 5.14a,d*). Binding profiles remained elevated throughout the 90 minute timecourse for both fluorescent VEGF-A ligands. When directly comparing the initial binding association at the HiBiT and SmBiT complex, kinetic profiles were similar for both $VEGF_{165}$b-TMR (*Figure 5.14b*) and $VEGF_{165}$a-TMR (*Figure 5.14e*). To enable comparisons with kinetics derived at the HiBiT complex, kinetic data were fit from the initial 90 minutes for $VEGF_{165}$b-TMR or 20 minutes for $VEGF_{165}$a-TMR. First, k_{obs} values were fit to each concentration of fluorescent ligand (*Figure 5.14c,f*). As observed at the HiBiT complex, there was a linear relationship between the rate constants and ligand concentration for both $VEGF_{165}$b-TMR (*Figure 5.14c;* $y = 0.0026x + 0.01$, $R^2 = 0.65$) and $VEGF_{165}$a-TMR (*Figure 5.14f;* $y = 0.0025x + 0.09$, $R^2 = 0.62$). These data also demonstrated that there was a slower k_{obs} derived at the SmBiT complex compared to the HiBiT complex for $VEGF_{165}$b-TMR. Second, kinetic parameters were also using a global association model with an unconstrained k_{on} (*Table 5.3*). There were no differences between the kinetic parameters derived for $VEGF_{165}$a-TMR between the HiBiT and SmBiT complex (Kruskal-Wallis test, Dunn's multiple comparisons test, $P>0.05$, n=5 per group).
In contrast, $VEGF_{165}$b-TMR had an even slower dissociation rate (k_{off}) from the SmBiT complex compared to the HiBiT complex ($P<0.05$, n=5 per group). This k_{off} was 5-fold slower from the SmBiT complex compared to NanoLuc-VEGFR2 expressed alone.

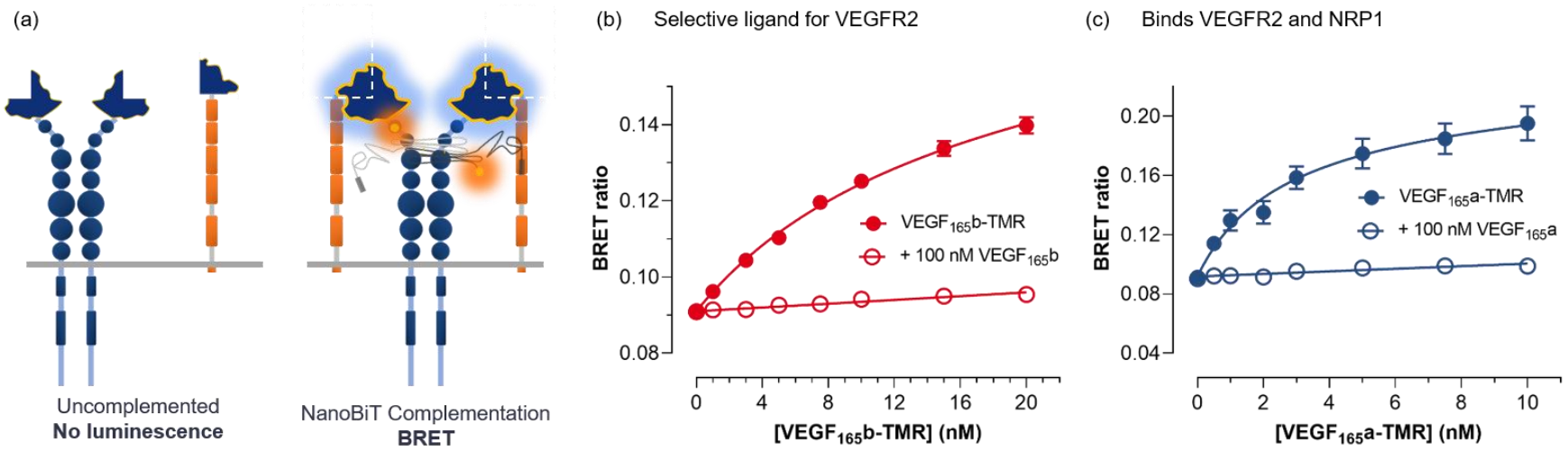


Figure 5.11 ***Saturation binding of fluorescent VEGF-A at a HiBiT complex of VEGFR2 and NRP1****. (a) VEGF-TMR ligand binding was monitored at a defined complex of LgBiT-VEGFR2 and HiBiT-NRP1. In the presence of furimazine, individual receptors do not emit luminescence in isolation. Upon NanoBiT complementation, luminescence emissions can excite the TMR fluorophore in close proximity. NanoBiT therefore only acts as a luminescent donor when VEGFR2 and NRP1 are in complex. (b,c) HEK293T-ReLuc2P cells were transfected in 6-well plates with equal amounts of LgBiT-VEGFR2 (750 ng cDNA/well) and HiBiT-NRP1 (750 ng cDNA/well). Following 24 hours, transfected cells were seeded in 96-well plates. On the day of experimentation, cells were incubated with increasing concentrations of VEGF$_{165}$b-TMR (b) or VEGF$_{165}$a-TMR (c). This was performed in the presence or absence of 100 nM VEGF$_{165}$b (b) or VEGF$_{165}$a (c) to determine non-specific binding. Following 60 minutes at 37°C, 10 µM furimazine was added for 10 minutes (37°C). Emissions were measured on the PHERAstar platereader (550-LP/460-480 nm). BRET ratios are expressed as mean ± S.E.M. from 3 independent experiments with duplicate wells. Derived equilibrium dissociation constants (pK$_d$) are in* Table 5.1.

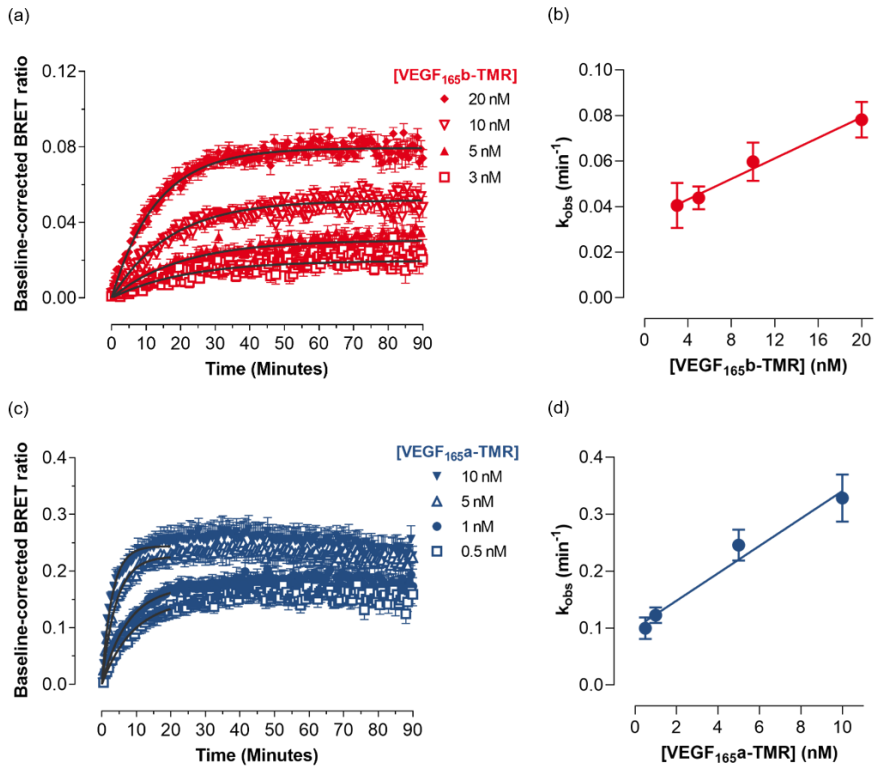


Figure 5.12 ***Kinetics of VEGF$_{165}$b-TMR and VEGF$_{165}$a-TMR binding at a HiBiT complex of VEGFR2 and NRP1****. HEK293T-ReLuc2P cells were transfected in 6-well plates with equal amounts of LgBiT-VEGFR2 (750 ng cDNA/well) and HiBiT-NRP1 (750 ng cDNA/well). Following 24 hours, transfected cells were seeded in 96-well plates. Cells were pre-treated with furimazine (10 µM) and left to equilibrate at 37°C for 10 minutes. (a) Cells were stimulated with 4 concentrations of VEGF$_{165}$b-TMR added at x=0. (b) Exponential association curves were fit to kinetic data for each concentration to derive the rate constant, k_{obs}. These were plotted against VEGF$_{165}$b-TMR concentration and fit against a linear regression (y = 0.0023x + 0.034, R^2 = 0.46). (c) Cells were stimulated with 4 concentrations of VEGF$_{165}$a-TMR. Kinetic data from the initial 20 minutes were fit to an exponential model. (d) The derived k_{obs} were plotted against each VEGF$_{165}$a-TMR concentration and fit with a linear regression (y = 0.0024x + 0.10, R^2 = 0.72). Emissions were simultaneously measured on the PHERAstar FS platereader every 30 seconds for 90 minutes at 37°C. BRET ratios were baseline-corrected to vehicle at each time point per replicate. Data represent mean ± S.E.M. from 5 independent experiments with duplicate wells in each independent experiment. Derived kinetic parameters are given in* Table 5.1.

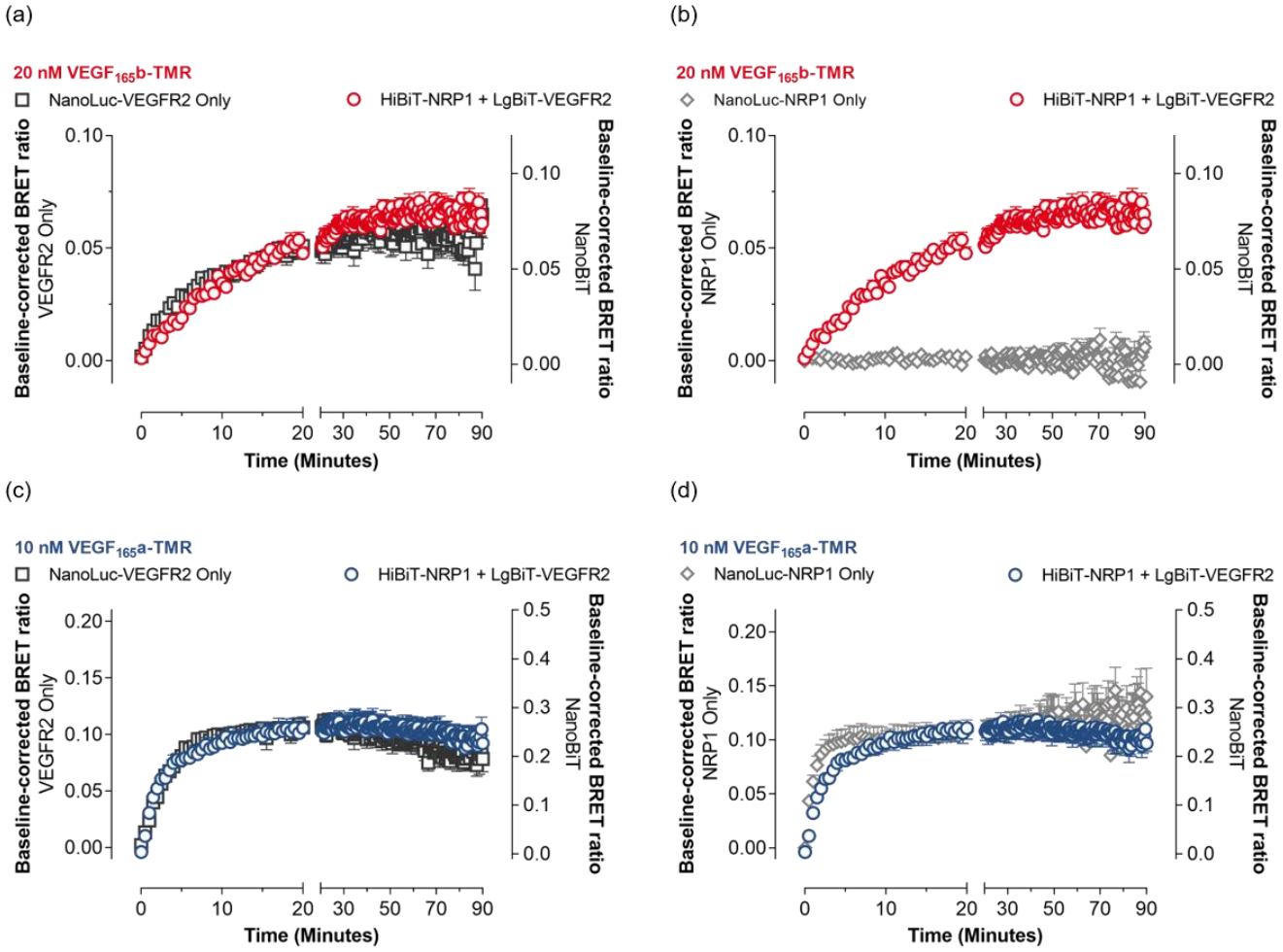


Figure 5.13 ***Real-time binding of fluorescent VEGF-A isoforms at isolated receptors compared to the NanoBiT complex.*** *See next page.*

*Figure 5.13 Ctd. (a) HEK293T-ReLuc2P cells were transfected in 6-well plates with equal amounts of LgBiT-VEGFR2 (750 ng cDNA/well) and HiBiT-NRP1 (750 ng cDNA/well). Alternatively, cells were transfected with equal amounts of NanoLuc-VEGFR2 or NanoLuc-NRP1 (750 ng cDNA/well) and empty pcDNA3.1/Zeo vector (750 ng cDNA/well). Following 24 hours, transfected cells were seeded in 96-well plates. On the day of experimentation, cells were pre-treated with furimazine (10 µM) and left to equilibrate at 37°C for 10 minutes. (a) On the same plate, the binding profile of 20 nM $VEGF_{165}$b-TMR at LgBiT-VEGFR2/HiBiT-NRP1 (*Figure 5.12*) was compared to cells only expressing NanoLuc-VEGFR2 (left y axis, open symbols). (b) The same BRET profile for 20 nM $VEGF_{165}$b-TMR at LgBiT-VEGFR2/HiBiT-NRP1 was compared to those obtained at NanoLuc-NRP1 in isolation. (c,d) Alternatively, cells were stimulated with 10 nM $VEGF_{165}$a-TMR. This compared binding at LgBiT-VEGFR2/HiBiT-NRP1 (*Figure 5.12*) to cells only expressing (c) NanoLuc-VEGFR2 or (d) NanoLuc-NRP1 (left y axis, open symbols). Emissions were simultaneously measured on the PHERAstar FS platereader every 30 seconds for 90 minutes at 37°C (550-LP/450-480 nm filter). BRET ratios were baseline-corrected to vehicle at each time point per experimental replicate. The x axis was split to highlight the initial association (Chapter 3) and long-term BRET signal (Chapter 4). Data represent mean ± S.E.M. from 5 independent experiments with duplicate wells. Derived k_{obs} values are presented in* Table 5.2*.*

Table 5.1 ***Summary of kinetic parameters derived at the NanoBiT complex for $VEGF_{165}$b-TMR and $VEGF_{165}$a-TMR.***

	Saturation pK_d	Kinetic pK_d	k_{on} ($min^{-1}M^{-1}$)	k_{off} (min^{-1})
$VEGF_{165}$b-TMR				
LgBiT-VEGFR2 + HiBiT-NRP1	7.82 ± 0.11 (3)	7.81 ± 0.10 (5)	$2.29x10^6 \pm 0.30x10^6$ (5)	0.037 ± 0.007 (5)
NanoLuc-VEGFR2	8.04 ± 0.06 (5)	8.07 ± 0.18 (5)	$7.29x10^6 \pm 1.84x10^6$ (5) **	0.060 ± 0.011 (5)
NanoLuc-NRP1	n/a	n/a	n/a	n/a
$VEGF_{165}$a-TMR				
LgBiT-VEGFR2 + HiBiT-NRP1	8.61 ± 0.09 (3)	8.83 ± 0.12 (5)	$3.12x10^7 \pm 0.43x10^7$ (5)	0.046 ± 0.007 (5)
NanoLuc-VEGFR2	8.75 ± 0.25 (5)	8.47 ± 0.23 (5)	$1.54x10^7 \pm 0.38x10^7$ (5)	0.055 ± 0.017 (5)
NanoLuc-NRP1	8.45 ± 0.13 (6)	8.40 ± 0.17 (5)	$7.11x10^7 \pm 2.33x10^7$ (5)	0.260 ± 0.050 (5) *

Parentheses represent the number of independent experiments, each with duplicate wells. Experiments with LgBiT-VEGFR2 + HiBiT-NRP1 were performed in *Figure 5.11* (Saturation) or *Figure 5.12* (Kinetics). Alternatively, binding parameters were determined at full-length NanoLuc-tagged receptors expressed alone in intact cells, as shown in *Table 3.3* (NanoLuc-VEGFR2) and *Table 3.5* (NanoLuc-NRP1). Kinetics at LgBiT-VEGFR2 + HiBiT-NRP1 were fit with an unconstrained k_{on}, therefore values are displayed for the saturating ligand concentration (20 nM $VEGF_{165}$b-TMR or 10 nM $VEGF_{165}$a-TMR). Each parameter for $VEGF_{165}$b-TMR was compared between the NanoBiT complex and NanoLuc-VEGFR2 with an unpaired t-test (pK_d) or Mann-Whitney test (k_{on}, k_{off}), neither of which were significant. Each parameter for $VEGF_{165}$a-TMR was compared between the NanoBiT- and NanoLuc-tagged receptors using a one-way ANOVA (pK_d) or Kruskal-Wallis test (k_{on}, k_{off}), followed by a Dunn's multiple comparisons test (* P<0.05, ** P<0.01).

Table 5.2 ***Comparison of k_{obs} values derived for $VEGF_{165}$b-TMR and $VEGF_{165}$a-TMR in matched experiments***.

	20 nM $VEGF_{165}$b-TMR (90 minutes)		10 nM $VEGF_{165}$a-TMR (20 minutes)	
	k_{obs} (min^{-1})	$t_{1/2}$ (min)	k_{obs} (min^{-1})	$t_{1/2}$ (min)
LgBiT-VEGFR2 + HiBiT-NRP1	0.08 ± 0.01	9.27 ± 1.01	0.33 ± 0.04	2.29 ± 0.36
NanoLuc-VEGFR2	0.11 ± 0.02	7.73 ± 1.84	0.31 ± 0.03	2.31 ± 0.18
NanoLuc-NRP1	n/a	n/a	0.93 ± 0.09 ***	0.77 ± 0.07 *

Data represent 5 independent experiments with duplicate wells. Kinetic values were fit from comparisons in matched experiments between the top fluorescent VEGF-A concentration in *Figure 5.13*. Half times of ligand/receptor association, $t_{1/2}$, were estimated ($t_{1/2} = 0.693/k_{obs}$) to enable comparisons with previous timecourse data. For $VEGF_{165}$b-TMR, kinetic parameters were compared between the NanoBiT complex (LgBiT-VEGFR2 + HiBiT-NRP1) and NanoLuc-VEGFR2 using a Wilcoxon matched-pairs signed rank test (not significant). For $VEGF_{165}$a-TMR, parameters were compared between the NanoBiT complex and either NanoLuc-VEGFR2 or NanoLuc-NRP1 using a repeated measures one-way ANOVA followed by a Holm-Šidák's multiple comparisons test (* P<0.05; *** P<0.001).

Table 5.3 ***Kinetic parameters for $VEGF_{165}$b-TMR and $VEGF_{165}$a-TMR at the HiBiT- and SmBiT- tagged heteromeric complex of VEGFR2/NRP1***.

	Kinetic pK_d	k_{on} ($min^{-1}M^{-1}$)	k_{off} (min^{-1})
$VEGF_{165}$b-TMR			
HiBiT Complex	7.81 ± 0.10	$2.29x10^6 \pm 0.30x10^6$	0.037 ± 0.007
SmBiT Complex	8.43 ± 0.17	$2.94x10^6 \pm 0.55x10^6$	0.012 ± 0.003 *
$VEGF_{165}$a-TMR			
HiBiT Complex	8.83 ± 0.12	$3.12x10^7 \pm 0.43x10^7$	0.046 ± 0.007
SmBiT Complex	8.83 ± 0.31	$2.83x10^7 \pm 0.69x10^7$	0.046 ± 0.020

Data were obtained from 5 independent experiments, each with duplicate wells. Each kinetic parameter was compared between the HiBiT or SmBiT complex for each fluorescent VEGF-A ligand. This either used an ordinary one-way ANOVA (pK_d) or a Kruskal-Wallis test (k_{on}, k_{off}), followed by a Dunn's multiple comparisons test (* P<0.05).

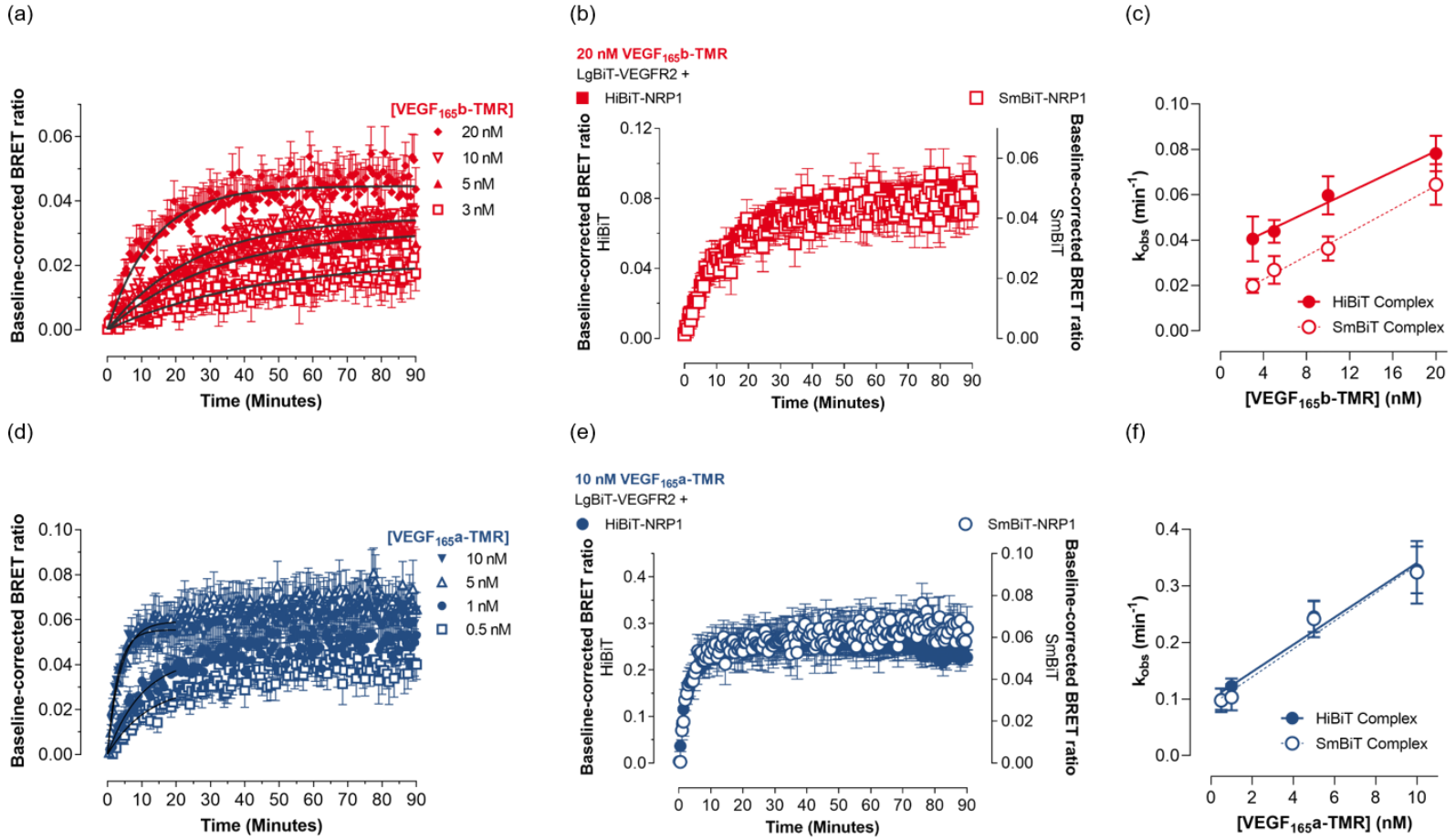


Figure 5.14 ***Kinetics of VEGF$_{165}$b-TMR and VEGF$_{165}$a-TMR at a VEGFR2/NRP1 SmBiT complex compared to HiBiT.*** *See next page.*

Figure 5.14. Ctd. HEK293T-ReLuc2P cells were transfected in 6-well plates with equal amounts of LgBiT-VEGFR2 (750 ng cDNA/well) and SmBiT-NRP1 (750 ng cDNA/well). Following 24 hours, transfected cells were seeded in 96-well plates. On the day of experimentation, cells were pre-treated with furimazine and left to equilibrate at 37°C for 10 minutes. (a,d) Four concentrations of $VEGF_{165}$b-TMR (a) or $VEGF_{165}$a-TMR (d) were added at x=0. (b) Kinetic data were fit to a global association model without a constrained k_{on} from the 90 minute timecourse (a) or initial 20 minutes. (d) The binding profile of 20 nM $VEGF_{165}$b-TMR was compared between cells expressing LgBiT-VEGFR2 and either HiBiT-NRP1 (left y axis, filled symbols; data from Figure 5.12*) or SmBiT-NRP1 (right y axis, open symbols; data from* (a)*). (e) The binding profile of 10 nM $VEGF_{165}$a-TMR was compared between cells co-expressing LgBiT-VEGFR2 with HiBiT-NRP1 or SmBiT-NRP1, as above. (c,f) The k_{obs} was fit for each concentration of fluorescent $VEGF_{165}$b-TMR (c) or $VEGF_{165}$a-TMR (f). These were compared to the k_{obs} plots for the HiBiT complex (*Figure 5.*12), both of which fit with a linear regression (see text). Emissions were simultaneously measured on the PHERAstar FS platereader every 30 seconds for 90 minutes at 37°C. BRET ratios were baseline-corrected to vehicle at each time point. Data represent mean ± S.E.M. from 5 independent experiments with duplicate wells in each experiment. Derived kinetic parameters are in* Table 5.3*.*

We previously demonstrated the influence of receptor localisation on ligand binding in living cells (Chapter 4), however it is unknown where the BRET signal is arising from in intact cells expressing the NanoBiT complex. As such, we imaged the localisation of luminescence emissions from receptors expressed in HEK293T cells (*Figure 5.15*). This bioluminescence widefield imaging system collects the short emission wavelengths of NanoLuc (λ_{Em} 460 nm), taking advantage of a highly sensitive camera and an imaging chamber that excludes external light (*Methods 2.6.3*). Cells were incubated with membrane-permeable furimazine. This substrate is oxidised by the enzymatic activity of both NanoLuc and complemented NanoBiT. Receptors were imaged in the absence of ligand, comparing the localisation of VEGFR2 or NRP1 tagged with full-length NanoLuc (*Figure 5.15a,b*) with that of the complemented HiBiT-NRP1/LgBiT-VEGFR2 complex (*Figure 5.15c*). In line with earlier imaging studies in living cells, NanoLuc-VEGFR2 was primarily localised at intracellular sites (*Figure 5.15a*). In contrast, NanoLuc-NRP1 was entirely localised at the plasma membrane (*Figure 5.15b*). The NanoBiT complex formed between HiBiT-NRP1 and LgBiT-VEGFR2 was localised around the plasma membrane and in some intracellular sites (*Figure 5.15c*). There was evidence that both NanoLuc-NRP1 and the NanoBiT complex were localised in filopodia-like projections emerging from the cell surface.

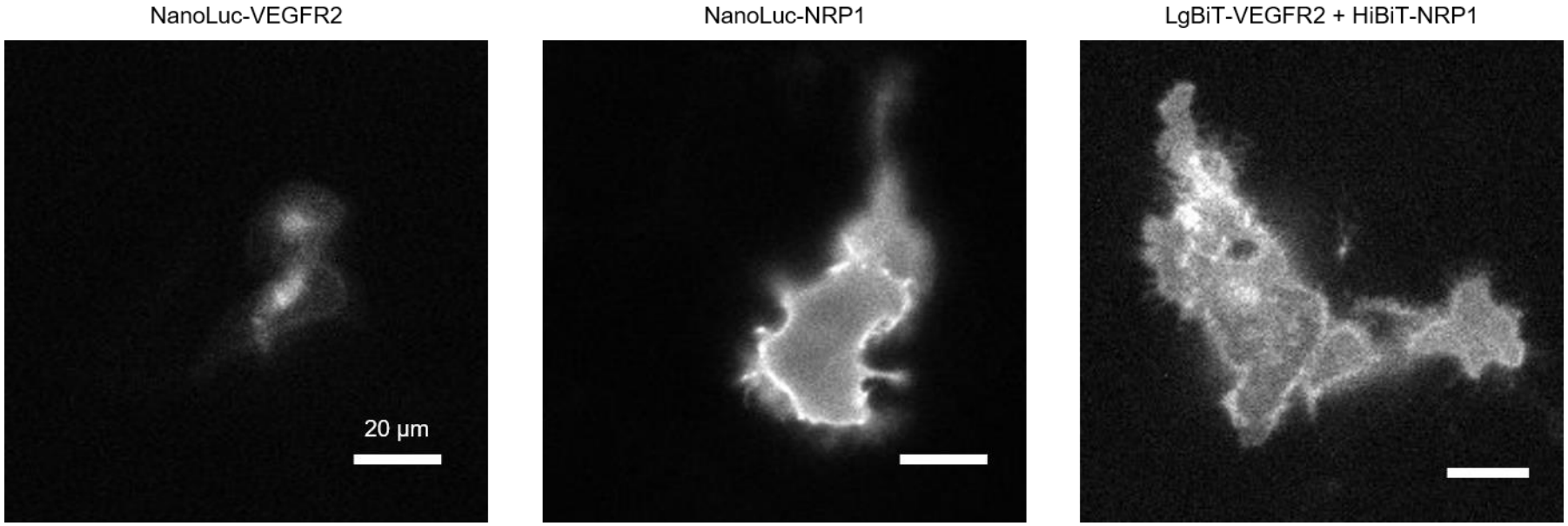


Figure 5.15 ***Localisation of luminescence emissions obtained using Olympus LV200 Bioluminescence Imaging****. HEK293T-ReLuc2P cells were transfected in 6-well plates with NanoLuc-VEGFR2 or NanoLuc-NRP1 (750 ng cDNA/well) and empty pcDNA3.1/Neo vector (750 ng cDNA/well). Alternatively, cells were transfected with LgBiT-VEGFR2 (750 ng cDNA/well) and HiBiT-NRP1 (750 ng cDNA/well). Following 24 hours, transfected cells were seeded into 35 mm² glass-bottomed dishes. Cells were incubated with furimazine for 10 minutes at 37°C (26 µM for full-length NanoLuc; 104 µM for NanoBiT complex). Cells were imaged live using a widefield Olympus LV200 Bioluminescence Imaging System (60X objective with 0.5X tube lens). Images are representative from 3 independent experiments.*

5.4 DISCUSSION

We previously quantified the pharmacology of VEGFR2 or NRP1 expressed in isolation in HEK293T cells (Chapters 3-4), however physiologically relevant systems co-express these receptors alongside one another (Whitaker et al., 2001; Prahst et al., 2008; Fantin et al., 2013; Koch et al., 2014; Lee-Montiel et al., 2015). Despite similar affinities for the same ligand ($VEGF_{165}$a-TMR), NRP1 has faster ligand binding kinetics than VEGFR2. In isolation, these receptors were also localised in distinct subcellular compartments in living cells. Here, we demonstrated that VEGFR2 and NRP1 were in close proximity (<10 nm) in HEK293T cells when expressed together. This corroborated published findings for constitutive heteromeric complex formation using receptor-receptor BRET with full-length receptors in living cells. It was unknown how this receptor/ co-receptor complex interacted with ligand considering their distinct pharmacology, therefore we established a novel assay system to quantify ligand binding at a defined complex using split tag technologies. Luminescence was only emitted from a heteromeric NanoBiT complex between a complemented LgBiT and HiBiT/SmBiT fragment. As such, BRET would only occur from a VEGFR2/NRP1 heteromer to VEGF-TMR bound at the complex. In light of previous data highlighting distinctions between VEGFR2 and NRP1 (Chapters 3-4), we developed a real-time technique to probe ligand binding dynamics at 37°C at a defined complex for insight into VEGF-A pharmacology in physiological systems through which VEGFR2 signalling is modulated by NRP1 co-expression.

This Chapter focussed on two key functionally distinct VEGF-A isoforms: prototypical $VEGF_{165}$a and 'anti-angiogenic' $VEGF_{165}$b. Although these isoforms only differ by six amino acid residues at their C-terminus, $VEGF_{165}$b is selective for VEGFR2 and unable to interact with NRP1. Despite observed physiological distinctions between VEGF-A isoforms, there were no differences observed at the level of ligand binding at NanoLuc-VEGFR2 expressed in isolation (Chapter 3). Monitoring ligand binding at a VEGFR2/NRP1 complex using NanoBiT complementation suggested $VEGF_{165}$b-TMR had a lower affinity than $VEGF_{165}$a-TMR. This distinction was also observed at NanoLuc-VEGFR2 in isolation, albeit to a lesser extent. Future experiments should use unlabelled $VEGF_{165}$b for displacement ligand binding experiments to directly investigate whether the VEGFR2/NRP1 complex decreased the affinity of $VEGF_{165}$b for VEGFR2. There were distinctions between fluorescent VEGF-A isoforms in their kinetic profiles at the NanoBiT complex. In terms of their long-term ligand binding profile, the BRET signal for $VEGF_{165}$b-TMR remained elevated in intact cells at the NanoBiT complex. This profile resembled isolated NanoLuc-VEGFR2 in membrane preparations, as opposed to the small decline in NanoBRET signal observed in intact cells (Chapter 4). The profile for $VEGF_{165}$a-TMR at the NanoBiT complex had a small decrease at later time points, however this was to a lesser extent than at NanoLuc-VEGFR2 in intact cells.

Interestingly, the initial association kinetics for both fluorescent VEGF-A isoforms with the NanoBiT complex were closer to those observed at NanoLuc-VEGFR2 in isolation compared to NanoLuc-NRP1. This was evident from the kinetic rate constant, k_{obs}, and residence times estimated for the saturating concentration of fluorescent probe. This was therefore contrary to our earlier proposal that the faster ligand binding kinetics at NRP1 might present ligand to VEGFR2 and increase the kinetics of ligand/receptor interactions. It would also be valuable to have a probe selective for NRP1 that could not interact with VEGFR2. The interaction interface between VEGF-A and VEGFR2 may be too large to disrupt ligand binding using site-directed mutagenesis. There is, however, a binding-dead mutant or NRP1 (Y297A) that disrupts the interface interacting with the C-terminus of $VEGF_{165}$a (Herzog et al., 2011; Fantin et al., 2014; Peach et al., 2018a). This could be used in future experiments to confirm whether VEGF-A/NRP1 interactions were responsible for distinctions between $VEGF_{165}$b and $VEGF_{165}$a, as opposed to interactions with other parts of the macromolecular complex.

In the absence of ligand, VEGFR2 and NRP1 were in close proximity (<10 nm, *Appendix 7*.5). This was demonstrated by monitoring BRET between NanoLuc-VEGFR2 and NRP1 tagged at the N-terminus with AlexaFluor488 via HaloTag or SnapTag. Unlike the FRET-based technique using C-terminal tagged receptors (King et al., 2018), the membrane-impermeant fluorophore isolated receptors successfully exported to the plasma membrane. In addition to this saturable BRET signal between VEGFR2 and NRP1, receptors enabled the complementation of a NanoBiT complex that was reduced in the presence of competing receptor. In addition, colocalisation was observed in live cell imaging studies in the absence or presence of ligand. These data agree with other groups demonstrating ligand-independent complex formation between VEGFR2 and NRP1 (Whitaker et al., 2001; Gelfand et al., 2014; King et al., 2018). The stoichiometry of VEGFR2/NRP1 complexes are unknown. As both VEGFR2 and NRP1 form oligomers, a larger multimeric receptor cluster could be formed as suggested for EGFR (Clayton et al., 2005; Saffarian et al., 2007; Wang et al., 2014; Needham et al., 2016). It remains unknown whether there is a direct interface between VEGFR2 and NRP1. The transmembrane domain has been proposed as a potential heterodimerisation site (Sarabipour and Mac Gabhann, 2017). If NRP1 modulates VEGFR2 via direct interactions that were spatially distinct from the VEGF-A binding site, NRP1 could be a novel receptor-mediated class of endogenous positive allosteric modulator (De Smet et al., 2014).

NanoBiT fragments were conjugated to each receptor in the heteromeric complex via flexible linker sequences. These successfully complemented to emit luminescence from a LgBiT-VEGFR2/HiBiT-NRP1 complex. These tags did not compromise receptor activity in terms of NFAT reporter gene signalling or ligand binding. Luminescence emissions from HiBiT and SmBiT complexes were reduced by increasing amounts of

competing HaloTag-VEGFR2 or HaloTag-NRP1. Previous work has shown that HiBiT had a higher intrinsic affinity to complement with LgBiT compared to SmBiT (Dixon et al., 2016). We demonstrated that luminescence emissions from the HiBiT complex were higher than the SmBiT complex, as seen in published studies using NanoBiT-tagged GPCRs (Botta et al., 2019). The intrinsic affinity between the HiBiT and LgBiT tag can vary according the expression system and protein conformation, as observed for chemokine GPCRs using the purified exogenous tag in different assay setups (White et al., 2020). While the intrinsic affinity between NanoBiT tags should be considered, there is already evidence that VEGFR2 and NRP1 form complexes under constitutive conditions and our experimental question focussed on the pharmacological properties of this defined heteromeric complex. Future studies could use this system to probe receptor internalisation using purified, membrane-impermeable HiBiT or LgBiT fragments (Boursier et al., 2020; Soave et al., 2020). For example, this technique could quantitatively probe the cell surface expression of NRP1 in cells co-expressing VEGFR2.

Imaging studies exploited the compatibility of HaloTag and SnapTag technologies to label distinct receptors co-expressed by the same cell. We used this to investigate the colocalisation of VEGFR2 and NRP1 in living cells at 37°C in the absence or presence of VEGF-A stimulation. Unlike immunofluorescent antibody labelling, this did not require cell fixation or cell permeabilisation to access internalised receptor. VEGFR2 and NRP1 were largely localised in distinct subcellular regions as previously shown when expressed independently in HEK293T cells. Membrane-impermeant substrates for both HaloTag and SnapTag allowed us to only label receptors that were successfully exported to the cell surface. VEGFR2 was predominantly intracellular whereas NRP1 was highly localised around the plasma membrane. As such, both receptors were still localised in distinct subcellular regions despite evidence for constitutive receptor-receptor interactions. There was also a large amount of NRP1 localised at cell-cell junctions. Other transmembrane proteins are present in endothelial cell-cell junctions, such as VE-cadherin (Vestweber, 2008). It is unknown whether these could form a larger complex influencing trans-cellular permeability. Interestingly, ligand stimulation decreased the amount of NRP1 at cell-cell junctions in cells co-expressing VEGFR2. This could lead to increased vascular permeability in endothelial cells, as a phenotype observed in response to VEGF-A stimulation in endothelial cells in published studies (*Introduction 1.4.3*). NRP1 was localised in filopodia-like projections in the absence or presence of VEGFR2 co-expression. Fantin et al. (2013, 2015) had previously observed that NRP1 was localised in the filopodia of endothelial tip cells. It is unknown whether this links to interactions between NRP1 and components of the extracellular matrix (Vander Kooi et al., 2007; Roth et al., 2008; Nasarre et al., 2010). Although images were obtained from living cells, there is still limited understanding of the dynamics of subcellular localisation of VEGFR2 and NRP1. Alternative real-time imaging techniques could be used in living

cells, such as Lattice Light Sheet microscopy that has enhanced spatial (Z) and temporal resolution compared to confocal microscopy with reduced cellular damage from laser excitation (Power and Huisken, 2017). Akin to the localisation of NRP1 in membrane projections, published work used this technique to quantify the dynamics of membrane ruffling in live cells (Condon et al., 2018). The axial spatial resolution could also monitor the trajectory of receptor-containing endosomes from the plasma membrane in real-time.

These data suggest that VEGFR2 and NRP1 were colocalised in intracellular compartments, as well as at the plasma membrane. This was observed using both live cell imaging and preliminary LV200 imaging studies. Published studies have demonstrated that VEGFR2 is subject to macropinocytosis in the absence or presence of ligand (Basagiannis and Christoforidis, 2016; Basagiannis et al., 2016). This bulk transport mechanism could engulf surrounding NRP1, regardless of the lack of NRP1 endocytosis when expressed alone. Having demonstrated that these receptors were in close proximity (<10 nm), it is feasible that NRP1 could non-selectively internalise alongside VEGFR2 in living cells. Muhl et al. (2016) investigated receptor colocalisation in HUVECs in the presence of VEGF-A stimulation, whereby VEGFR2 and NRP1 were colocalised in intracellular sites following 20 minute stimulation. Lee-Montiel et al. (2015) imaged VEGFR2 and NRP1 colocalisation in un-stimulated HUVECs. These data suggested that NRP1 was primarily colocalised with VEGFR2 at the plasma membrane, as well as VEGFR1 and VEGFR3 (Lee-Montiel et al., 2015). In our studies, receptor localisation was relatively heterogeneous across cells. Having taken a diverse population of cells into consideration, there were interesting distinctions between VEGF-A isoforms in terms of VEGFR2/NRP1 colocalisation. In the presence of $VEGF_{165}$b selective for VEGFR2, there was decreased colocalisation between VEGFR2 and NRP1. Future studies should probe this distinction between VEGF-A isoforms using receptor-receptor BRET in the presence VEGF-A stimulation. In the presence of a ligand that binds both receptors, there was an increased correlation in the amount of VEGFR2 colocalised with NRP1. The resolution limit of basic confocal microscopy does not enable us to delineate receptor colocalisation at a molecular level, therefore observations are limited to whether receptors are localised at the plasma membrane or in subcellular sites. Confocal imaging could be exploited for FRET-based imaging, as this would isolate receptors that were in close proximity (<10 nm). Single-molecule tracking techniques would be invaluable to monitor the localisation and dynamics of VEGFR2 and NRP1. Damioli et al. (2017) used Fluorescence Recovery After Photobleaching on endothelial cells expressing VEGFR2 with the cytoplasmic domain replaced with a C-terminal fluorophore. Here, $VEGF_{165}$a stimulation led to decreased diffusion of VEGFR2 on the plasma membrane. Another published study using Total Internal Reflection Microscopy in endothelial cells demonstrated a higher immobile proportion in the presence of ligand (Rocha-Azevedo et

al., 2019). In both cases, endothelial cells would co-express NRP1 and the contribution of this co-receptor is unknown.

The question remains regarding where the BRET signal is arising from when using the NanoBiT-tagged VEGFR2/NRP1 complex as a donor in living HEK293T cells. Furimazine substrate is membrane-permeable, therefore luminescence could be emitted from complexes anywhere in the cell. We previously demonstrated the importance of the subcellular localisation of receptors on monitoring ligand binding at NanoLuc-tagged receptors using BRET (Chapter 4). This was particularly evident for the kinetics of fluorescent VEGF-A isoforms at NanoLuc-VEGFR2 in isolation, while NanoLuc-NRP1 remained at the plasma membrane. Imaging the site of luminescence emissions from the HiBiT complex suggested that these complexes were localised at both the plasma membrane and at intracellular sites. This was similar to observations from live cell imaging with HaloTag-VEGFR2 and SnapTag-NRP1. The binding profile for VEGFR2-selective $VEGF_{165}$b-TMR remained elevated throughout the 90 minute timecourse. This could suggest that $VEGF_{165}$b-TMR bound the complex in a relatively stable local environment. In contrast, there was a small decline in BRET signal upon stimulation with $VEGF_{165}$a-TMR. Interacting with both receptors led to a change in local environment of VEGF-A/VEGFR2/NRP1 that reduced BRET with the HiBiT complex following 30-60 minutes, although to a lesser extent than in the absence of NRP1. There may also be a population of NRP1 localised in intracellular sites that could complex with constitutively trafficking VEGFR2. This could be further probed using the Bioluminescence Imaging System comparing complexes in the presence of distinct VEGF-A isoforms.

NRP1 is a promising drug target due to its high receptor expression in malignant cancers (Jubb et al., 2012; Goel and Mercurio, 2013; Lee et al., 2014b). Despite its ability to upregulate VEGF-A/VEGFR2 signalling in physiological and patho-physiology, the mechanism by which NRP1 upregulates VEGFR2 signalling is unknown. Koch et al. (2014) demonstrated that VEGFR2 can be differentially modulated when NRP1 was expressed on neighbouring cells as opposed to the same cell. This has important implications for VEGFR2 expressed in blood vessels adjacent to neighbouring tumour cells that overexpress NRP1. While Ballmer-Hofer et al. (2011) demonstrated that NRP1 influenced the subcellular localisation of VEGFR2, there is limited understanding of how NRP1 directly affects the ligand binding dynamics of VEGFR2. Our novel approach isolated ligand binding at a defined complex of VEGFR2 and NRP1 for the first time, suggesting that NRP1 did not increase the affinity or association binding kinetics of $VEGF_{165}$a at VEGFR2. This study did, however, highlight distinctions between VEGF-A isoforms in terms of their long-term binding profiles at a defined heteromeric complex. These differences between VEGF-A isoforms may link to their distinct abilities to engage both receptors within the constitutive VEGFR2/NRP1 heteromer and influence subcellular localisation.

5.5 CHAPTER 5 CONCLUSIONS

Considering distinctions between the pharmacology of VEGFR2 and NRP1, we explored differences between VEGF-A isoforms in living cells that co-expressed both receptors. Techniques were used to gain specific insight into the spatial resolution of receptor localisation and temporal resolution of ligand binding. Imaging studies suggested that receptors were colocalised at both the plasma membrane and intracellular sites. VEGFR2 is subject to constitutive trafficking and bulk transport, therefore NRP1 could be transported to intracellular sites alongside VEGFR2 in a non-selective manner. Receptor-receptor BRET suggested that NanoLuc-VEGFR2 and fluorescently tagged NRP1 formed of a heteromeric complex in close proximity (<10 nm). To isolate ligand binding pharmacology at a defined receptor/co-receptor complex, we developed an approach exploiting NanoBiT complementation technology such that BRET only occurred from a heteromeric VEGFR2/NRP1 complex. We confirmed that these tagged receptors led to NanoBiT complementation with an optimal configuration of LgBiT-VEGFR2 and HiBiT-NRP1. These tags had minimal luminescence in isolation and receptors were successfully exported to the plasma membrane. Furthermore, luminescence from the NanoBiT complex was reduced by increasing amounts of competing receptor.

At a defined complex, the pharmacology of distinct VEGF-A isoforms were quantified to investigate how complex formation influenced ligand binding. These studies focussed on $VEGF_{165}b$, a selective isoform that could not interact with NRP1. This was compared to $VEGF_{165}a$, the 'prototypical' VEGF-A isoform containing residues that bind with both receptors in the heteromeric complex. The NanoBiT complex had a similar nanomolar affinity as NanoLuc-VEGFR2 or NanoLuc-NRP1 expressed alone in prior studies. In contrast, there were distinctions in the dynamics of how the NanoBiT complex interacted with these fluorescent VEGF-A isoforms. Unlike $VEGF_{165}a$-TMR, the BRET profile of $VEGF_{165}b$-TMR remained elevated at the NanoBiT complex for the 90 minute timecourse. Interestingly, the association binding kinetics were more similar to VEGFR2 than the faster kinetics observed at NRP1. NRP1 can interact with a number of growth factors (West et al., 2005; Banerjee et al., 2006; Rizzolio et al., 2012; Muhl et al., 2017), therefore understanding how NRP1 co-expression influences RTK function has implications for other receptors contributing to drug resistance. In drug discovery, NRP1 could be a feasible target in oncology with fewer side effects than non-selective RTKIs due to its high expression localised to tumours.

Chapter 6.
General Discussion & Conclusions

6.1 GENERAL DISCUSSION

VEGF-A is a key mediator of angiogenesis in both health and disease (*Introduction 1.1)*. While VEGF-A primarily signals via the RTK VEGFR2, signalling is potentiated by co-receptor NRP1 (*Introduction 1.2-1.5*). Considering the relevance of VEGF-A/VEGFR2/NRP1 in drug development (*Introduction 1.6*), this project quantified the pharmacology of distinct VEGF-A isoforms at VEGFR2 and NRP1. Despite the large size of the dimeric peptide, VEGF-A was modified with TMR at a single amino acid residue per monomer. Proximity-based BRET was used to monitor the real-time ligand binding of fluorescent VEGF-A to NanoLuc- or NanoBiT-tagged receptors. This applied technologies originally developed for GPCRs to different classes of receptors, including an RTK and a type I transmembrane co-receptor protein, for the first time. As a result, we gained novel understanding into the spatial and temporal dynamics of receptor/ligand interactions at specific receptors expressed alone or in a defined heteromeric complex.

Chapter 3 characterised novel fluorescent VEGF-A isoforms to quantify their ligand binding pharmacology at full-length VEGFR2 or NRP1 (Peach et al., 2018a). This characterised $VEGF_{165}$b-TMR and $VEGF_{121}$a-TMR, alongside previously published $VEGF_{165}$a-TMR (Kilpatrick et al., 2017). BRET was used to monitor their real-time ligand binding at 37°C in living HEK293T cells. This highlighted distinctions between the kinetics of ligand binding and subcellular localisation of VEGFR2 and NRP1.

Chapter 4 investigated the influence of VEGFR2 endocytosis and phosphorylation on ligand binding (Peach et al., 2019). $VEGF_{xxx}$x-TMR/VEGFR2 endocytosis was quantified in terms of ligand potency and colocalisation with Rab5. We prevented VEGFR2 phosphorylation and signalling using pharmaceutical and genetic interventions. This did not inhibit endocytosis, therefore membrane preparations were used to monitor ligand binding in the absence of the internalisation component. These data showed an interplay between VEGFR2 endocytosis and ligand binding dynamics.

Chapter 5 then probed receptor localisation and ligand binding dynamics in cells co-expressing both VEGFR2 and NRP1. This compared $VEGF_{165}$b (selective for VEGFR2) and $VEGF_{165}$a (binds VEGFR2 and NRP1), exploiting fluorescent VEGF-A isoforms from Chapter 3. Having shown VEGFR2 and NRP1 form receptor/co-receptor complexes, we applied NanoBiT complementation technologies to monitor real-time ligand binding at the defined heteromeric complex. This highlighted distinctions between the binding dynamics of VEGF-A isoforms in the presence of NRP1.

Data were discussed in depth at the end of each Chapter. Here, this insight will be discussed in the context of key biological questions regarding the molecular pharmacology of VEGF-A ligand binding at VEGFR2 and NRP1.

What are the differences between the pharmacology of VEGF-A isoforms?

Numerous groups have observed distinctions between VEGF-A isoforms in endothelial cells that often express both VEGFR2 and NRP1 (*Introduction Table 1.1*). Studies described in Chapters 3-4 investigated receptors expressed on their own in HEK293T cells lacking NRP1 expression. Here, there were minimal distinctions between VEGF-A isoforms at VEGFR2 alone in terms of their binding affinities (Chapter 3), stimulation of NFAT reporter gene signalling (Chapter 3) and ability to drive ligand/receptor endocytosis (Chapter 4). When we consider the structural distinctions between VEGF-A isoforms (*Introduction Figure 1.4*), alternative splicing affects the residues responsible for interactions with macromolecules besides VEGFR2. Not all VEGF-A isoforms were able to interact with NRP1 (Chapter 3). As such, expression of other components may be required to reveal distinctions between VEGF-A isoforms, as suggested by differences between $VEGF_{165}$a and $VEGF_{165}$b/$VEGF_{121}$a in stimulating HUVEC proliferation (Chapter 3). Investigating the VEGFR2/NRP1 complex revealed distinctions in the spatiotemporal dynamics of $VEGF_{165}$b (selective for VEGFR2) compared to $VEGF_{165}$a (binds VEGFR2 and NRP1). There were differences observed in ligand binding kinetics at the VEGFR2/NRP1 complex and their effect on colocalisation between VEGFR2 and NRP1.

The physiological expression of $VEGF_{165}$b itself has been questioned (Bridgett et al., 2017; Dardente et al., 2020). Previous studies detected $VEGF_{165}$b by PCR and antibodies, therefore this could detect the residues present in VEGF-Ax resulting from programmed translational readthrough. Published studies have shown functional similarities between $VEGF_{165}$b and VEGF-Ax (*Introduction 1.3.2*), therefore both endogenous partial agonists should be investigated in further studies. It is also important to consider the physiological concentrations of VEGF-A isoforms in the body. These were estimated in the pM range (Clegg and Mac Gabhann, 2017), therefore lower than the potency (pEC_{50}) values derived to stimulate signalling and internalisation (nM range). This could suggest that large local VEGF-A secretions are required to interact with receptors and initiate signalling. Then again, the distribution of VEGF-A ligands is unlikely to be uniform due to direct interactions between specific VEGF-A isoforms and the ECM (*Introduction 1.3*). This could create ‘sinks’ of specific isoforms with high concentrations nearby an endothelial cell surrounded by a dense ECM network. These differences in local concentrations may explain differences between signalling outcomes in response to VEGF-A isoforms.

What is the pharmacology of VEGFR2, NRP1 and the VEGFR2/NRP1 complex?

Unlike the signalling cascades downstream of VEGFR2, NRP1 cannot signal independently (*Introduction 1.5*). Prior studies investigating the binding affinities for VEGF-A alone led the field to believe VEGFR2 and NRP1 had a similar pharmacology in terms of ligand binding (*Table 3.1*). We observed differences in the spatial and temporal aspects of VEGFR2 and NRP1, both in the absence and presence of ligand, using techniques that isolated the pharmacology of tagged receptors. Despite similar affinities for the same ligand, $VEGF_{165}$a-TMR had faster ligand binding kinetics at NanoLuc-NRP1 than NanoLuc-VEGFR2 when expressed on their own (Chapter 3). There were also distinctions in receptor localisation. NRP1 receptors labelled with membrane impermeant dyes were expressed at the plasma membrane and did not internalise upon VEGF-A stimulation in living cells (Chapter 3). In contrast, VEGFR2 was subject to complex constitutive trafficking and enabled $VEGF_{xxx}$x-TMR internalisation into intracellular endosomes (Chapters 3-4). In membrane preparations that lacked this endocytic component, we observed a large difference in ligand binding dynamics between membranes and intact cells at VEGFR2; there was no difference for NRP1 (Chapter 4). Due to these distinctions between VEGFR2 and NRP1, we investigated the pharmacology of receptors co-expressed in the same cell. VEGFR2 and NRP1 formed a heteromeric receptor/co-receptor complex in the absence of ligand stimulation (Chapter 5). Monitoring ligand binding dynamics at a defined VEGFR2/NRP1 heteromer, ligand association to the complex reflected the kinetics observed at NanoLuc-VEGFR2 alone.

Throughout our studies, NRP1 was expressed more highly than VEGFR2 (Chapters 3-5). This reflected the relative proportion of receptors endogenously expressed in endothelial cells (Imoukhuede and Popel, 2011; Lee-Montiel et al., 2015). The stoichiometry of the ligand/receptor/co-receptor complex remains unknown. Within the VEGFR2/NRP1 heteromer, $VEGF_{165}$a could theoretically interact with VEGFR2 and NRP1 simultaneously. A basic macromolecular complex could form between a VEGFR2 dimer, NRP1 oligomer and a bridging VEGF-A dimer (2:2:2 ratio). This could also form larger receptor clusters, as demonstrated for EGFRs (Clayton et al., 2005; Saffarian et al., 2007; Wang et al., 2014; Needham et al., 2016). While this thesis focussed on VEGFR2 and NRP1, receptor complexes could include other macromolecules. For example, αVβ3 integrin can interact with both VEGFR2 (Soldi et al., 1999; Borges et al., 2000) and NRP1 (Robinson et al., 2009). More recently, VEGFR2 was also shown to be in close proximity to GPCRs also expressed by endothelial cells (Kilpatrick et al., 2019). These higher order complexes could modulate the pharmacology of VEGFR2 and/or NRP1.

How does local cellular context modulate ligand/receptor pharmacology?

Numerous factors in living cells can influence receptor pharmacology, thus counteracting some assumptions made to simplify quantitative pharmacological models (*Introduction 1.6.2*). This project considered the dynamics of ligand and receptor interactions in terms of VEGF-A pharmacology at VEGFR2/NRP1. In HEK293T cells, VEGFR2 was internalised within 30 minutes of fluorescent VEGF-A stimulation to subcellular regions (Chapter 3). VEGFR2 endocytosis influenced the dynamics of VEGF-A/VEGFR2 binding, whereby a component of binding kinetics could be attributed to the local acidic pH in early endosomes (Chapter 4). Subcellular localisation also influences receptor signalling with evidence for endosomal VEGFR2 responsible for ERK signalling and endothelial cell proliferation (Gourlaouen et al., 2013; Fearnley et al., 2016). We demonstrated throughout this thesis that VEGFR2 was primarily localised in endosomes, regardless of inhibiting phosphorylation (Chapter 4) or NRP1 co-expression (Chapter 5). Endosomes have a unique microenvironment compared to the plasma membrane with high receptor concentrations, distinct membrane lipids, local proteolytic enzymes and mobility for trafficking to distinct subcellular compartments. These subcellular receptors are also inaccessible to extracellular membrane-impermeable drugs. Ballmer-Hofer et al. (2011) suggested that NRP1 modulates the route of VEGFR2 trafficking. It is therefore important to investigate the mechanism underlying NRP1-mediated VEGFR2 upregulation in living cells where the dynamics of biological processes occur at 37°C.

Other extracellular and intracellular aspects of cell biology could influence VEGF-A pharmacology at VEGFR2/NRP1. The ECM network surrounding cells can modulate local VEGF-A ligand bioavailability (*Introduction 1.3.3)*. The ECM can also directly interact with NRP1 through the glycosylation of specific residues as a proteoglycan-like structure (Shintani et al., 2006; Windwarder et al., 2016). Components of the ECM were shown to enhance VEGF-A binding at VEGFR2 and NRP1 (Teran and Nugent, 2015). This could alter their pharmacology in disease states, such as the stiff ECM of the tumour microenvironment that encourages tumour invasion and metastasis (Gkretsi and Stylianopoulos, 2018). Components integral to the cell can also influence receptor dynamics. The cytoskeleton was shown to modulate the diffusion of other receptor classes within the plasma membrane (Kusumi and Sako, 1996; Fujiwara et al., 2016; Sungkaworn et al., 2017). Here, the picket and fence model proposes that receptor diffusion is restricted in membrane microdomains divided by protein ‘pickets’ and an actin cytoskeleton ‘fence’. NRP1 can indirectly interact with the cytoskeleton via synectin and myosin VI (*Introduction 1.5.2*). Another membrane protein that interacts with both the ECM and cytoskeleton, CD44, was recently characterised as a ‘picket’ that directly modified receptor clustering (Freeman et al., 2018). As it is unknown how transient interactions between NRP1 and synectin are, questions remain over whether NRP1

would constrain, enhance or direct the diffusion of VEGFR2. The diffusion of VEGFR2 alone has been monitored in endothelial cells (Damioli et al., 2017; Rocha-Azevedo et al., 2019), both of which showing that ligand stimulation reduced receptor diffusion rates. GPCRs also had a slower receptor diffusion rate in the presence of agonists (Yanagawa et al., 2018). While confocal imaging has revealed novel distinctions between VEGFR2 and NRP1 localisation at the subcellular level (Chapter 3), there is no understanding of NRP1 receptor diffusion within the plasma membrane or the influence of intracellular (cytoskeleton) or extracellular (ECM) factors.

6.2 FUTURE DIRECTIONS

Knockout of VEGF-A, VEGFR2 and NRP1 led to embryonic lethality (*Introduction 1.4.3, Introduction 1.5.3*), demonstrating the physiological importance of this signalling system in development. Blood vessels, however, express other ligand and receptor subtypes that contribute to angiogenesis and vascular permeability. First, studies could probe the pharmacology of other interacting membrane proteins co-expressed by endothelial cells (*Figure 6.1a*). VEGFR1, VE-cadherin and αVβ3 integrin could be investigated in terms of their signalling, localisation, ligand binding and ability to form complexes with VEGFR2 or NRP1. For example, VEGFR1 is often 'disregarded' as a decoy receptor. However, VEGFR1 forms heterodimers with VEGFR2 and has a higher binding affinity for $VEGF_{165}$a (*Introduction 1.4*). Recent studies also demonstrated that the VEGFR1 extracellular domain had slower ligand dissociation rates than VEGFR2 (Teran and Nugent, 2018). To investigate full-length receptors, BRET could first monitor real-time ligand binding dynamics at NanoLuc-VEGFR1 in living cells using the fluorescent VEGF-A variants characterised in this thesis. The effect of VEGFR1/VEGFR2 heterodimer formation on ligand binding could then be monitored with NanoBiT complementation technology (e.g. LgBiT-VEGFR2 and HiBiT-tagged VEGFR1). Early work also demonstrated that VEGFR1 could form a complex with NRP1 (Fuh et al., 2000), although the functional relevance of this was not investigated further. These studies would investigate higher order macromolecular complexes, investigating how receptors co-expressed by endothelial cells contribute to VEGF-A pharmacology.

Second, studies should explore VEGFR2/NRP1 in increasingly translational systems that represent the appropriate cellular and tissue-specific context (*Figure 6.1b*). This project exploited techniques that isolated the pharmacology of defined receptors using tagged proteins. To reflect the context of an endothelial cell, endogenous receptors could be tagged with CRISPR/Cas9 technologies (White et al., 2017, 2020). For example, the spatial dynamics of tagged receptors in living endothelial cells could be monitored using membrane-impermeant fluorescent tags (e.g. HaloTag, or HiBiT complemented with HaloTag-LgBiT). Progressing this further, 3D human cell co-culture systems could model the blood vessel endothelium (Schöneberg et al., 2018) or interactions between tumour cells and the endothelium (Amann et al., 2017). Here, real-time VEGFR2/NRP1 pharmacology could be isolated in endothelial cells in the presence of other cell types. This could test the hypothesis that NRP1 has distinct effects on VEGFR2 pharmacology when expressed by the same cell or neighbouring cell (Koch et al., 2014). Initial studies highlighted the potential to use fluorescence and luminescence-based techniques *in vivo* (Bhaumik and Gambhir, 2002; Alcobia et al., 2018). For example, vessels from rats expressing tagged receptors in their endothelial cells could be isolated for pressure myography (Halpern et al., 1984; Lawton et al., 2019). This would ultimately aim to probe the specific, real-time pharmacology of VEGFR2 and NRP1 in a living organism,

comparing healthy (e.g. quiescent vasculature) and disease states (e.g. tumour angiogenesis).

There are also key mechanistic questions remaining regarding how NRP1 modulates VEGFR2 at a molecular level. Third, further experiments should probe the dynamics of VEGFR2 and NRP1 receptor diffusion (*Figure 6.1c*). Studies should compare receptors expressed alone with those co-expressed as a complex, as well as in the absence or presence of VEGF-A stimulation. Sophisticated single-molecule imaging techniques could quantify the diffusion rates of HaloTag-VEGFR2 and SnapTag-NRP1 in living cells, such as using Fluorescence Correlation Spectroscopy (Briddon et al., 2018). The localisation of NRP1 in filopodia-like projections in HEK293T cells (Chapters 3,5), as well as in tip cells (Fantin et al., 2013, 2015), could prompt studies to compare receptor diffusion in distinct subcellular regions. For example, there may be distinct diffusion between receptors in filopodia at the basolateral region of the cell with receptors at the apical region away from the glass surface. Understanding the dynamics of intracellular receptors trafficking away from the plasma membrane would be valuable. Lattice Light Sheet microscopy could be used for real-time imaging of 3D samples to probe the effect of NRP1 co-expression and ligand stimulation. Understanding how receptors move in a living cell at 37°C would provide novel insight compared to antibody labelling in fixed cells. These experiments could address the hypothesis that NRP1 acts as an immobile 'picket' - via interactions with the cytoskeleton and ECM - that modulates VEGFR2 diffusion.

Finally, mechanistic studies should interrogate how NRP1 upregulates VEGFR2 signalling from a functional perspective. NRP1 interacts with synectin via the SEA motif, thus indirectly with myosin VI (*Figure 6.1d*). Despite this basic understanding, very few studies have directly investigated the purpose of these interactions. Furthermore, there is no understanding of the temporal or spatial profile of the synectin adaptor protein. Preliminary experiments could probe the dynamics of a fluorescent variant of synectin (e.g. synectin-mCherry). BRET could be used to monitor the real-time recruitment of synectin to NRP1 upon $VEGF_{165}$a or $VEGF_{165}$b/VEGF-Ax stimulation (e.g. NRP1 tagged at the C-terminus with NanoLuc). Confocal microscopy could then monitor the spatial aspects of synectin localisation, as well as HaloTag-VEGFR2/SnapTag-NRP1 localisation, with respect to the cytoskeleton (e.g. localising actin with LifeAct-GFP). These studies could address the hypothesis that NRP1 encourages VEGFR2 to follow trafficking conduits through indirect interactions with the cytoskeleton.

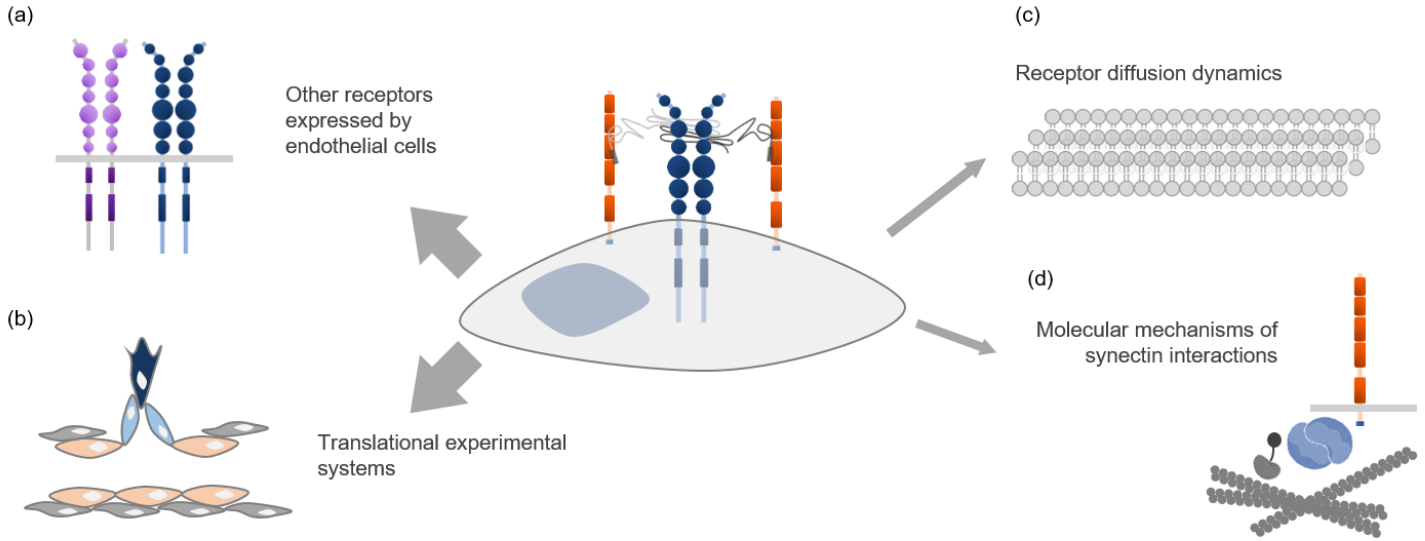


Figure 6.1 ***Future directions to investigate the real-time pharmacology of VEGFR2 and NRP1****. We investigated full-length VEGFR2 and NRP1 in living cells (middle panel). Further approaches are divided into those that broaden perspectives (thick arrows, left panel) or molecular mechanisms that narrow the focus (thin arrows, right panel). (a) Endothelial cells express other receptors that modulate VEGF-A-induced signalling. The formation of higher order complexes between other receptors and VEGFR2/NRP1 could be investigated in terms of their localisation and functional consequences. (b) Receptor pharmacology should be investigated in increasingly translational systems, such as using endothelial cells in quiescent vasculature or models of the tumour microenvironment. (c) Real-time imaging techniques could be used to monitor the dynamics of VEGFR2 and NRP1 diffusion rates, in the absence or presence of VEGF-A stimulation. (d) Mechanistic studies of how NRP1 modulates VEGFR2 should probe synectin (blue), particularly interactions with NRP1 and myosin VI with the cytoskeleton.*

6.3 KEY CONCLUSIONS

The data presented in this thesis identified novel distinctions in how VEGF-A interacts with key receptors involved in tumour angiogenesis. Despite numerous approved anti-cancer therapeutics targeting VEGF-A/VEGFR2 signalling, there was limited quantitative pharmacological understanding of VEGF-A isoforms at full-length VEGFR2 or NRP1 in living cells (reviewed in Peach et al., 2018b). In collaboration with Promega Corporation, $VEGF_{165}$a, $VEGF_{165}$b and $VEGF_{121}$a were labelled at a single site with TMR. BRET was used to quantify the real-time ligand binding dynamics of fluorescent VEGF-A isoforms at full-length VEGFR2 or NRP1 in living cells at 37°C. **First**, this technique was able to discriminate between VEGF-A isoforms at two distinct classes of membrane protein expressed in isolation in HEK293T cells. While all VEGF-A isoforms had similar nanomolar affinities at VEGFR2, not all isoforms were able to interact with NRP1. We also revealed marked differences in the dynamics of $VEGF_{165}$a-TMR ligand binding at VEGFR2 and NRP1 for the first time, despite similar binding affinities. NRP1 remained at the plasma membrane upon ligand stimulation, whereas VEGF-A internalised with VEGFR2 into endosomes (published in Peach et al., 2018a). **Second**, we gained insight into the role of VEGFR2 endocytosis on ligand binding dynamics. VEGF-A/VEGFR2 endocytosis was not dependent of RTK signalling, however inhibiting VEGFR2 phosphorylation led to an elevated BRET ratio. Using an assay setup that isolated ligand/receptor interactions in homogenised membrane preparations allowed us to demonstrate than an acidic pH reflecting endosomes reduced the residence time of VEGF-A at VEGFR2 (published in Peach et al., 2019). **Third**, we demonstrated that VEGFR2 and NRP1 formed a heteromeric complex when co-expressed in living cells. We developed techniques to isolate the ligand binding dynamics at a defined VEGFR2/NRP1 complex. $VEGF_{165}$a-TMR had association binding kinetics that reflected binding at VEGFR2. Despite only interacting with VEGFR2, $VEGF_{165}$b-TMR had a unique ligand binding profile at the complex that remained elevated in living cells. Sponsored by the AJ Clark Scholarship (British Pharmacological Society), this thesis project quantified the pharmacology of receptors contributing to important physiological processes such as angiogenesis in health and disease.

Chapter 7.
Appendix

7.1 Biochemical Characterisation of $VEGF_{xxx}$x-TMR

To determine the labelling specificity of TMR on $VEGF_{165}$b and $VEGF_{121}$a, colleagues at Promega performed liquid chromatography-tandem mass spectrometry (LC-MS/MS) on protein fragments of labelled and unlabelled VEGF-A isoforms. Protein fragments were obtained following digestion with trypsin and GluC /LysC proteases. These fragments covered the entire peptide sequence for $VEGF_{165}$b (*Figure 7.1*) and $VEGF_{121}$a (*Figure 7.2*). LC-MS/MS chromatograms obtained for the N-terminal fragments demonstrate distinct peaks for unlabelled and labelled compounds. Upon addition of the TMR fluorophore for the labelled analogue, there was a longer retention time due to its higher mass compared to the unlabelled analogue. We did not observe any non-specific labelling of the other 14 Cys residues in $VEGF_{165}$b or 8 Cys residues in $VEGF_{121}$a. This confirmed selective labelling of a single Cys residue. The ion count was used to determine the percentage of the sample successfully labelled, showing a large proportion of labelling with 97% for $VEGF_{165}$b-TMR and 94-99% for $VEGF_{121}$a-TMR (*Table 7.1*). LC-MS/MS data was also used to calculate the mass of the chemical modification compared to unlabelled compound. This showed a mass increase of 817 Da (*Table 7.2*), consistent with the moiety in *Figure 3.1.*

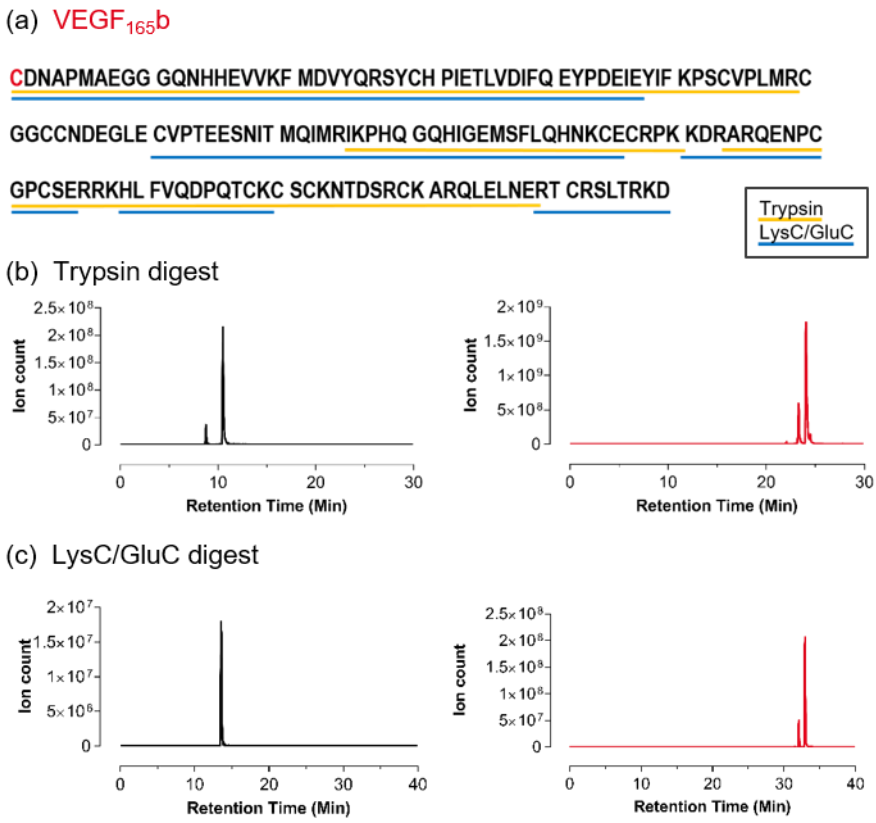


Figure 7.1 ***LC-MS/MS analysis of VEGF$_{165}$b-TMR.*** *(a) Endoproteinases were used to obtain protein fragments across the VEGF$_{165}$b amino acid sequence (refer to key). The modified N-terminal Cys residue is highlighted (red). Protein identity was confirmed by searching the MS/MS spectra using the Mascot search engine (Matrix Science Inc, Boston, USA) against a human database (SwissProt). The highest scoring hit was the VEGF sequence. (b) LC-MS/MS analysis of the N-terminal fragment digested with trypsin protease (CDNAPMAEGGGQNHHEVVK). This compares chromatograms for unlabelled (left) or TMR-labelled (right). (c) LC-MS/MS analysis of the N-terminal fragment digested by LysC and GluC (CDNAPMAE). Retention times and mono-isotopic masses are given in* Table 7.1*. Differences in mass are calculated in* Table 7.2*.*

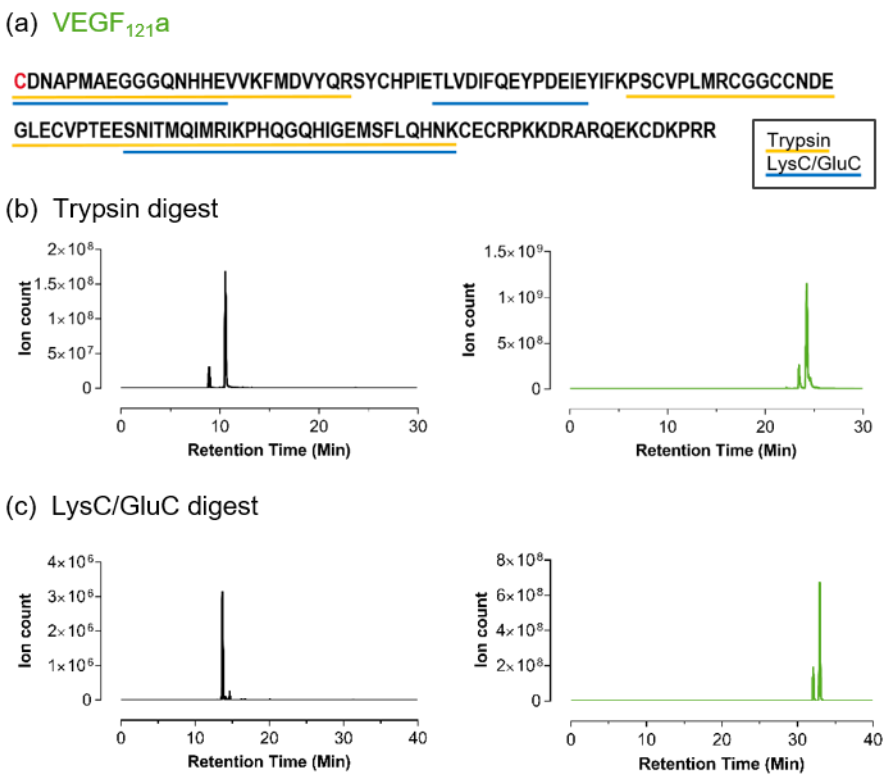


Figure 7.2 ***LC-MS/MS analysis of VEGF$_{121}$a-TMR.*** *(a) Endoproteinases were used to obtain protein fragments across the amino acid sequence of VEGF$_{121}$a. The modified N-terminal Cys residue is highlighted (red). Protein identity was confirmed by searching the MS/MS spectra using the Mascot search engine (Matrix Science Inc, Boston, USA) against a human database (SwissProt). The highest scoring hit was the VEGF sequence. (b) LC-MS/MS analysis of the N-terminal fragment digested with trypsin protease (CDNAPMAEGGGQNHHEVVK). This compares chromatograms for unlabelled (left) or TMR-labelled (right). (c) LC-MS/MS analysis of the N-terminal fragment digested by LysC and GluC (CDNAPMAE). Retention times and mono-isotopic masses are given in* Table 7.1*. Differences in mass are calculated in* Table 7.2*.*

Table 7.1 ***Labelling efficiency quantified from LC-MS/MS profiles following protease digestion of VEGF or VEGF$_{xxx}$x-TMR****.*

Peptide sequence	Digest	Isoform	Mass/charge (m/z)	Charge (z)	Mass [M+H]*	Retention Time (Min)	Peak Area	Sample	%	% Labelled
CDNAPMAEGGGQNHHEVVK	Trypsin	VEGF$_{165}$b	498.97	4	1992.89	10.5	1.36E+08	Labelled	2.9	97.1
		VEGF$_{165}$b	498.97	4	1992.89	10.5	4.66E+09	Unlabelled	100	
		VEGF$_{121}$a	498.97	4	1992.89	10.5	6.20E+08	Labelled	6.1	93.9
		VEGF$_{121}$a	498.97	4	1992.89	10.3	1.01E+10	Unlabelled	100	
CDNAPMAE	LysC/GluC	VEGF$_{165}$b	425.66	2	850.31	13.7	5.26E+06	Labelled	3.5	96.5
		VEGF$_{165}$b	425.66	2	850.31	13.6	1.52E+08	Unlabelled	100	
		VEGF$_{121}$a	425.66	2	850.31	13.5	1.14E+07	Labelled	1.2	98.8
		VEGF$_{121}$a	425.66	2	850.31	13.6	9.23E+08	Unlabelled	100	

Labeling efficiencies (%) were determined by comparing the integrated peak areas of the unmodified proteolytic peptides in the labelled and unlabelled samples that were digested with trypsin or LysC/GluC. *Mono-isotopic mass at a single charge assumed that the peptide takes up a single proton. Mono-isotopic mass [M+H] was calculated as (m/z)*z – (z-1).

Table 7.2 ***Addition of an 817 Da moiety from LC-MS/MS profiles for labelled peptide fragments****.*

Peptide sequence	Digest	Isoform	Mass/charge (m/z)	Charge (z)	Mass of labelled peptide [M+H]*	Mass of unlabelled peptide [M+H]*	Mass Difference (Da)
CDNAPMAEGGGQNHHEVVK	Trypsin	VEGF$_{165}$b	937.39	3	2810.16	1992.89	817.27
	Trypsin	VEGF$_{121}$a	937.39	3	2810.16	1992.80	817.27
CDNAPMAE	LysC/GluC	VEGF$_{165}$b	834.30	2	1667.59	850.31	817.28
	LysC/GluC	VEGF$_{121}$a	834.30	2	1667.59	850.31	817.28

*Mono-isotopic mass at a single charge assumed that the peptide takes up a single proton. Mono-isotopic mass [M+H] was calculated as (m/z)*z – (z-1).

To investigate whether ligands were appropriately glycosylated and dimerised, $VEGF_{xxx}$x-TMR ligands were subjected to fluorescence SDS-PAGE analysis to indicate protein mass. The expected mass of $VEGF_{165}$b-TMR and $VEGF_{121}$a-TMR dimers were 40.5 kDa and 30.5 kDa respectively, including the 817 Da addition of the 6-CBT-PEG-TMR moiety. As shown in amino acid sequences (*Figure 7.1a* and *Figure 7.2a)*, the endogenous 26 amino acid signal peptide was removed and replaced by an additional Cys. Concentrations of fluorescent VEGF-A isoforms were determined at Promega Corporation using quantification of TMR fluorescence on a gel. This was then confirmed by Dr Kilpatrick with solution-based Fluorescence Correlation Spectroscopy (Kilpatrick et al., 2017; Peach et al., 2018).

The addition of 100 mM dithiothreitol (DTT) confirmed that, in non-reducing conditions, both $VEGF_{165}$b-TMR and $VEGF_{121}$a-TMR isoforms were largely present as homodimers (*Figure 7.3a*). There were, however, numerous bands present in the DTT+ gels for $VEGF_{121}$a-TMR. This could represent the lower percentage of labelled sample. Deglycosylation by PNGase then confirmed that purified $VEGF_{165}$b-TMR was glycosylated (*Figure 7.3b*). $VEGF_{121}$a-TMR treated with PNGase suggested ligand was present in both glycosylated and non-glycosylated forms under normal conditions.

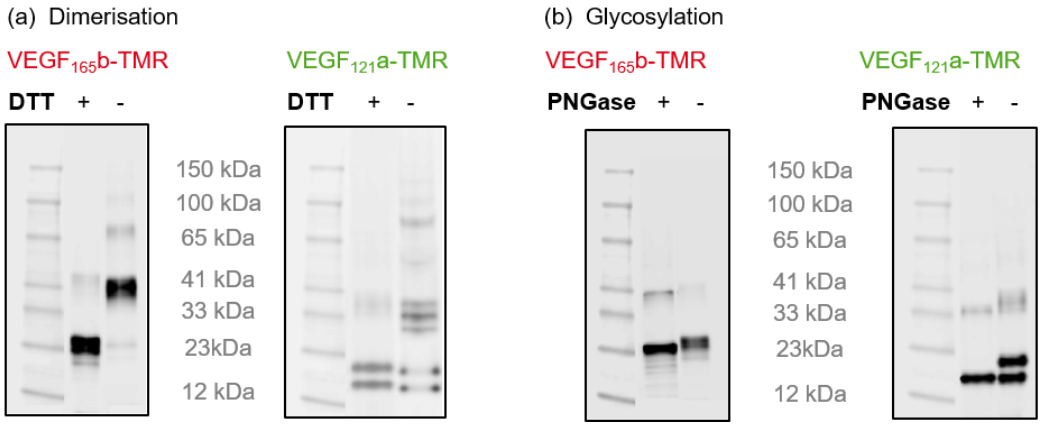


Figure 7.3 ***Fluorescence SDS-PAGE confirmed $VEGF_{xxx}$x-TMR dimerisation and glycosylation.*** *(a) Fluorescence SDS-PAGE was used to determine protein mass in the presence and absence of 100 mM DTT. As this reduces disulphide bonds, this indicated $VEGF_{165}$b-TMR or $VEGF_{121}$a-TMR were dimeric. Protein mass corresponding to the ladder is central to each panel. (b) Fluorescent VEGF-A variants were analysed in the presence and absence of PNGase to cleave N-linked oligosaccharides. SDS-PAGE gels were excited at 532 nm and emissions were measured at 580 nm, exploiting the added red-shifted TMR fluorophore.*

7.2 DNA and Amino Acid Sequences

(a) **IL-6/NanoLuc Sequence**

MNSFSTSAFGPVAFSLGLLLVLPAAFPAPVFTLEDFVGDWRQTAGYNLDQVLE QGGVSSLFQNLGVSVTPIQRIVLSGENGLKIDIHVIIPYEGLSGDQMGQIEKIFKVVYPVDD HHFKVILHYGTLVIDGVTPNMIDYFGRPYEGIAVFDGKKITVTGTLWNGNKIIDERLINPDG SLLFRVTINGVTGWRLCERILA

(b)

Nanoluc IL6 (secNluc) reporter [Nanoluc luciferase reporter vector pNL1.3[secNluc]]

Sequence ID:	AFI79293.1	Length: 199	
Score	Identities	Positives	Gaps
403 bits(1036)	199/199(100%)	199/199(100%)	0/199(0%)

(c)

Nanoluc luciferase reporter vector pNL1.3[secNluc], complete sequence

Sequence ID:	JQ437372.1	Length: 3194	
Score	Identities	Gaps	Strand
1103 bits(597)	597/597(100%)	0/597(0%)	Plus/Plus

Figure 7.4 ***NanoLuciferase (NanoLuc) sequence***. *(a) Peptide sequence of the tag in* Figure 2.1b-c*, highlighting the IL-6 signal sequence in grey. (b) BLAST against the protein sequence. (b) BLAST against the DNA sequence.*

(a) **IL-6/HaloTag Sequence**

MNSFSTSAFGPVAFSLGLLLVLPAAFPAPRAEIGTGFPFDPHYVEVLGERMHYV
DVGPRDGTPVLFLHGNPTSSYVWRNIIPHVAPTHRCIAPDLIGMGKSDKPDLGYFFDDH
VRFMDAFIEALGLEEVVLVIHDWGSALGFHWAKRNPERVKGIAFMEFIRPIPTWDEWPEF
ARETFQAFRTTDVGRKLIIDQNVFIEGTLPMGVVRPLTEVEMDHYREPFLNPVDREPLW
RFPNELPIAGEPANIVALVEEYMDWLHQSPVPKLLFWGTPGVLIPPAEAARLAKSLPNCK
AVDIGPGLNLLQEDNPDLIGSEIARWLSTLEISG

(b)

interleukin 6 (interferon, beta 2), isoform CRA_b [Homo sapiens]

Sequence ID:	EAW93757.1	Length: 98	
Score	Identities	Positives	Gaps
91.8 bits(209)	29/29(100%)	29/29(100%)	0/29(0%)

HaloTag protein [HaloTag control vector]

Sequence ID:	ADN27525.1	Length: 297	
Score	Identities	Positives	Gaps
603 bits(1556)	296/296(100%)	296/296(100%)	0/296(0%)

(c)

Homo sapiens interleukin 6 (IL6), transcript variant 1, mRNA

Sequence ID: NM_000600.5		Length: 1127	
Score	Identities	Gaps	Strand
148 bits(80)	3e-31 82/83(99%)	0/83(0%)	Plus/Plus

Flexi vector pFN28K HaloTag(R) CMV-neo, complete sequence

Sequence ID: JN129498.1		Length: 5535	
Score	Identities	Gaps	Strand
1642 bits(889)	889/889(100%)	0/889(0%)	Plus/Plus

Figure 7.5 ***HaloTag sequence****. (a) Peptide sequence from the tag shown in* Figure 2.2b,c,*, highlighting the IL-6 signal sequence in grey. (b) BLAST against the protein sequence, including separate entries for the signal sequence and tag peptide for full coverage. (b) BLAST against the DNA sequences.*

(a) **5HT3A/SnapTag Sequence**

MRLCIPQVLLALFLSMLTGPGEGSRKLTLDKDCEMKRTTLDSPLGKLELSGCEQ
GLHEIKLLGKGTSAADAVEVPAPAAVLGGPEPLMQATAWLNAYFHQPEAIEEFPVPALH
HPVFQQESFTRQVLWKLLKVVKFGEVISYQQLAALAGNPAATAAVKTALSGNPVPILIPC
HRVVSSSGAVGGYEGGLAVKEWLLAHEGHRLGKPGLG

(b)

serotonin-gated ion channel subunit A short splice variant [Mus musculus]

Sequence ID:	AAT37716.1	Length: 483	
Score	Identities	Positives	Gaps
83.3 bits(189)	25/25(100%)	25/25(100%)	0/25(0%)

Snap ICAM-1 fusion protein [synthetic construct]

Sequence ID:	AIZ77117.1	Length: 716	
Score	Identities	Positives	Gaps
70 bits(951)	181/181(100%)	181/181(100%)	0/181(0%)

(c)

Mus musculus serotonin-gated ion channel subunit A short splice variant (Htr3a) mRNA, complete cds, alternatively spliced

Sequence ID: AY605711.1		Length: 1452	
Score	Identities	Gaps	Strand
141 bits(76)	76/76(100%)	0/76(0%)	Plus/Plus

Synthetic construct Snap ICAM-1 fusion protein gene, complete cds

Sequence ID: KM555101.1		Length: 2151	
Score	Identities	Gaps	Strand
1005 bits(544)	544/544(100%)	0/544(0%)	Plus/Plus

Figure 7.6 ***SnapTag sequence****. (a) Peptide sequence of the tag in* Figure 2.2d*, highlighting the signal sequence in grey. (b) BLAST against the protein sequence, as separate entries for the signal sequence and tag peptide for full coverage. (b) BLAST against the DNA sequence.*

(a) **IL-6/LgBiT Sequence**

MNSFSTSAFGPVAFSLGLLLVLPAAFPAPRLVFTLEDFVGDWEQTAAYNLDQVL
EQGGVSSLLQNLAVSVTPIQRIVRSGENALKIDIHVIIPYEGLSADQMAQIEEVFKVVYPVD
DHHFKVILPYGTLVIDGVTPNMLNYFGRPYEGIAVFDGKKITVTGTLWNGNKIIDERLITPD
GSMLFRVTINS

(b)

Nanoluc IL6 (secNluc) reporter [Nanoluc luciferase reporter vector pNL1.3[secNluc]]
Sequence ID: AFI79293.1 Length: 199

Score	Identities	Positives	Gaps
60.8 bits(146)	29/29(100%)	29/29(100%)	0/29(0%)

fusion protein of luciferase and GCaMP6f [synthetic construct]
Sequence ID: BBI93218.1 Length: 590

Score	Identities	Positives	Gaps
325 bits(832)	158/158(100%)	158/158(100%)	0/158(0%)

(c)

Homo sapiens interleukin 6 (IL6), transcript variant 1, mRNA
Sequence ID: NM_000600.5 Length: 1127

Score	Identities	Gaps	Strand
148 bits(80)	82/83(99%)	0/83(0%)	Plus/Plus

N198 pBiT1.1-N [TK/LgBiT] Vector
Sequence: Obtained from *https://www.promega.com/-/media/files/vector-sequences/luciferase/pbit1-1n-tk-lgbit-vector.txt?la=en*
Length: 3858 Range 1: 818 to 1291

Score	Identities	Gaps	Strand
876 bits(474)	474/474(100%)	0/474(0%)	Plus/Plus

Figure 7.7 ***LgBiT sequence***. *(a) Peptide sequence of the tag in* Figure 2.1d*, highlighting the IL-6 signal sequence in grey. (b) BLAST against the protein sequence, as separate entries for the signal sequence and tag peptide for full coverage. (b) BLAST against the DNA sequence.*

(a) **IL-6/HiBiT Sequence**

MNSFSTSAFGPVAFSLGLLLVLPAAFPAPRVSGWRLFKKIS

(b)

interleukin 6 (interferon, beta 2), isoform CRA_b [Homo sapiens]

Sequence ID:	Length: 98		
Score	Identities	Positives	Gaps
91.8 bits(209)	29/29(100%)	29/29(100%)	0/29(0%)

Peptide 86, V S G W R L F K K I S

Sequence: Obtained from *Dixon et al. (2016) ACS Chem Biol*

Length: 11

Score	Identities	Positives	Gaps
38.8 bits(84)	11/11(100%)	11/11(100%)	0/11(0%)

(c)

Homo sapiens interleukin 6 (IL6), transcript variant 1, mRNA

Sequence ID:	NM_000600.5	Length: 1127	
Score	Identities	Gaps	Strand
148 bits(80)	82/83(99%)	0/83(0%)	Plus/Plus

pBiT3.1-N [CMV/HiBiT/Blast] Vector

Sequence: Obtained from *https://promega.media/-/media/files/vector-sequences/luciferase/pbit31ncmvhibitblastvector.txt*

Length: 4326 Range 1: 1193 to 1225

Score	Identities	Gaps	Strand
62.1 bits(33)	33/33(100%)	0/33(0%)	Plus/Plus

Figure 7.8 ***HiBiT sequence***. *(a) Peptide sequence of the tag in* Figure 2.1e*, highlighting the signal sequence in grey. (b) BLAST against the protein sequence, as separate entries for the signal sequence and tag peptide for full coverage. (b) BLAST against the DNA sequence.*

(a) **IL-6/SmBiT Sequence**

MNSFSTSAFGPVAFSLGLLLVLPAAFPAPRVTGYRLFEEIL

(b)

interleukin 6 (interferon, beta 2), isoform CRA_b [Homo sapiens]

Sequence ID:	EAW93757.1	Length: 98	
Score	Identities	Positives	Gaps
91.8 bits(209)	29/29(100%)	29/29(100%)	0/29(0%)

Peptide 114, V T G Y R L F E E I L

Sequence:	Obtained from *Dixon et al. (2016) ACS Chem Biol*		
Length: 11			
Score	Identities	Positives	Gaps
38.8 bits(84)	11/11(100%)	11/11(100%)	0/11(0%)

(c)

Homo sapiens interleukin 6 (IL6), transcript variant 1, mRNA

Sequence ID:	NM_000600.5	Length: 1127	
Score	Identities	Gaps	Strand
148 bits(80)	82/83(99%)	0/83(0%)	Plus/Plus

N199 pBiT2.1-N [TK/SmBiT] Vector

Sequence:	Obtained from *https://www.promega.com/products/protein-interactions/live-cell-protein-interactions/nanobit-ppi-starter-systems/-/media/585b1fa2fa0a4fe3a5a9e2d8260fb4bb.ashx*		
Length: 3417	Range 1: 818 to 850		
Score	Identities	Gaps	Strand
62.1 bits(33)	33/33(100%)	0/33(0%)	Plus/Plus

Figure 7.9 ***SmBiT sequence****. (a) Peptide sequence of the tag in* Figure 2.1e*, highlighting the signal sequence in grey. (b) BLAST against the protein sequence, as separate entries for the signal sequence and tag peptide for full coverage. (b) BLAST against the DNA sequence.*

(a) **NRP1 Sequence**

MFRNDKCGDTIKIESPGYLTSPGYPHSYHPSEKCEWLIQAPDPYQRIMINFNPH
FDLEDRDCKYDYVEVFDGENENGHFRGKFCGKIAPPPVVSSGPFLFIKFVSDYETHGAG
FSIRYEIFKRGPECSQNYTTPSGVIKSPGFPEKYPNSLECTYIVFAPKMSEIILEFESFDLE
PDSNPPGGMFCRYDRLEIWDGFPDVGPHIGRYCGQKTPGRIRSSSGILSMVFYTDSAIA
KEGFSANYSVLQSSVSEDFKCMEALGMESGEIHSDQITASSQYSTNWSAERSRLNYPE
NGWTPGEDSYREWIQVDLGLLRFVTAVGTQGAISKETKKKYYVKTYKIDVSSNGEDWITI
KEGNKPVLFQGNTNPTDVVVAVFPKPLITRFVRIKPATWETGISMRFEVYGCKITDYPCS
GMLGMVSGLISDSQITSSNQGDRNWMPENIRLVTSRSGWALPPAPHSYINEWLQIDLGE
EKIVRGIIIQGGKHRENKVFMRKFKIGYSNNGSDWKMIMDDSKRKAKSFEGNNNYDTPE
LRTFPALSTRFIRIYPERATHGGLGLRMELLGCEVEAPTAGPTTPNGNLVDECDDDQAN
CHSGTGDDFQLTGGTTVLATEKPTVIDSTIQSEFPTYGFNCEFGWGSHKTFCHWEHDN
HVQLKWSVLTSKTGPIQDHTGDGNFIYSQADENQKGKVARLVSPVVYSQNSAHCMTFW
YHMSGSHVGTLRVKLRYQKPEEYDQLVWMAIGHQGDHWKEGRVLLHKSLKLYQVIFEG
EIGKGNLGGIAVDDISINNHISQEDCAKPADLDKKNPEIKIDETGSTPGYEGEGEGDKNIS
RKPGNVLKTLDPILITIIAMSALGVLLGAVCGVVLYCACWHNGMSERNLSALENYNFELV
DGVKLKKDKLNTQSTYSEAV*

(b)

neuropilin-1 isoform a precursor [Homo sapiens]

Sequence ID:	NP_003864.4	Length: 923	
Score	Identities	Positives	Gaps
1881 bits(4872)	901/902(99%)	901/902(99%)	0/902(0%)

(c)

Homo sapiens neuropilin 1 (NRP1), transcript variant 1, mRNA

Sequence ID:	NM_003873.6	Length: 5640	
Score	Identities	Gaps	Strand
4975 bits(2694)	2702/2706(99%)	0/2706(0%)	Plus/Plus

Figure 7.10 ***NRP1*** **sequencing**. *(a) Peptide sequence lacking the preliminary signal sequence. (b) BLAST against the protein sequence. (b) BLAST against the DNA sequence.*

(a) **VEGFR2 Sequence**

SVGLPSVSLDLPRLSIQKDILTIKANTTLQITCRGQRDLDWLWPNNQSGSEQRV
EVTECSDGLFCKTLTIPKVIGNDTGAYKCFYRETDLASVIYVYVQDYRSPFIASVSDQHGV
VYITENKNKTVVIPCLGSISNLNVSLCARYPEKRFVPDGNRISWDSKKGFTIPSYMISYAG
MVFCEAKINDESYQSIMYIVVVVGYRIYDVVLSPSHGIELSVGEKLVLNCTARTELNVGID
FNWEYPSSKHQHKKLVNRDLKTQSGSEMKKFLSTLTIDGVTRSDQGLYTCAASSGLMT
KKNSTFVRVHEKPFVAFGSGMESLVEATVGERVRIPAKYLGYPPPEIKWYKNGIPLESNH
TIKAGHVLTIMEVSERDTGNYTVILTNPISKEKQSHVVSLVVYVPPQIGEKSLISPVDSYQY
GTTQTLTCTVYAIPPPHHIHWYWQLEEECANEPSQAVSVTNPYPCEEWRSVEDFQGGN
KIEVNKNQFALIEGKNKTVSTLVIQAANVSALYKCEAVNKVGRGERVISFHVTRGPEITLQ
PDMQPTEQESVSLWCTADRSTFENLTWYKLGPQPLPIHVGELPTPVCKNLDTLWKLNA
TMFSNSTNDILIMELKNASLQDQGDYVCLAQDRKTKKRHCVVRQLTVLERVAPTITGNLE
NQTTSIGESIEVSCTASGNPPPQIMWFKDNETLVEDSGIVLKDGNRNLTIRRVRKEDEGL
YTCQACSVLGCAKVEAFFIIEGAQEKTNLEIIILVGTAVIAMFFWLLLVIILRTVKRANGGEL
KTGYLSIVMDPDELPLDEHCERLPYDASKWEFPRDRLKLGKPLGRGAFGQVIEADAFGI
DKTATCRTVAVKMLKEGATHSEHRALMSELKILIHIGHHLNVVNLLGACTKPGGPLMVIVE
FCKFGNLSTYLRSKRNEFVPYKTKGARFRQGKDFVGAIPVDLKRRLDSITSSQSSASSG
FVEEKSLSDVEEEEAPEDLYKDFLTLEHLICYSFQVAKGMEFLASRKCIHRDLAARNILLS
EKNVVKICDFGLARDIFKDPDFVRKGDARLPLKWMAPETIFDRVYTIQSDVWSFGVLLWE
IFSLGASPYPGVKIDEEFCRRLKEGTRMRAPDYTTPEMYQTMLDCWHGEPSQRPTFSE
LVEHLGNLLQANAQQDGKDFIVLPISETLSMEEDSGLSLPTSPVSCMEEEEVCDPKFHFD
NTAGISQYLQNSKRKSRPVSVKTFEDIPLEEPEVKVIPDDNQTDSGMVLASEELKTLEDR
TKLSPSFGGMVPSKSRESVASEGSNQTSGYQSGYHSDDTDTTVYSSEEAELLKLIEIGV
QTGSTAQILQPDSGTTLSSPPV*

(b)

vascular endothelial growth factor receptor 2 [Homo sapiens]

Sequence ID:	NP_002244.1/AAC16450.1		Length: 1356
Score	Identities	Positives	Gaps
2769 bits(7178)	1331/1336(99%)	1336/1336(100%)	0/1336(0%)

(c)

Homo sapiens kinase insert domain receptor (KDR), mRNA

Sequence ID:	NM_002253.3/AF063658.1		Length: 5849
Score	Identities	Gaps	Strand
7374 bits(3993)	4003/4008(99%)	0/4008(0%)	Plus/Plus

Figure 7.11 ***VEGFR2*** **sequence**. (*a) Peptide sequence lacking the preliminary signal sequence, highlighting tyrosine phosphorylation deficient mutants (yellow). (b) BLAST against the protein sequence. (b) BLAST against the DNA sequence.*

7.3 Buffer Composition

All buffer and ligand chemical concentrations were calculated according to the following equation:

Equation 7.1.

$$concentration\ (M) = \frac{mass\ (g)}{volume\ (L)\ x\ molecular\ weight\ (g/mol)}$$

Buffer pH was measured with the pH Meter SB-11 (Sartorius) and adjusted using 3 M sodium hydroxide or concentrated hydrochloric acid.

7.3.1 HEPES Buffered Saline Solution (HBSS)

Prior to the addition of D-Glucose*, HBSS was prepared at a 10X stock concentration in 1 L ddH_2O and the pH was adjusted to 7.45. This was then autoclaved to sterilise buffer without denaturing glucose and stored at 4°C. In order of the molar proportion of their components, 1X HBSS was composed of:

Sodium chloride	145 mM
HEPES buffer	10 mM
D-Glucose*	10 mM
Potassium chloride	5 mM
Sodium pyruvate	2 mM
Sodium bicarbonate	1.5 mM
Calcium chloride dihydrate	1.3 mM
Magnesium sulphate heptahydrate	1 mM

7.3.2 Tris-acetate-EDTA (TAE) Buffer

TAE buffer was prepared at a 50X stock concentration in 1 L ddH_2O. This was stored at room temperature. 1X TAE buffer was composed of:

Trizma® base	40 mM
Acetic acid	20 mM (57.1 ml glacial acetic acid)
EDTA dihydrate	1 mM (dissolved at pH 8.0)

7.4 Principles of Fluorescence

Fluorophores absorb light energy, which excites electrons to a higher energy state. As electrons return back to their ground state, energy is emitted as light (*hv*). This photon emission is the basis of fluorescence. Some energy dissipates during the excitation period, therefore emitted photons have less energy and a longer wavelength. This is observed by the rightward Stoke's shift between the maximum excitation and maximum emission peak in the spectra for each fluorophore (*Figure 7.12*). The specific wavelengths of excitation and emission for each fluorophore are determined by their structural and chemical environment.

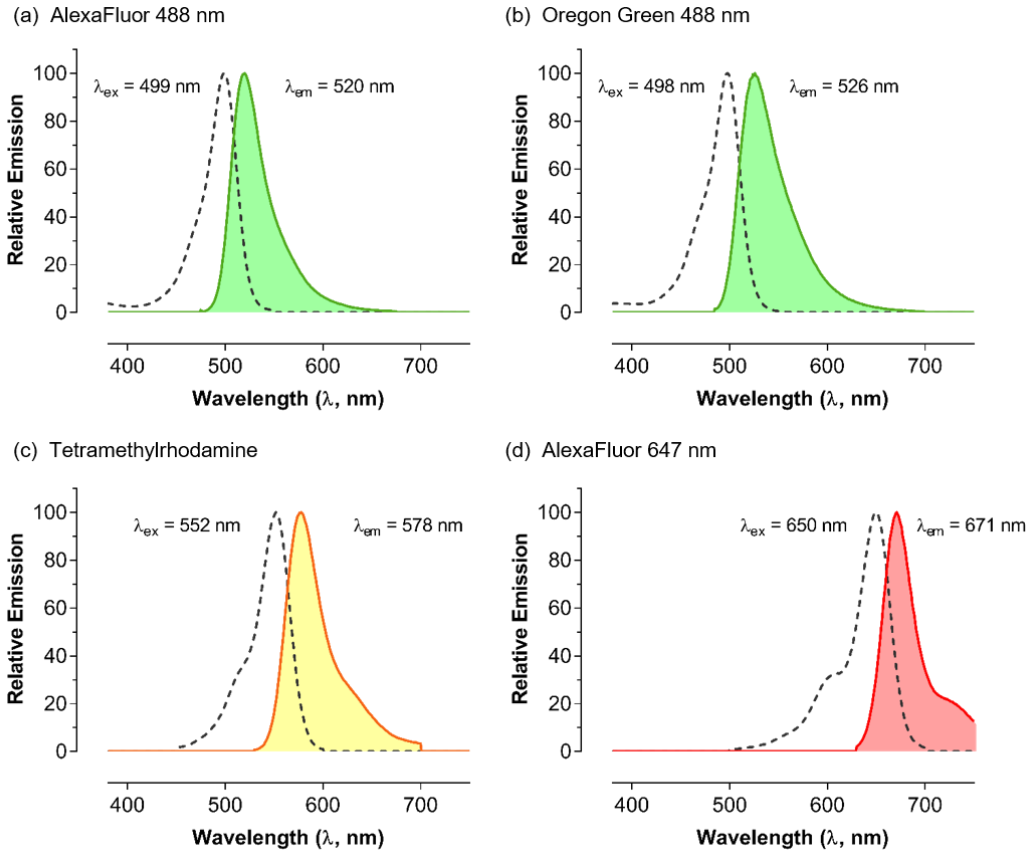


Figure 7.12 ***Fluorophore spectra****. Spectra for (a) AlexaFluor488, (b) Oregon Green, (c) tetramethylrhodamine and (d) AlexaFluor647, illustrating their excitation spectrum (dashed line) and emission spectrum (solid line). The peak excitation wavelength (λ_{ex}) and emission wavelength (λ_{em}) is shown. Data were obtained from Thermo Fisher SpectraViewer.*

7.5 Principles of Resonance Energy Transfer

Resonance energy transfer (RET) is an electrodynamic process occurring between a donor molecule in its excited state and an acceptor molecule in its ground state. Fluorescence-based RET involves energy transfer resulting from long-range dipole-dipole interactions between donor and acceptor fluorophores. There are also orientation constraints between the dipole moments. Bioluminescence-based RET replaces the fluorescent donor with a bioluminescent donor, but the same principles apply. The rate of energy transfer from donor to acceptor, $k_T(r)$, is described by Equation 7.2. The Förster distance, R_0, is the distance at which RET is 50% efficient. This typically ranges between 2-9 nm, or 20-90 Å (Lakowicz, 2006).

Equation 7.2.

$$k_T(r) = \frac{1}{\tau_D}\left(\frac{R_0}{r}\right)^6$$

Equation 7.2 describes: the Förster distance, R_0; decay time of the donor, τ_D; the distance between donor and acceptor, r. Rate therefore depends on distance. This is proportional to $1/r^6$. Förster distance can be predicted by donor and acceptor spectral properties. The interdependence between distance (r) and energy transfer efficiency, $k_T(r)$, can be plotted as a sigmoidal curve (*Figure 7.13*). Looyenga et al. (2016) predicted the theoretical Förster distance for numerous acceptor fluorophores with NanoLuc as an donor (2.8-4.5 nm). This demonstrates that RET only occurs at a distance <10 nm.

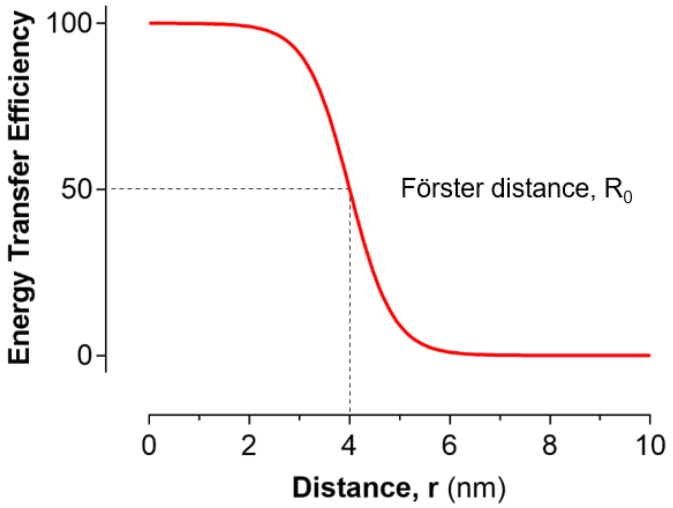


Figure 7.13 ***Dependence of resonance energy transfer (RET) efficiency on distance between the donor and acceptor****. This uses a representative donor-acceptor pair with a Förster distance of 4 nm. In this system, RET occurs <8 nm.*

7.6 Graphical Functions

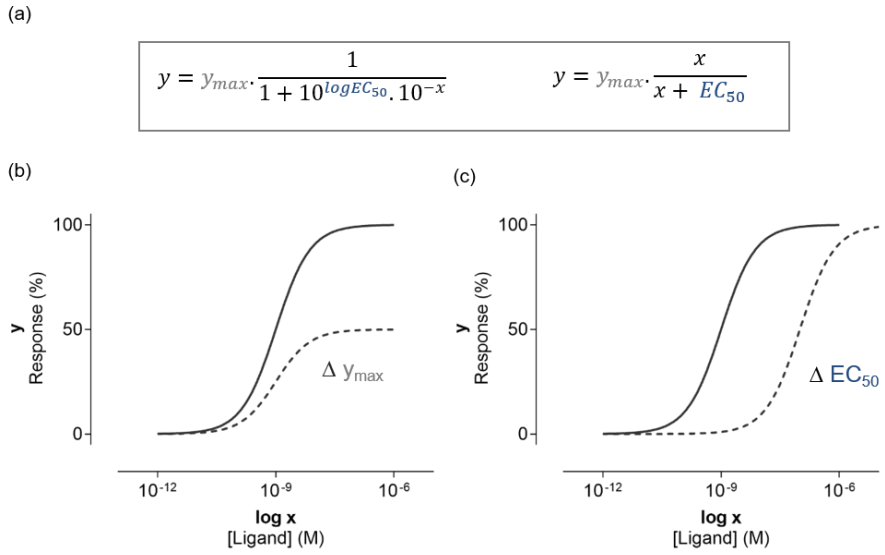


Figure 7.14 ***Sigmoidal functions****. (a) Derivation of a logarithmic sigmoidal function calculating EC_{50}, expressed in terms of concentration. (b) The effect of changing parameters in this logarithmic equation, whereby the dashed line represents a lower maximum response (y_{max}). (c) Compared to the solid line (EC_{50} = 10^{-9} M), the dashed line represents a ligand with a lower efficacy (EC_{50} = 10^{-7} M). This is because a higher ligand concentration is required for the same response.*

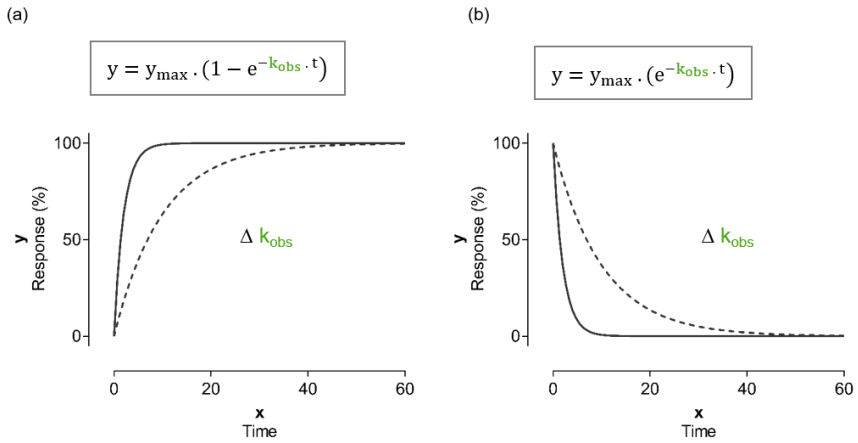


Figure 7.15 ***Monoexponential functions over time****. (a) Exponential associations are plotted using e, the base of a natural logarithm. (b) Exponential dissociation over time. Compared to the solid line (k_{obs} = 0.5), both dashed lines represent a smaller, slower rate constant (k_{obs} = 0.1) in* (a) *and* (b)*.*

Chapter 8.
References

Aaij C & Borst P. (1972) The gel electrophoresis of DNA. *Biochim Biophys Acta.* 269: 192–200.

Abramowicz M, Zuccotti G, & Pflomm JM. (2015) VEGF inhibitors for AMD and diabetic macular edema. Med Lett Drugs Ther. 57: 41–42.

Abu-Ghazaleh R, Kabir J, Jia H, Lobo M, & Zachary I. (2001) Src mediates stimulation by vascular endothelial growth factor of the phosphorylation of focal adhesion kinase at tyrosine 861, & migration and anti-apoptosis in endothelial cells. *Biochem J*. 360: 255–64.

Achen MG, Jeltsch M, Kukk E, Mäkinen T, Vitali A, Wilks AF, et al. (1998) Vascular endothelial growth factor D (VEGF-D) is a ligand for the tyrosine kinases VEGF receptor 2 (Flk1) and VEGF receptor 3 (Flt4). *Proc Natl Acad Sci USA*. 95: 548–53.

Adamis AP, Shima DT, Tolentino MJ, Gragoudas ES, Ferrara N, Folkman J, et al. (1996) Inhibition of Vascular Endothelial Growth Factor Prevents Retinal Ischemia-Association Iris Neovascularisation in a Nonhuman Primate. *Arch Opthamol*. 114: 66–71.

Adams RH, & Alitalo K. (2007) Molecular regulation of angiogenesis and lymphangiogenesis. *Nat Rev Mol Cell Biol*. 8: 464–78.

Ahmadova Z, Yagublu V, Forg T, Hajiyeva Y, Jesenofsky R, Hafner M, et al. (2014) Fluorescent resonance energy transfer imaging of VEGFR dimerization. *Anticancer Res*. 34: 2123–34.

Aiello LP, Arrigg PG, Shah ST, Keyt BA, Avery RL, Jampel HD, et al. (1994) Vascular Endothelial Growth Factor in Ocular Fluid of Patients with Diabetic Retinopathy and Other Retinal Disorders. *N Engl J Med*. 331: 1480–7.

Alberts B, Johnson A, Lewis J, Raff M, Roberts K, Walker P. (2008) *Molecular Biology of the Cell*. 5th edition. New York: Garland Science.

Alcobia DC, Ziegler AI, Kondrashov A, Comeo E, Mistry S, Kellam B, et al. (2018) Visualizing Ligand Binding to a GPCR In Vivo Using NanoBRET. *iScience*. 6: 280–88.

Alexander S, Fabbro D, Kelly E, Marrion NV, Peters JA, Faccenda E, et al. (2017) The Concise Guide To Pharmacology 2017/18: Catalytic receptors. *Br J Pharmacol*. 174: S225–71.

Algire GH, Chalkley HW, Legallais FY, & Park HD. (1945) Vasculae Reactions of Normal and Malignant Tissues in Vivo. I. Vascular Reactions of Mice to Wounds and to Normal and Neoplastic Transplants. *J Natl Cancer Inst*. 6: 73–85.

Alkim C, Alkim H, Koksal AR, Boga S, & Sen I (2015) Angiogenesis in inflammatory bowel disease. *Int J Inflam*. doi: 10.1155/2015/970890. 1–10.

Amann A, Zwierzina M, Koeck S, Gamerith G, Pechriggl E, Huber JM, et al. (2017) Development of a 3D angiogenesis model to study tumour-endothelial cell interactions and the effects of anti-angiogenic drugs. *Sci Rep*. 7: 1–13.

Appleton B, Wu P, Maloney J, Yin JP, Liang WC, Stawicki S, et al. (2007) Structural studies of neuropilin/antibody complexes provide insights into semaphorin and VEGF binding. *EMBO J*. 26: 4902–12.

Armesilla AL, Lorenzo E, Gómez del Arco P, Martínez-Martínez S, Alfranca A, & Redondo JM. (1999) Vascular Endothelial Growth Factor Activates Nuclear Factor of Activated T Cells in Human Endothelial Cells: a Role for Tissue Factor Gene Expression. *Mol Cell Biol*. 19: 2032–43.

Ashikari-Hada S, Habuchi H, Kariya Y, & Kimata K. (2005) Heparin regulates vascular endothelial growth factor165-dependent mitogenic activity, tube formation, and its receptor phosphorylation of human endothelial cells. Comparison of the effects of heparin and modified heparins. *J Biol Chem*. 280: 31508–15.

Atlas D & Levitzki A. (1977) Probing of beta-adrenergic receptors by novel fluorescent beta-adrenergic blockers. *Proc Natl Acad Sci USA*. 74: 5290–94.

Auriau J, Roujeau C, Choucair ZB, Oishi A, Derviaux C, Roux T, et al. (2018) Gain of affinity for VEGF165 binding within the VEGFR2/NRP1 cellular complex detected by an HTRF-based binding assay. *Biochem Pharmacol*. 158: 45–59.

Ayoub MA, See HB, Seeber RM, Armstrong SP, & Pfleger KDG. (2013) Profiling Epidermal Growth Factor Receptor and Heregulin Receptor 3 Heteromerization Using Receptor Tyrosine Kinase Heteromer Investigation Technology. PLoS One. 8: 1-10.

Azizi G, Boghozian R, & Mirshafiey A. (2014) The potential role of angiogenic factors in rheumatoid arthritis. *Int J Rheum Dis*. 17: 369–83.

Ballmer-Hofer K, Andersson AE, Ratcliffe LE, & Berger P. (2011) Neuropilin-1 promotes VEGFR-2 trafficking through Rab11 vesicles thereby specifying signal output. *Blood*. 118: 816–26.

Banerjee S, Sengupta K, Dhar K, Mehta S, D'Amore P, Dhar G, et al. (2006) Breast Cancer Cells Secreted Platelet-Derived Growth Factor-Induced Motility of Vascular Smooth Muscle Cells Is Mediated Through Neuropilin-1. *Mol Carcinog*. 45: 871–80.

Banks RE, Forbes MA, Kinsey SE, Stanley A, Ingham E, Walters C, et al. (1998) Release of the angiogenic cytokine vascular endothelial growth factor (VEGF) from platelets: significance for VEGF measurements and cancer biology. *Br J Cancer*. 77: 956–64.

Barratt SL, Blythe T, Jarrett C, Ourradi K, Shelley-Fraser G, Day MJ, et al. (2017) Differential Expression of VEGF-A xxx Isoforms Is Critical for Development of Pulmonary Fibrosis. *Am J Respir Crit Care Med*. 196: 479–93.

Basagiannis D, & Christoforidis S. (2016) Constitutive endocytosis of VEGFR2 protects the receptor against shedding. *J Biol Chem*. 291: 16892–903.

Basagiannis D, Zografou S, Murphy C, Fotsis T, Morbidelli L, Ziche M, et al. (2016) VEGF induces signalling and angiogenesis by directing VEGFR2 internalisation via macropinocytosis. *J Cell Sci*. 129: 4091–104.

Basagiannis D, Zografou S, Galanopoulou K, & Christoforidis S. (2017) Dynasore impairs VEGFR2 signalling in an endocytosis- independent manner. *Sci Rep*. 7: 1–11.

Bates D, Cui T-G, Doughty JM, Winkler M, Sugiono M, Shields JD, et al. (2002) $VEGF_{165}b$, an inhibitory splice variant of vascular endothelial growth factor, is down-regulated in renal cell carcinoma. *Cancer Res*. 62: 4123–31.

Bates DO, Mavrou A, Qiu Y, Carter JG, Hamdollah-Zadeh M, Barratt S, et al. (2013) Detection of VEGF-A_{xxx}b Isoforms in Human Tissues. *PLoS One*. 8: 1–10.

Becker PM, Waltenberger J, Yachechko R, Mirzapoiazova T, Sham J, Lee C, et al. (2005) Neuropilin-1 Regulates Vascular Endothelial Growth Factor-Mediated Endothelial Permeability. *Circ Res*. 96: 1257–65.

Bellacosa A, Testa JR, Staal SP, & Tsichlis PN. (1991) A retroviral oncogene, akt, encoding a serine-threonine kinase containing an SH2-like region. *Science*. 254: 274–7.

Berisio R, Ciccarelli L, Squeglia F, De Simone A, & Vitagliano, L. (2012) Structural and Dynamic Properties of Incomplete Immunoglobulin-like Fold Domains Protein. *Pept Lett*. 19: 1045–53.

Berse B, Brown LF, Van de Water L, Dvorak HF, & Senger DR. (1992) Vascular permeability factor (vascular endothelial growth factor) gene is expressed differentially in normal tissues, macrophages, and tumors. *Mol Biol Cell*. 3: 211–20.

Bhaumik S, & Gambhir SS. (2002) Optical imaging of Renilla luciferase reporter gene expression in living mice. *Proc Natl Acad Sci USA*. 99: 377–82.

Blobel CP. (2005) ADAMs: Key components in EGFR signalling and development. *Nat Rev Mol Cell Biol*. 6: 32–43.

Boeuf FL, Houle F, & Huot J. (2004) Regulation of vascular endothelial growth factor receptor 2-mediated phosphorylation of focal adhesion kinase by heat shock protein 90 and Src kinase activities. *J Biol Chem*. 279: 39175–85.

Borges E, Jan Y, & Ruoslahti E. (2000) Platelet-derived growth factor receptor β and vascular endothelial growth factor receptor 2 bind to the β 3 integrin through its extracellular domain. *J Biol Chem*. 275: 39867–73.

Borriello L, Montès M, Lepelletier Y, Leforban B, Liu WQ, Demange L, et al. (2014) Structure-based discovery of a small non-peptidic Neuropilins antagonist exerting in vitro and in vivo anti-tumor activity on breast cancer model. *Cancer Lett*. 349: 120–127.

Botta J, Bibic L, Killoran P, McCormick P, & Howell L. (2019) Design and development of stapled transmembrane peptides that disrupt the activity of G-protein coupled receptor oligomers. *J Biol Chem*. 294: 16587-603.

Boursier ME, Levin S, Zimmerman K, Machleidt T, Hurst R, Butler BL, et al. (2020) The luminescent HiBiT peptide enables selective quantitation of GPCR ligand engagement and internalization in living cells. *J Biol Chem*. doi:10.1074/jbc.RA119.011952.

Briddon SJ, Kilpatrick LE, & Hill SJ. (2018) Studying GPCR Pharmacology in Membrane Microdomains: Fluorescence Correlation Spectroscopy Comes of Age. *Trends Pharmacol Sci*. 39: 158–74.

Bridgett S, Dellett M, & Simpson DA. (2017) RNA-Sequencing data supports the existence of novel VEGFA splicing events but not of $VEGFA_{xxx}b$ isoforms. *Sci Rep*. 7:1–11.

Brogi E, Wu T, & Namiki A. (1994) Indirect angiogenic cytokines upregulate VEGF and bFGF gene expression in vascular smooth muscle cells, whereas hypoxia upregulates VEGF expression only. *Circulation*. 90: 649–52.

Brozzo MS, Bjelic S, Kisko K, Schleier T, Leppanen VM, Alitalo K, et al. (2011) Thermodynamic and structural description of allosterically regulated VEGF receptor 2 dimerization. *Blood*. 119: 1781–88.

Bryan BA, Dennstedt E, Mitchell DC, Walshe TE, Noma K, Loureiro R, et al. (2010) RhoA/ROCK signaling is essential for multiple aspects of VEGF-mediated angiogenesis. *FASEB J*. 24: 3186–95.

Bylund DB, & Toews ML. (1993) Radioligand binding methods practical guide and tips. *Am J Physiol*. 265: 421–29.

Cai H, & Reed RR. (1999) Cloning and characterization of neuropilin-1-interacting protein: a PSD- 95/Dlg/ZO-1 domain-containing protein that interacts with the cytoplasmic domain of neuropilin-1. *J Neurosci*. 19: 6519–27.

Carmeliet P, Ferreira V, Breier G, Pollefeyt S, Kieckens L, Gertsenstein M, et al. (1996) Abnormal blood vessel development and lethality in embryos lacking a single VEGF allele. *Nature*. 380: 435–39.

Carmeliet P. (2005) Angiogenesis in life, disease and medicine. *Nature*. 438: 932–36.

Carter J, Wheal A, Hill SJ, & Woolard J. (2015) Effects of receptor tyrosine kinase inhibitors on $VEGF_{165}a$- and $VEGF_{165}b$-stimulated gene transcription in HEK-293 cells expressing human VEGFR2. *Br J Pharmacol*. 172: 3141–50.

Carter JJ, Fretwell LV, & Woolard J. (2017) Effects of 4 multitargeted receptor tyrosine kinase inhibitors on regional hemodynamics in conscious, freely moving rats. *FASEB J*. 31: 1193–203.

Castro M, Nikolaev VO, Palm D, Lohse MJ, & Vilardaga JP. (2005) Turn-on switch in parathyroid hormone receptor by a two-step parathyroid hormone binding mechanism. *Proc Natl Acad Sci USA*. 102: 16084–89.

Catena R, Larzabal L, Larrayoz M, Molina E, Hermida J, Agorreta J, et al. (2010) $VEGF_{121}b$ and $VEGF_{165}b$ are weakly angiogenic isoforms of VEGF-A. *Mol Cancer*. 9: 1–14.

Cébe Suarez S, Pieren M, Cariolato L, Arn S, Hoffman U, Bogucki A, et al. (2006) A VEGF-A splice variant defective for heparan sulfate and neuropilin-1 binding shows attenuated signaling through VEGFR-2. *Cell Mol Life Sci*. 63: 2067–77.

Chan CL, Ewert KK, Majzoub RN, Hwu YK, Liang KS, Leal C, et al. (2014) Optimizing cationic and neutral lipids for efficient gene delivery at high serum content. *J Gene Med*. 16: 84–96.

Chen Y, Wiesmann C, Fuh G, Li B, Christinger HW, McKay P, et al. (1999) Selection and analysis of an optimized anti-VEGF antibody: crystal structure of an affinity-matured Fab in complex with antigen. *J Mol Biol*. 293: 865–81.

Chen X, Liu H, Focia PJ, Shim AHR, & He X. (2008) Structure of macrophage colony stimulating factor bound to FMS: diverse signaling assemblies of class III receptor tyrosine kinases. *Proc Natl Acad Sci USA*. 105: 18267–72.

Chen XL, Nam JO, Jean C, Lawson C, Walsh CT, Goka E, et al. (2012) VEGF-Induced Vascular Permeability Is Mediated by FAK. *Dev Cell*. 22: 146–57.

Chen L, & Flies DB. (2013) Molecular mechanisms of T cell co-stimulation and co-inhibition. *Nat Rev Immunol*. 13: 227–42.

Chittenden TW, Claes F, Lanahan AA, Autiero M, Palac RT, Tkachenko EV, et al. (2006) Selective Regulation of Arterial Branching Morphogenesis by Synectin. *Dev Cell*. 10: 783–95.

Cho KO, Hunt CA, & Kennedy MB. (1992) The rat brain postsynaptic density fraction contains a homolog of the drosophila discs-large tumor suppressor protein. *Neuron*. 9: 929–42.

Chung AS, & Ferrara N. (2011) Developmental and pathological angiogenesis. *Annu Rev Cell Dev Biol*. 27: 563–84.

Claffey KP, Senger DR, & Spiegelman BM. (1995) Structural requirements for dimerization, glycosylation, secretion, and biological function of VPF/VEGF. *Biochim Biophys Acta*. 1246: 1–9.

Clark AJ. (1933) The Mode of Action of Drugs on Cells. 1st edition. London: Edward Arnold.

Clayton AHA, Walker F, Orchard SG, Henderson C, Fuchs D, Rothacker J, et al. (2005) Ligand-induced dimer-tetramer transition during the activation of the cell surface epidermal growth factor receptor - A multidimensional microscopy analysis. *J Biol Chem*. 280: 30392–99.

Clegg LE, & Mac Gabhann F. (2017) A computational analysis of in vivo VEGFR activation by multiple co-expressed ligands. *PLoS Comput Biol*. 13: 1–33.

Condon ND, Heddleston JM, Chew TL, Luo L, McPherson PS, Ioannou MS, et al. (2018) Macropinosome formation by tent pole ruffling in macrophages. *J Cell Biol*. 217: 3873–85.

Coon BG, Baeyens N, Han J, Budatha M, Ross TD, Fang JS, et al. (2015) Intramembrane binding of VE-cadherin to VEGFR2 and VEGFR3 assembles the endothelial mechanosensory complex. *J Cell Biol*. 208: 975–86.

Corti F, & Simons M. (2017) Modulation of VEGF receptor 2 signaling by protein phosphatases. *Pharmacol Res*. 115: 107–23.

Cudmore MJ, Hewett PW, Ahmad S, Wang K-Q, Cai M, Al-Ani, B, et al. (2012) The role of heterodimerization between VEGFR-1 and VEGFR-2 in the regulation of endothelial cell homeostasis. *Nat Commun*. 3: 1–12.

Cunningham SA, Arrate MP, Brock TA, & Waxham MN. (1997) Interactions of FLT-1 and KDR with Phospholipase C γ: Identification of the Phosphotyrosine Binding Sites. *Biochem Biophys Res Commun*. 240: 635–39.

Damioli V, Salvadori A, Beretta GP, Ravelli C, & Mitola S. (2017) Multi-physics interactions drive VEGFR2 relocation on endothelial cells. *Sci Rep*. 7: 1–11.

Dar AC, & Shokat KM. (2011) The Evolution of Protein Kinase Inhibitors from Antagonists to Agonists of Cellular Signaling. *Annu Rev Biochem*. 80: 769–95.

Dardente H, English WR, Valluru MK, Kanthou C, & Simpson D. (2020) Debunking the Myth of the Endogenous Antiangiogenic $Vegfa_{xxx}b$ Transcripts. Trends Endocrinol Metab. doi: https://doi.org/10.1016/j.tem.2020.01.014. 1–12.

Davis MI, Hunt JP, Herrgard S, Ciceri P, Wodicka LM, Pallares G, et al. (2011) Comprehensive analysis of kinase inhibitor selectivity. *Nat Biotechnol*. 29: 1046–51.

De Smet F, Christopoulos A, & Carmeliet P (2014) Allosteric targeting of receptor tyrosine kinases. *Nat Biotechnol*. 32: 1113–20.

dela Paz NG, Walshe TE, Leach LL, Saint-Geniez M, & D'Amore PA. (2012) Role of shear-stress-induced VEGF expression in endothelial cell survival. *J Cell Sci*. 125: 831–43.

Delcombel R, Janssen L, Vassy R, Gammons M, Haddad O, Richard B, et al. (2013) New prospects in the roles of the C-terminal domains of VEGF-A and their cooperation for ligand binding, cellular signaling and vessels formation. *Angiogenesis*. 16: 353–71.

Deng Y, Zhang X, & Simons M. (2015) Molecular controls of lymphatic VEGFR3 signaling. *Arterioscler Thromb Vasc Biol*. 35: 421–29.

Di Guglielmo GM, Baass PC, Ou WJ, Posner BI, & Bergeron JJ. (1994) Compartmentalization of SHC, GRB2 and mSOS, and hyperphosphorylation of Raf-1 by EGF but not insulin in liver parenchyma. *EMBO J*. 13: 4269–77.

Dixelius J, Mäkinen T, Wirzenius M, Karkkainen MJ, Wernstedt C, Alitalo K, et al. (2003) Ligand-induced Vascular Endothelial Growth Factor Receptor-3 (VEGFR-3) Heterodimerization with VEGFR-2 in Primary Lymphatic Endothelial Cells Regulates Tyrosine Phosphorylation Sites. *J Biol Chem*. 278: 40973–79.

Dixon AS, Schwinn MK, Hall MP, Zimmerman K, Otto P, Lubben TH, et al. (2016) NanoLuc Complementation Reporter Optimized for Accurate Measurement of Protein Interactions in Cells. *ACS Chem Biol* .11: 400–408.

Djordjevic S, & Driscoll PC. (2013) Targeting VEGF signalling via the neuropilin co-receptor. *Drug Discov Today*. 18: 447–55.

Doherty GJ, & McMahon HT. (2009) Mechanisms of Endocytosis. *Annu Rev Biochem*. 78: 857–902.

Domigan CK, Ziyad S, & Iruela-Arispe ML. (2015) Canonical and noncanonical vascular endothelial growth factor pathways: New developments in biology and signal transduction. *Arterioscler Thromb Vasc Biol*. 35: 30–39.

Donato DM, Ryzhova LM, Meenderink LM, Kaverina I, & Hanks SK. (2010) Dynamics and mechanism of p130Cas localization to focal adhesions. *J Biol Chem*. 285: 20769–79.

Dosch DD, & Ballmer-Hofer K. (2010) Transmembrane domain-mediated orientation of receptor monomers in active VEGFR-2 dimers. *FASEB J*. 24: 32–38.

DuBridge RB, Tang P, Hsia HC, Leong PM, Miller JH, & Calos MP. (1987) Analysis of mutation in human cells by using an Epstein-Barr virus shuttle system. *Mol Cell Biol*. 7: 379–87.

Ebos JML, Bocci G, Man S, Thorpe PE, Hicklin DJ, Zhou D, et al. (2004) A naturally occurring soluble form of vascular endothelial growth factor receptor 2 detected in mouse and human plasma. *Mol Cancer Res*. 2: 315–26.

Eswarappa SM, Potdar AA, Koch WJ, Fan Y, Vasu K, Lindner D, et al. (2014) Programmed translational readthrough generates antiangiogenic VEGF-Ax. *Cell*. 157: 1605–18.

Evans IM, Kennedy SA, Paliashvili K, Santra T, Yamaji M, Lovering RC, et al. (2017) Vascular Endothelial Growth Factor (VEGF) Promotes Assembly of the p130Cas Interactome to Drive Endothelial Chemotactic Signaling and Angiogenesis. *Mol Cell Proteomics*. 16: 168–80.

Evans IM, Yamaji M, Britton G, Pellet-Many C, Lockie C, Zachary IC, et al. (2011) Neuropilin-1 signaling through p130Cas tyrosine phosphorylation is essential for growth factor-dependent migration of glioma and endothelial cells. *Mol Cell Biol*. 31: 1174–85.

Ewan LC, Jopling HM, Jia H, Mittar S, Bagherzadeh A, Howell GJ, et al. (2006) Intrinsic tyrosine kinase activity is required for vascular endothelial growth factor receptor 2 ubiquitination, sorting and degradation in endothelial cells. *Traffic*. 7: 1270–82

Fairbrother WJ, Champe MA, Christinger HW, Keyt BA, & Starovasnik MA. (1998) Solution structure of the heparin-binding domain of vascular endothelial growth factor. *Structure*. 6: 637–48.

Fantin A, Schwarz Q, Davidson K, Normando EM, Denti L, & Ruhrberg C. (2011) The cytoplasmic domain of neuropilin 1 is dispensable for angiogenesis, but promotes the spatial separation of retinal arteries and veins. *Development*. 138: 4185–91.

Fantin A, Vieira JM, Plein A, Denti L, Fruttiger M, Pollard JW, et al. (2013) NRP1 acts cell autonomously in endothelium to promote tip cell function during sprouting angiogenesis. *Blood*. 121: 2352–62.

Fantin A, Herzog B, Mahmoud M, Yamaji M, Plein A, Denti L, et al. (2014) Neuropilin 1 (NRP1) hypomorphism combined with defective VEGF-A binding reveals novel roles for NRP1 in developmental and pathological angiogenesis. *Development*. 141: 556–62.

Fantin A, Lampropoulou A, Gestri G, Raimondi C, Senatore V, Zachary I, et al. (2015) NRP1 Regulates CDC42 Activation to Promote Filopodia Formation in Endothelial Tip Cells. *Cell Rep*. 11: 1577–90.

Farnsworth RH, Lackmann M, Achen MG, & Stacker SA. (2014) Vascular remodeling in cancer. *Oncogene*. 33: 3496–3505.

Fearnley GW, Odell AF, Latham AM, Mughal NA, Bruns AF, Burgoyne NJ, et al. (2014) VEGF-A isoforms differentially regulate ATF-2-dependent VCAM-1 gene expression and endothelial-leukocyte interactions. *Mol Biol Cell*. 25: 2509–21.

Fearnley GW, Bruns AF, Wheatcroft SB, & Ponnambalam S. (2015) VEGF-A isoform-specific regulation of calcium ion flux, transcriptional activation and endothelial cell migration. *Biol Open*. 4: 731–42.

Fearnley GW, Smith GA, Abdul-Zani I, Yuldasheva N, Mughal NA, Homer-Vanniasinkam, S, et al. (2016) VEGF-A isoforms program differential VEGFR2 signal transduction, trafficking and proteolysis. *Biol Open*. 5: 571–83.

Ferrara N, & Henzel W. (1989) Pituitary follicular cells secrete a novel heparin-binding growth factor specific for vascular endothelial cells. *Biochem Biophys Res Commun*. 161: 851–58.

Ferrara N, Carver-Moore K, Chen H, Dowd M, Lu L, O'Shea KS, et al. (1996) Heterozygous embryonic lethality induced by targeted inactivation of the VEGF gene. *Nature*. 380: 439–42.

Finlay DB, Duffull SB, Glass M. (2020) 100 years of modelling ligand–receptor binding and response: A focus on GPCRs. *Br J Pharmacol*. 177: 1472–84.

Folkman J. (1971) Tumour Angiogenesis: Therapeutic Implications. *N Engl J Med*. 285: 1182–86.

Folkman J. (1972) Angiogenesis in psoriasis: therapeutic implications. *J Invest Dermatol*. 59: 40–43.

Folkman J. (1974) Tumor angiogenesis. *Adv Cancer Res*. 19: 331–58.

Forsythe JA, Jiang B, Iyer NV, Agani F, & Leung SW. (1996) Activation of vascular endothelial growth factor gene transcription by hypoxia-inducible factor Activation of Vascular Endothelial Growth Factor Gene Transcription by Hypoxia-Inducible Factor 1. *Mol Cell Biol*.16: 4604–12.

Franco M, Roswall P, Cortez E, Hanahan D, & Pietras K. (2011) Pericytes promote endothelial cell survival through induction of autocrine VEGF-A signaling and Bcl-w expression. *Blood*. 118: 2906–17.

Franklin MC, Navarro EC, Wang Y, Patel S, Singh P, Zhang Y, et al. (2011) The structural basis for the function of two anti-VEGF receptor 2 antibodies. *Structure*. 19: 1097–1107.

Frantz C, Stewart KM, Weaver VM, Frantz C, Stewart KM, & Weaver VM. (2010) The extracellular matrix at a glance. *J Cell Sci*. 123: 4195–4200.

Freed DM, Alvarado D, & Lemmon MA. (2015) Ligand regulation of a constitutively dimeric EGF receptor. *Nat Commun*. 6: 1–7.

Freeman SA, Vega A, Riedl M, Collins RF, Ostrowski PP, Woods EC, et al. (2018) Transmembrane Pickets Connect Cyto- and Pericellular Skeletons Forming Barriers to Receptor Engagement. *Cell*. 172: 305-12.

Friedman Ohana R, Hurst R, Vidugiriene J, Slater MR, Wood KV, & Urh M. (2011) HaloTag-based purification of functional human kinases from mammalian cells. *Protein Expr Purif*. 76: 154–64.

Friedman Ohana R, Kirkland TA, Woodroofe CC, Levin S, Uyeda HT, Otto P, et al. (2015) Deciphering the Cellular Targets of Bioactive Compounds Using a Chloroalkane Capture Tag. *ACS Chem Biol*. 10: 2316–24.

Friedman Ohana R, Hurst R, Rosenblatt M, Levin S, Machleidt T, Kirkland TA, et al. (2019) Utilizing a Simple Method for Stoichiometric Protein Labeling to Quantify Antibody Blockade. *Sci Rep*. 9: 1–12.

Fuh G, Garcia KC, & de Vos AM. (2000) The interaction of neuropilin-1 with vascular endothelial growth factor and its receptor flt-1. *J Biol Chem*. 275: 26690–95.

Fujiwara TK, Iwasawa K, Kalay Z, Tsunoyama TA, Watanabe Y, Umemura YM, et al. (2016) Confined diffusion of transmembrane proteins and lipids induced by the same actin meshwork lining the plasma membrane. *Mol Biol Cell*. 27: 1101–19.

Gagnon ML, Bielenberg DR, Gechtman Z, Miao HQ, Takashima S, Soker S, et al. (2000) Identification of a natural soluble neuropilin-1 that binds vascular endothelial growth factor: In vivo expression and antitumor activity. *Proc Natl Acad Sci USA*. 97: 2573–78.

Gampel A, Moss L, Jones MC, Brunton V, Norman JC, & Mellor H. (2006) VEGF regulates the mobilization of VEGFR2/KDR from an intracellular endothelial storage compartment. *Blood*. 108: 2624–31.

Gaudry M, Brégerie O, Andrieu V, El Benna J, Pocidalo M-A, & Hakim, J. (1997) Intracellular pool of vascular endothelial growth factor in human neutrophils. *Blood*. 90: 4153–61.

Gavard J, & Gutkind JS. (2006) VEGF controls endothelial-cell permeability by promoting the β-arrestin-dependent endocytosis of VE-cadherin. *Nat Cell Biol*. 8: 1223–34.

Geisse S, & Fux C. (2009) Recombinant Protein Production by Transient Gene Transfer into Mammalian Cells. *Methods in Enzymology* (Academic Press Inc). 223–38.

Gelfand MV, Hagan N, Tata A, Oh W-J, Lacoste B, Kang K-T, et al. (2014) Neuropilin-1 functions as a VEGFR2 co-receptor to guide developmental angiogenesis independent of ligand binding. *eLife*. 3: 1–18.

Gent J, van Kerkhof P, Roza M, Bu G, & Strous GJ. (2002) Ligand-independent growth hormone receptor dimerization occurs in the endoplasmic reticulum and is required for ubiquitin system-dependent endocytosis. *Proc Natl Acad Sci USA*. 99: 9858–63.

Gerber H-P, McMurtrey A, Kowalski J, Yan M, Keyt BA, Dixit V, et al. (1998) Vascular Endothelial Growth Factor Regulates Endothelial Cell Survival through the Phosphatidylinositol 3'-Kinase / Akt Signal. *J Biol Chem*. 273: 30336–43.

Gerhardt H, Golding M, Fruttiger M, Ruhrberg C, Lundkvist A, Abramsson A, et al. (2003) VEGF guides angiogenic sprouting utilizing endothelial tip cell filopodia. *J Cell Biol*. 161: 1163–77.

Gille H, Kowalski J, Li B, LeCouter J, Moffat B, Zioncheck TF, et al. (2001) Analysis of biological effects and signaling properties of Flt-1 (VEGFR-1) and KDR (VEGFR-2): A reassessment using novel receptor-specific vascular endothelial growth factor mutants. *J Biol Chem*. 276: 3222–30.

Gitay-Goren H, Soker S, Vlodavsky I, & Neufeld G. (1992) The binding of vascular endothelial growth factor to its receptors is dependent on cell surface-associated heparin-like molecules. *J Biol Chem*. 267: 6093–98.

Gkretsi V, & Stylianopoulos T. (2018) Cell adhesion and matrix stiffness: Coordinating cancer cell invasion and metastasis. Front Oncol. 8: 1–7.

Goel HL, & Mercurio AM. (2013) VEGF targets the tumour cell. *Nat Rev Cancer*. 13: 871–82.

Goh LK, & Sorkin A. (2013) Endocytosis of Receptor Tyrosine Kinases. *Cold Spring Harb Perspect Biol*. 5: 1–17.

Goldberg MA, & Schneider TJ. (1994) Similarities between the oxygen-sensing mechanisms regulating the expression of vascular endothelial growth factor and erythropoietin. *J Biol Chem*. 269: 4355–59.

Gorden P, Carpentier JL, Cohen S, & Orci L. (1978) Epidermal growth factor: Morphological demonstration of binding, internalization, and lysosomal association in human fibroblasts. *Proc Natl Acad Sci USA*. 75: 5025–29.

Gordon EJ, Fukuhara D, Weström S, Padhan N, Sjöström EO, van Meeteren L, et al. (2016) The endothelial adaptor molecule TSAd is required for VEGF-induced angiogenic sprouting through junctional c-Src activation. *Sci Signal.* 9: 1–14.

Gotink KJ, & Verheul HMW. (2010) Anti-angiogenic tyrosine kinase inhibitors: What is their mechanism of action? *Angiogenesis*. 13: 1–14.

Gourlaouen M, Welti JC, Vasudev NS, & Reynolds AR. (2013) Essential Role for Endocytosis in the Growth Factor-stimulated Activation of ERK1/2 in Endothelial Cells. *J Biol Chem*. 288: 7467–80.

Gragoudas ES, Adamis AP, Cunningham ET, Feinsod M, & Guyer D. (2005) Pegaptanib for neovascular age-related macular degeneration. *N Engl J Med*. 351: 2805–16.

Graham FL, Smiley J, Russell WC, & Nairn R. (1977) Characteristics of a human cell line transformed by DNA from human adenovirus type 5. *J Gen Virol*. 36: 59–72.

Grant BD, & Donaldson JG. (2009) Pathways and mechanisms of endocytic recycling. *Nat Rev Mol Cell Biol*. 10: 597–608.

Graupera M, & Potente M. (2013) Regulation of angiogenesis by PI3K signaling networks. *Exp Cell Res*. 319: 1348–55.

Gschwind A, Fischer OM, & Ullrich A. (2004) The discovery of receptor tyrosine kinases: targets for cancer therapy. *Nat Rev Cancer*. 4: 361–70.

Gu C, Limberg BJ, Whitaker B, Perman B, Leahy DJ, Rosenbaum JS, et al. (2002) Characterization of neuropilin-1 structural features that confer binding to semaphorin 3A and vascular endothelial growth factor 165. *J Biol Chem*. 277: 18069–76.

Gu C, Rodriguez ER, Reimert DV, Shu T, Fritzsch B, Richards LJ, et al. (2003) Neuropilin-1 conveys semaphorin and VEGF signaling during neural and cardiovascular development. *Dev Cell*. 5: 45–57.

Guo H-F, & Vander Kooi CW. (2015) Neuropilin Functions as an Essential Cell Surface Receptor. *J Biol Chem*. 290: 29120–26.

Guzmán-Hernández ML, Potter G, Egervári K, Kiss JZ, & Balla T. (2014) Secretion of VEGF-165 has unique characteristics, including shedding from the plasma membrane. *Mol Biol Cell*. 25: 1061–72.

Haigler HT, McKanna JA, & Cohen S (1979) Rapid stimulation of pinocytosis in human carcinoma cells A-431 by epidermal growth factor. *J Cell Biol*. 83: 260–65.

Haj FG, Verveer PJ, Squire A, Neel BG, & Bastiaens PIH. (2002) Imaging sites of receptor dephosphorylation by PTP1B on the surface of the endoplasmic reticulum. *Science*. 295: 1708–11.

Hall MP, Unch J, Binkowski BF, Valley MP, Butler BL, Wood MG, et al. (2012) Engineered luciferase reporter from a deep sea shrimp utilizing a novel imidazopyrazinone substrate. *ACS Chem Biol*. 7: 1848–57.

Halpern W, Osol G, & Coy GS. (1984) Mechanical behavior of pressurized in vitro prearteriolar vessels determined with a video system. *Ann Biomed Eng*. 12: 463–79.

Hanahan D, & Folkman J. (1996) Patterns and emerging mechanisms of the angiogenic switch during tumorigenesis. *Cell*. 86: 353–64.

Hanahan D, & Weinberg RA. (2000) The Hallmarks of Cancer. *Cell*. 100: 57–70.

Hanahan D, & Weinberg RA. (2011) Hallmarks of cancer: The next generation. *Cell*. 144: 646–74.

Hanks SK, Quinn AM, & Hunter T (1988) The protein kinase family: Conserved features and deduced phylogeny of the catalytic domains. *Science*. 241: 42–52.

Hanks SK, & Hunter T. (1995) The eukaryotic protein kinase superfamily: Kinase (catalytic) domain structure and classification. *FASEB J*. 9: 576–96.

Harper SJ, & Bates D. (2008) VEGF-A splicing: the key to anti-angiogenic therapeutics? *Nat Rev Cancer*. 8: 880–87.

Hasegawa M, Nishigaki N, Washio Y, Kano K, Harris PA, Sato H, et al. (2007) Discovery of novel benzimidazoles as potent inhibitors of TIE-2 & VEGFR-2 tyrosine kinase receptors. *J Med Chem*. 50: 4453–70.

Hayashi M, Majumdar A, Li X, Adler J, Sun Z, Vertuani S, et al. (2013) VE-PTP regulates VEGFR2 activity in stalk cells to establish endothelial cell polarity and lumen formation. *Nat Commun*. 4: 1–15.

Hayden EC. (2009) Cutting off cancer's supply lines. *Nat Med*. 458: 686–87.

He Z, & Tessier-Lavigne M. (1997) Neuropilin is a receptor for the axonal chemorepellent semaphorin III. *Cell*. 90: 739–51.

Hébert TE, Galés C, & Rebois RV. (2006) Detecting and imaging protein-protein interactions during G protein-mediated signal transduction in vivo and in situ by using fluorescence-based techniques. *Cell Biochem Biophys*. 45: 85–109.

Hernandez I, Bott SW, Patel AS, Wolf CG, Hospodar AR, Sampathkumar S, et al. (2018) Pricing of Monoclonal Antibody Therapies: Higher If Used for Cancer? *Am J Manag Care*. 24: 109–12.

Hertig A. (1935) Angiogenesis in the early human chorion and in the primary placenta of the macaque monkey. *Contrib Embryol*. 25: 79–81.

Hervé MA, Buteau-Lozano H, Mourah S, Calvo F, & Perrot-Applanat M. (2005) VEGF189 stimulates endothelial cells proliferation and migration in vitro and up-regulates the expression of Flk-1/KDR mRNA. *Exp Cell Res*. 309: 24–31.

Herzog B, Pellet-Many C, Britton, G Hartzoulakis B, & Zachary IC. (2011) VEGF binding to NRP1 is essential for VEGF stimulation of endothelial cell migration, complex formation between NRP1 and VEGFR2, and signaling via FAK Tyr407 phosphorylation. *Mol Biol Cell*. 22: 2766–76.

Holash J, Davis S, Papadopoulos N, Croll SD, Ho L, Russell M, et al. (2002) VEGF-Trap: A VEGF blocker with potent antitumor effects. *Proc Natl Acad Sci USA*. 99: 11393–98.

Holmes DI, & Zachary I. (2005) The VEGF family - angiogenic factors in health and disease. *Genome Biol*. 6: 1–10.

Holmqvist K, Cross MJ, Rolny C, Hägerkvist R, Rahimi N, Matsumoto T, et al. (2004) The adaptor protein Shb binds to tyrosine 1175 in vascular endothelial growth factor (VEGF) receptor-2 and regulates VEGF-dependent cellular migration. *J Biol Chem*. 279: 22267–75.

Hornig C, Barleon B, Ahmad S, Vuorela P, Ahmed A, & Weich HA. (2000) Release and Complex Formation of Soluble VEGFR-1 from Endothelial Cells and Biological Fluids. *Lab Investig*. 80: 443–54.

Houck K, Leung DW, Rowland AM, Winer J, & Ferrara N. (1992) Dual regulation of vascular endothelial growth factor bioavailability by genetic and proteolytic mechanisms. *J Biol Chem*. 267: 26031–37.

Hu CD, Chinenov Y, & Kerppola TK. (2002) Visualization of interactions among bZIP and Rel family proteins in living cells using bimolecular fluorescence complementation. *Mol Cell*. 9: 789–98.

Hu CD, & Kerppola TK. (2003) Simultaneous visualization of multiple protein interactions in living cells using multicolor fluorescence complementation analysis. *Nat Biotechnol*. 21: 539–45.

Huang X, Gottstein C, Brekken RA, & Thorpe PE. (1998) Expression of soluble VEGF receptor 2 and characterization of its binding by surface plasmon resonance. *Biochem Biophys Res Commun*. 252: 643–48.

Huang K, Andersson C, Roomans GM, Ito N, & Claesson-Welsh L. (2001) Signaling properties of VEGF receptor-1 and -2 homo- and heterodimers. *Int J Biochem Cell Biol*. 33: 315–24.

Huang X, Zhou G, Wu W, Duan Y, Ma G, Song J, et al. (2017) Genome editing abrogates angiogenesis in vivo. *Nat Commun*. 8: 1–8.

Hueso L, Rios-Navarro C, Ruiz-Sauri A, Chorro FJ, Nunez J, Sanz MJ, et al. (2017) Dynamics and implications of circulating anti-angiogenic VEGF-A_{165}b isoform in patients with ST-elevation myocardial infarction. *Sci Rep.* 7: 1–14.

Huse M, & Kuriyan J. (2002) The conformational plasticity of protein kinases. *Cell*. 109: 275–82.

Hyde CAC, Giese A, Stuttfeld E, Abram Saliba J, Villemagne D, Schleier T, et al. (2012) Targeting extracellular domains D4 & D7 of vascular endothelial growth factor receptor 2 reveals allosteric receptor regulatory sites. *Mol Cell Biol.* 32: 3802–13.

Ilien B, Franchet C, Bernard P, Morisset S, Weill CO, Bourguignon JJ, et al. (2003) Fluorescence resonance energy transfer to probe human M1 muscarinic receptor structure and drug binding properties. *J Neurochem*. 85: 768–78.

Imoukhuede PI, & Popel AS. (2011) Quantification and cell-to-cell variation of vascular endothelial growth factor receptors. *Exp Cell Res*. 317: 955–65.

Ishida A, Murray J, Saito Y, Kanthou C, Benzakour O, Shibuya M, et al. (2001) Expression of vascular endothelial growth factor receptors in smooth muscle cells. *J Cell Physiol*. 188: 359–68.

Itoh M, Nagafuchi A, Yonemura S, Kitani-Yasuda T, Tsukita S, & Tsukita S. (1993) The 220-kD protein colocalizing with cadherins in non-epithelial cells is identical to ZO-1, a tight junction-associated protein in epithelial cells: cDNA cloning and immunoelectron microscopy. *J Cell Biol*. 121: 491–502.

Iyer S, & Acharya KR. (2011) Tying the knot: The cystine signature and molecular-recognition processes of the vascular endothelial growth factor family of angiogenic cytokines. *FEBS J*. 278: 4304–22.

Jaffe EA, Nachman RL, Becker CG, & Minick CR. (1973) Culture of human endothelial cells derived from umbilical veins Identification by morphologic and immunologic criteria. *J Clin Invest*. 52: 2745–56.

Jakobsson L, Franco CA, Bentley K, Collins RT, Ponsioen B, Aspalter IM, et al. (2010) Endothelial cells dynamically compete for the tip cell position during angiogenic sprouting. *Nat Cell Biol*. 12: 943–53.

Jarvis A, Allerston CK, Jia H, Herzog B, Garza-Garcia A, Winfield N, et al. (2010) Small molecule inhibitors of the neuropilin-1 vascular endothelial growth factor A (VEGF-A) interaction. *J Med Chem*. 53: 2215–26.

Jia H, Bagherzadeh A, Hartzoulakis B, Jarvis A, Löhr M, Shaikh S, et al. (2006) Characterization of a bicyclic peptide neuropilin-1 (NP-1) antagonist (EG3287) reveals importance of vascular endothelial growth factor exon 8 for NP-1 binding and role of NP-1 in KDR signalling. *J Biol Chem*. 281: 13493–502.

Jiménez N, Krouwer VJD, & Post JA. (2013) A new, rapid and reproducible method to obtain high quality endothelium in vitro. *Cytotechnology*. 65: 1–14.

Jin ZG, Ueba H, Tanimoto T, Lungu AO, Frame MD, & Berk BC (2003) Ligand Independent Activation of VEGF Receptor 2 by Fluid Shear Stress Regulates Activation of Endothelial Nitric Oxide Synthase. *Circ Res*. 31: 354–63.

Johnson KE, & Wilgus TA. (2014) Vascular Endothelial Growth Factor and Angiogenesis in the Regulation of Cutaneous Wound Repair. *Adv Wound Care*. 3: 647–61.

Jopling HM, Odell AF, Hooper NM, Zachary IC, Walker JH, & Ponnambalam S. (2009) Rab GTPase regulation of VEGFR2 trafficking and signaling in endothelial cells. *Arterioscler Thromb Vasc Biol*. 29: 1119–24.

Jopling HM, Howell GJ, Gamper N, & Ponnambalam S. (2011) The VEGFR2 receptor tyrosine kinase undergoes constitutive endosome-to-plasma membrane recycling. *Biochem Biophys Res Commun*. 410: 170–76.

Jopling HM, Odell AF, Pellet-Many C, Latham AM, Frankel P, Sivaprasadarao A, et al. (2014) Endosome-to-Plasma Membrane Recycling of VEGFR2 Receptor Tyrosine Kinase Regulates Endothelial Function and Blood Vessel Formation. *Cells*. 3: 363–85.

Joukov V, Pajusola K, Kaipainen A, Chilov D, Lahtinen I, Kukk E, et al. (1996) A novel vascular endothelial growth factor, VEGF-C, is a ligand for the Flt4 (VEGFR-3) and KDR (VEGFR-2) receptor tyrosine kinases. *EMBO J*. 15: 290–98.

Jubb AM, Strickland LA, Liu SD, Mak J, Schmidt M, & Koeppen H. (2012) Neuropilin-1 expression in cancer and development. *J Pathol*. 226: 50–60.

Kabrun N, Bühring HJ, Choi K, Ullrich A, Risau W, & Keller G. (1997) Flk-1 expression defines a population of early embryonic hematopoietic precursors. *Development*. 124: 2039–48.

Kadonosono T, Yamano A, Goto T, Tsubaki T, Niibori M, Kuchimaru T, et al. (2015) Cell penetrating peptides improve tumor delivery of cargos through neuropilin-1-dependent extravasation. *J Control Release*. 201: 14–21.

Kamba T, & McDonald DM. (2007) Mechanisms of adverse effects of anti-VEGF therapy for cancer. *Br J Cancer*. 96: 1788–95.

Kang Z, Zhu H, Jiang W, & Zhang S. (2013) Protocatechuic Acid Induces Angiogenesis through PI3K-Akt-eNOS-VEGF Signalling Pathway. *Basic Clin Pharmacol Toxicol*. 113: 221–27.

Katoh M. (2013) Functional proteomics, human genetics and cancer biology of GIPC family members. *Exp Mol Med.* 45: 1–9.

Kawamura H, Li X, Goishi K, van Meeteren LA, Jakobsson L, Cébe-Suarez S, et al. (2008a) Neuropilin-1 in regulation of VEGF-induced activation of p38MAPK and endothelial cell organization. *Blood*. 112: 3638–49.

Kawamura H, Li X, Harper SJ, Bates D, & Claesson-Welsh, L. (2008b) Vascular Endothelial Growth Factor (VEGF)-A_{165}b Is A Weak In vitro Agonist for VEGF Receptor-2 Due to Lack of Coreceptor Binding and Deficient Regulation of Kinase Activity. *Cancer Res*. 68: 4683–92.

Kawasaki T, Kitsukawa T, Bekku Y, Matsuda Y, Sanbo M, Yagi T, et al. (1999) A requirement for neuropilin-1 in embryonic vessel formation. *Development*. 126: 4895–902.

Kelly KL, & Ruderman NB. (1993) Insulin-stimulated phosphatidylinositol 3-kinase Association with a 185- kDa tyrosine-phosphorylated protein (IRS-1) and localization in a low density membrane vesicle. *J Biol Chem*. 268: 4391–98.

Kenakin T. (2013) New concepts in pharmacological efficacy at 7TM receptors. *Br J Pharmacol*. 168: 554–75.

Kenakin TP. (2014*) A Pharmacology Primer: Techniques for More Effective and Strategic Drug Discovery*. 4th edition. Elsevier Inc.

Kenakin, T. (2016) The mass action equation in pharmacology. *Br J Clin Pharmacol*. 81: 41–51.

Kendall RL, & Thomas KA. (1993) Inhibition of vascular endothelial cell growth factor activity by an endogenously encoded soluble receptor. *Proc Natl Acad Sci USA*. 90: 10705–09.

Keppler A, Gendreizig S, Gronemeyer T, Pick H, Vogel H, & Johnsson K. (2003) A general method for the covalent labeling of fusion proteins with small molecules in vivo. *Nat Biotechnol*. 21: 86–89.

Keppler A, Pick H, Arrivoli C, Vogel H, & Johnsson K. (2004) Labeling of fusion proteins with synthetic fluorophores in live cells. *Proc Natl Acad Sci USA*. 101: 9955–59.

Kerr MC, & Teasdale RD. (2009) Defining macropinocytosis. *Traffic*. 10: 364–71.

Keyt BA, & Berleau LT. (1996) The Carboxyl-terminal Domain(111-165) of Vascular Endothelial Growth Factor Is Critical for Its Mitogenic Potency. *J Biol Chem*. 271: 7788–95.

Kieran MW, Kalluri R, & Cho Y-J. (2012) The VEGF pathway in cancer and disease: responses, resistance, and the path forward. *Cold Spring Harb Perspect Med*. 2: 1–17.

Kilpatrick LE, Friedman Ohana R, Alcobia DC, Riching K, Peach CJ, Wheal AJ, et al. (2017) Real-time analysis of the binding of fluorescent $VEGF_{165}$a to VEGFR2 in living cells: Effect of receptor tyrosine kinase inhibitors and fate of internalized agonist-receptor complexes. *Biochem Pharmacol*. 136: 62–75.

Kilpatrick LE, Alcobia DC, White CW, Peach CJ, Glenn JR, Zimmerman K, et al. (2019) Complex Formation between VEGFR2 and the β2-Adrenoceptor. *Cell Chem Biol*. 26: 830–41.

Kim KJ, Li B, Houck K, Winer J, & Ferrara N. (1992) The Vascular Endothelial Growth Factor Proteins: Identification of Biologically Relevant Regions by Neutralizing Monoclonal Antibodies. *Growth Factors*. 7: 53–64.

King C, Wirth D, Workman S, & Hristova K. (2018) Interactions between NRP1 and VEGFR2 molecules in the plasma membrane. *Biochim Biophys Acta Biomembr*. 1860: 2118–25.

Kirkbride KC, Ray BN, & Blobe GC. (2005) Cell-surface co-receptors: Emerging roles in signaling and human disease. *Trends Biochem Sci*. 30: 611–21.

Kisko K, Brozzo MS, Missimer J, Schleier T, Menzel A, Leppänen V-M, et al. (2011) Structural analysis of vascular endothelial growth factor receptor-2/ligand complexes by small-angle X-ray solution scattering. *FASEB J*. 25: 2980–86.

Kitsukawa T, Shimono A, Kawakami A, Kondoh H, & Fujisawa H. (1995) Overexpression of a membrane protein, neuropilin, in chimeric mice causes anomalies in the cardiovascular system, nervous system and limbs. *Development*. 121: 4309–18.

Kobayashi T, Gu F, & Gruenberg J. (1998) Lipids, lipid domains and lipid-protein interactions in endocytic membrane traffic. *Semin Cell Dev Biol*. 9: 517–26.

Koch S, Tugues S, Li X, Gualandi L, & Claesson-Welsh L. (2011) Signal transduction by vascular endothelial growth factor receptors. *Biochem J*. 437: 169–83.

Koch S, van Meeteren LA, Morin E, Testini C, Weström S, Björkelund H, et al. (2014) NRP1 Presented in trans to the endothelium arrests VEGFR2 endocytosis, preventing angiogenic signaling and tumor initiation. *Dev Cell*. 28: 633–46.

Kozak M. (1987) At least six nucleotides preceding the AUG initiator codon enhance translation in mammalian cells. *J Mol Biol*. 196: 947–50.

Krilleke D, DeErkenez A, Schubert W, Giri I, Robinson GS, Ng YS, et al. (2007) Molecular mapping and functional characterization of the VEGF164 heparin-binding domain. *J Biol Chem*. 282: 28045–56.

Kublaoui B, Lee J, & Pilch PF. (1995) Dynamics of signaling during insulin-stimulated endocytosis of its receptor in adipocytes. *J Biol Chem*. 270: 59–65.

Kusumi A, & Sako Y. (1996) Cell surface organization by the membrane skeleton. *Curr Opin Cell Biol*. 8: 566–74.

Kvanta A, Algvere PV, Berglin L, & Seregard S. (1996) Subfoveal fibrovascular membranes in age-related macular degeneration express vascular endothelial growth factor. *Investig Ophthalmol Vis Sci*. 37: 1929–34.

Labrecque L, Royal I, Surprenant DS, Patterson C, Gingras D, & Beliveau R. (2003) Regulation of VEGFR2 activity by caveolin-1 and plasma membrane cholesterol. *Mol Biol Cell*. 14: 334–47.

Lai T, Vlahos N, Shih I, & Zhao Y (2014) Expression patterns of VEGF and Flk-1 in human endometrium at the various phases of the natural menstrual cycle. *Hum Reprod*. 16: 3–9.

Lakowicz JR. (2006) *Principles of fluorescence spectroscopy*. 3rd edition. New York: Springer.

Lamalice L, Houle F, Jourdan G, & Huot J. (2004) Phosphorylation of tyrosine 1214 on VEGFR2 is required for VEGF-induced activation of Cdc42 upstream of SAPK2/p38. *Oncogene*. 23: 434–45.

Lamalice L, Houle F, & Huot J. (2006) Phosphorylation of Tyr1214 within VEGFR-2 triggers the recruitment of Nck and activation of Fyn leading to SAPK2/p38 activation and endothelial cell migration in response to VEGF. *J Biol Chem*. 281: 34009–20.

Lampugnani MG, Orsenigo F, Gagliani MC, Tacchetti C, & Dejana E. (2006) Vascular endothelial cadherin controls VEGFR-2 internalization and signaling from intracellular compartments. *J Cell Biol*. 174: 593–604.

Lanahan AA, Hermans K, Claes F, Kerley-Hamilton JS, Zhuang ZW, Giordano FJ, et al. (2010) VEGF receptor 2 endocytic trafficking regulates arterial morphogenesis. *Dev Cell*. 18: 713–24.

Lanahan A, Zhang X, Fantin A, Zhuang Z, Rivera-Molina F, Speichinger K, et al. (2013) The neuropilin 1 cytoplasmic domain is required for VEGF-A-dependent arteriogenesis. *Dev Cell*. 25: 156–68.

Lanahan AA, Lech D, Dubrac A, Zhang J, Zhuang ZW, Eichmann A, et al. (2014) PTP1b is a physiologic regulator of vascular endothelial growth factor signaling in endothelial cells. *Circulation*. 130: 902–09.

Langley JN. (1905) On the reaction of cells and of nerve-endings to certain poisons, chiefly as regards the reaction of striated muscle to nicotine and to curare. *J Physiol*. 33: 374–413.

Lawton PF, Lee MD, Saunter CD, Girkin JM, McCarron JG, & Wilson C. (2019) VasoTracker, a Low-Cost and Open Source Pressure Myograph System for Vascular Physiology. Front Physiol. 10: 1–17.

Lee P, Goishi K, Davidson AJ, Mannix R, Zon L, & Klagsbrun M. (2002) Neuropilin-1 is required for vascular development and is a mediator of VEGF-dependent angiogenesis in zebrafish. *Proc Natl Acad Sci USA*. 99: 10470–75.

Lee CC, Kreusch A, McMullan D, Ng K, & Spraggon G. (2003) Crystal structure of the human neuropilin-1 b1 domain. *Structure*. 11: 99–108.

Lee MY, Luciano, AK, Ackah E, Rodriguez-Vita J, Bancroft T, Eichmann A, et al. (2014a) Endothelial Akt1 mediates angiogenesis by phosphorylating multiple angiogenic substrates. *Proc Natl Acad Sci USA*. 111: 12865–70.

Lee SW, Lee JE, Yoo CY, Ko MS, Park CS, & Yang SH. (2014b) NRP-1 expression is strongly associated with the progression of pituitary adenomas. *Oncol Rep*. 32: 1537–42.

Lee-Montiel FT, Li P, & Imoukhuede PI. (2015) Quantum dot multiplexing for the profiling of cellular receptors. *Nanoscale*. 18504–14.

Lemmon MA, & Schlessinger J. (2010) Cell signaling by receptor tyrosine kinases. *Cell*. 141: 1117–34.

Leppanen VM, Prota AE, Jeltsch M, Anisimov A, Kalkkinen N, Strandin T, et al. (2010) Structural determinants of growth factor binding & specificity by VEGF receptor 2. *Proc Natl Acad Sci USA*. 107: 2425–30.

Leung D, Cachianes G, Kuang W, Goeddel D, & Ferrara N. (1989) Vascular endothelial growth factor is a secreted angiogenic mitogen. *Science*. 246: 1306–09.

Li X, Padhan N, Sjöström EO, Roche FP, Testini C, Honkura N, et al. (2016) VEGFR2 pY949 signalling regulates adherens junction integrity and metastatic spread. *Nat Commun*. 7: 1–16.

Liang WC, Dennis MS, Stawicki S, Chanthery Y, Pan Q, Chen Y, et al. (2007) Function Blocking Antibodies to Neuropilin-1 Generated from a Designed Human Synthetic Antibody Phage Library. *J Mol Biol*. 366: 815–29.

Lim JI, Spee C, Hangai M, Rocha J, Ying HS, Ryan SJ, et al. (2005) Neuropilin-1 expression by endothelial cells and retinal pigment epithelial cells in choroidal neovascular membranes. *Am J Ophthalmol*. 140: 1044–50.

Liu Y, Cox SR, Morita T, & Kourembanas S. (1995) Hypoxia regulates vascular endothelial growth factor gene expression in endothelial cells: Identification of a 5' enhancer. *Circ Res*. 77: 638–43.

Loenen WAM, Dryden DTF, Raleigh EA, Wilson GG, & Murray NE. (2014) Highlights of the DNA cutters: A short history of the restriction enzymes. *Nucleic Acids Res*. 42: 3–19.

Lohse MJ, Nuber S, & Hoffmann C. (2012) Fluorescence / Bioluminescence Resonance Energy Transfer Techniques to Study G-Protein-Coupled Receptor Activation and Signaling. *Pharmacol Rev*. 64: 299–336.

Looyenga B, VanOpstall C, Lee Z, Bell J, Lodge E, Wrobel K, et al. (2016) Determination of GLUT1 Oligomerization Parameters using Bioluminescent Förster Resonance Energy Transfer. *Sci Rep*. 6: 1–14.

Los GV, Encell LP, McDougall MG, Hartzell DD, Karassina N, Simpson D, et al. (2008) HaloTag: A Novel Protein Labeling Technology for Cell Imaging and Protein Analysis. *ACS Chem Biol*. 3: 373–82.

Lu D, Shen J, Vil MD, Zhang H, Jimenez X, Bohlen P, et al. (2003) Tailoring in Vitro Selection for a Picomolar Affinity Human Antibody Directed against Vascular Endothelial Growth Factor Receptor 2 for Enhanced Neutralizing Activity. *J Biol Chem*. 278: 43496–507.

Mac Gabhann F, & Popel AS. (2007) Dimerization of VEGF receptors and implications for signal transduction: A computational study. *Biophys Chem*. 128: 125–39.

Machleidt T, Woodroofe CC, Schwinn MK, Méndez J, Robers MB, Zimmerman K, et al. (2015) NanoBRET - A Novel BRET Platform for the Analysis of Protein-Protein Interactions. *ACS Chem Biol*. 10: 1797–804.

Macián F, López-Rodríguez C, & Rao A. (2001) Partners in transcription: NFAT and AP-1. *Oncogene*. 20: 2476–89.

Maehle AH, Prull CR, & Halliwell RF. (2002) The emergence of the drug receptor theory. *Nat Rev Drug Discov*. 1: 637–41.

Magliery TJ, Wilson CGM, Pan W, Mishler D, Ghosh I, Hamilton AD, et al. (2005) Detecting protein-protein interactions with a green fluorescent protein fragment reassembly trap: Scope and mechanism. *J Am Chem Soc*. 127: 146–57.

Maglione D, Guerriero V, Viglietto G, Grazia Ferraro M, Aprelikova O, Alitalo K, et al. (1993) Two alternative mRNAs coding for the angiogenic factor, placenta growth factor (PlGF), are transcribed from a single gene of chromosome 14. *Oncogene*. 8: 925–31.

Makrides SC. (1999) Components of vectors for gene transfer and expression in mammalian cells. *Protein Expr Purif*. 17: 183–202.

Mamluk R, Gechtman Z, Kutcher ME, Gasiunas N, Gallagher J, & Klagsbrun M. (2002) Neuropilin-1 binds vascular endothelial growth factor 165, placenta growth factor-2, and heparin via its b1b2 domain. *J Biol Chem*. 277: 24818–25.

Manders EMM, Stap J, Brakenhoff GJ, Van Driel, R, & Aten JA. (1992) Dynamics of three-dimensional replication patterns during the S-phase, analysed by double labelling of DNA and confocal microscopy. *J Cell Sci*. 103: 857–62.

Manders EMM, Verbeek FJ, & Aten JA. (1993) Measurement of co-localization of objects in dual-colour confocal images. *J Microsc*. 169: 375–82.

Manni S, Kisko K, Schleier T, Missimer J, & Ballmer-Hofer K. (2014a) Functional & structural characterization of the kinase insert and the carboxy terminal domain in VEGF receptor 2 activation. *FASEB J*. 28: 4914–23.

Manni S, Mineev KS, Usmanova D, Lyukmanova EN, Shulepko MA, Kirpichnikov MP, et al. (2014b) Structural and functional characterization of alternative transmembrane domain conformations in VEGF receptor 2 activation. *Structure*. 22: 1077–89.

Manning G, Whyte DB, Martinez R, Hunter T, & Sudarsanam S. (2002) The protein kinase complement of the human genome. Science 298: 1912–34.

Markovic-Mueller S, Stuttfeld E, Asthana M, Weinert T, Bliven S, Goldie KN, et al. (2017) Structure of the Full-length VEGFR-1 Extracellular Domain in Complex with VEGF-A. *Structure*. 25: 341–352.

Marmor MD, & Yarden Y. (2004) Role of protein ubiquitylation in regulating endocytosis of receptor tyrosine kinases. *Oncogene*. 23: 2057–70.

Maruyama I. (2014) Mechanisms of Activation of Receptor Tyrosine Kinases: Monomers or Dimers. *Cells*. 3: 304–30.

Matsumoto T, Bohman S, Dixelius J, Berge T, Dimberg A, Magnusson P, et al. (2005) VEGF receptor-2 Y951 signaling and a role for the adapter molecule TSAd in tumor angiogenesis. *EMBO J*. 24: 2342–53.

Matsumoto K, & Ema M. (2014) Roles of VEGF-A signalling in development, regeneration, and tumours. *J Biochem*. 156: 1–10.

Mattila E, Auvinen K, Salmi M, & Ivaska J. (2008) The protein tyrosine phosphatase TCPTP controls VEGFR2 signalling. *J Cell Sci*. 121: 3570–80.

Maxfield FR, & Yamashiro DJ (1987) Endosome acidification and the pathways of receptor-mediated endocytosis. *Adv Exp Med Biol*. 225: 189–98.

McMullen ME, Bryant PW, Glembotski CC, Vincent PA, & Pumiglia KM. (2005) Activation of p38 has opposing effects on the proliferation and migration of endothelial cells. *J Biol Chem*. 280: 20995–1003.

McTigue M, Murray BW, Chen JH, Deng YL, Solowiej J, & Kania RS. (2012) Molecular conformations, interactions, and properties associated with drug efficiency and clinical performance among VEGFR TK inhibitors. *Proc Natl Acad Sci USA*. 109: 18281–89.

McVey M, Ramsay D, Kellett E, Rees S, Wilson S, Pope AJ, et al. (2001) Monitoring receptor oligomerization using time-resolved fluorescence resonance energy transfer and bioluminescence resonance energy transfer. *J Biol Chem*. 276: 14092–99.

Melamed E, Lahav M, & Atlas D. (1976) Beta-adrenergic receptors in rat myocardium: Direct detection by a new fluorescent beta-blocker. *Experientia*. 32: 1387–89.

Mellberg S, Dimberg A, Bahram F, Hayashi M, Rennel E, Ameur A, et al. (2009) Transcriptional profiling reveals a critical role for tyrosine phosphatase VE-PTP in regulation of VEGFR2 activity and endothelial cell morphogenesis. *FASEB J*. 23: 1490–1502.

Meyer RD, Mohammadi M, & Rahimi N. (2006) A single amino acid substitution in the activation loop defines the decoy characteristic of VEGFR-1/FLT-1. *J Biol Chem*. 281: 867–75.

Miao HQ, Hu K, Jimenez X, Navarro E, Zhang H, Lu D, et al. (2006) Potent neutralization of VEGF biological activities with a fully human antibody Fab fragment directed against VEGF receptor 2. *Biochem Biophys Res Commun*. 345: 438–45.

Miller JW, Adamis AP, Shima DT, D'Amore PA, Moulton RS, O'Reilly MS, et al. (1994) Vascular endothelial growth factor/vascular permeability factor is temporally and spatially correlated with ocular angiogenesis in a primate model. *Am J Pathol*. 145: 574–84.

Miller JW, Le Couter J, Strauss EC, & Ferrara N. (2013) Vascular Endothelial Growth Factor A in Intraocular Vascular Disease. *Ophthalmology*. 120: 106–14.

Milligan G. (2001) Oligomerisation of G-protein-coupled receptors. *J Cell Sci*. 114: 1265–71.

Mineur P, Colige AC, Deroanne CF, Dubail J, Kesteloot F, Habraken Y, et al. (2007) Newly identified biologically active and proteolysis-resistant VEGF-A isoform VEGF111 is induced by genotoxic agents. *J Cell Biol*. 179: 1261–73.

Mitola S, Ravelli C, Moroni E, Salvi V, Leali D, Ballmer-Hofer K, et al. (2010) Gremlin is a novel agonist of the major proangiogenic receptor VEGFR2. *Blood*. 116: 3677–80.

Moens S, Goveia J, Stapor PC, Cantelmo AR, & Carmeliet P. (2014) The multifaceted activity of VEGF in angiogenesis - Implications for therapy responses. *Cytokine Growth Factor Rev*. 25: 473–82.

Monje P, Hernández-Losa J, Lyons RJ, Castellone MD, & Gutkind JS. (2005) Regulation of the transcriptional activity of c-Fos by ERK: A novel role for the prolyl isomerase Pin1. *J Biol Chem*. 280: 35081–84.

Mota F, Fotinou C, Rhana R, Chan AWE, Yelland T, Arooz MT, et al. (2018) Architecture & Hydration of the Arginine Binding Site of Neuropilin-1. *FEBS J*. 285: 1290–1304.

Muhl L, Folestad EB, Gladh H, Wang Y, Moessinger C, Jakobsson L, et al. (2017) Neuropilin 1 binds platelet-derived growth factor (PDGF)-D and is a co-receptor in PDGF-D/PDGF receptor β signalling. *J Cell Sci*. 130: 1364–78.

Mukherjee S, Ghosh RN, & Maxfield FR. (1997) Endocytosis. *Physiol Rev*. 77: 759–803.

Muller YA, Li B, Christinger HW, Wells JA, Cunningham BC, & de Vos AM. (1997) Vascular endothelial growth factor: crystal structure and functional mapping of the kinase domain receptor binding site. *Proc Natl Acad Sci USA*. 94: 7192–97.

Muller YA, Heiring C, Misselwitz R, Welfle K, & Welfle H. (2002) The cystine knot promotes folding and not thermodynamic stability in vascular endothelial growth factor. J Biol Chem. 277: 43410–16.

Mulligan LM. (2014) RET revisited: expanding the oncogenic portfolio. *Nat Rev Cancer*. 14: 173–86.

Mullis KB. (1990) The unusual origin of the polymerase chain reaction. *Sci Am*. 262: 56–65.

Murphy JE, Padilla BE, Hasdemir B, Cottrell GS, & Bunnett NW. (2009) Endosomes: a legitimate platform for the signaling train. *Proc Natl Acad Sci USA*. 106: 17615–22.

Nabi IR, & Le PU. (2003) Caveolae/raft-dependent endocytosis. *J Cell Biol*. 161: 673–77.

Naccache S, Hasson T, & Horowitz A. (2006) Binding of internalized receptors to the PDZ domain of GIPC/synectin recruits myosin VI to endocytic vesicles. *Proc Natl Acad Sci USA*. 103: 12735–40.

Nakamura F, Tanaka M, Takahashi T, Kalb RG, & Strittmatter SM. (1998) Neuropilin-1 extracellular domains mediate semaphorin D/III-induced growth cone collapse. *Neuron*. 21: 1093–100.

Nakayama M, Nakayama A, van Lessen M, Yamamoto H, Hoffmann S, Drexler HCA, et al. (2013) Spatial regulation of VEGF receptor endocytosis in angiogenesis. *Nat Cell Biol*. 15: 249–60.

Namiki A, Brogi E, Kearney M, Kim EA, Wu T, Couffinhal T, et al. (1995) Hypoxia induces vascular endothelial growth factor in cultured human endothelial cells. *J Biol Chem*. 270: 31189–95.

Narayanan R, Kuppermann BD, Jones C, & Kirkpatrick P. (2006) Ranibizumab. *Nat Rev Drug Discov*. 5: 815–16.

Narazaki M, & Tosato G. (2006) Ligand-induced internalization selects use of common receptor neuropilin-1 by VEGF165 and semaphorin3A. *Blood*. 107: 3892–901.

Nasarre C, Roth M, Jacob L, Roth L, Koncina E, Thien A, et al. (2010) Peptide-based interference of the transmembrane domain of neuropilin-1 inhibits glioma growth in vivo. *Oncogene*. 29: 2381–92.

Needham SR, Roberts SK, Arkhipov A, Mysore VP, Tynan CJ, Zanetti-Domingues LC, et al. (2016) EGFR oligomerization organizes kinase-active dimers into competent signalling platforms. *Nat Commun*. 7: 1–14.

Neubig RR, Spedding M, Kenakin T, & Christopoulos A. (2003) International Union of Pharmacology Committee on Receptor Nomenclature and Drug Classification. XXXVIII Update on terms and symbols in quantitative pharmacology. *Pharmacol Rev*. 55: 597–606.

Niedel JE, Kahane I, & Cuatrecasas P. (1979) Receptor-mediated internalization of fluorescent chemotactic peptide by human neutrophils. *Science*. 205: 1412–14.

Nieminen T, Toivanen PI, Rintanen N, Heikura T, Jauhiainen S, Airenne KJ, et al. (2014) The impact of the receptor binding profiles of the vascular endothelial growth factors on their angiogenic features. *Biochim Biophys Acta*. 1840: 454–63.

Nilsson I, Bahram F, Li X, Gualandi L, Koch S, Jarvius M, et al. (2010) VEGF receptor 2/-3 heterodimers detected in situ by proximity ligation on angiogenic sprouts. *EMBO J*. 29: 1377–88.

Nissen NN, Polverini PJ, Koch AE, Volin MV, Gamelli RL, & DiPietro LA. (1998) Vascular endothelial growth factor mediates angiogenic activity during the proliferative phase of wound healing. *Am J Pathol*. 152: 1445–52.

Nowak DG, Woolard J, Amin EM, Konopatskaya O, Saleem MA, Churchill AJ, et al. (2008) Expression of pro- and anti-angiogenic isoforms of VEGF is differentially regulated by splicing and growth factors. *J Cell Sci*. 121: 3487–3495.

Ogawa S, Oku A, Sawano A, Yamaguchi S, Yazaki Y, & Shibuya M. (1998) A novel type of vascular endothelial growth factor, VEGF-E (NZ-7 VEGF). *J Biol Chem*. 273: 31273–82.

Oh P, McIntosh DP, & Schnitzer JE. (1998) Dynamin at the neck of caveolae mediates their budding to form transport vesicles by GTP-driven fission from the plasma membrane of endothelium. *J Cell Biol*. 141: 101–14.

Oladipupo SS, Kabir AU, Smith C, Choi K, & Ornitz DM (2018) Impaired tumor growth and angiogenesis in mice heterozygous for Vegfr2 (Flk1). *Sci Rep*. 8: 1–10.

Olofsson B, Pajusola K, Kaipainen A, von Euler G, Joukov V, Saksela O, et al. (1996) Vascular endothelial growth factor B, a novel growth factor for endothelial cells. *Proc Natl Acad Sci USA*. 93: 2576–81.

Olsson A-K, Dimberg A, Kreuger J, & Claesson-Welsh L. (2006) VEGF receptor signalling - in control of vascular function. *Nat Rev Mol Cell Biol*. 7: 359–71.

Oltean S, Gammons M, Hulse R, Hamdollah-Zadeh M, Mavrou A, Donaldson L, et al. (2012) SRPK1 inhibition in vivo: modulation of VEGF splicing and potential treatment for multiple diseases. *Biochem Soc Trans*. 40: 831–35.

Ourradi K, Blythe T, Jarrett C, Barratt SL, Welsh GI, & Millar AB. (2017) VEGF isoforms have differential effects on permeability of human pulmonary microvascular endothelial cells. *Respir Res*. 18: 1–12.

Pagès G, & Pouysségur J. (2005) Transcriptional regulation of the Vascular Endothelial Growth Factor gene - A concert of activating factors. *Cardiovasc Res*. 65: 564–73.

Pallet N, Thervet E, & Timsit MO. (2014) Angiogenic response following renal ischemia reperfusion injury: New players. *Prog En Urol*. 24: 20–25.

Pan Q, Chathery Y, Wu Y, Rathore N, Tong RK, Peale F, et al. (2007) Neuropilin-1 binds to VEGF121 and regulates endothelial cell migration and sprouting. *J Biol Chem*. 282: 24049–56.

Pang H-B, Braun GB, Friman T, Aza-Blanc P, Ruidiaz ME, Sugahara KN, et al. (2014) An endocytosis pathway initiated through neuropilin-1 and regulated by nutrient availability. *Nat Commun*. 5: 1–12.

Pang H-B, Braun GB, & Ruoslahti E. (2015) Neuropilin-1 and heparan sulfate proteoglycans cooperate in cellular uptake of nanoparticles functionalized by cationic cell-penetrating peptides. *Sci Adv*. 1: 1–7.

Pang V, Bates DO, & Leach L. (2017) Regulation of human feto-placental endothelial barrier integrity by vascular endothelial growth factors: Competitive interplay between VEGF-A_{165}a, VEGF-A_{165}b, PIGF and VE-cadherin. *Clin Sci.* 131: 2763–75.

Parascandola J. (1982) AJ Clark: quantitative pharmaocology and the receptor theory. *Trends Pharmacol Sci*. 41: 421–23.

Parker MW, Xu P, Li X, & Vander Kooi CW. (2012) Structural basis for selective vascular endothelial growth factor-A (VEGF-A) binding to neuropilin-1. *J Biol Chem*. 287: 11082–89.

Patnaik A, LoRusso PM, Messersmith WA, Papadopoulos KP, Gore L, Beeram M, et al. (2014) A Phase Ib study evaluating MNRP1685A, a fully human anti-NRP1 monoclonal antibody, in combination with bevacizumab and paclitaxel in patients with advanced solid tumors. *Cancer Chemother Pharmacol*. 73: 951–60.

Patz A. (1984) Retinal neovascularization: Early contributions of Professor Michaelson and recent observations. *Br J Ophthalmol*. 68: 42–46.

Paulmurugan R, Massoud TF, Huang J, & Gambhir SS. (2004) Molecular Imaging of Drug-Modulated Protein-Protein Interactions in Living Subjects. *Cancer Res*. 64: 2113–19.

Peach CJ, Kilpatrick LE, Friedman Ohana R, Zimmerman K, Robers MB, Wood KV, et al. (2018a) Real-Time Ligand Binding of Fluorescent VEGF-A Isoforms that Discriminate between VEGFR2 and NRP1 in Living Cells. *Cell Chem Biol*. 25: 1208–18.

Peach CJ, Mignone VW, Arruda MA, Hill SJ, Kilpatrick LE, & Woolard J. (2018b) Molecular Pharmacology of VEGF-A Isoforms: Binding and Signalling at VEGFR2. *Int J Mol Sci.* 19: 1–27.

Peach CJ, Kilpatrick LE, Woolard J, & Hill SJ. (2019) Comparison of the ligand binding properties of fluorescent VEGF-A isoforms to VEGFR2 in living cells and membrane preparations using NanoBRET. *Br J Pharmacol*. 176: 3220–35.

Pear WS, Nolan GP, Scott ML, & Baltimore D. (1993) Production of high-titer helper-free retroviruses by transient transfection. *Proc Natl Acad Sci USA*. 90: 8392–96.

Pearse BMF. (1976) Clathrin: A unique protein associated with intracellular transfer of membrane by coated vesicles. *Proc Natl Acad Sci USA*. 73: 1255–59.

Pearse BM, & Robinson MS. (1984) Purification and properties of 100-kd proteins from coated vesicles and their reconstitution with clathrin. *EMBO J*. 3: 1951–57.

Pellet-Many C, Frankel P, Jia H, & Zachary I. (2008) Neuropilins: structure, function and role in disease. *Biochem J*. 411: 211–26.

Peretz D, Gitay-Goren H, Safran M, Kimmel N, Gospodarowicz D, & Neufeld G. (1992) Glycosylation of Vascular Endothelial Growth Factor is not required for mitogenic activity. *Biochem Biophys Res Commun*. 182: 1340–47.

Pfleger KDG, & Eidne KA. (2006) Illuminating insights into protein-protein interactions using bioluminescence resonance energy transfer (BRET). *Nat Methods*. 3: 165–74.

Pingoud A, Fuxreiter M, Pingoud V, & Wende W. (2005) Type II restriction endonucleases: Structure and mechanism. *Cell Mol Life Sci*. 62: 685–707.

Pinskey JM, Franks NE, McMellen AN, Giger RJ, & Allen BL. (2017) Neuropilin-1 promotes Hedgehog signaling through a novel cytoplasmic motif. *J Biol Chem*. 297: 15192-204.

Plate KH, Breier G, Weich HA, & Risau W. (1992) Vascular endothelial growth factor is a potential tumour angiogenesis factor in human gliomas in vivo. *Nature*. 359: 845–48.

Pollard TD, & De La Cruz EM. (2013) Take advantage of time in your experiments: A guide to simple, informative kinetics assays. *Mol Biol Cell*. 24: 1103–10.

Polte TR, & Hanks SK. (1995) Interaction between focal adhesion kinase and Crk-associated tyrosine kinase substrate p130Cas. *Proc Natl Acad Sci USA*. 92: 10678–82.

Poltorak Z, Cohen T, Sivan R, Kandelis Y, Spira G, Vlodavsky I, et al. (1997) VEGF 145 , a Secreted Vascular Endothelial Growth Factor Isoform That Binds to Extracellular Matrix. *J Biol Chem*. 272: 7151–58.

Poole TJ, & Coffin JD. (1989) Vasculogenesis and angiogenesis: Two distinct morphogenetic mechanisms establish embryonic vascular pattern. *J Exp Zool*. 251: 224–31.

Potente M, Gerhardt H, & Carmeliet P. (2011) Basic and therapeutic aspects of angiogenesis. *Cell*. 146: 873–87.

Potente M, & Mäkinen T. (2017) Vascular heterogeneity and specialization in development and disease. *Nat Rev Mol Cell Biol*. 18: 477–94.

Power RM, & Huisken J. (2017) A guide to light-sheet fluorescence microscopy for multiscale imaging. *Nat Methods*. 14: 360–73.

Praefcke GJK, & McMahon HT. (2004) The dynamin superfamily: Universal membrane tubulation and fission molecules? *Nat Rev Mol Cell Biol*. 5: 133–147.

Prahst C, Héroult M, Lanahan AA, Uziel N, Kessler O, Shraga-Heled N, et al. (2008) Neuropilin-1-VEGFR-2 complexing requires the PDZ-binding domain of neuropilin-1. *J Biol Chem*. 283: 25110–14.

Presta LG, Chen H, O'Connor SJ, Chisholm V, Meng YG, Krummen L, et al. (1997) Humanization of an anti-vascular endothelial growth factor monoclonal antibody for the therapy of solid tumors and other disorders. *Cancer Res*. 57: 4593–99.

Pritchard-Jones RO, Dunn DBA, Qiu Y, Varey AHR, Orlando A, Rigby H, et al. (2007) Expression of $VEGF_{xxx}b$, the inhibitory isoforms of VEGF, in malignant melanoma. *Br J Cancer*. 97: 223–30.

Qiu Y, Bevan H, Weeraperuma S, Wratting D, Murphy D, Neal CR, Bates DO, Harper SJ (2008) Mammary alveolar development during lactation is inhibited by the endogenous antiangiogenic growth factor isoform, $VEGF_{165}b$. *FASEB J*. 22: 1104–12.

Rahimi N, Dayanir V, & Lashkari K. (2000) Receptor chimeras indicate that the vascular endothelial growth factor receptor-1 (VEGFR-1) modulates mitogenic activity of VEGFR-2 in endothelial cells. *J Biol Chem*. 275: 16986–92.

Rask-Andersen M, Masuram S, & Schiöth HB. (2014) The Druggable Genome: Evaluation of Drug Targets in Clinical Trials Suggests Major Shifts in Molecular Class and Indication. *Annu Rev Pharmacol Toxicol*. 54: 9–26.

Reed B, Cefalu C, Bellaire B, Cardelli J, Louis T, Salamon J, et al. (2005) GLUT1CBP(TIP2/GIPC1) Interactions with GLUT1 and Myosin VI: Evidence Supporting an Adapter Function for GLUT1CBP. *Mol Biol Cell*. 16: 4183–201.

Rennel E, Waine E, Guan H, Schüler Y, Leenders W, Woolard J, et al. (2008) The endogenous anti-angiogenic VEGF isoform, $VEGF_{165}$b inhibits human tumour growth in mice. *Br J Cancer*. 98: 1250–57.

Rink J, Ghigo E, Kalaidzidis Y, & Zerial M. (2005) Rab conversion as a mechanism of progression from early to late endosomes. *Cell*. 122: 735–49.

Risau W, & Lemmon V. (1988) Changes in the vascular extracellular matrix during embryonic vasculogenesis and angiogenesis. *Dev Biol*. 125: 441–50.

Rizzolio S, Rabinowicz N, Rainero E, Lanzetti L, Serini G, Norman J, et al. (2012) Neuropilin-1-dependent regulation of EGF-receptor Signaling. *Cancer Res*. 72: 5801–11.

Robinson DR, Wu Y-M, & Lin S-F. (2000) The protein tyrosine kinase family of the human genome. *Oncogene*. 19: 5548–57.

Robinson SD, Reynolds LE, Kostourou V, Reynolds AR, da Silva RG, Tavora B, et al. (2009) αvβ3 Integrin Limits the Contribution of Neuropilin-1 to Vascular Endothelial Growth Factor-induced Angiogenesis. *J Biol Chem*. 284: 33966–81.

Rocha-Azevedo B, Lee S, Dasgupta A, Vega AR, de Oliveria LR, Kim T, et al. (2019) Heterogeneity in VEGF Receptor-2 mobility and organization on the endothelial cell surface leads to diverse activation models by VEGF. *bioRxiv*. doi:https://doi.org/10.1101/800946.

Rogers MS, & D'Amato RJ. (2012) Common polymorphisms in angiogenesis. *Cold Spring Harb Perspect Med*. 2: 1–19.

Roosterman D, Cottrell GS, Padilla BE, Muller L, Eckman CB, Bunnett NW, et al. (2007) Endothelin-converting enzyme 1 degrades neuropeptides in endosomes to control receptor recycling. *Proc Natl Acad Sci USA*. 104: 11838–43.

Roskoski R. (2008) VEGF receptor protein-tyrosine kinases: Structure and regulation. *Biochem Biophys Res Commun*. 375: 287–91.

Roskoski R. (2012) ERK1/2 MAP kinases: Structure, function, and regulation. *Pharmacol Res*. 66: 105–43.

Roskoski R. (2015a) A historical overview of protein kinases and their targeted small molecule inhibitors. *Pharmacol Res*. 100: 1–23.

Roskoski R. (2015b) Src protein-tyrosine kinase structure, mechanism, and small molecule inhibitors. *Pharmacol Res*. 94: 9–25.

Rossignol M, Gagnon ML, & Klagsbrun M. (2000) Genomic organization of human neuropilin-1 and neuropilin-2 genes: identification and distribution of splice variants and soluble isoforms. *Genomics*. 70: 211–22.

Roth L, Nasarre L, Dirrig-Grosch S, Aunis D, Cremel G, Hubert P, et al. (2008) Transmembrane Domain Interactions Control Biological Functions of Neuropilin-1. *Mol Biol Cell*. 19: 646–54.

Roy S, Bag AK, Singh RK, Talmadge JE, Batra SK, & Datta K. (2017) Multifaceted role of neuropilins in the immune system: Potential targets for immunotherapy. *Front Immunol*. 8: 1–27.

Ruch C, Skiniotis G, Steinmetz MO, Walz T, & Ballmer-Hofer K. (2007) Structure of a VEGF–VEGF receptor complex determined by electron microscopy. *Nat Struct Mol Biol*. 14: 249–50.

Ruoslahti E. (2017) Tumor penetrating peptides for improved drug delivery. *Adv Drug Deliv Rev*. 110: 3–12.

Sabin F. (1917) Origin and development of the primitive vessels of the chick and of the pig. *Contrib to Embryol*. 25: 79–81.

Saffarian S, Li Y, Elson EL, & Pikey LJ. (2007) Oligomerization of the EGF receptor investigated by live cell fluorescence intensity distribution analysis. *Biophys J*. 93: 1021–31.

Sakurai Y, Ohgimoto K, Kataoka Y, Yoshida N, & Shibuya M (2005) Essential role of Flk-1 (VEGF receptor 2) tyrosine residue 1173 in vasculogenesis in mice. *Proc Natl Acad Sci USA*. 102: 1076–81.

Salikhova A, Wang L, Lanahan AA, Liu M, Simons M, Leenders WPJ, et al. (2008) Vascular endothelial growth factor and semaphorin induce neuropilin-1 endocytosis via separate pathways. Circ Res 103: 1–18.

Sarabipour S, & Hristova K (2016a) Mechanism of FGF receptor dimerization and activation. *Nat Commun*. 7: 1–12.

Sarabipour S, Ballmer-Hofer K, & Hristova K. (2016b) VEGFR-2 conformational switch in response to ligand binding. *eLife*. 5: 1–23.

Sarabipour S, & Mac Gabhann F (2017) VEGF-A121a binding to Neuropilins – A concept revisited. *Cell Adh Migr*. 12: 204–11.

Schaller MD. (2010) Cellular functions of FAK kinases: Insight into molecular mechanisms and novel functions. *J Cell Sci*. 123: 1007–13.

Schlessinger J. (2000) Cell Signaling by Receptor Tyrosine Kinases. *Cell*. 103: 211–25.

Schöneberg J, De Lorenzi, F, Theek B, Blaeser A, Rommel D, Kuehne AJC, et al. (2018) Engineering biofunctional in vitro vessel models using a multilayer bioprinting technique. *Sci Rep*. 8: 1–13.

Scita G, & Di Fiore PP. (2010) The endocytic matrix. *Nature*. 463: 464–73.

Seeman P, Cheng D, & Iles GH. (1973) Structure of Membrane Holes in Osmotic & Saponin Hemolysis*. J Cell Biol*. 56: 1056–64.

Seerapu HR, Borthakur S, Kong N, Agrawal S, Drazba J, Vasanji A, et al. (2013) The cytoplasmic domain of neuropilin-1 regulates focal adhesion turnover. *FEBS Lett*. 587: 3392–99.

Senger D, Galli S, Dvorak A, Perruzzi C, Harvey V, & Dvorak H. (1983) Tumor Cells Secrete a Vascular Permeability Factor That Promotes Accumulation of Ascites Fluid. *Science*. 219: 983–85.

Senger D, Perruzzi C, Feder J, & Dvorak H. (1986) A Highly Conserved Vascular Permeability Factor Secreted by a Variety of Human & Rodent Tumor Cell Lines. *Cancer Res*. 46: 5629–32.

Shalaby F, Rossant J, Yamaguchi TP, Gertsenstein M, Wu XF, Breitman ML, et al. (1995) Failure of blood-island formation & vasculogenesis in Flk-1-deficient mice. *Nature*. 376: 62–66.

Shang G, Brautigam CA, Chen R, Lu D, & Torres-Vázquez J. (2017) Structure analyses reveal a regulated oligomerization mechanism of the PlexinD1 / GIPC / myosin VI complex. eLife. 6:1–25.

Shibuya M. (2013) Vascular endothelial growth factor and its receptor system: physiological functions in angiogenesis and pathological roles in various diseases. *J Biochem*. 153: 13–19.

Shintani Y, Takashima S, Asano Y, Kato H, Liao Y, Yamazaki S, et al. (2006) Glycosaminoglycan modification of neuropilin-1 modulates VEGFR2 signaling. *EMBO J*. 25: 3045–55.

Shiying W, Boyun S, Jianye Y, Wanjun Z, Ping T, Jiang L, et al. (2017) The Different Effects of VEGFA121 and VEGFA165 on Regulating Angiogenesis Depend on Phosphorylation Sites of VEGFR2. *Inflamm Bowel Dis*. 23: 603–16.

Shweiki D, Itin A, Soffer D, & Keshet E. (1992) Vascular endothelial growth factor induced by hypoxia may mediate hypoxia-initiated angiogenesis. *Nature*. 359: 843–45.

Sigismund S, Woelk T, Puri C, Maspero E, Tacchetti C, Transidico P, et al. (2005) Clathrin-independent endocytosis of ubiquitinated cargos. *Proc Natl Acad Sci USA*. 102: 2760–65.

Simon M, Rockl W, Hornig C, Grone E, Theis H, Weich H, et al. (1998) Receptors of Vascular Endothelial Growth Factor / Vascular Permeability Factor (VEGF / VPF) in Fetal and Adult Human Kidney : Localization & [^{125}1] VEGF Binding. *J Am Soc Nephrol*. 9: 1032–44.

Simon T, Gagliano T, & Giamas G. (2017) Direct Effects of Anti-Angiogenic Therapies on Tumor Cells: VEGF Signaling. *Trends Mol Med*. 23: 282–92.

Simons M, & Eichmann A. (2015) Molecular controls of arterial morphogenesis. *Circ Res*. 116: 1712–24.

Simons M, Gordon E, & Claesson-Welsh L. (2016) Mechanisms and regulation of endothelial VEGF receptor signalling. *Nat Rev Mol Cell Biol*. 17: 611–25.

Singh NK, Hansen DE, Kundumani-Sridharan V, & Rao GN. (2013) Both Kdr and Flt1 play a vital role in hypoxia-induced Src-PLD1-PKCgamma-cPLA2 activation and retinal neovascularization. *Blood*. 121: 1911–23.

Sklar LA, Finney DA, Oades ZG, Jesaitis AJ, Painter RG, & Cochrane CG. (1984) The dynamics of ligand-receptor interactions. *J Biol Chem*. 259: 5661–69.

Smith GA, Fearnley GW, Tomlinson DC, Harrison MA, & Ponnambalam S. (2015) The cellular response to vascular endothelial growth factors requires co-ordinated signal transduction, trafficking and proteolysis. *Biosci Rep*. 35: 1–15.

Smith GA, Fearnley GW, Abdul-Zani I, Wheatcroft SB, Tomlinson DC, Harrison MA, et al. (2016) VEGFR2 Trafficking, Signaling and Proteolysis is Regulated by the Ubiquitin Isopeptidase USP8. *Traffic*. 17: 53–65.

Soave M, Kellam B, Woolard J, Briddon SJ, & Hill SJ. (2020) NanoBiT Complementation to Monitor Agonist-Induced Adenosine A1 Receptor Internalization. *SLAS Discov*. 25: 186–94.

Soker S, Fidder H, Neufeld G, & Klagsbrun M. (1996) Characterization of Novel Vascular Endothelial Growth Factor (VEGF) Receptors on Tumor Cells That Bind VEGF via Its Exon 7-encoded Domain. *J Biol Chem*. 271: 5761–67.

Soker S, Takashima S, Miao HQ, Neufeld G, & Klagsbrun M. (1998) Neuropilin-1 Is Expressed by Endothelial & Tumor Cells as an Isoform-Specific Receptor for Vascular Endothelial Growth Factor. *Cell*. 92: 735–45.

Soker S, Miao HQ, Nomi M, Takashima S, & Klagsbrun M. (2002) VEGF165 mediates formation of complexes containing VEGFR-2 and neuropilin-1 that enhance VEGF165-receptor binding. *J Cell Biochem*. 85: 357–68.

Soldi R, Mitola S, Strasly M, Defilippi P, Tarone G, & Bussolino F (1999) Role of α(v)β3 integrin in the activation of vascular endothelial growth factor receptor-2. *EMBO J*. 18: 882–92.

Songyang Z, Carraway KL, Eck MJ, Harrison SC, Feldman RA, Mohammadi M, et al. (1995) Catalytic specificity of protein-tyrosine kinases is critical for selective signalling. *Nature*. 373: 536–39.

Sridharan R, Zuber J, Connelly SM, Mathew E, & Dumont ME. (2014) Fluorescent approaches for understanding interactions of ligands with G protein coupled receptors. *Biochim Biophys Acta Biomembr*. 1838: 15–33.

Starovasnik MA, Christinger HW, Wiesmann C, Champe MA, de Vos AM, & Skelton, NJ. (1999) Solution structure of the VEGF-binding domain of Flt-1: comparison of its free and bound states. *J Mol Biol*. 293: 531–44.

Starzec A, Vassy R, Martin A, Lecouvey M, di Benedetto M, Crépin M, et al. (2006) Antiangiogenic and antitumor activities of peptide inhibiting the vascular endothelial growth factor binding to neuropilin-1. *Life Sci*. 79: 2370–81.

Starzec A, Ladam P, Vassy R, Badache S, Bouchemal N, Navaza A, et al. (2007) Structure-function analysis of the antiangiogenic ATWLPPR peptide inhibiting VEGF165 binding to neuropilin-1 and molecular dynamics simulations of the ATWLPPR/neuropilin-1 complex. *Peptides*. 28: 2397–402.

Stephenson RP. (1956) A modification of receptor theory. *Br J Pharmacol*. 11: 379–93.

Stoddart L, Johnstone EKM, Wheal AJ, Goulding J, Robers MB, Machleidt T, et al. (2015a) Application of BRET to monitor ligand binding to GPCRs. *Nat Methods*. 12: 661–3.

Stoddart LA, Kilpatrick LE, Briddon SJ, & Hill SJ. (2015b) Probing the pharmacology of G protein-coupled receptors with fluorescent ligands. *Neuropharmacology*. 98: 48–57.

Stoddart LA, White CW, Nguyen K, Hill SJ, & Pfleger KDG. (2016) Fluorescence- and bioluminescence-based approaches to study GPCR ligand binding. *Br J Pharmacol*. 173: 3028–37.

Stuible M, & Tremblay ML. (2010) In control at the ER: PTP1B and the down-regulation of RTKs by dephosphorylation and endocytosis. *Trends Cell Biol*. 20: 672–79.

Sugahara KN, Teesalu T, Karmali PP, Kotamraju VR, Agemy L, Girard OM, et al. (2009) Tissue-Penetrating Delivery of Compounds & Nanoparticles into Tumors. *Cancer Cell.* 16: 510–20.

Sugahara KN, Teesalu T, Prakash Karmali P, Ramana Kotamraju V, Agemy L, Greenwald DR, et al. (2010) Coadministration of a Tumor-Penetrating Peptide Enhances the Efficacy of Cancer Drugs. *Science.* 328: 1031–35.

Sun Z, Li X, Massena S, Kutschera S, Padhan N, Gualandi L, et al. (2012) VEGFR2 induces c-Src signaling and vascular permeability in vivo via the adaptor protein TSAd. *J Exp Med*. 209: 1363–77.

Sungkaworn T, Jobin M-L, Burnecki K, Weron A, Lohse MJ, & Calebiro D. (2017) Single-molecule imaging reveals receptor–G protein interactions at cell surface hot spots. Nature. 550: 543–47.

Swendeman S, Mendelson K, Weskamp G, Horiuchi K, Deutsch U, Scherle P, et al. (2008) VEGF-A stimulates ADAM17-dependent shedding of VEGFR2 and crosstalk between VEGFR2 & ERK signalling. *Circ Res*. 103: 916–18.

Takagi S, Kasuya Y, Shimizu M, Matsuura T, Tsuboi M, Kawakami A, et al. (1995) Expression of a cell adhesion molecule, neuropilin, in the developing chick nervous system. *Dev Biol*. 170: 207–22.

Takahashi T, Ueno H, & Shibuya M. (1999) VEGF activates protein kinase C-dependent, but Ras-independent Raf-MEK-MAP kinase pathway for DNA synthesis in primary endothelial cells. *Oncogene*. 18: 2221–30.

Takahashi T, Yamaguchi S, Chida K, & Shibuya M. (2001) A single autophosphorylation site on KDR / Flk-1 is essential for VEGF-A-dependent activation of PLC-g and DNA synthesis in vascular endothelial cells. *EMBO J*. 20: 2678–78.

Takashima S, Kitakaze M, Asakura M, Asanuma H, Sanada S, Tashiro F, et al. (2002) Targeting of both mouse neuropilin-1 and neuropilin-2 genes severely impairs developmental yolk sac & embryonic angiogenesis. *Proc Natl Acad Sci USA*. 99: 3657–62.

Tao Q, Backer MV, Backer JM, & Terman BI. (2001) Kinase Insert Domain Receptor (KDR) Extracellular Immunoglobulin-like Domains 4-7 Contain Structural Features That Block Receptor Dimerization and Vascular Endothelial Growth Factor-induced Signaling. *J Biol Chem*. 276: 21916–23.

Taylor SS, & Kornev AP. (2011) Protein kinases: Evolution of dynamic regulatory proteins. *Trends Biochem Sci*. 36: 65–77.

Teesalu T, Sugahara KN, Kotamraju VR, & Ruoslahti E. (2009) C-end rule peptides mediate neuropilin-1-dependent cell, vascular, and tissue penetration. *Proc Natl Acad Sci USA*. 106: 16157–62.

Teran M, & Nugent MA. (2015) Synergistic binding of Vascular Endothelial Growth Factor-A and its receptors to heparin selectively modulates complex affinity. *J Biol Chem*. 290: 16451–62.

Teran M, & Nugent MA. (2018) Characterization of receptor binding kinetics for Vascular Endothelial Growth Factor-A using SPR. *Anal Biochem*. 564: 21–31.

Thieltges KM, Avramovic D, Piscitelli CL, Mueller SM, Kaspar H, Kurt B, et al. (2018) Characterization of a drug - targetable allosteric site regulating vascular endothelial growth factor signalling. *Angiogenesis*. 21: 533–43.

Tischer E, Mitchell R, Hartman T, Silva M, Gospodarowicz D, Fiddes JC, et al. (1991) The Human Gene for Vascular Endothelial Growth-Factor - Multiple Protein Forms Are Encoded Through Alternative Exon Splicing. *J Biol Chem*. 266: 11947–54.

Tonks NK, Diltz CD, & Fischer EH. (1988) Purification of the major protein-tyrosine-phosphatases of human placenta. *J Biol Chem*. 263: 6722–30.

Tonks NK, & Neel BG. (2001) Combinatorial control of the specificity of protein tyrosine phosphatases. *Curr Opin Cell Biol*. 13: 182–95.

Traub LM, Downs MA, Westrich JL, & Fremont DH. (1999) Crystal structure of the α appendage of AP-2 reveals a recruitment platform for clathrin-coat assembly. *Proc Natl Acad Sci USA*. 96: 8907–12.

Tummino PJ, & Copeland RA. (2008) Residence time of receptor-ligand complexes and its effect on biological function. *Biochemistry*. 47: 5481–92.

Uchida K, Uchida S, Nitta K, Yumura W, Marumo F, & Nihei H. (1994) Glomerular endothelial cells in culture express and secrete vascular endothelial growth factor. *Am J Physiol*. 266: 1–8.

Ullrich A, & Schlessinger J. (1990) Signal transduction by receptors with tyrosine kinase activity. *Cell*. 61: 203–12.

van den Hoff M, Labruyere WT, Moorman A, & Lamers WH. (1993) Mammalian gene expression is improved by use of a longer SV40 early polyadenylation cassette. *Nucleic Acids Res*. 1: 4987–88.

Vander Kooi CW, Jusino MA, Perman B, Neau DB, Bellamy HD, & Leahy DJ. (2007) Structural basis for ligand and heparin binding to neuropilin B domains. *Proc Natl Acad Sci USA*. 104: 6152–57.

Varey AHR, Rennel ES, Qiu Y, Bevan HS, Perrin RM, Raffy S, et al. (2008) $VEGF_{165}b$, an antiangiogenic VEGF-A isoform, binds and inhibits bevacizumab treatment in experimental colorectal carcinoma: Balance of pro- and antiangiogenic VEGF-A isoforms has implications for therapy. *Br J Cancer*. 98: 1366–79.

Ved N, Hulse RP, Bestall SM, Donaldson LF, Bainbridge JW, & Bates DO (2017) Vascular endothelial growth factor-A 165 b ameliorates outer-retinal barrier and vascular dysfunction in the diabetic retina. *Clin Sci*. 131: 1225–43.

Vempati P, Popel AS, & Mac Gabhann F. (2014) Extracellular regulation of VEGF: Isoforms, proteolysis, and vascular patterning. *Cytokine Growth Factor Rev*. 25: 1–19.

Venables JP. (2006) Unbalanced alternative splicing and its significance in cancer. *BioEssays*. 28: 378–86.

Verstraete K, & Savvides SN. (2012) Extracellular assembly and activation principles of oncogenic class III receptor tyrosine kinases. *Nat Rev Cancer*. 12: 753–66.

Vestweber D. (2008) VE-cadherin: The major endothelial adhesion molecule controlling cellular junctions & blood vessel formation. *Arterioscler Thromb Vasc Biol*. 28: 223–32.

Volz B, Orberger G, Porwoll S, Hauri HP, & Tauber R. (1995) Selective reentry of recycling cell surface glycoproteins to the biosynthetic pathway in human hepatocarcinoma HepG2 cells. *J Cell Biol*. 130: 537–51.

Von Wronski MA, Raju N, Pillai R, Bogdan NJ, Marinelli ER, Nanjappan P, et al. (2006) Tuftsin binds neuropilin-1 through a sequence similar to that encoded by exon 8 of vascular endothelial growth factor. *J Biol Chem*. 281: 5702–10.

Wagner MJ, Stacey MM, Liu BA, & Pawson T. (2013) Molecular mechanisms of SH2- and PTB-Domain-containing proteins in receptor tyrosine kinase signalling. *Cold Spring Harb Perspect Biol*. 5: 1–19.

Waksman G, Kominos D, Robertson SC, Pant N, Baltimore D, Birge RB, et al. (1994) Crystal structure of the phosphotyrosine recognition domain SH2 of the Src oncogene product complexed with tyrosine-phosphorylated peptides. *Nature*. 40: 611–18.

Waltenberger J, Claesson-Welsh L, Siegbahn A, Shibuya M, & Heldin C. (1994) Different Signal-Transduction Properties of Kdr and Flt1, 2 Receptors for Vascular Endothelial Growth-Factor. *J Biol Chem*. 269: 26988–95.

Wang L, Mukhopadhyay D, & Xu X. (2006) C terminus of RGS-GAIP-interacting protein conveys neuropilin-1-mediated signaling during angiogenesis. *FASEB J*. 20: 1513–15.

Wang Y, Gao J, Guo X, Tong T, Shi X, Li L, et al. (2014) Regulation of EGFR nanocluster formation by ionic protein-lipid interaction. *Cell Res*. 24: 959–76.

Webb DJ, Donais K, Whitmore LA, Thomas SM, Turner CE, Parsons JT, et al. (2004) FAK-Src signalling through paxillin, ERK and MLCK regulates adhesion disassembly. *Nat Cell Biol*. 6: 154–61.

Weddell JC, & Imoukhuede PI. (2017) Integrative meta-modeling identifies endocytic vesicles, late endosome and the nucleus as the cellular compartments primarily directing RTK signalling. *Integr Biol*. 9: 464–84.

Wedge SR, Kendrew J, Hennequin LF, Valentine PJ, Barry ST, Brave SR, et al. (2005) AZD2171: A highly potent, orally bioavailable, vascular endothelial growth factor receptor-2 tyrosine kinase inhibitor for the treatment of cancer. *Cancer Res*. 65: 4389–400.

Weekes CD, Beeram M, Tolcher AW, Papadopoulos KP, Gore L, Hegde P, et al. (2014) A phase I study of the human monoclonal anti-NRP1 antibody MNRP1685A in patients with advanced solid tumors. *Invest New Drugs*. 32: 653–60.

Wells AL, Lin AW, Chen LQ, Safer D, Cain SM, Hasson T, et al. (1999) Myosin VI is an actin-based motor that moves backwards. *Nature*. 401: 505–08.

West MA, Bretscher MS, & Watts C. (1989) Distinct endocytotic pathways in epidermal growth factor-stimulated human carcinoma A431 cells. *J Cell Biol*. 109: 2731–39.

West MA, Prescott AR, Eskelinen EL, Ridley AJ, & Watts C. (2000) Rac is required for constitutive macropinocytosis by dendritic cells but does not control its downregulation. *Curr Biol*. 10: 839–48.

West DC, Rees CG, Duchesne L, Patey SJ, Terry CJ, Turnbull JE, et al. (2005) Interactions of multiple heparin binding growth factors with neuropilin-1 and potentiation of the activity of fibroblast growth factor-2. *J Biol Chem*. 280: 13457–64.

Whitaker GB, Limberg BJ, & Rosenbaum JS. (2001) Vascular Endothelial Growth Factor Receptor-2 and Neuropilin-1 Form a Receptor Complex that is Responsible for the Differential Signaling Potency of VEGF165 and VEGF121. *J Biol Chem*. 276: 25520–31.

White CW, Vanyai HK, See HB, Johnstone EKM, & Pfleger KDG. (2017) Using NanoBRET and CRISPR/Cas9 to monitor proximity to a genome-edited protein in real-time. *Sci Rep*. 7: 1–14.

White CW, Caspar B, Vanyai HK, Pfleger KDG & Hill, SJ. (2020) CRISPR-Mediated Protein Tagging with Nanoluciferase to Investigate Native Chemokine Receptor Function and Conformational Changes. Cell Chem Biol. doi: 10.1016/j.chembiol.2020.01.010. 1–12.

Wiesmann C, Fuh G, Christinger HW, Eigenbrot C, Wells JA, & de Vos AM. (1997) Crystal Structure at 17 Å Resolution of VEGF in Complex with Domain 2 of the Flt-1 Receptor. *Cell*. 91: 695–704.

Wimmer-Kleikamp SH, Janes PW, Squire A, Bastiaens PIH, & Lakmann M. (2004) Recruitment of Eph receptors into signaling clusters does not require ephrin contact. *J Cell Biol*. 164: 661–66.

Windwarder M, Yelland T, Djordjevic S, & Altmann F. (2016) Detailed characterization of the O-linked glycosylation of the neuropilin-1 c/MAM-domain. *Glycoconj J*. 33: 387–97.

Witmer AN, Dai J, Weich HA, Vrensen GFJM, & Schlingemann, RO. (2002) Expression of vascular endothelial growth factor receptors 1, 2, and 3 in quiescent endothelia. *J Histochem Cytochem*. 50: 767–77.

Woods DF, & Bryant PJ. (1991) The discs-large tumor suppressor gene of Drosophila encodes a guanylate kinase homolog localized at septate junctions. *Cell*. 66: 451–64.

Woolard J, Wang W, Bevan HS, Qiu Y, Morbidelli L, Pritchard-Jones RO, et al. (2004) $VEGF_{165}b$, an Inhibitory Vascular Endothelial Growth Factor Splice Variant: Mechanism of Action, In vivo Effect On Angiogenesis and Endogenous Protein Expression. *Cancer Res.* 64: 7822–35.

Woolard J, Bevan HS, Harper SJ, & Bates D. (2009) Molecular diversity of VEGF-A as a regulator of its biological activity. *Microcirculation*. 16: 572–92.

World Health Organization. (2019) *World Health Organization Model List of Essential Medicines*. 21st edition. Geneva: WHO. Licence: CC BY-NC-SA 3.0 IGO.

Wu P, Nielsen TE, & Clausen MH. (2015) FDA-approved small-molecule kinase inhibitors. *Trends Pharmacol Sci*. 36: 422–39.

Xie Y, Mansouri M, Rizk A, & Berger P. (2019) Regulation of VEGFR2 trafficking and signaling by Rab GTPase-activating proteins. *Sci Rep*. 9: 1–12.

Xin H, Zhong C, Nudleman E, & Ferrara N. (2016) Evidence for Pro-angiogenic Functions of VEGF-Ax. *Cell*. 167: 275–284.

Xu D, Fuster MM, Lawrence R, & Esko JD. (2011) Heparan sulfate regulates VEGF165- and VEGF121- mediated vascular hyperpermeability. *J Biol Chem*. 286: 737–45.

Yamada Y, Nezu JI, Shimane M, & Hirata Y. (1997) Molecular cloning of a novel vascular endothelial growth factor, VEGF-D. *Genomics*. 42: 483–88.

Yamamoto H, Rundqvist H, Branco C, & Johnson RS. (2016) Autocrine VEGF Isoforms Differentially Regulate Endothelial Cell Behavior. *Front Cell Dev Biol*. 4: 1–12.

Yamano S, Dai J, & Moursi AM. (2010) Comparison of transfection efficiency of nonviral gene transfer reagents. *Mol Biotechnol*. 46: 287–300.

Yamazaki Y, Matsunaga Y, Tokunaga Y, Obayashi S, Saito M, & Morita T. (2009) Snake venom vascular endothelial growth factors (VEGF-Fs) exclusively vary their structures and functions among species. *J Biol Chem*. 284: 9885–91.

Yanagawa M, Hiroshima M, Togashi Y, Abe M, Yamashita T, Shichida Y, et al. (2018) Single-molecule diffusion-based estimation of ligand effects on G protein–coupled receptors. Sci Signal. 11: 1–16.

Yanagi Y. (2008) Age-related macular degeneration. *N Engl J Med*. 358: 2606–17.

Yang Y, Yuzawa S, & Schlessinger J. (2008) Contacts between membrane proximal regions of the PDGF receptor ectodomain are required for receptor activation but not for receptor dimerization. *Proc Natl Acad Sci USA*. 105: 7681–86.

Yang Y, Xie P, Opatowsky Y, & Schlessinger J. (2010) Direct contacts between extracellular membrane-proximal domains are required for VEGF receptor activation & cell signalling. *Proc Natl Acad Sci USA*. 107: 1906–11.

Ye X, Abou-Rayyah Y, Bischoff J, Ritchie A, Sebire NJ, Watts P, et al. (2016) Altered ratios of pro- and anti-angiogenic VEGF-A variants and pericyte expression of DLL4 disrupt vascular maturation in infantile haemangioma. *J Pathol*. 239: 139–51.

Yelland T, & Djordjevic S. (2016) Crystal Structure of the Neuropilin-1 MAM Domain: Completing the Neuropilin-1 Ectodomain Picture. *Structure*. 24: 2008–15.

Yuzawa S, Opatowsky Y, Zhang Z, Mandiyan V, Lax I, & Schlessinger J. (2007) Structural Basis for Activation of the Receptor Tyrosine Kinase KIT by Stem Cell Factor. *Cell*. 130: 323–34.

Zhou HJ, Xu Z, Wang Z, Zhang H, Simons M, & Min W. (2018) SUMOylation of VEGFR2 regulates its intracellular trafficking and pathological angiogenesis. *Nat Commun*. 9: 1–16.

Zhu Z, Hattori K, Zhang H, Jimenez X, Ludwig DL, Dias S, et al. (2003) Inhibition of human leukemia in an animal model with human antibodies directed against vascular endothelial growth factor receptor 2. Correlation between antibody affinity & biological activity. *Leukemia*. 17: 604–11.